Atmospheric monitoring and gamma-ray data analysis with the H.E.S.S. telescope array

Spangler, Denise Helen

Spangler, Denise Helen (2008) *Atmospheric monitoring and gamma-ray data analysis with the H.E.S.S. telescope array*, Durham theses, Durham University. Available at Durham E-Theses Online: http://etheses.dur.ac.uk/2544/

Atmospheric Monitoring and Gamma-ray Data Analysis with the H.E.S.S. Telescope Array

by

Denise Helen Spangler

Durham
University

Submitted in conformity with the requirements
for the degree of Doctor of Philosophy

Department of Physics
University of Durham
South Road
Durham. UK.

Abstract

The High Energy Stereoscopic System (H.E.S.S.) consists of an array of four ground-based imaging atmospheric Cherenkov telescopes. The aim of the system is to detect Cherenkov radiation emitted from extensive air showers caused by very high energy gamma-ray radiation interacting with the atmosphere. The implementation of more than one telescope allows multiple views of a single extensive air shower, providing a more accurate reconstruction of the event and offerring greater cosmic ray background suppression, allowing better analysis of gamma rays. Unlike charged particles, gamma rays reach the Earth in the direction in which they were emitted thus allowing us to investigate the emission mechanisms and properties of various gamma-ray sources.

Since Cherenkov radiation is produced and propagates through the atmosphere, the atmosphere plays a large role in the detection of gamma rays and must be monitored carefully. This thesis will explore the effects of the atmosphere on the H.E.S.S. telescopes and gamma-ray analysis and is structured as follows: The first chapter highlights all the important aspects of very high energy (VHE) gamma-ray astronomy focusing on the H.E.S.S. system. Chapter 2 gives a general overview of active galactic nuclei (AGN) and the extragalactic background light (EBL) as a precursor to data analysis in Chapter 4. Chapter 3 discusses the atmosphere and atmospheric monitoring performed at the H.E.S.S. site. I present data analysis of the four atmospheric monitoring instruments revealing seasonal trends and cross-correlations between instruments. Chapter 4 contains the heart of the thesis, where all aspects from the previous chapters are integrated to show the effects of the atmosphere on the H.E.S.S. system and subsequent AGN and EBL data analysis. I first compare trigger rate data from the telescopes and data from the atmospheric monitoring instruments. It is shown that backscatter, sky radiance, and transmissivity are correlated to the trigger rate to various degrees. It is then shown that gamma-ray data is less affected by varying atmospheric conditions, especially for the higher energy gamma rays. Active atmospheric calibration is then presented as a way to correct gamma-ray data when there is a large amount of low-lying aerosols in the atmosphere. This method is subsequently used to correct the gamma-ray fluxes for 2 AGN, PKS 2155-304 and H 2356-309. It is shown that the correction works best for the higher flux source PKS 2155-304 rather than H 2356-309 whose flux is often consistent with zero. These AGN are then used to calculate upper limits to the EBL using a simple monoenergetic model. The upper limits to the EBL in the wavelength range of 0.4-1 μm are shown to be consistent with the results from the most exhaustive study of the EBL testing over 8 million EBL shapes. Chapter 5 is the concluding chapter discussing future work to be done at H.E.S.S. site, with the addition of a new LIDAR and VHE telescope, and beyond.

Contents

Declaration

The material contained within this thesis has not previously been submitted for a degree at the Durham University or any other university. The research reported within this thesis has been conducted by the author unless indicated otherwise.

Copyright Notice

Acknowledgements

Thank you to everyone who pushed me to finish. If it wasn't without those who believed in me I would probably be wandering the Ecuadorian rainforests.

Thank you to my family who has always been supportive of me making the trek half way around the world to study the things that are so out of this world. Thanks to Dr. Paula Chadwick for all the help in getting me through this thing and for invaluable feedback on the rough versions of my thesis. Thanks to Dr. Roland Le Gallou who supported me through the first half of my journey and to Dr. Sam Nolan who helped me along to the finish line. Thanks to the rest of the Durham Gamma-ray Group for all the laughs and tomfoolery, and Christos...it's been real.

And last but not least thanks to Mark Saunders who gave me infinite love and support through the most grueling stages of my PhD and who read the reread my thesis with the most painful scrutiny.

This thesis has been made possible and was funded by the Physics Department and the Durham Doctoral Fellowship Scheme.

Dedication

I dedicate this work to all the particles that made this possible. Particularly, protons, electrons, muons, and of course, the highly energetic gamma ray.

I would also like to dedicate this thesis to the parents who created me and to the parents who created them, and so on and so on...

To standing on the shoulders of giants...

"God is the collective Universe."

Chapter 1

Very High Energy Gamma-ray Astronomy

Gamma rays are the most energetic form of radiation, with energies ranging from ~100 keV (10^5 eV) to over 100 TeV (10^{14} eV). This range spans nine orders of magnitude, which is approximately the range of X-rays to microwaves, and so there are pronounced differences between the lowest and highest ends of this range. Namely, there are distinct methods for detecting different bands of energy. These energy boundaries are arbitrary and are listed in Table 1 as defined by Weekes [152].

Gamma rays with energies greater than ~30 MeV are dominated by non-thermal processes and are a means to observe the extraordinary and extreme Universe. The discriminating factor separating high energy (HE) and very high energy (VHE) gamma rays is the physics involved in their *detection*. High energy gamma rays are detected in space above the atmosphere by pair production while the highest energies (VHE and ultra high energy (UHE)) are indirectly detected on the ground due to their extremely low flux. At the present time AGILE is the only running space-based experiment [103], while GLAST is set to launch in 2008 [113]. There are many ground-based experiments running or in development and will be briefly discussed in Section 1.5. This thesis will focus on H.E.S.S., a leading system of ground-based VHE gamma-ray telescopes.

The High Energy Stereoscopic System (H.E.S.S.) is a ground-based gamma-ray observatory used to detect VHE gamma rays, an important part of the total gamma-ray spectrum. Very high energy gamma rays are an exciting way to look at the different objects in the Universe, opening a door to the newest field in astronomy. Moreover, VHE gamma rays hold a key to understanding long standing problems in astronomy such as

Table 1.1: The different gamma-ray energy ranges and their detection methods [152].

Gamma Rays	Energy Range	Detection Method
Low Energy (LE)	100 - 300 keV	photoelectric effect
Medium Energy (ME)	300 keV - 30 MeV	Compton scattering
High Energy (HE)	30 MeV - 100 GeV	pair production
Very High Energy (VHE)	100 GeV - 100 TeV	Cherenkov radiation
Ultra High Energy (UHE)	>100 TeV	extensive air showers

the origins of cosmic rays and information about the extragalactic background light.

1.1 Cosmic Rays

In 1912, pioneering work was undertaken by Victor Hess[1] in attempt to investigate the source of ionisation in the atmosphere. He risked life and limb in balloon experiments armed with a gold leaf electroscope to measure this ionisation up to altitudes reaching over 5 km. On his flights he discovered that ionisation increased with altitude. This claim was then confirmed by Werner Kölhorster travelling up to even greater heights of 9 km. This increasing ionisation was attributed to particles originating from outside of the Earth, and was coined 'cosmic rays' in 1926 by Robert Millikan who wrongly thought these particles to be gamma rays due to their penetrating power. It wasn't until the 1930s, through cosmic ray measurements at varying latitudes, that cosmic rays were confirmed to be charged particles [132].

We now know that cosmic rays are high energy particles composed mainly of nuclei (97% by number) and 3% electrons. The nuclei consist of 87% protons, 12% helium, and 1% heavier elements [101]. The energy density of high energy cosmic rays (with energy per nucleon > 1 GeV) is approximately 1 eV cm^{-3}. This quantity is comparable to the energy density of the interstellar magnetic field (~ 0.2 eV cm^{-3}), the local energy density of starlight (~ 0.3 eV cm^{-3}), and the energy density of the microwave background radiation (~ 0.3 eV cm^{-3}) [101]. This highlights the fact that cosmic rays contribute a significant fraction of energy to the Universe.

The energy distribution of cosmic rays takes the shape of a power law, suggesting 'non-thermal' processes are used to accelerate the particles; 'non-thermal' technically

---

[1] It is in honour of Victor Hess that the discussed system used to probe into the nature of cosmic rays through VHE gamma rays is named H.E.S.S.

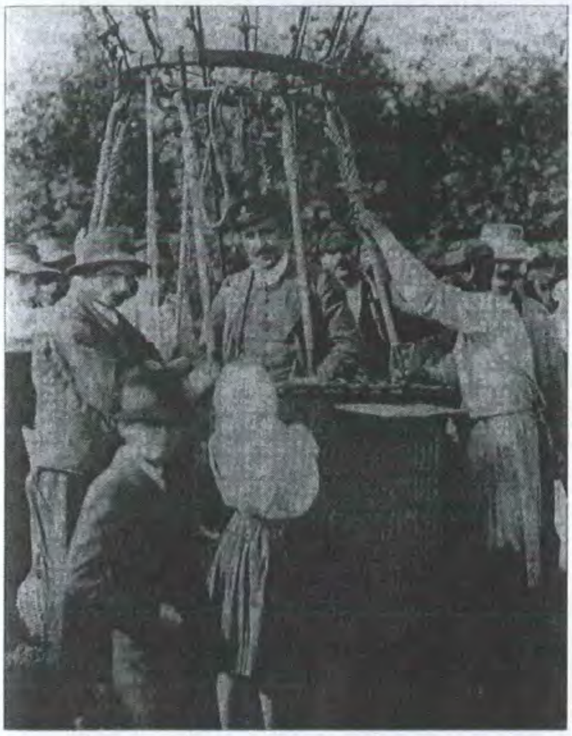

Figure 1.1: Victor Hess on his famous balloon flight in 1912, from [69].

refers to the fact that the spectrum is continuous and non-Maxwellian. In practice, non-thermal refers to radiation that cannot be accounted for by blackbody radiation or thermal Bremsstrahlung [102]. Figure 1.2 shows the energy distribution of cosmic rays spanning 31 orders of magnitude, with marked features of the spectrum called the *knee* and *ankle*, points where the spectrum changes slope.

Cosmic rays with energies less than $\sim 10^{14}$ eV travel in twisted paths influenced by galactic and extragalactic magnetic fields. Figure 1.3 shows the trajectory of a charged particle influenced by the Earth's magnetic field. It can be seen that information about the point of origin is lost.

Galactic cosmic rays are thought to come from supernova explosions based on current supernova shock models, with particles being accelerated to relativistic energies through shock fronts [152], but conclusive observational evidence has not been found to support this theory. From these shock models, TeV gamma-ray emission from high energy cosmic rays is predicted. Thus, detection of gamma rays should give us information about the acceleration sites of cosmic rays. Since gamma rays travel in straight lines from their place

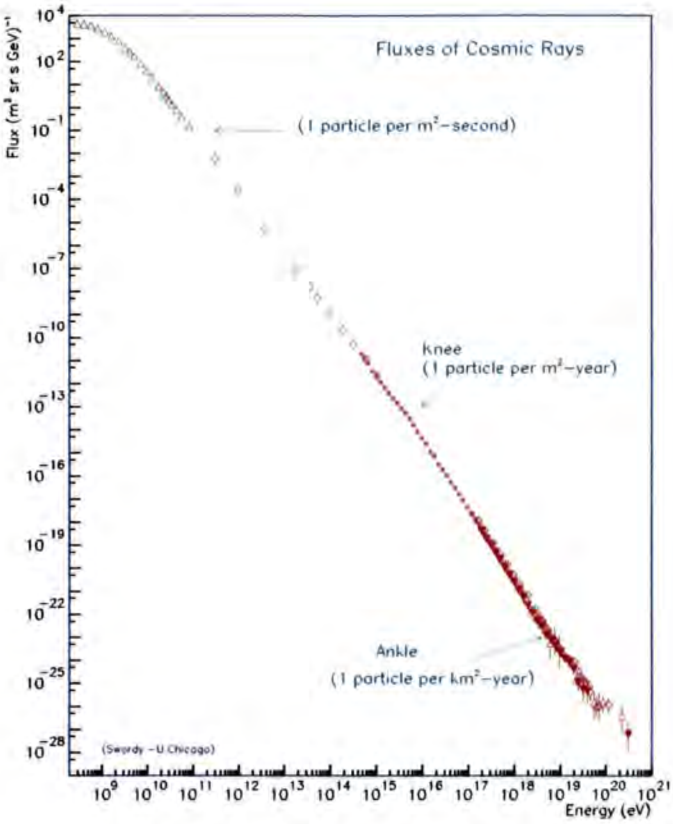

Figure 1.2: The cosmic ray spectrum measured from above the atmosphere from data compiled by [49]. The spectrum exhibits a power-law behaviour above 10^9 eV until the *knee* of the spectrum where it changes slope and again at the *ankle*. It is also remarkable to note that the differential flux spans 31 orders of magnitude.

of origin[2], models can be tested to investigate how sources emit VHE radiation through the acceleration of cosmic ray particles such as electrons or protons.

With the advent of gamma-ray astronomy, we are closer to understanding cosmic-ray acceleration, specifically from the supernova remnant RX J1713.7-3946. The X-ray and gamma-ray spectrum from this source indicates the acceleration of charged particles to energies greater than 100 TeV [27]. It is also thought that gamma-ray emission comes from accelerated protons along with electrons in regions with high densities, but such processes are difficult to disentangle without multi-wavelength studies [5]. Whereas ob-

---

[2] It should be noted that neutrinos and neutrons are neutrally charged and therefore travel in straight lines from their point of origin. However, neutrinos with their small interaction cross section are much harder to detect, while free neutrons decay into protons with a half-life of 10.3 minutes.

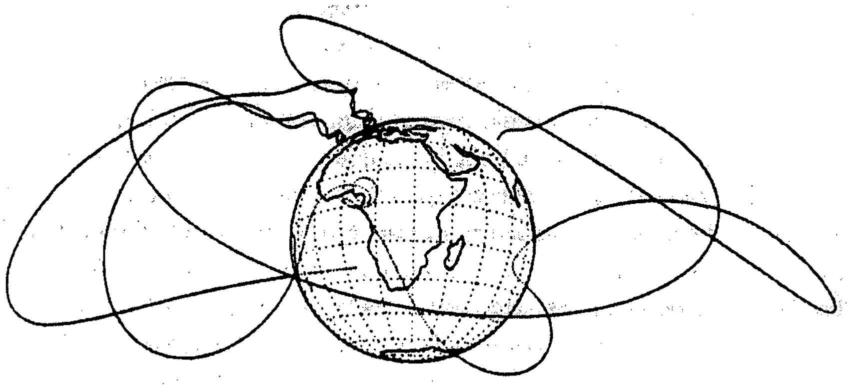

Figure 1.3: Cosmic rays travelling in twisted paths due to the Earth's magnetic field, from [69].

servations of other supernova remnants can be explained by electron acceleration alone, this is the first source to give possible verification for the acceleration of protons to such high energies. Other sources that would be potential sites for cosmic ray acceleration are typically supernova remnants associated with molecular clouds, which would provide sufficient particle density for the interaction and acceleration of hadrons [111].

1.2 VHE Gamma Ray Interactions

Gamma-ray interactions come in many forms. Gamma rays can be produced through interactions with matter and radiation fields; they can result from hadronic interactions through particle decay; they can be destroyed through pair production interacting with matter or other photons, or they can be produced through particle annihilations. These processes are well studied physical phenomena and will be explained briefly in this section.

1.2.1 Compton Scattering

Compton scattering is an inelastic scattering process in which a photon scatters off an electron (or any charged particle), transferring energy from the photon to the electron, as shown in Figure 1.4. The amount of energy transfer can be derived from conservation of energy and momentum. Assuming the electron is initially at rest, the change in wavelength of the incoming, λ_0, and scattered photon, λ_1 is,

$$\lambda_1 - \lambda_0 = h/m_e c(1 - \cos\theta_{IC}) \tag{1.1}$$

where h is the Planck constant, m_e is the mass of the electron, c is the speed of light, and θ_{IC} is the angle between the photon's incoming and scattered path. The Compton wavelength is defined as $\lambda_C \equiv h/m_e c$ and represents the typical change of wavelength. For long wavelengths, $\lambda \gg \lambda_C$ (or alternatively, a photon energy $\epsilon_0 = hc/\lambda_0 \ll m_e c^2$), the change in wavelength is negligibly small, and it can be assumed that there is no change in photon energy in the rest frame of the electron. This is a case of elastic scattering that can be described by classical Thomson scattering. For photon energies, $\epsilon_0 >> m_e c^2$, quantum effects come into play and Compton scattering becomes less efficient due to a smaller (Klein-Nishina) cross section than that of the Thomson cross section.

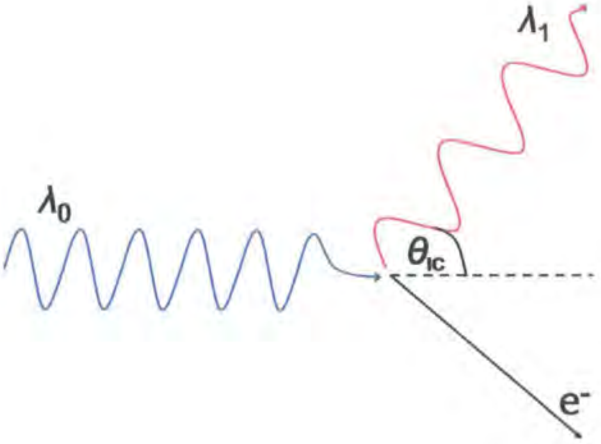

Figure 1.4: Compton scattering of a high energy photon off an electron at rest.

Inverse Compton Scattering

In gamma-ray production, it is not photons transferring energy to electrons, but electrons transferring energy to photons that is important. Energy may be transferred from a fast moving electron to a lower energy photon in a process known as inverse Compton (IC) scattering. The way in which relativistic electrons transfer energy to low energy photons to create high energy photons can be described by looking at the relation between the incoming and scattered photon in two frames: the observer's frame (F) and the rest frame of the electron (F'), illustrated in Figure 1.5. The equations describing this relation can be found in [128] and are,

$$\begin{aligned}\epsilon_0' &= \epsilon_0\gamma(1-\beta\cos\theta)\\ \epsilon_1 &= \epsilon_1'\gamma(1+\beta\cos\theta')\end{aligned}$$

where ϵ_0' is the energy of the photon as seen in the electron's frame and ϵ_1 is the final energy of the photon seen by the observer. For the case of relativistic electrons, the ratio of energies between the incoming photon and scattered photon measured by the observer, and the energy of the photon in the electron's frame is, $1 : \gamma^2 : \gamma$, where γ is the Lorentz factor characterising the electron's relativistic motion. This ratio holds provided that the condition for Thomson scattering is met in the rest frame of the electron (where the photon energy does not change). Photons up to energies of 100 keV (in the electron frame) can satisfy this condition and electrons can have Lorentz factors up to $\gamma = 10^4$. This shows that photons can be boosted up to very high energies through IC scattering.

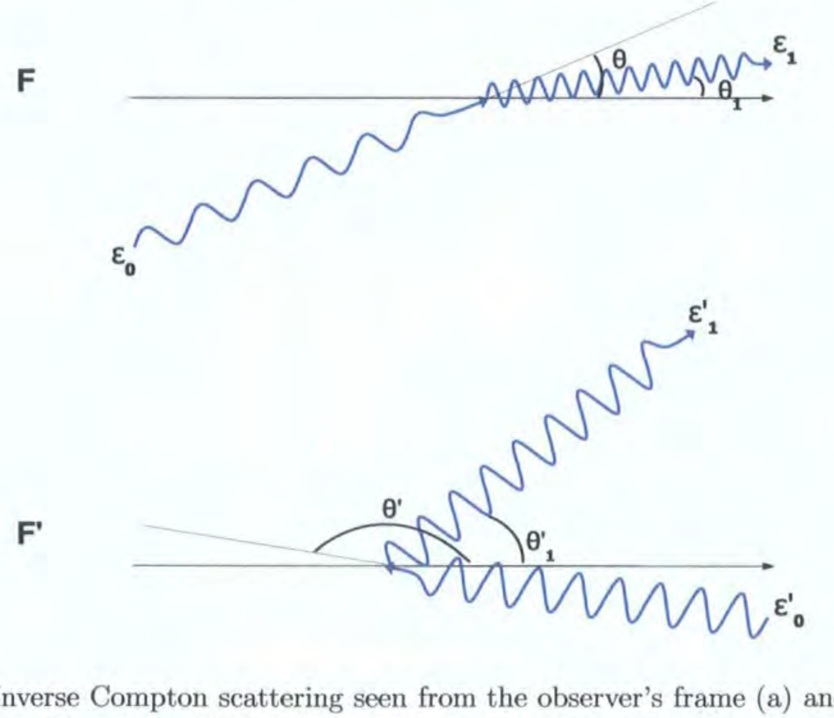

Figure 1.5: Inverse Compton scattering seen from the observer's frame (a) and the electron's stationary frame (b), adapted from [128].

Inverse Compton scattering is a gamma-ray production method that dominates many environments. Some of these include, but are not limited to: active galactic nuclei [14, 10], supernova remnants [20, 5], pulsar wind nebulae [15, 21], and microquasar jets [11].

1.2.2 Synchrotron Radiation

The treatment of proton synchrotron radiation is identical to the more common electron synchrotron radiation, but is scaled to the proton mass. For this reason synchrotron radiation is discussed in the context of electrons.

The force of a magnetic field causes a non-relativistic electron to move in a circular or helical path with the frequency [73],

$$\omega_c = \frac{eB}{m_e c}, \tag{1.2}$$

where e is the charge of an electron, and B is the magnetic field magnitude. This electron will radiate electromagnetic waves equally in all directions, like a dipole, with a frequency of ω_c, as shown in Figure 1.6(a). Conversely, relativistic electrons will radiate energy in the shape of a cone that is beamed forward in the direction of the electron's instantaneous velocity, as shown in in Figure 1.6(b). The angle of emission of the cone is given by [151],

$$\theta_S \approx \frac{m_e c^2}{E_e} = \frac{1}{\gamma}, \tag{1.3}$$

where E_e is the energy of the electron. In general, radiation will be observed from a relativistic electron with the frequency,

$$\omega_r = \frac{\omega_c}{\gamma}, \tag{1.4}$$

Therefore, a viewer situated perpendicular to the electron's plane of rotation will observe pulses of synchrotron emission with a period, $P = 2\pi/\omega_r$. The width of the observed pulses (Δt_o) is smaller than the time between the pulses (Δt) by a factor of $\Delta s/c$, where $\Delta s = 2a/\gamma$ is the distance travelled by the particle and a is the gyromagnetic radius, as shown in Figure 1.6(c). Using the relativistic equations of motion for a particle in a magnetic field,

$$\gamma m_e \frac{\Delta \mathbf{v}}{\Delta t} = \frac{e}{c}\mathbf{v} \times \mathbf{B} \tag{1.5}$$

with $|\Delta v| = v\Delta\theta$. Solving for $\Delta t = (2m_e c)/(eB \sin\alpha) = 2/(\omega_c \sin\alpha)$, where α is the angle between the velocity of the particle and magnetic field, the width of the observed pulses therefore becomes [128],

$$\Delta t_o = \Delta t - (\Delta s/c) = \Delta t\left(1 - \frac{v^2}{c^2}\right) \approx (\gamma^3 \omega_r \sin\alpha)^{-1} \tag{1.6}$$

where $\Delta s = \Delta v \Delta t$ and $(1 - v^2/c^2) \approx 1/(2\gamma^2)$.

The spectrum of the synchrotron pulse is found through the Fourier transform of the pulse's electric field and contains harmonics of the frequency ω_r [73]. The spectrum over a range of frequencies can often be approximated by a power law with a spectral index, Γ. Therefore, the relation between frequency ω and the power per unit frequency is, $P(\omega) \propto \omega^{-\Gamma}$. In astrophysical situations, a power law distribution of electrons is often taken to be the source of synchrotron radiation. Consequently, as derived in [128], the spectral indices of synchrotron radiation and the electrons that produce that radiation can be related by, $\Gamma = (p-1)/2$, where p is the spectral index of the electron population. This implies that if the spectral index of the synchrotron spectrum can be measured, the distribution of electrons can be known.

Another important feature of synchrotron radiation is its high level of polarisation. The polarisation for a single electron in a magnetic field can reach up to 75% [128] and ranges from 10-75% in astrophysical environments [1]. This marked feature helps to identify synchrotron radiation.

Synchrotron radiation has been detected in radio waves up to X-rays, depending on the magnetic field and electron energy distribution of the source. Typical magnetic fields in astronomical objects range from microgauss in interstellar space [33] up to 10^{14} Gauss in highly magnetised pulsars [155]. Such radiation emitted from particles accelerated along strong magnetic field lines is called curvature radiation in which the magnetic field is so strong that particles travel along the field lines [102].

Synchrotron radiation is thought to be the process driving non-thermal X-ray emission from active galactic nuclei [14], supernova remnants [21, 20] and pulsar wind nebulae [15], and is a red flag for particles being accelerated to very high energies. Most importantly for VHE astronomy, synchrotron radiation can also provide a target photon population for inverse Compton scattering of synchrotron photons to very high gamma-ray energies [86], such as in the synchrotron self-Compton (SSC) model [73, 126] generally applied to AGN gamma-ray emission scenarios, as will be discussed in Section 2.1.3.

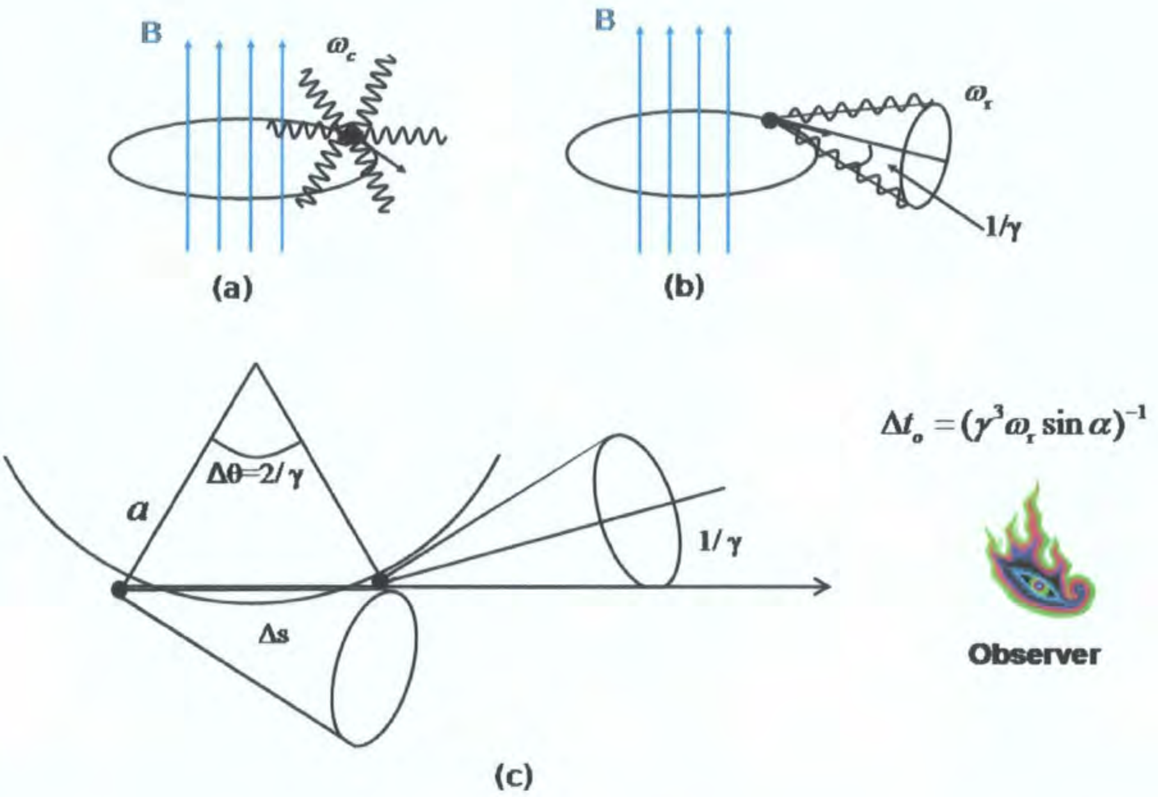

Figure 1.6: (a) Shows dipole radiation emitted from a non-relativistic electron, (b) shows beamed synchrotron radiation from a relativistic electron, and (c) shows pulsed synchrotron emission observed from the line-of-sight of an observer, adapted from [151, 128].

1.2.3 Electronic Bremsstrahlung

Bremsstrahlung[3] is generally produced by the deceleration of a charged particle in the electric field of an ion. From the point of view of the electron's rest frame, Bremsstrahlung radiation can also be thought of as Compton scattered light of a virtual photon from the ion's electromagnetic field. These two different views of Bremsstrahlung are pictured in Figure 1.7. In an astrophysical context, Bremsstrahlung radiation is considered to come from a spectrum of relativistic electrons in a gas. The production of Bremsstrahlung radiation depends on the density of the gas and the energy distribution of electrons. These relativistic electrons produce gamma rays of approximately the same energy and

---

[3] German for "braking radiation."

energy spectrum [152].

Bremsstrahlung is an important process used to probe various electron acceleration sites. A few applications of Bremsstrahlung are as follows: Bremsstrahlung radiation can be used to investigate galactic cosmic ray electrons and giant molecular clouds. Below 1 GeV, Bremsstrahlung gamma rays are produced by the same electrons responsible for galactic synchrotron radiation. Bremsstrahlung is also thought to be the main contributor (along with IC scattering) to the diffuse gamma-ray emission at energies less than 100 MeV [3]. Bremsstrahlung is also important to the understanding of discrete sources such as supernova remnants and plerions [3]. Lastly, Bremsstrahlung is the process that produces secondary photons in electromagnetic particle showers which is a property that allows VHE gamma rays to be detected from the ground.

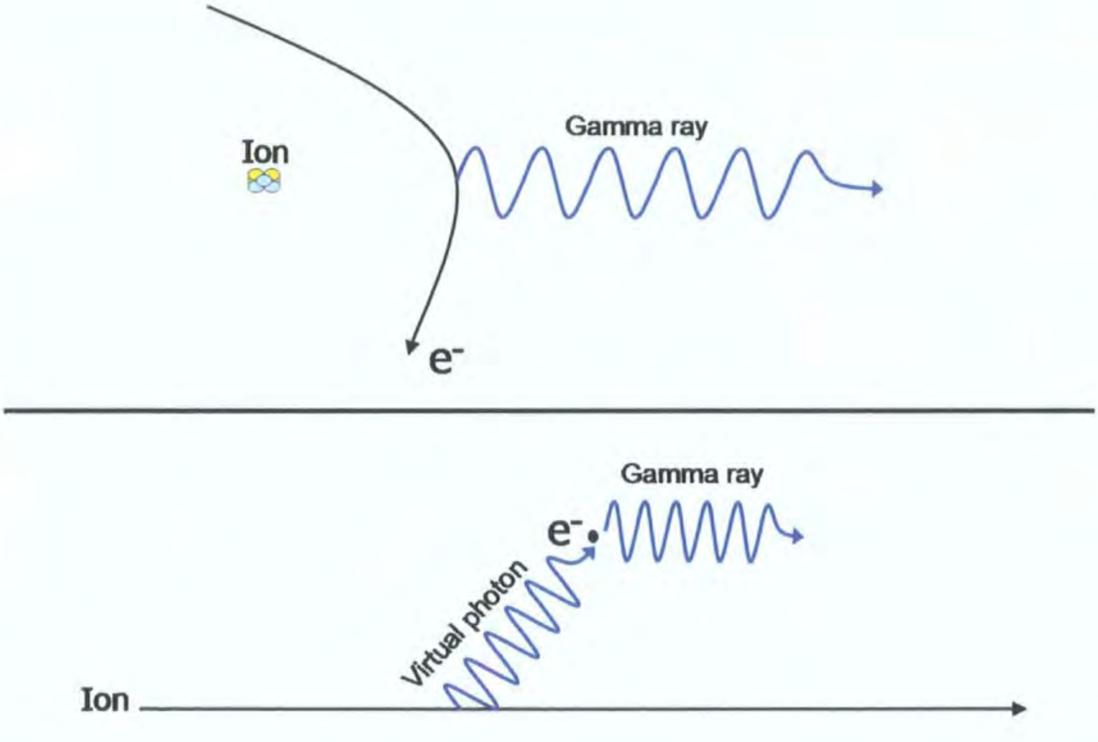

Figure 1.7: A gamma ray is emitted from an electron being decelerated in the electromagnetic field of an atomic nucleus (top). Bremsstrahlung can also be thought of as Compton scattering of an electron and a virtual photon from the ion's electromagnetic field (bottom).

1.2.4 Hadronic Interactions

Gamma-ray emission through hadronic interactions mainly comes from high energy protons interacting with matter producing neutral pions (π^0). Neutral pions subsequently decay into two gamma rays. This process is shown in Figure 1.8.

Detecting gamma-ray emission from hadronic interactions is crucial to the understanding of the origin of cosmic rays, as discussed in Section 1.1. Gamma rays from pion decay are most likely to be found in regions of high molecular density where particles can be accelerated to high energies, such as in the shock fronts of supernova remnants [111].

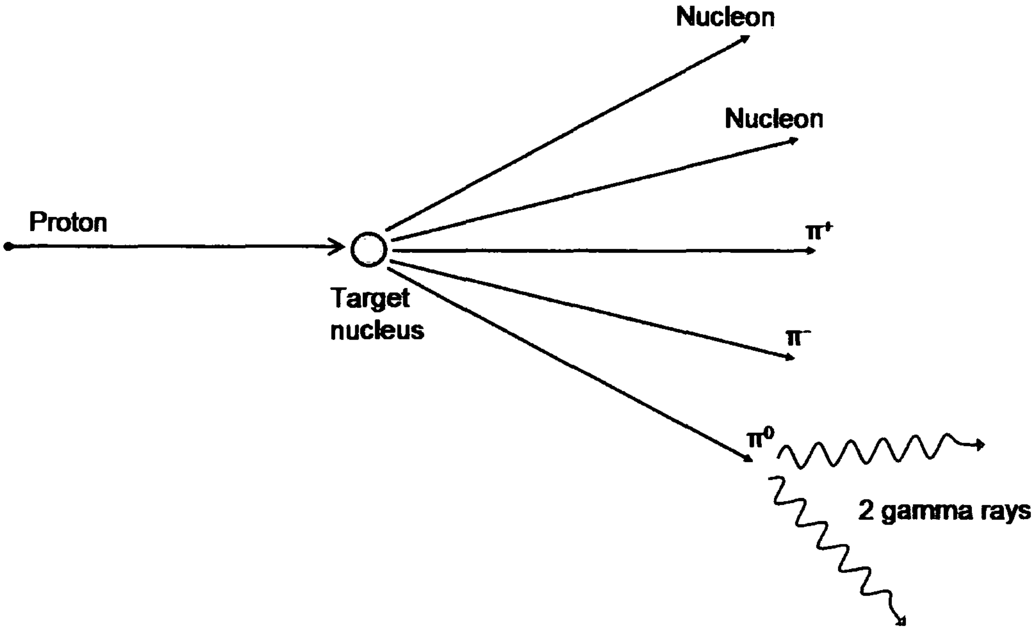

Figure 1.8: Gamma-ray emission via π^0 decay, from [152].

1.2.5 Electron-Positron Pair Production with Photons and Matter

Gamma rays interacting with low energy photons annihilate to produce electron-positron pairs shown schematically by $\gamma + \gamma \rightarrow e^- + e^+$ and in Figure 1.9. Annihilation is only possible when the sum of energies of the two photons are of the order of $2m_ec^2$ or greater, corresponding to the rest mass of the electron and positron.

For example, a 1 TeV gamma ray will interact with a near infrared photon on the order of 0.5 eV. Infrared photons come from re-emitted starlight from atomic and molecular clouds and are abundant in the universe. Therefore, pair production must be taken into account when observing TeV sources from redshifts greater than about 0.1 [152]. This will be crucial when talking about the infrared component of the extragalactic background light (EBL) discussed in Section 2.2.

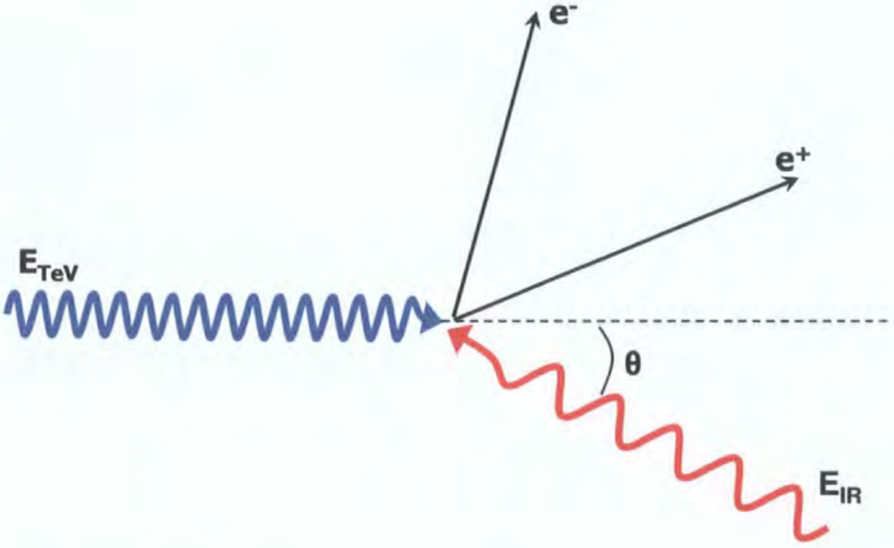

Figure 1.9: Pair production by a high energy photon colliding with a low energy photon producing an electron-positron pair.

Gamma rays can also create electron-positron pairs when they interact with matter. In Section 1.4, it will be shown how this process allows gamma rays to be indirectly detected from the ground. The mean free path $\lambda = 1/(N\sigma_{pp})$, the typical distance a gamma ray will travel before it pair produces, depends on the number density of the medium, N, and the cross section for interaction, $\sigma_{pp} \approx 10^{-26}$ cm^2. The density of the interstellar medium (ISM) and intergalactic medium (IGM) is approximately 1 atom

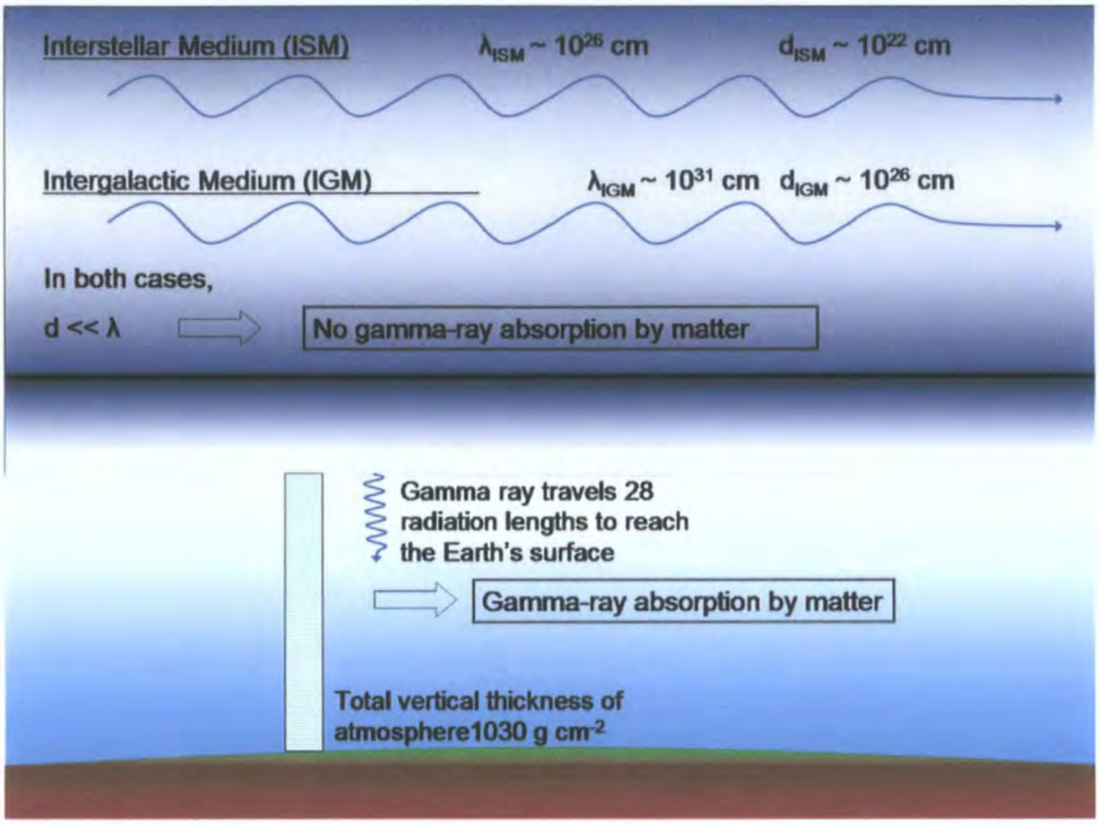

Figure 1.10: The top of the illustration shows a gamma ray travelling through space where there is no gamma ray absorption by matter. The bottom illustration shows a gamma ray interacting with the Earth's atmosphere where matter densities are high.

cm^{-3} and 10^{-5} atoms cm^{-3} corresponding to mean free paths of $\lambda_{ISM} = 10^{26}$ cm and $\lambda_{IGM} = 10^{31}$ cm, respectively. Typical distances travelled through the ISM and IGM are $d_{ISM} = 10^{22}$ cm and $d_{IGM} = 10^{26}$ cm. Such relatively small distances and large mean free paths ($d \ll \lambda$) makes gamma ray absorption by matter in space virtually non-existent. However, the radiation length[4] for a gamma ray is 38 g cm^{-2}. The total vertical thickness of the atmosphere is 1030 g cm^{-2}, so a gamma ray traverses about 28 radiation lengths to reach the surface. Therefore, pair production on matter becomes centrally important on a terrestrial level.

---

[4] The radiation length describes amount of material a typical gamma ray will travel through before it pair produces and is equal to $\rho\lambda$, the density of the material times the mean free path.

1.3 Sources of VHE Gamma Rays

Very high energy gamma rays have mainly been detected from supernova remnants, microquasars, pulsar wind nebulae, and active galactic nuclei. These constitute many interesting classes of objects that can be studied through VHE gamma-ray astronomy and are introduced in the following section.

Discoveries made in the last couple of years provide many firsts for VHE gamma-ray astronomy and illustrates a very exciting time with many more discoveries sure to come. This section will highlight some recent H.E.S.S. discoveries and observations, while recent review of VHE gamma-ray sources can be found in [44].

1.3.1 Galactic Sources

The most populated areas of the galaxy is where one might expect to find sources of VHE gamma rays. For this reason, the galactic plane was scanned to investigate different source classes of VHE gamma rays and to search for unknown types of emitters [22]. The first H.E.S.S. survey of the inner galaxy ($-30° < l < 30°$, $-3° < b < 3°$) revealed 14 previously unknown VHE sources with a detection significance of $> 4\sigma$, many that are possibly associated with SNRs, PWNe, or X-ray binaries (XRB), and 3 with no plausible counterparts at other wavelengths.

The central 200 parsecs of our galaxy harbours several potential sites for particle acceleration, and hence VHE emission. Three discrete sources have been detected in the region. The first one lies about 5" from the supermassive blackhole Sagittarius A*, another is coincident with a SNR, G0.9+0.1. The third is an unidentified source $\sim 1°$ away from Sagittarius A*, HESS J1743-303 and has no clear counterparts at other wavelengths. Upon subtraction of these sources, diffusive gamma-ray emission is found and is correlated with molecular clouds in the region. This is the first case that such a correlation has been found at these energies [80].

The pulsar wind nebula of the Crab Nebula was the first firm VHE gamma-ray detection in 1989 with the Whipple telescope [153]. Since then, the Crab has become the standard candle for VHE gamma-ray astronomy as the strongest known source in the sky (as well as being reliably constant). The VHE spectrum of the Crab is shown in Figure 1.11. Since the Crab has been detected, supernova remnants (SNRs) and pulsar wind nebulae (PWNe) have been found to be the most common type of VHE galactic source. Binary systems and star-forming regions are also a type of source with a few sources contributing to the growing VHE gamma-ray catalogue.

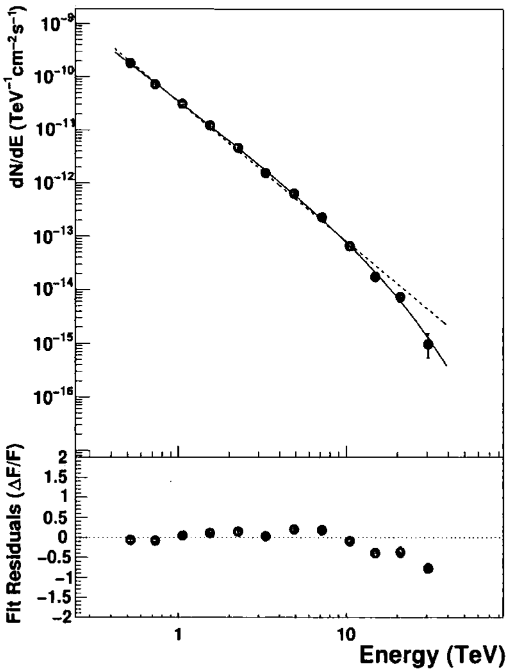

Figure 1.11: The Crab Nebula spectrum [21]. The Crab is the standard candle for VHE gamma-ray astronomy due to its strong and constant flux.

Supernova Remnants

Supernova remnants (SNRs) are leftover material from exploded stars. Upon explosion they release tremendous amounts of gravitational energy accelerating particles to relativistic speeds. Subsequent acceleration of particles takes place in the magnetic fields of the SNR's expanding shock fronts. Supernovae are prime candidates for accelerating cosmic rays in the Milky Way because they are thought to be the only population of objects capable of supplying the galaxy with such great energies. For example, the gravitation energy released in the core collapse of a supernova explosion is,

$$\Delta E_{grav} \approx \frac{GM_c}{R_c} \approx 10^{46}\ \mathrm{J} \tag{1.7}$$

where G is the gravitational constant, M_c is the mass of the collapsed core ($\sim 1.5 M_{\odot}$), and R_c is the final radius of the collapsed core which is $\sim$ 20 km in the case of a neutron star. The energy of 10^{46} J compared to the energy radiated by the supernova in a year ($\sim 10^{44}$ J) or the energy required to eject the outer layers of the star ($\sim 10^{45}$ J) are only a fraction of the released energy. The energy source needed to fill the galaxy with a cosmic ray energy density of $\sim$1 eV cm^{-3} over the time it would take a cosmic ray to travel to

Earth from the other side of the galaxy is $\leq 10^{45}$ J. This is again a small fraction of the total energy released upon explosion.

The mechanism of particle acceleration through magnetic fields is thought to be well understood theoretically, yet unequivocal evidence for the production of high energy protons in supernova remnants have proven hard to find [5].

RX J1713.7-3946 is a SNR where proton acceleration is thought to occur in the north-eastern rim of the supernova shell where gamma-ray, X-ray, and molecular densities are the highest. Figure 1.12 shows an image of the remnant taken with the H.E.S.S. telescopes and is the first image taken in VHE gamma-rays. RX J1713.7-3946 was observed over 3 years with an unprecedented precision of 0.06° revealing the detailed structure of the remnant. The spectrum extends over 3 orders of magnitude with significant emission approaching 100 TeV. This energy coverage is presumably at the limit of present generation Cherenkov telescopes. Data suggests a leptonic as well as a hadronic acceleration of these particles to energies greater than 100 TeV [5, 27]. This is a key source in understanding where cosmic rays come from, as are others such as RX J0852.0-4622.

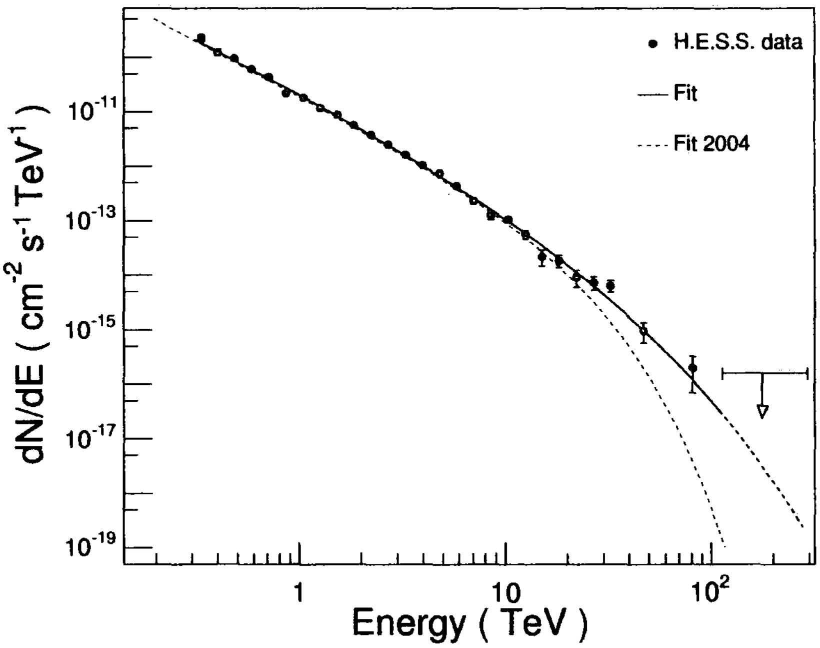

Figure 1.12: The spectrum of RX J1713.7-3946, extending 3 orders of magnitude, which is presumably the limit of present generation Cherenkov telescopes [27].

RX J0852.0-4622, a shell-type SNR similar to RX J1713.7-3946, is the largest extended source (2° in diameter) ever resolved by a Cherenkov telescope, and is shown in Figure

1.13. The observed gamma-ray spectrum extends over 2 orders of magnitude, and is highly correlated with X-ray and radio observations. The possibility for leptonic and/or hadronic gamma-ray emission depends on the distance to the source, which remains contested [20].

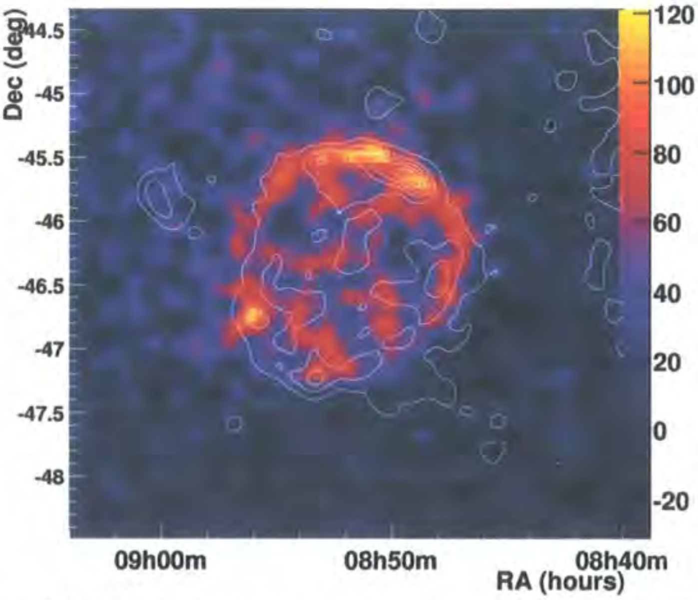

Figure 1.13: RX J0852.0-4622 is the largest source to be observed in VHE gamma rays, with a morphology similar to RX J1713.7-3946, extending an area 16 times the area of the moon [20]. The colour axis refers to the excess gamma-ray counts above the background.

Pulsar Wind Nebulae

A growing number of extended objects seem to be associated with pulsar wind nebulae (PWN) in the galactic plane. The most notable results in this class of objects are the Crab Nebula [21], MSH-15-52 (HESS J1514-591) [7], Vela-X (HESS J0835-455) [18], HESS J1825-137 [15], and two sources in the Kookaburra region (HESS J1420-607 and HESS J1418-609) [13]. VHE gamma-ray emission from these sources is generally modelled by IC scattering from interactions with the cosmic microwave background (CMB) or another seed photon population.

MSH-15-52 provided the first image of an extended PWN in the VHE range, shown in Figure 1.14. The image reveals an elliptically shaped emission region coincident with X-ray and radio emission along its jet axis [7].

There is VHE gamma-ray emission coincident with the asymmetric PWN associated with Vela-X [18]. The spectrum shows the first observed peak[5] at VHE energies. The

---

[5] Many sources are modelled by double peaked emission: the first peak from synchrotron radiation at

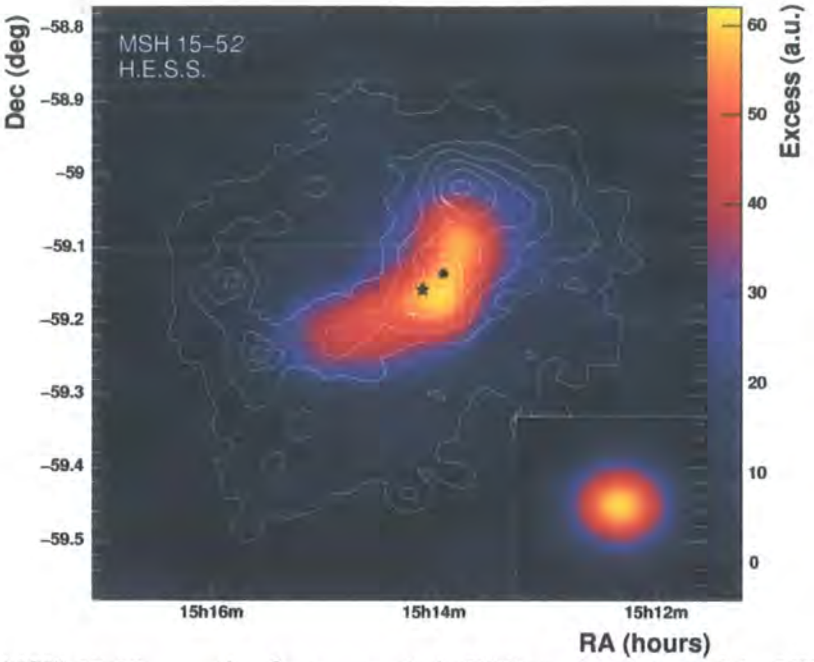

Figure 1.14: MSH 15-52 was the first extended PWN to be detected in VHE gamma rays. The white contour lines denote the X-ray count rate measured with ROSAT. The black point and black star lie at the pulsar position and centre of the VHE gamma-ray excess respectively [7]. The colours refer to the excess gamma-ray counts above the background. The image at the right bottom corner of the figure is the point spread function, which is the simulated size of emission coming from a point source.

spectral distribution of X-rays and gamma rays is shown in Figure 1.15.

HESS J1825-137 is another asymmetric PWN, like Vela-X, and was first detected in the first H.E.S.S. galactic scan [22] and followed up with pointed observations [15]. Many gamma rays were observed from this source allowing a thorough statistical analysis to be performed. The results show the first energy dependent morphology in the VHE gamma-ray regime, displaying a softening (steepening) of the energy spectrum at larger distances from the pulsar position, or equivalently, the decrease in source size with increasing energy of gamma rays, shown in Figure 1.16. The variation of spectral index with distance is thought to be attributed to IC and synchrotron cooling of electrons that are continuously being accelerated.

The Kookaburra is region of compact and extended radio and X-ray sources extensively studied in the search for counterparts to the unidentified EGRET source 3EG J1420-6038/GeV J1417-6100 [13]. VHE gamma-ray emission has been detected at the 'wings' of

---

low energies (radiowaves to X-rays) and the second from inverse Compton scattering at higher energies, see Section 2.1.3

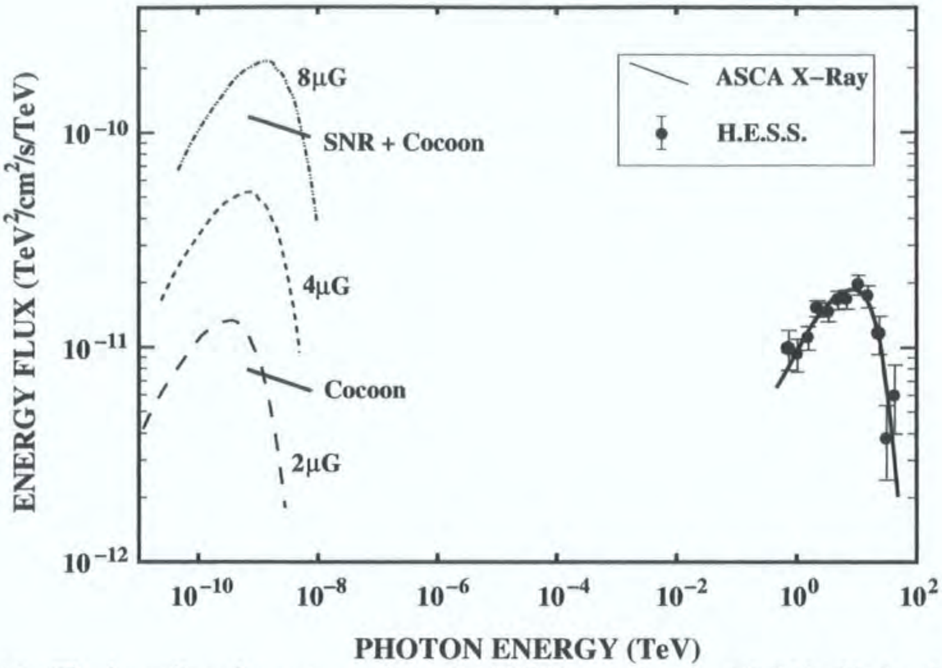

Figure 1.15: The broadband spectrum from the PWN associated with Vela-X showing the first observed peak at VHE gamma-ray energies [18].

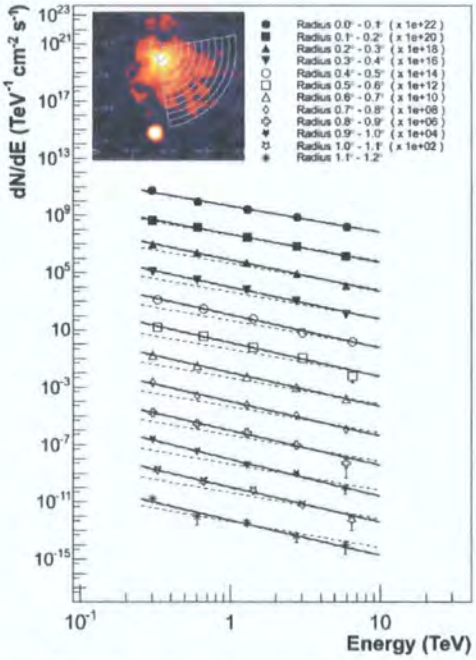

Figure 1.16: The spectrum of HESS J1825-137 shown at various distances from the centre of emission. This is the first source to show an energy dependent morphology [15].

the Kookaburra and are most possibly associated with two candidate offset PWN, shown in Figure 1.17.

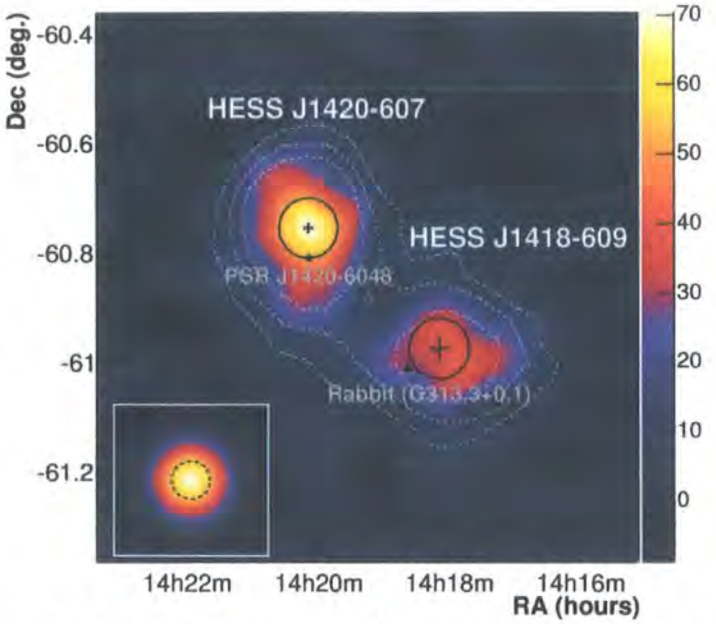

Figure 1.17: The 'wings' of the Kookaburra showing VHE gamma-ray emission thought to be coming from 2 offset pulsar wind nebulae. The white contours denote 5σ (outermost), 7.5σ, and 10σ significance levels. The position of the candidate pulsar is marked with a star and the position of the Rabbit PWN is marked by a black triangle. The best-fit positions from gamma-ray emission are marked by the crosses [13]. The colour axis refers to the excess gamma-ray counts above the background.

Binary Systems

LS 5039 is a high mass X-ray binary comprised of a compact object and a massive 20 solar mass star in an eccentric 3.9 day orbit. The spectral index was found to vary with orbital position, which provides the first indication of gamma-ray absorption within an astrophysical source. Modulation of the energy spectrum could arise from changes in the maximum energy of electrons responsible for the radiation, from changes in the dominant radiative mechanism, and/or from the angular dependence of the IC scattering effect [11].

The binary system PSR B1259-63 is a radio pulsar orbiting a massive, luminous Be star in a highly eccentric orbit. This system was the first variable galactic source detected in VHE gamma rays, shown in Figure 1.19. The most likely scenario of particle acceleration is a variation of the standard model of pulsar driven nebulae, which accelerates electrons to multi-TeV energies and undergoes inverse Compton scattering on synchrotron radiation and on the dense photon field of the Be star. It is also plausible that gamma-ray emission may be associated with protons interacting with the dense ambient gas during times when the pulsar interacts with the equatorial disk [8].

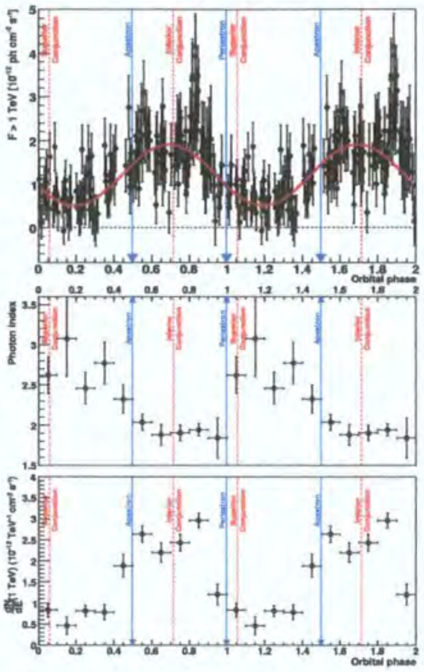

Figure 1.18: The integrated flux for > 1 TeV (top), spectral index (middle), and differential flux (bottom) for the X-ray binary LS 5039. This is the first source to exhibit a varying spectral index with orbital position, indicating gamma-ray absorption within an astrophysical source [11].

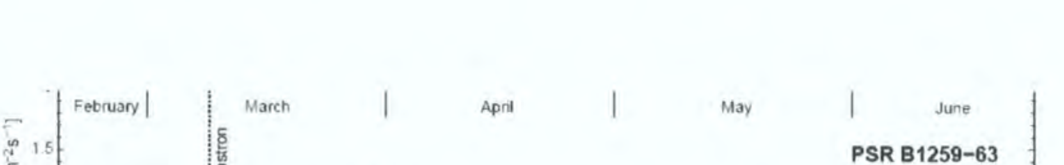

Figure 1.19: Shows the daily integral flux above 380 GeV as measured by H.E.S.S. This radio pulsar PSR B1259 was the first variable galactic source detected in VHE gamma rays [8].

Star Forming Regions

Westerlund 2 is the first star forming region to show VHE gamma-ray emission. It is a young stellar cluster located in a well-known HII region RCW 49, containing 500 X-ray point sources. The many proposed scenarios for gamma-ray emission are: emission from the colliding wind zone of WR20a (the most massive of all confidently measured binary systems in our Galaxy residing in Westerlund 2), collective stellar winds from the extraordinary ensemble of hot and massive stars in the stellar cluster, diffusive shock acceleration in a wind-blown bubble created by the stars at the cluster core, and from supersonic winds breaking out into the interstellar medium [24].

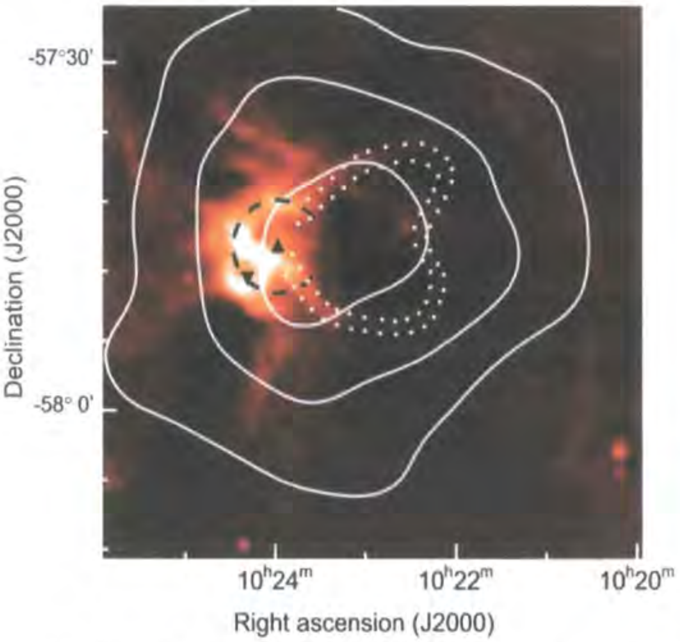

Figure 1.20: Westerlund 2 is the first observed star forming region to emit VHE gamma-rays. The solid white lines show the significance contours (5, 7 and 9 σ) of the gamma-ray emission, overlaid on a radio image from the Molonglo Observatory Synthesis Telescope. The dashed black line indicates the Westerlund 2 stellar cluster while the triangle shows the position of WR 20a. The white dots are depressions in the radio map indicating the wind-blown bubble around WR20a. See text for discussion of possible acceleration mechanisms [24].

Dark Matter

The standard picture of the Universe predominantly used by cosmologists today is that of a lambda cold dark matter (ΛCDM) Universe resulting from hierarchical structure formation. In this model, galaxies are predicted to be embedded in dark matter (DM) halos with a pronounced density cusp in their centre. It is predicted that the annihilation of dark matter particles may give rise to gamma rays, neutrinos, and cosmic rays, where the annihilation rate of dark matter is proportional to the square of its density and so would be the greatest at the galactic centre. It is for this reason that a modelled dark matter signal coming from the centre of our galaxy is compared to the H.E.S.S. VHE gamma-ray data. Results have shown that the observed VHE gamma-ray spectrum is not compatible with the most convenient DM particle annihilation scenarios, as shown in Figure 1.21. It is thus likely that the bulk of the emission is provided by astrophysical non-DM processes [19].

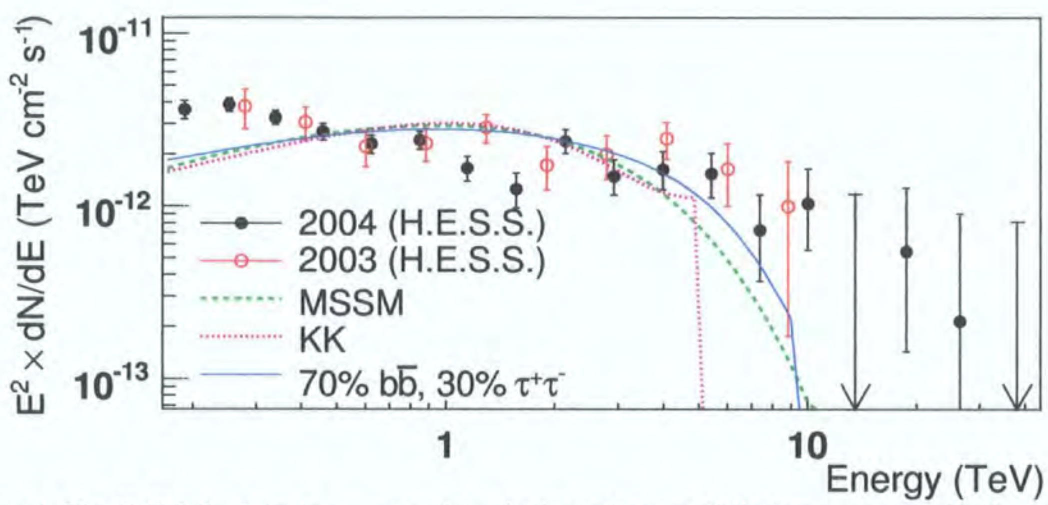

Figure 1.21: H.E.S.S. data is compared to dark matter annihilation scenarios in the centre of the galaxy. Theoretical curves for dark matter annihilation show no fit to the H.E.S.S. data, implying that emission is due to non-DM processes [19].

1.4 How VHE Gamma Rays are Detected

As shown in Section 1.2.5, the atmosphere is opaque to very high energy gamma rays, so they cannot be detected directly on the ground. On the other hand, it is not plausible to detect them in space due to the large collection areas needed to detect their low flux. Fortunately, VHE gamma rays are able to be detected indirectly on the ground through the relativistic air showers they produce. These showers in turn interact with atmospheric particles creating Cherenkov radiation that we can detect.

The most effective method of detecting VHE gamma rays is by collecting Cherenkov radiation with reflecting optical telescopes fitted with a high speed camera. This, along with the methods used to separate the VHE gamma-ray signal from the overwhelming background signal created by cosmic rays, is collectively called the imaging atmospheric Cherenkov technique (IACT).

1.4.1 Extensive Air Showers

Extensive air showers (EAS) are created by gamma rays or cosmic rays interacting with particles in the atmosphere producing a cascade of secondary particles that propagate to the surface of the Earth. There are many important differences between the two types of showers, which will discussed separately in the following sections.

Gamma-ray Air Showers

A gamma ray with an energy greater than 10 MeV initiates an air shower by pair production as it travels through the atmosphere [152]. These showers are of electromagnetic nature consisting of electrons, positrons, and photons. The cross section for pair production is fairly constant for gamma-ray energies $\gtrsim$ 100 MeV and will pair produce around 10 kilometres above sea level (a.s.l.) [152]. The higher energy showers are more penetrating compared to the lower energy showers due to the increased amount of energetic particles and Cherenkov light produced.

The simplest model of an electromagnetic shower was developed by Bethe and Heitler [37] and is shown in Figure 1.22. A gamma-ray air shower begins when a VHE gamma ray creates an electron-positron pair by interacting with the electric field of an atmospheric molecule (N_2 or O_2). The electron and positron are assumed to share the energy of the primary gamma ray equally and are therefore moving relativistically. When the relativistic electron or positron comes into the electric field of an atomic nucleus, the lepton gets deflected thereby losing kinetic energy (Bremsstrahlung). This kinetic energy gets emitted in the form of a high energy gamma ray. The secondary gamma ray then pair produces, allowing the process to repeat. The air shower no longer undergoes Bremsstrahlung when ionisation becomes the dominant energy loss mechanism for electrons and positrons. This takes place when the kinetic energy of the particles reaches less than 84 MeV [152]. Pair production also stops when photoelectric absorption and Compton scattering become the dominant energy loss mechanisms for the photons [101].

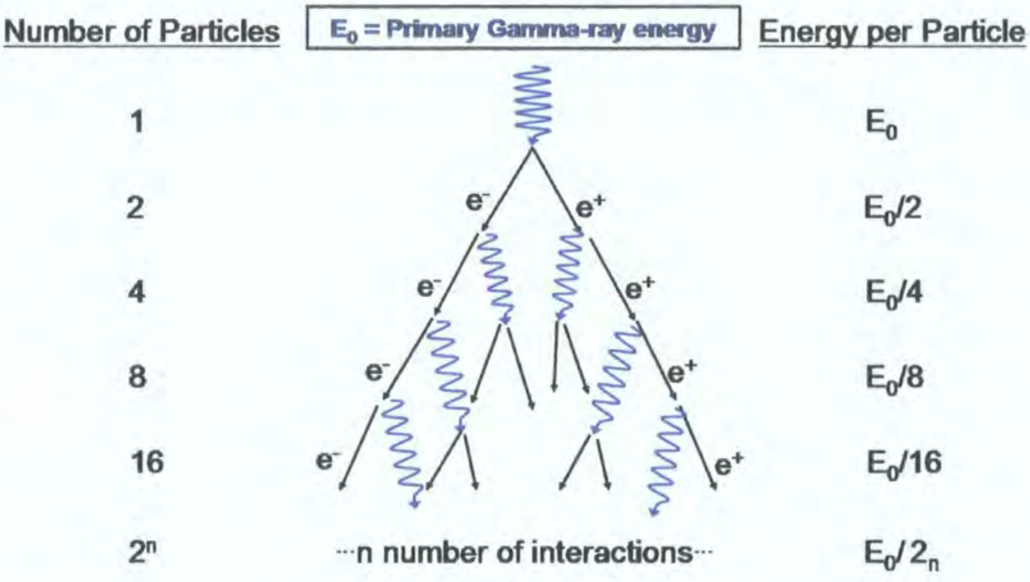

Figure 1.22: Model of an electromagnetic shower described by Bethe and Heitler [37].

Hadronic Air Showers

Hadronic showers are produced when a high energy proton or nucleus directly collides with another nucleus in the atmosphere. Hadronic air showers are naturally more complicated due to the myriad of particles that can be produced through nuclear interactions. The products of the collision generally consist of pions, lighter nuclei, nucleons, strange particles, and antinucleons.

Pions of all charges are produced in almost equal numbers and posses very high energy. Neutral pions decay into two gamma rays ($\pi^0 \rightarrow \gamma + \gamma$) within a lifetime of 8×10^{-17} s^1. These gamma rays can then start their own electromagnetic showers. Charged pions have a longer lifetime of 1.2×10^{-8} s^1 and can either interact with another atmospheric nucleus, as in the case of the original hadron, or decay into muons ($\pi^+ \rightarrow \mu^+ + \nu_\mu$ or $\pi^- \rightarrow \mu^- + \bar{\nu_\mu}$). Charged muons can in turn decay into positrons or electrons and their accompanying neutrinos, or if energetic enough, due to their longer lifetimes of 2.2×10^{-6} s^1, can penetrate to the surface of the Earth. The products of a hadronic air shower will generally multiply until the energy per particle drops to around 1 GeV, which is the energy required for multiple pion production [101]. Figure 1.23 shows the development of a hadronic shower.

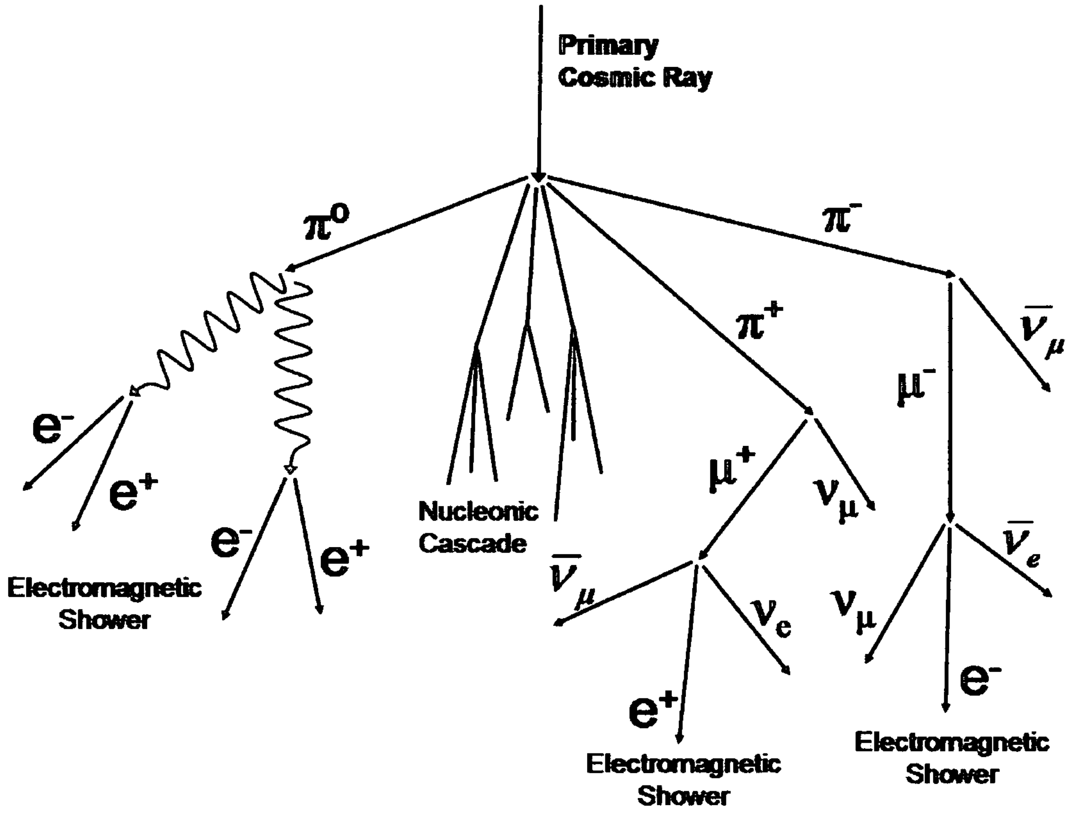

Figure 1.23: The development of a hadronic shower, from [101].

1.4.2 Cosmic Ray Background

Cosmic rays consisting of protons and alpha particles (hadrons) make up the majority of particles hitting the atmosphere, with electrons making up roughly 3% and heavier ions making up less than 1% of the total cosmic ray population.

While gamma-ray initiated showers are of primary importance, cosmic ray showers cannot be ignored because they provide a huge background ($10^3 - 10^4$ times the gamma-ray signal) for gamma-ray astronomy. Fortunately, hadronic and gamma-ray showers have different properties that can be used to separate the two.

The radiation length for a proton is 80 g cm^{-2} compared to 38 g cm^{-2} for a gamma ray. This means that gamma rays will initiate particle showers higher up in the atmosphere than protons. The major difference between hadronic showers and gamma-ray showers are the types of particles they produce, explained in the previous section. As a consequence, gamma-ray showers produce two to three times more Cherenkov light than a hadron of the same primary energy. Another distinguishing feature between the two types of showers is that the particles in a hadronic shower are noticeably more dispersive and irregular than gamma-ray showers. This is shown in Figure 1.24.

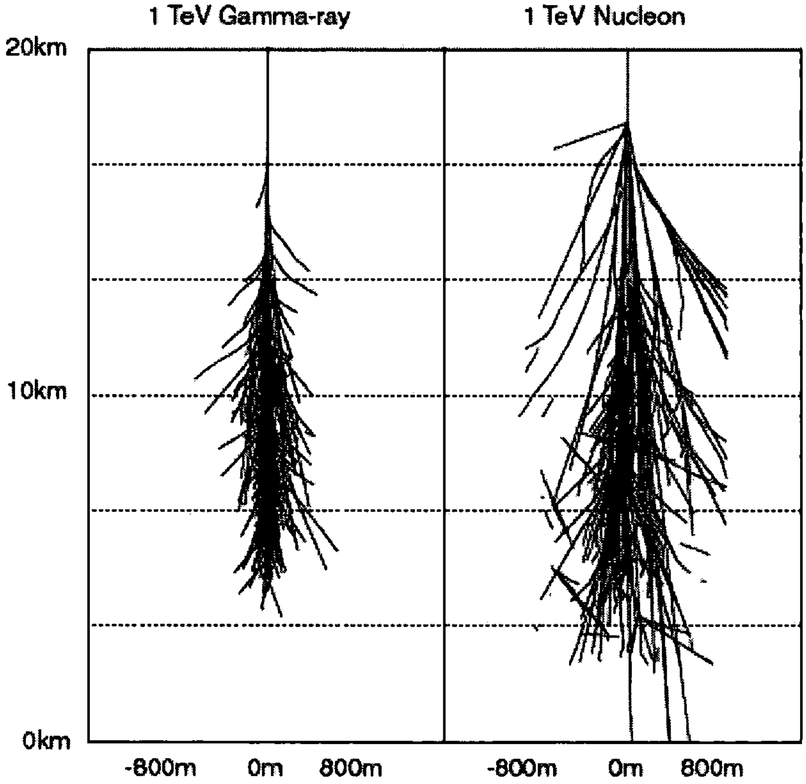

Figure 1.24: Simulations of particle showers initiated by a 1 TeV gamma ray (left) and a 1 TeV hadron (right). The differences between the showers are visually apparent in the size and shape (Courtesy of Hugh Dickinson).

Electrons are also a part of the cosmic-ray background, but produce electromagnetic showers of the same nature as gamma rays. It is therefore difficult to distinguish this background from the gamma-ray showers, but they are not of great importance due to their low flux at high energies [63]. However, with the method described in [81], the first measurement of the cosmic ray electron spectrum above 1 TeV has been obtained with an exponential cutoff at ~ 1.8 TeV.

Muons are a byproduct of hadronic showers produced in the lower part of the atmosphere and produce their own special Cherenkov signal. The abundance of muons can be a nuisance because their Cherenkov signal can be mistaken for a gamma-ray signal. Although, the localisation of muon production close to ground level means that their Cherenkov signal is emitted close to the telescopes and can generally be eliminated through coincident observation with multiple telescopes [63].

1.4.3 Cherenkov Radiation

When a charged particle in an extensive air shower, such as a electron or muon, moves through the atmosphere, the charged particle's electromagnetic field polarises the atmospheric molecules surrounding it. As the particle moves away from the molecules, the molecules radiate as a consequence of returning back to their nonpolarised equilibrium state.

If the particle is moving non-relativistically, the polarisation is symmetrical around and along the particle's trajectory, and the radiation emitted interferes destructively. Therefore no radiation is detected.

If the particle is moving faster than the phase velocity of light in the atmosphere, $v > c/n$, where v is the speed of the particle, c is the speed of light, and n is the refractive index of the atmosphere, there is a non-symmetrical dipole field along the trajectory that produces detectable radiation [152]. In other words, as the particle moves through the medium, the wavefronts of the emitted radiation created by the particle at an earlier time cross with wavefronts emitted some time later. These wavefronts interfere constructively forming coherent radiation. This observable radiation is called Cherenkov radiation, shown in Figure 1.25.

The amount of Cherenkov light emitted per pathlength is given by [68],

$$\frac{dN}{dx} = 2\pi\alpha z^2 \int_{\lambda_1}^{\lambda_2} \left(1 - \frac{1}{(\beta n(\lambda))^2}\right) \frac{1}{\lambda^2} d\lambda \tag{1.8}$$

where z is the charge of the particle, α is the fine structure constant, and $\beta = v/c$. The intensity of Cherenkov light does not increase indefinitely to shorter wavelengths such as X-rays due to the dependence of wavelength on the refractive index. The index of refraction in most materials becomes less than 1 in X-rays and suppresses any emission.

Cherenkov radiation is emitted at an angle of $\cos\theta_c = c/(nv)$ or $\theta_c = \arccos(1/(n\beta)) \approx \sqrt{2(n-1)}$ with respect to the direction of motion of the particle, shown in Figure 1.25. Typical angles for emission in the atmosphere are $\theta_c \approx 1 - 2°$. This corresponds to a Cherenkov light pool from one air shower spreading out over an area with a radius of ~120 m. Although Cherenkov light spreads over a large area on the ground, it is also very faint and very brief. Its density is on the order of ~100 photons per m^2, depending on the altitude, while the signal lasts a few nanoseconds. It is therefore necessary to create large telescopes (area $\gg 1$ m^2) with fast electronics sensitive enough to detect this light [3].

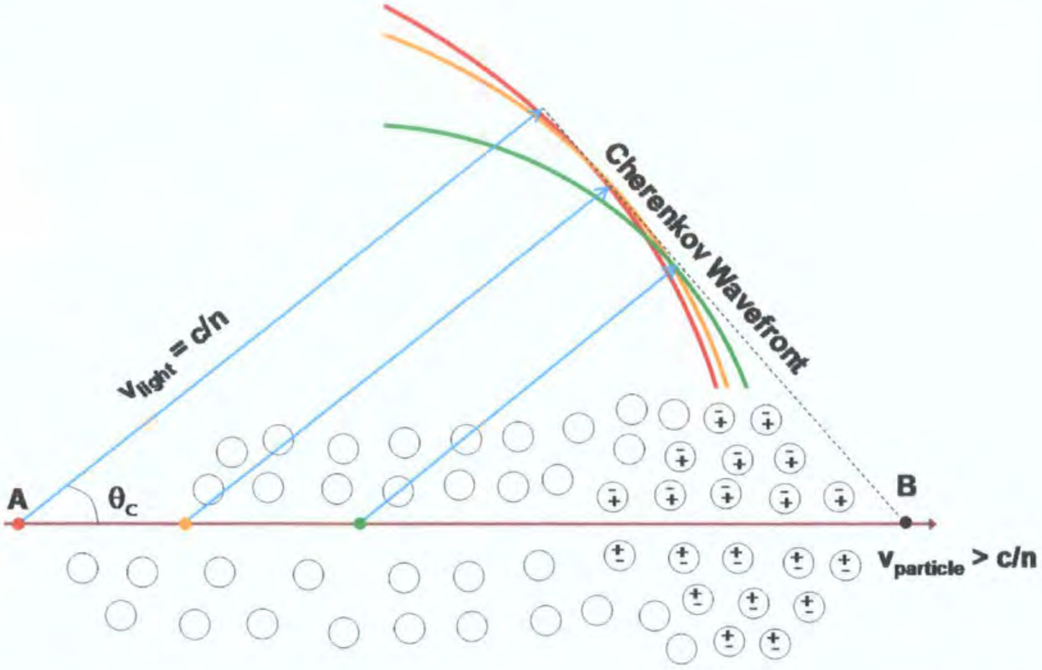

Figure 1.25: Illustration of a particle moving faster than the speed of light through a medium emitting Cherenkov radiation. The Cherenkov wavefront is where the electromagnetic waves interfere constructively, producing Cherenkov radiation.

1.4.4 The Imaging Atmospheric Cherenkov Technique

The most efficient and cost effective method developed to detect Cherenkov radiation uses imaging atmospheric Cherenkov telescopes (IACTs) with cameras made up of photomultiplier tubes (PMTs) sensitive to Cherenkov light. The development of this technique was pioneered by the Whipple Collaboration [89] while the stereoscopic setup was pioneered by HEGRA [51] and is illustrated in Figure 1.26.

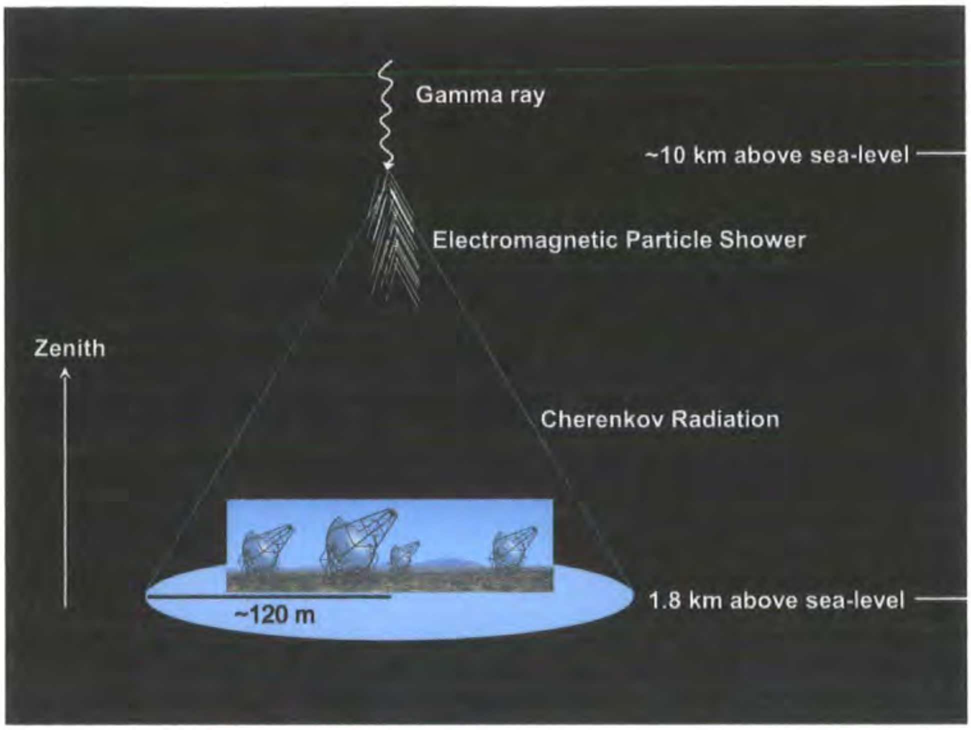

Figure 1.26: The Cherenkov technique showing a gamma ray hitting the atmosphere creating a particle shower and Cherenkov light.

The Cherenkov technique analyses the images of Cherenkov radiation produced by atmospheric air showers. This Cherenkov radiation is emitted in a light cone spreading over a large area of thousands of metres, which makes it favourable to detect this radiation. However, it is unfortunate that cosmic ray initiated particle cascades outnumber gamma-ray initiated showers by a factor of about a thousand. It is essential that the IACT is effective in regards to background subtraction of Cherenkov light produced by hadrons in order to extract a statistically significant gamma-ray signal. The IACT method allows for an effective elimination of unwanted hadronic background to almost 100% [63] while retaining 50-80% of gamma rays [54, 100].

Hadronic signal rejection can be achieved by analysing the variation of the size, shape, and orientation of the shower image parameters. Gamma-ray showers produce elliptical (when the shower core is off-axis from the telescope) images in which the major axis of the ellipse points to the centre of the telescope's field of view, whereas hadronic cascades produce images that show no preferential direction or orientation (shown in Figure 1.27).

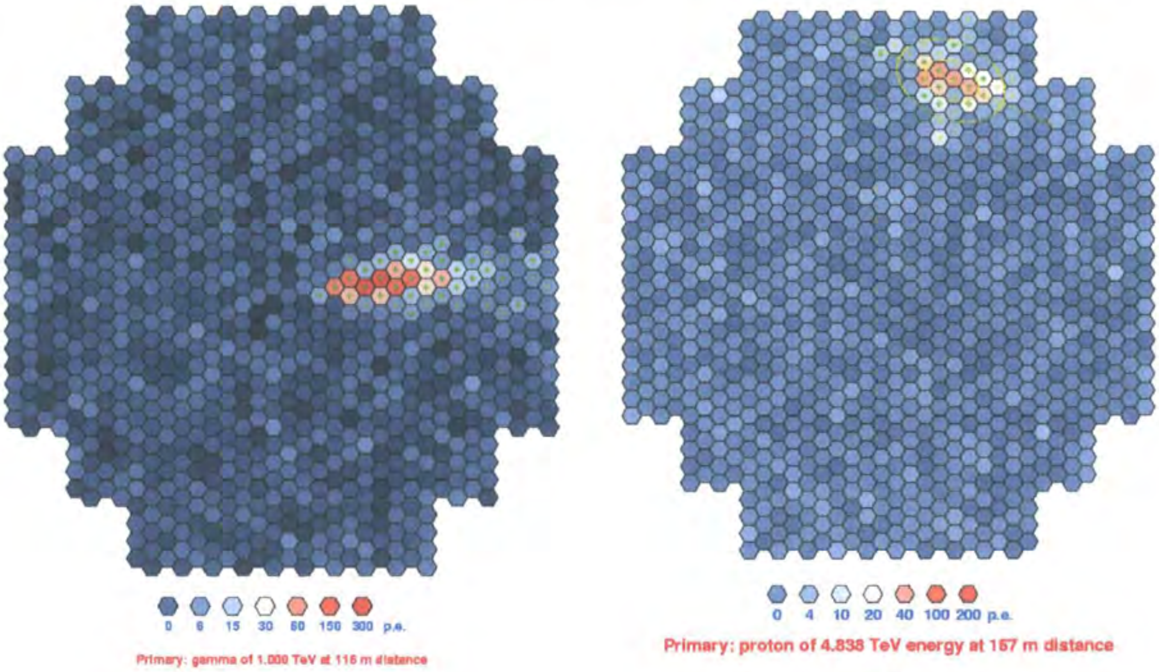

(a) (b)

Figure 1.27: Simulated images of Cherenkov radiation from a (a) gamma-ray air shower and (b) proton air shower. It can be seen that the gamma-ray image is a nice elliptical shape pointing to the centre of the camera while the proton shower is dimmer and points in a random direction.

The emission of Cherenkov light with height emitted from gamma-ray and hadronic showers is shown in Figure 1.28 where it can be seen how the lateral distribution of Cherenkov light has an effect on the image observed on the ground. Another distinguishing feature, lacking in hadronic showers, is a 'Cherenkov ring' which is the rise in the lateral distribution of Cherenkov photons at a radial distance of ~120 m caused by the variation in the Cherenkov emission angle with height. The Cherenkov ring is observed from gamma-ray energies greater than 100 GeV [63] and is shown in Figure 1.29. The effect of the Earth's magnetic field is also illustrated by Figure 1.29. The presence of a magnetic field (curves 2 and 4) results in the dispersion of the air shower and a subsequent spreading out of Cherenkov light.

How H.E.S.S. analyses Cherenkov images will be discussed in Section 1.6, but first I will discuss the properties of the H.E.S.S. telescope array.

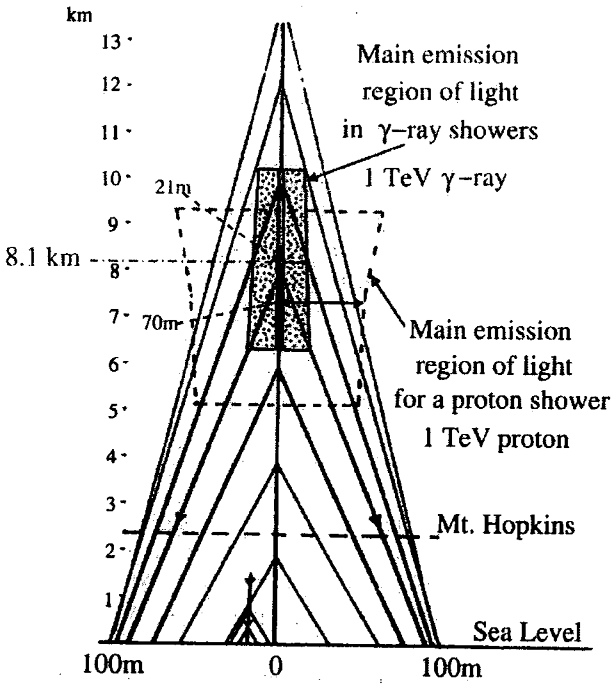

Figure 1.28: Amount of Cherenkov radiation being emitted at different heights of a simulated electromagnetic shower [63]. The angled lines show the Cherenkov light paths. The dotted region is where 50% of light is emitted from a 1 TeV gamma-ray shower whereas the dashed box indicates the main region of emission for a 1 TeV proton. It can be seen that the proton is emitting at a lower height and has a more dispersive shower than of a gamma-ray initiated shower.

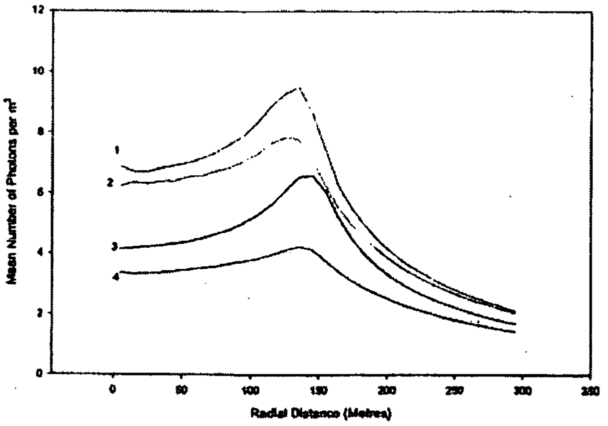

Figure 1.29: Lateral distributions of Cherenkov radiation of 100 GeV showers for the H.E.S.S. site (curves 1 and 2) and Narrabri, Australia (curves 3 and 4), from [118]. The Cherenkov ring is apparent in the rise of photon density around 120-150 m. Also, curves 1 and 3 are in the presence of no geomagnetic field while curves 2 and 4 take into account the geomagnetic field. It can be seen that curves 2 and 4 have a lower photon density resulting from the dispersion of the air shower and Cherenkov light.

1.5 VHE Gamma-ray Telescopes

VHE gamma-ray astronomy has grown from the confirmation of Cherenkov light by air showers using a single PMT in the focus of a 25 cm parabolic mirror in 1953 [71], to the use of complex systems of electronics, mirrors, data analysis techniques developed by major multinational collaborations around the world. There are currently 4 major IACT telescopes in operation with 2 in the southern and 2 in the northern hemisphere. Table 1.5 lists the major IACTs and some of their main operational properties. A review of these and other experiments using different techniques can be found in [44]. A review of past experiments can be found in [152, 63].

Table 1.2: Major imaging atmospheric Cherenkov telescopes currently in operation, from [44].

Experiment	Location	# of Telescopes	Energy Threshold	FOV[6]
CANGAROO III [156]	Australia	3/4	250 GeV	4°
HESS [21]	Namibia	4	100 GeV	5°
MAGIC [32]	La Palma	1	50 GeV	3.5°
VERITAS [82]	Arizona (USA)	4	100 GeV	3.5°

1.5.1 H.E.S.S. Telescope Array

The H.E.S.S. site in Namibia, 23° 16′ S 16° 30′ 1800 m a.s.l., was chosen for its excellent seeing conditions. Phase I of the H.E.S.S. system was completed in December 2003 and consists of 4 IACTs, each with a total area of 107 m^2, arranged in a square with 120 meter sides (shown in Figure 1.30), optimised to the lateral spread of a Cherenkov light pool.

Each telescope is made up of 380 spherical mirror facets each 60 cm in diameter. The mirrors are set up in a Davies-Cotton configuration [52]. In this configuration all the facets have the same focal length and are situated on a spherically curved surface. The diameter of each telescope is $d = 13$ m with a focal length of $f = 15$ m [36].

The camera has a field view of 5° containing 916 pixels per camera with a pixel size of 0.16° = 2.8 mrad. This large field of view makes it easy to observe extended sources such as supernova remnants, which can have angular sizes up to 2°. The pixels consist of photomultiplier tubes (PMTs), sensitive to Cherenkov light of wavelength 300-500 nm,

---

[6] FOV = Field of view.

with Winston light cones placed in front of the PMTs. The Winston light cones are quartz coated aluminiumised plastic funnels which work to increase the light collecting area of the PMTs while reducing stray light from the ground. The point spread function (the image width of a point source) of the camera is 0.23 mrad for an image seen from the telescope's optical axis, but grows with angular distance from its axis. The point spread function was designed to be smaller than the pixel size and has met this requirement with a smaller size than was predicted [36]. This is a testament to the excellence of the H.E.S.S. system due to the fact that the point spread function depends on the quality of the mirror facets, the precision of mirror alignment, and on the mechanical stability of the steel dish and facet supports.

The electronics of signal recording from the telescopes was designed such that the PMT signals are integrated over 16 ns, fully containing the Cherenkov signal of a few nanoseconds.

There are two CCD cameras located on the telescopes, a 'Lid' CCD and a 'Sky' CCD. The Lid CCD is located at the centre of the telescope dish and records images reflected from the closed PMT camera lid. This CDD serves to check the alignment of the mirror facets. The Sky CCD is located about half way from the centre to the edge of the dish. This CCD acts as a guide telescope to improve the precision of the telescope pointing.

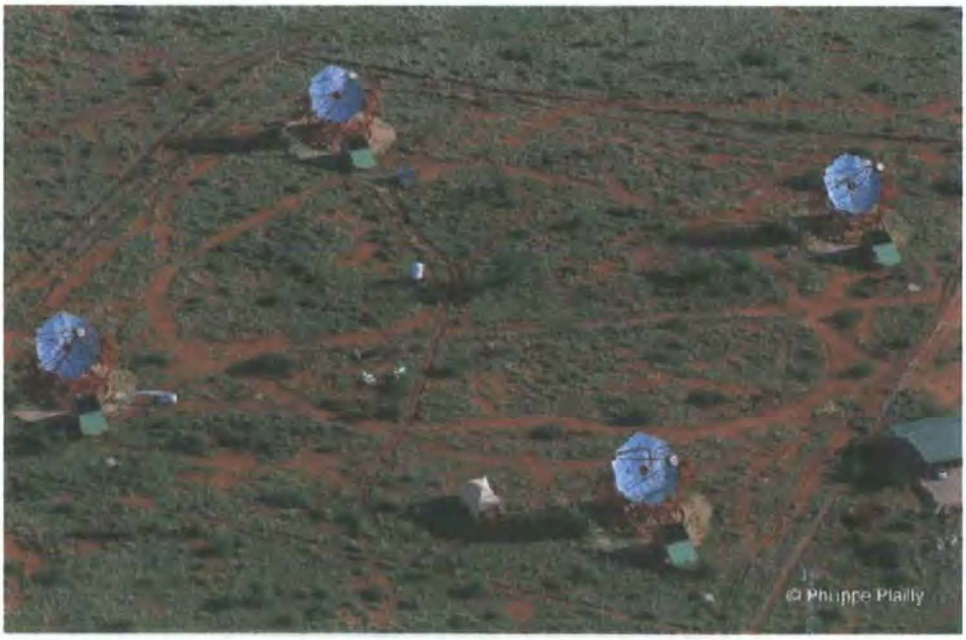

© Philippe Plailly

Figure 1.30: An aerial view of the H.E.S.S. site of the 4 telescope stereoscopic setup.

The H.E.S.S. telescopes are setup as a stereoscopic system. Since the Cherenkov light pool extends over a large circular area (~40,000 m^2) on the surface of the Earth, each telescope can observe a given shower from a different perspective, resulting in a more accurate reconstruction of the shower geometry, better angular resolution, energy resolution, and background suppression [36].

H.E.S.S. detects photon energies from 100 GeV to above 30 TeV [27], has a flux sensitivity down to about 10^{-11} photons cm^{-2} s^{-1} (1% of the Crab Nebula's flux for $E_\gamma > 100$ GeV), and has angular resolution better than 0.1° allowing a position error of 30″.

1.6 H.E.S.S. Standard Analysis

H.E.S.S. standard analysis is used for reconstructing the direction and energy of incident gamma rays, and for determining the energy spectrum and flux of detected sources, while rejecting the large cosmic-ray background [34].

While there are other independent techniques used such as 3D model analysis [100, 54], standard analysis has been used in all H.E.S.S. publications and will be discussed in detail.

Observations are taken in 28 minute interval runs. When two or more telescopic data signals are coincidently triggered, the data are sampled over a 16 ns interval and the event becomes a candidate for event reconstruction. The analogue signal from each triggered pixel is amplified via two channels (high gain and low gain) and converted into digital (ADC) signals that are then sent to the computer farm to be processed. If the event is free from hardware malfunctions (e.g. too many turned off pixels) and poor observing conditions (e.g. clouds), it is sent along the analysis chain for calibration and image cleansing.

1.6.1 Calibration

The process of calibrating the ADC signal involves converting each pixel signal into a corrected number of photoelectrons. The number of photoelectrons is corrected for the differences in the performance of each pixel. The corrected photoelectron amplitude for high and low gain channels is given by [4],

$$A^{HG} = \frac{ADC^{HG} - P^{HG}}{\gamma_e^{ADC}} \times FF \tag{1.9}$$

and

$$A^{LG} = \frac{ADC^{LG} - P^{LG}}{\gamma_e^{ADC}} \times (HG/LG) \times FF \tag{1.10}$$

where ADC^{HG} and $\mathrm{ADC}^{\mathrm{LG}}$ are the uncorrected digital signals for the high and low gain channels, P^{HG} and P^{LG} are their pedestal values, γ_e^{ADC} is the value of high gain in digital counts per photoelectron, (HG/LG) is the amplification ratio of high to low gain, and FF is the flatfield coefficient. Pedestal values measure the electronic noise of the cameras and are defined as the mean digital value recorded in the absence of Cherenkov light. The flatfielding coefficient corrects for different optical and quantum efficiencies between pixels within the camera.

Imaging cleansing is done to remove noise from the image and requires a pixel to have a signal greater than 10 (or 5) photoelectrons (PEs) and a neighbouring pixel to have a signal larger than 5 (or 10) PEs. This ensures the selection of only the pixels containing Cherenkov light.

1.6.2 Hillas Parameterisation

After image cleansing, the moments of the images are parameterised using Hillas-type analysis [63]. The zeroth moment is defined as the sum of all signals in all pixels after cleaning. The first-order moments describe the position of the image. The second-order moments describe the extent of the image. The third-order moments may be interpreted in terms of describing the overall shape of the image in the focal plane. Some of the most important shower image parameters are *size*, *length*, *width*, *distance*, *miss*, *alpha*, and *azwidth*. These parameters are defined in terms of their moments in Appendix B and are shown in Figure 1.31.

Images must pass size and distance cuts in order for the shower event to be reconstructed. The size cut requires the image to have a total minimum signal to ensure proper reconstruction while the distance cut requires that the centre of gravity of the image to be less than 2° from the centre of the camera so as to avoid cutting off any part of the image by the edge of the camera [34] .

1.6.3 Geometrical Reconstruction

Geometrical reconstruction of the image is performed to determine the direction of the incident particle and shower core. This is done using the major elliptical axis of each image (Figure 1.32). The shower direction is determined by a weighted average of the

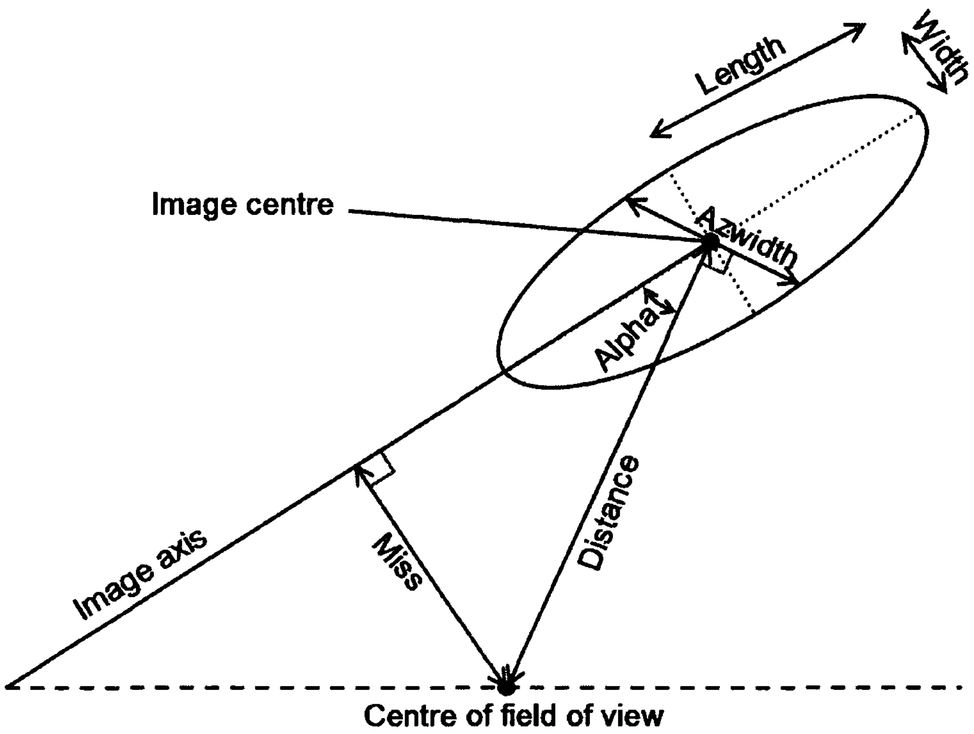

Figure 1.31: Hillas parameters of an idealised gamma-ray Cherenkov light image, from [63].

intersections of all pairs of major axes projected in the field of view of the telescope. The shower core location is determined by the intersections of the axes relative to each telescope's position, projected into the plane perpendicular to the telescope's pointing direction. The typical angular resolution per event is ~ 0.1° and the average accuracy in determining the shower core is ~ 10 m [34].

Length and width parameters are the most important for background elimination but have poor acceptance at high energies and do not account for more than one telescope, so parameters that scale with energy and take multiple telescopes into account, mean-scaled-width (MSW) and mean-scaled-length (MSL), were developed by HEGRA [51]. H.E.S.S. takes this one step further and introduces a parameter called mean-reduced-scaled-width (MRSW) and mean-reduced-scaled-length (MRSL) given by,

$$\mathrm{MRSW} = \frac{1}{\mathrm{N_{tel}}} \sum_{\mathrm{i=0}}^{\mathrm{N_{tel}}} \frac{\mathrm{width_i} - \langle \mathrm{width_i} \rangle}{\sigma_\mathrm{i}} \qquad (1.11)$$

where N_{tel} is the number of telescopes triggered, $\mathrm{width_i}$ is the measured width of the image,

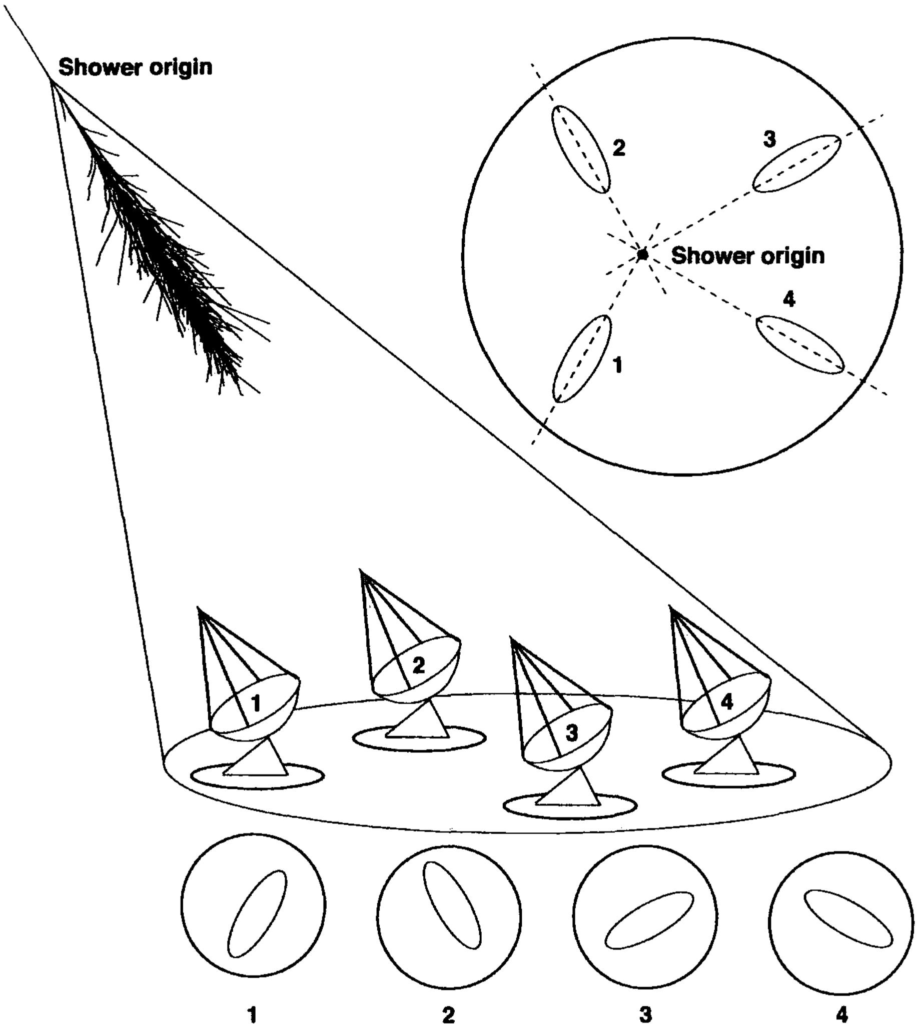

Figure 1.32: Illustration of a gamma-ray air shower and the Cherenkov images produced in the camera. The intersection of the major axis of each image is used to determine the position of the shower core (Courtesy of Hugh Dickinson).

$\langle \mathrm{width_i} \rangle$ and σ_i are the expected simulated values of the width and standard deviation for gamma rays based on the observed image intensity, reconstructed impact parameter (the distance between the point of impact of the image and the shower core), and zenith angle. A similar equation is found for MRSL.

Two other important cuts are on θ^2, the square of the angular distance between the reconstructed shower position and source position, and a cut on the total number of photoelectrons contained in the image. There is a standard set of cuts applied to all points sources with $\theta^2 < 0.0125°$ requiring at least 80 PEs in the image. In addition, cuts can be optimised to 'hard' and 'loose' if the spectrum is known. Hard cuts, optimised for a 1% Crab Nebula flux source with a 2.0 spectral index, require $\theta^2 < 0.01°$ with at least 200 PEs. These cuts result in a higher energy threshold, but with 20% better angular resolution and less systematic effects in eliminating background. They are also best suited for studying the structure of hard-spectrum sources. Loose cuts, optimised for a Crab Nebula flux source with a 3.2 spectral index, require $\theta^2 < 0.04°$ with only 40 PEs. Loose cuts were designed for the spectral study of bright sources at lower energies where the increased background is not an issue.

Table 1.3: Cuts on θ^2 and the photoelectron (PE) threshold for various cuts used in standard H.E.S.S. analysis.

	θ^2 (°)	PE Threshold (PEs)	Ideally for
Standard	0.0125	80	All sources
Hard	0.01	200	Low flux, hard spectra
Loose	0.04	40	High flux, soft spectra

1.6.4 Energy Spectrum and Flux Determination

The energy of each event, or gamma ray, is estimated by using look-up tables containing the mean energy of simulated gamma-rays as a function of image size and impact parameter. The image size is the intensity of the image and the impact parameter is calculated during geometrical reconstruction as described above. These two values are then used to find the energy from each telescope. The energy of the observed gamma ray is then the mean of the energies estimated for each telescope. The energy resolution for all energies is found to be ~ 15%.

To determine the energy spectrum, the data is first logarithmically binned in energy. The bins for which the average energy bias, $(E_{fit} - E_{true})/E_{true}$, (with estimated energy, E_{fit}, and simulated energy, E_{true}), is greater than 10% are thrown out to avoid any unnecessary systematic effects. This places a low-energy *safe threshold* on events. The effective area calculated for each event is a function of the fit energy and zenith angle, and is determined by the Cherenkov light pool and properties of the detector given by,

$$A_{eff}(E_{fit}, ZA) = \frac{N_T(E_{fit}, ZA)}{N_S(E_{fit}, ZA)} \times \pi r^2 \qquad (1.12)$$

where $N_T(E_{fit}, ZA)$ is the number of trigger events, $N_S(E_{fit}, ZA)$ is the number of simulated events, and πr^2 is the area over which Cherenkov light can be detected. Each energy bin of the spectrum is given by,

$$F_i = \frac{O_i - B_i}{\Delta E_i t_i} \tag{1.13}$$

where, $O_i = \sum_{i=0}^{N_{on}}(1/A_{eff}E^{-\Gamma})$, is the sum of on source events, and $B_i = \alpha \sum_{i=0}^{N_{off}}(1/A_{eff}E^{-\Gamma})$ is the sum of off source events normalised by, α, accounting for the greater area of the off source. The exposure time of each bin is given by t_i with an energy width of ΔE_i. The spectral index is initially assumed to be $\Gamma = 2.0$. If the index is found to deviate from this assumption, the collection area is recalculated using the previous result and the spectrum is rederived. This process continues until the results converge [10].

The observed excess of gamma rays is then fit to a differential energy spectrum. Generally the spectrum is fit to a power law,

$$\frac{dN}{dE} = I_0 \left(\frac{E}{E_0}\right)^{-\Gamma}, \tag{1.14}$$

where I_0 is the differential flux normalisation, E_0 is the energy at which the flux is normalised, and Γ is the spectral index of the source. The spectrum can also be fit to a power law with an exponential cutoff

$$\frac{dN}{dE} = I_0 \left(\frac{E}{E_0}\right)^{-\Gamma} \exp^{(-E/E_{cut})}, \tag{1.15}$$

where E_{cut} is the cuff-off energy. A broken power law spectrum can also be fit by

$$\frac{dN}{dE} = I_0 \left(\frac{E_{break}}{E_0}\right)^{(\Gamma_2 - \Gamma_1)} \left(\frac{E}{E_0}\right)^{-\Gamma_2} \tag{1.16}$$

where E_{break} is the energy of the break point in TeV, and Γ_1 and Γ_2 are the spectral indices before and after the break point.

The integrated flux above an energy threshold is then calculated from the excess, (Δ), the zenith angle exposure, Z(t), and the effective area ($A_{eff}(E_{true}, Z)$) as a function simulated (true) energy through the following equation,

$$\Delta = \int_{E_{min}}^{E_{max}} \int_{t_{start}}^{t_{stop}} \left(\frac{dN}{dE} A_{eff}(E_{true}, Z(t))\right) dt\, dE. \tag{1.17}$$

For a power law spectrum, the integral flux I is calculated as, $I = \int_{E_{min}}^{E_{max}}(dN/dE)\, dE = \int_{E_{min}}^{E_{max}} I_0(E/E_0)^{-\Gamma} dE$. The systematic error on the integral flux is $\sim 20\%$ [34].

Simulation Programs

Since VHE gamma-ray telescopes do not have a standard gamma-ray source for calibration, data cannot be analysed without comparing observations to simulations. The modelling of all the known processes essential to detecting VHE gamma rays (described in the previous sections) makes these programs invaluable tools for H.E.S.S. and are the backbone of ground-based VHE gamma-ray astronomy.

CORSIKA (COsmic Ray SImulations for KAscade) is a detailed Monte Carlo program that simulates extensive air showers initiated by high energy cosmic-ray particles and tracks the development of shower particles through the atmosphere. These simulations can be compared with results from various high energy experiments for data analysis. The program is highly sophisticated and dynamic as it is kept up-to-date and accounts for all the known processes of high energy strong and electromagnetic interactions [78].

CORSIKA is made up of various program systems designated to model specified interactions. The main components of CORSIKA are: 2 models for hadronic interactions at low energies, 5 models for hadronic interactions at high energies, an adjustable program that describes hadronic interactions in agreement with experimental data, and 2 models for electromagnetic interactions [78]. Development of the program has allowed for further options to be incorporated into the program, namely the production of neutrinos and Cherenkov radiation, essential for VHE gamma-ray astronomy.

Sim_hessarray is the program that takes data from air shower simulations and runs it through a telescope array simulation to see what should be observed by the H.E.S.S. telescopes. Sim_hessarray produces look-up tables that are used to compare with real data in order to determine all the relevant information about the observed gamma ray.

MODTRAN is a program that models transmissivity along a path through the atmosphere. Any kind of atmosphere can be modelled (from a tropical model to a sub-arctic winter) and the optical depth is calculated for various layers of the atmosphere. H.E.S.S. uses a desert aerosol model consisting of quartz sand particles. Varying the wind speed parameter of the model from 0 to 30 m s^{-1} increases the amount of aerosols in the lower 2 km of the atmosphere [93]. The importance of being able to adjust the wind parameter and hence the concentration of aerosols will be apparent in Chapter 4.

1.7 General Conclusions

I began the chapter by highlighting the how gamma rays aid in the understanding of cosmic rays. The next chapter will discuss how gamma rays are important for cosmology, namely, through the study of gamma-ray emission from active galactic nuclei affected by the extragalactic background light.

I have then illustrated the ways in which gamma rays are created and interact with matter and radiation. I then briefly discussed the important discoveries H.E.S.S. has made since it has been in operation, adding extensively to the VHE source catalogue.

Lastly, I have discussed the power of the H.E.S.S. telescopes and the fruition of the Cherenkov technique after over 40 years of development. The atmospheric importance to the IACT technique will be discussed in greater detail in Chapter 3 and implemented in Chapter 4.

Chapter 2

Active Galactic Nuclei and the Extragalactic Background Light

This chapter will discuss active galactic nuclei (AGN) and TeV gamma-ray attenuation with the extragalactic background light (EBL). It will be shown how TeV gamma rays from AGN can be used to probe the EBL due to photon-photon annihilation of TeV photons with low energy photons travelling cosmological distances.

2.1 Active Galactic Nuclei

An active galactic nucleus (AGN) is a compact region at the centre of a galaxy, which has a much higher luminosity over part or all of the electromagnetic spectrum compared to normal galaxies. The radiation from AGN is believed to be a result of accretion on to the supermassive black hole at the centre of its host galaxy.

The study of AGN is important for many reasons. Due to the detection of certain types of AGN in very high energy (VHE) gamma rays, they are special laboratories for extreme physics. Also, AGN are so energetic they are able to probe the Universe on large scales, which makes them essential to studying the formation and evolution of the Universe [146].

2.1.1 Physical Characteristics

The driving force of every AGN is a supermassive black hole (SMBH) at the centre of its host galaxy, which powers the AGN luminosity by gravitational potential energy. There is an accretion disk that surrounds the black hole in which matter gets pulled towards it, losing angular momentum through viscous or turbulent processes [146]. This accretion energy is very powerful. Compared to nuclear fusion energy, it is roughly 100 times more efficient at releasing energy.

AGNs that are bright in the radio waveband (termed 'radio-loud' AGN) contain jets, while only weak jets are observed from some radio-quiet AGN. A jet from an AGN is a collimated stream of relativistic plasma orientated perpendicular to the accretion disk. It can be imagined that part of the accretion energy or rotational energy of the SMBH is used to project matter and energy into a jet. Although it is not known exactly how or why this happens, any candidate mechanism must at least be able to accelerate the material to bulk Lorentz factors of $\sim$10 and collimate the flow to angles of $\sim$0.1 radians. The most popular mechanisms generally involve magnetohydrodynamical winds driven by rapidly rotating black holes, but remain rather speculative [95]. The AGN jet as well as the other major features of AGN are illustrated in Figure 2.1.

Emission lines observed from AGN are caused by the photoionisation of the AGN's continuum. Line production depends on the density of the gas around the accretion disk, its ionisation state, temperature and distribution of atomic state populations, the background photon intensity, and the ability of the emitted photons to escape [95]. Above and below the accretion disk are fast moving clouds that emit broad optical and UV emission lines. These emission lines are termed 'broad-line emission'. AGN with broad-line emission features are generally classified as 'Type 1' AGN. Further away from the accretion disk, slower moving clouds emit narrow emission lines. These emission lines are called 'narrow-line emission' and are associated with 'Type 2' AGN.

Outside the accretion disk is an obscuring torus or cloud that prevents infrared to UV light from penetrating direct lines of sight.

Most AGN are variable to some degree, but blazars have been found to be the most rapidly varying class of AGN at all wavelengths. Variability gives us information about the emission region of the radiation as the source cannot vary quicker than the time it takes light to travel the size of the object.

AGN can be classified into a variety of different categories based on the observations of the major features described above. The unified model of AGN states that the appearance of an AGN depends on the orientation to the observer due to the anisotropic nature of AGN emission and/or obscuration of radiation. It therefore follows that the different classifications of AGN are largely due to random orientation angles rather than from different intrinsic properties.

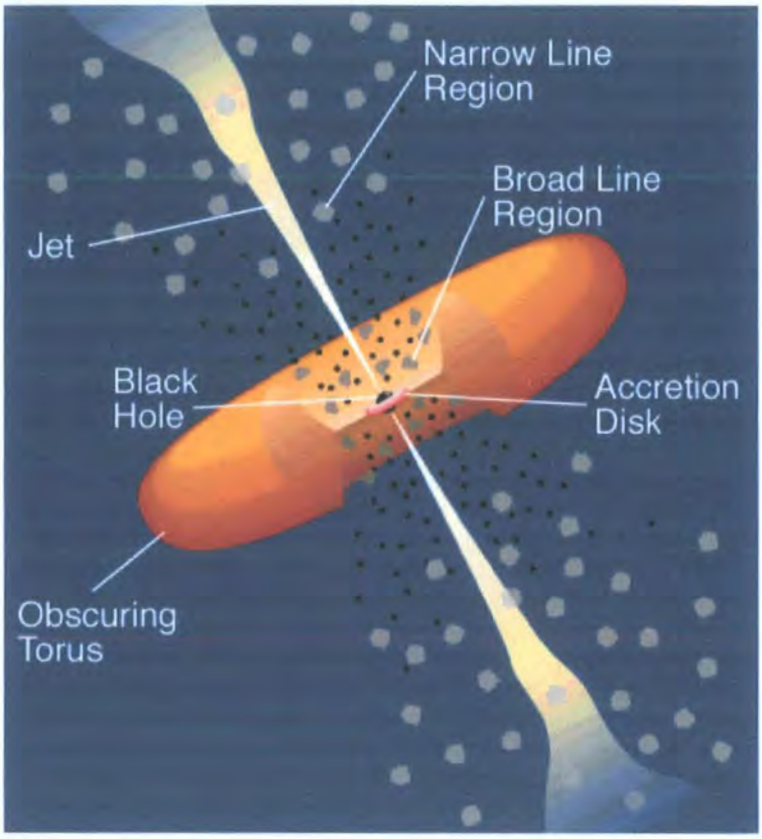

Figure 2.1: The main features of AGN, from [146]. See text for discussion.

2.1.2 Types of AGN

AGN can most easily be split into two main categories: radio-loud and radio-quiet AGN, which largely depends on the presence of a jet. Further classification reveals these two categories to be split into different types, namely Type 1 and Type 2, where Type 1 specifies AGN showing broad-line emission from the fast moving clouds above the accretion disk and Type 2 alternatively specifies those AGN showing narrow-line emission from the slower moving clouds further away from the accretion disk. Type 1 and Type 2 can be split once again into groups of high and low luminosity.

Type 0 is a special type reserved for those AGN with unusual spectral characteristics thought to have a small angle to the line-of-sight, such as blazars. Some types of AGN cross categories and are not strictly defined. This confusion has a historical basis, as technology improved, so did observations as well as the classification schemes. Figure 2.2 outlines the different types of AGN and how they are generally classified [95].

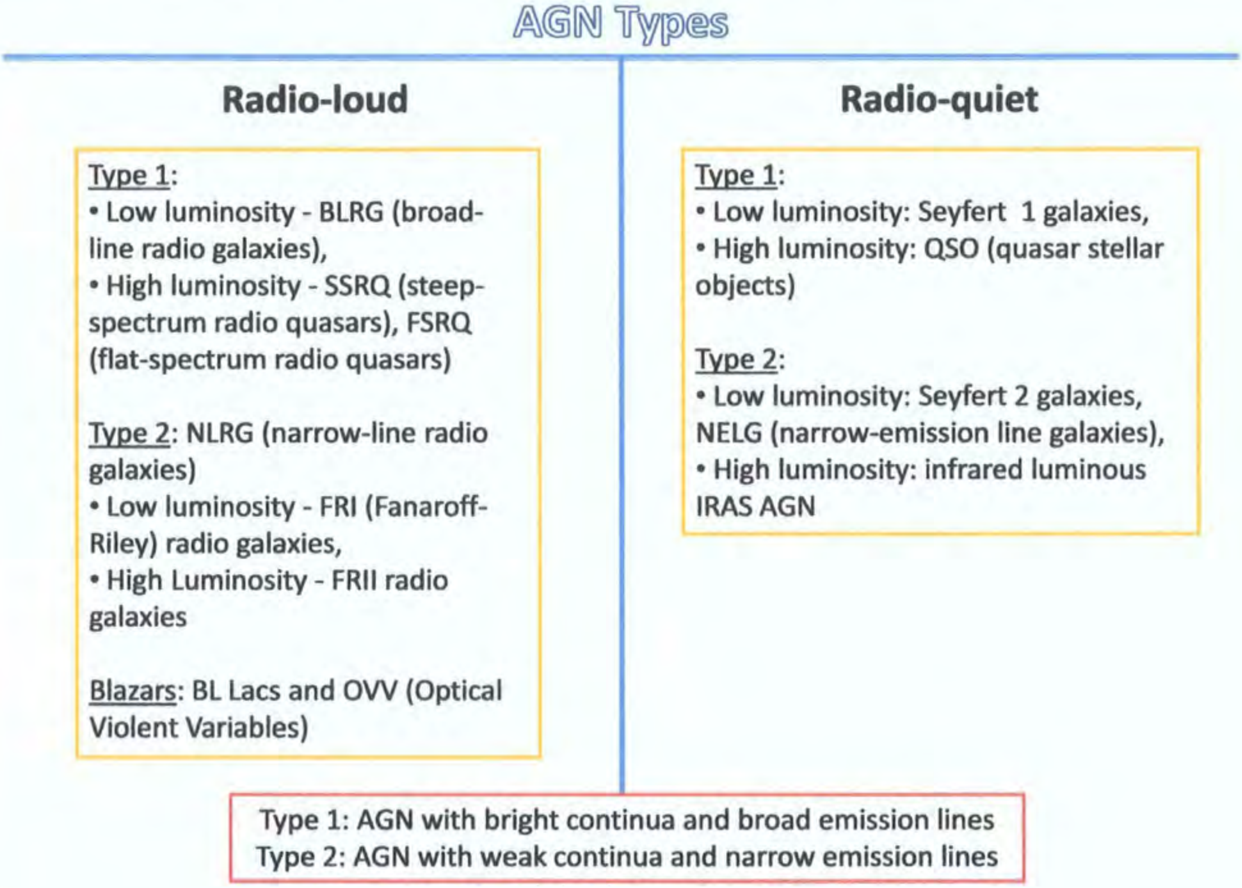

AGN Types

Radio-loud

Type 1:
- Low luminosity - BLRG (broad-line radio galaxies),
- High luminosity - SSRQ (steep-spectrum radio quasars), FSRQ (flat-spectrum radio quasars)

Type 2: NLRG (narrow-line radio galaxies)
- Low luminosity - FRI (Fanaroff-Riley) radio galaxies,
- High Luminosity - FRII radio galaxies

Blazars: BL Lacs and OVV (Optical Violent Variables)

Radio-quiet

Type 1:
- Low luminosity: Seyfert 1 galaxies,
- High luminosity: QSO (quasar stellar objects)

Type 2:
- Low luminosity: Seyfert 2 galaxies, NELG (narrow-emission line galaxies),
- High luminosity: infrared luminous IRAS AGN

Type 1: AGN with bright continua and broad emission lines
Type 2: AGN with weak continua and narrow emission lines

Figure 2.2: AGN categories and the types of AGN corresponding to each category, adapted from [95].

2.1.3 Blazars

Blazars are a class of AGN whose jet is pointed nearly head-on to the line of sight of the observer. The beamed emission radiated from the jet is Doppler-boosted, thereby enhancing the flux of the radiation [66]. They also exhibit rapid variability at all wavelengths on time scales from years to minutes [146, 23]. They are of such interest for VHE gamma-ray astronomy because blazars have been the major class of AGN detected in this energy range.

The broadband spectrum of a blazar is dominated by non-thermal emission from its relativistic jet and takes the form of a double-peaked structure. The spectrum is generally explained by the synchrotron self-Compton (SSC) mechanism [126, 86, 94] in the framework of relativistic jet models [72, 38] where particles are accelerated in shock fronts up the jet [60]. In SSC jet emission models, relativistic electrons are responsible for the production of the first emission peak via synchrotron radiation, while the second peak arises from inverse Compton scattering of the synchrotron photons by the same relativistic electrons. An alternative model proposes a similar mechanism at work, except that the seed photons for IC scattering come from an 'external' source such as from the accretion disk, gas clouds above and below the disk, or from the cosmic microwave background (CMB). This model is hence referred to as the external Compton scattering (ECS) mechanism [61, 133].

While leptonic models of VHE emission are commonly used, models involving protons are not to be excluded. These models involve adding a relativistic proton population into the jet. One such model is the proton induced cascade model where protons with maximum Lorentz factors in the range of $10^9 - 10^{11}$ generate hard photons with energies from keV to TeV via pion and pair photoproduction and subsequent synchrotron cascade reprocessing [107]. VHE gamma-rays could also be produced from synchrotron radiation from these extremely high energy protons ($E > 10^{19}$ eV) in highly magnetised regions ($B \sim 10 - 100$ G) with large Doppler factors ($\delta \simeq 10 - 30$) [2].

The two main subclasses of blazars are BL Lacs and Optical Violent Variables (OVV). The main difference between the two is that OVVs can sometimes show emission lines while BL Lacs do not. BL Lacs are of main interest to TeV gamma-ray astronomy and are classified according to the frequency location of their two peaks. High-frequency peaked BL Lacs (HBL) are classified as low power objects with their first spectral peak occurring at UV to X-rays with their second peak extending up to gamma-ray energies. Low-frequency peaked BL Lacs (LBL) are more powerful than HBLs with their respect peaks shifted to lower frequencies than that of HBLs [48].

2.1.4 Detected AGN VHE Emitters

As of December 2007, there have been 20 AGN detected by VHE gamma-ray telescopes. Eighteen of those 20 are high-frequency peaked BL Lacs while one is the original BL Lac, which is a low-frequency peaked BL Lac, first detected in gamma rays in 2007 [30]. The odd one out is M87, which is a Fanaroff-Riley class 1 radio galaxy discovered as a

VHE gamma-ray emitter in 2006 [17]. HBLs have proved to be more efficient particle accelerators than LBLs because (assuming a SSC model) the synchrotron spectrum of HBLs extends to higher energies than LBLs, implying the presence of higher energy electrons, which would produce an inverse Compton spectrum extending to higher energies [43]. However, the discovery of BL Lac has shown that LBLs have the potential to emit VHE gamma rays, with the case being that the detection of BL Lac's gamma-ray emission corresponds to a rise in its optical flux [30].

The first TeV AGN detection was of the blazar Mrk 421 ($z = 0.031$) observed in 1992 with the Whipple telescope [123]. The next AGN detected at TeV energies was another nearby blazar Mrk 501 ($z = 0.034$) in 1995, followed by 1ES 2344+514 ($z = 0.044$) in 1998 [43], both again detected with Whipple. These AGN were 3 of the closest known BL Lacs, suggesting at the time that TeV photons are strongly attenuated by interactions with the extragalactic background light [123] until the fourth BL Lac detected at TeV energies, PKS2155-304 ($z = 0.117$) in 1999 observed with the Mark 6 telescope [45]. The spectral energy distributions (SED) of all 4 BL Lacs were consistent with each other and displayed variability, providing observational evidence for the picture of VHE emission from BL Lacs we have today.

The discovery of the first 4 TeV emitting BL Lacs in a span of 7 years was followed by a tentative detection of 1ES 1959+650 in 1999 by the Utah Seven Telescope Array [115] and the detection of H 1496+248 in 2001 with the Whipple telescope [84]. It was only until H.E.S.S. and MAGIC came into operation that the rate of AGN detection has been steadily increasing from 6 BL Lacs detected in 2004 to 20 AGN detected by 2007.

The observations of TeV gamma rays from blazars suggest that jets are a strong source for particle acceleration. One such exception to the rule is the detection of M87 with its jet pointed $\sim 30^\circ$ from the line-of-sight of the Earth. The size constraint of the TeV emission derived from the observed variability of days has proposed a challenge to current TeV emission models while excluding many emission models. One excluded model includes the possibility of M87's extended jet as the source of particle acceleration. Two possible sites for emission include a peculiar knot (a site of many violent events detected by X-ray flares), or the nucleus of M87 [17].

For cosmology, an important effect of TeV gamma rays from AGN is that they can be used to probe the extragalactic background light (EBL) [138]. The attenuated TeV emission calculated from two high-redshift blazars, H2356-309 and 1ES 1101-323, has suggested that the Universe is less opaque than was once thought, implying that most

Table 2.1: A list of all the detected TeV gamma-ray AGN, as of December 2007.

AGN	Type	Redshift	Spectral Index	Discovery
M87	FRI Radio	0.0043	2.2±0.15	H.E.S.S. (2006) [17]
Mkn 421	HBL	0.031	2.1±0.1	Whipple (1992) [123]
Mkn 501	HBL	0.034	2.25±0.2	Whipple (1995) [125]
1ES 2344+514	HBL	0.044	2.65±0.17	Whipple (1998) [43]
Mkn 180	HBL	0.045	3.3±0.7	MAGIC (2006) [29]
1ES 1959+650	HBL	0.047	2.78±0.12	7 TA (1999) [115]
BL Lac	LBL	0.069	3.6±0.5	MAGIC (2007) [30]
PKS 0548-322	HBL	0.069	n/a	H.E.S.S. (2007) [142]
PKS 2005-489	HBL	0.070	4.0±0.4	H.E.S.S. (2005) [9]
RGB J0152+017	HBL	0.080	n/a	H.E.S.S. (2007) [114]
PKS 2155-304	HBL	0.117	3.32±0.06	Durham (1999) [45]
H 1426+28	HBL	0.129	2.6±0.6	Whipple (2001) [84]
1ES 0229+200	HBL	0.1396	2.4±0.3	H.E.S.S (2007) [26]
H 2356-309	HBL	0.165	3.1±0.2	H.E.S.S. (2006) [14]
1ES 1101-232	HBL	0.186	2.9±0.2	H.E.S.S. (2005) [144]
1ES 1218+30.4	HBL	0.182	3.0±0.4	MAGIC (2007) [28]
1ES 0347-121	HBL	0.188	3.4±0.4	H.E.S.S. (2007) [25]
1ES 1101+496	HBL	0.212	4.0±0.5	MAGIC (2007) [106]
PG 1553+113	HBL	>0.25	4.0±0.6	H.E.S.S. (2006)[16]
3C 279	HBL	0.536	n/a	MAGIC (2007) [143]
Total	20			

of the EBL can be resolved mainly from galaxy counts [105, 12] and that objects farther away have greater potential to be detected. The next section will discuss in more detail the impact the EBL has on VHE gamma-rays from AGN and how, in turn, the EBL can be inferred from our current understanding of VHE emission.

2.2 The Extragalactic Background Light

The extragalactic background light (EBL) is a diffuse background light that spans from microwave to gamma-ray energies. This light contains all the radiation that has ever been emitted over the entire history of the Universe. Its spectral energy distribution is distorted by the redshifting of photons as they travel to us from different sources at different distances [121]. Due to the homogeneity of the Universe on large scales, this light is expected to be isotropic.

The microwave component of the EBL, the well-known cosmic microwave background

(CMB) discovered in 1965 [119], was predicted as the result of the big bang theory where the CMB is the emitted radiation from the Universe turning optically transparent. The discovery of the CMB provided strong support for the notion of a hot, early evolving Universe and led to the recognition of the significance of a cosmic infrared background (CIB). The CIB probes physics in the Universe between the present epoch and the last scattering surface, and is complementary to the CMB, which probes mainly the physics at last scattering [87]. In such a Universe, one would expect a CIB to be associated with the formation of structure and the condensation of primordial matter from a redshift of ~1100 [77]. The other components of the EBL from X-rays to gamma rays mainly comes from AGN, supernovae, or gamma-ray bursts and have been measured by the ASCA, HEAO, COMPTEL, SAS-2, and EGRET satellites [92].

The EBL from UV to far-infrared wavelengths is likely to be the dominant radiant energy in the Universe after the CMB [77]. The CIB is of particular interest to VHE gamma-ray astronomy for the reason that the cross section for photon-photon annihilation with a TeV photon peaks with infrared photons (discussed in detail in Section 4.8.1).

One of the main issues in modern cosmology is to explain the formation and structure in the Universe. The assembly of matter into stars and galaxies and the subsequent evolution of such systems is accompanied by the release of energy powered by gravitational and nuclear processes [77]. Cosmic expansion and the absorption of short-wavelength radiation by dust and re-emission at long wavelengths will shift a significant part of this radiant energy into infrared background radiation. The earliest epoch for the production of this background occurred when star formation began and continues through the present epoch. The CIB is thus an integrated summary of the collective star-forming events, starburst activity, and other luminous events in cosmic history to the present time, and its measurement provides new insight into those processes by constraining the rates of star formation and metal production as a function of time [87].

Since the CIB carries important information about the galaxy and star formation history of the Universe, there is no uniquely predicted spectrum of the CIB since relative contributions of its various components depend on the cosmological history of star formation, the production of heavy elements, and the nature of dark matter in the Universe [59]. However, something may be said about its general shape. The structure of its energy distribution is expected to be observed as a double-peaked spectrum. The first peak is produced by starlight around 1 μm while the second peak around 150 μm is the result of starlight that has been absorbed and re-emitted by dust in galaxies [110, 56]. For convenience, the CIB is generally divided in 3 regions, the near-IR (NIR) 1 to 5-10 μm, the mid-IR 5-10 to 50-100 μm (MIR), and the far-IR (FIR) 50-100 to 500 μm [87].

Until the late 1990s, there had been no definite measurements of the infrared background radiation. This is because measurement of the CIB is difficult due to foreground emissions caused by starlight, interstellar dust, or zodiacal light [77].

2.2.1 Detections and Limits on the CIB

The CIB has few defining observational characteristics on which to base a detection. The radiation is of extragalactic origin and is therefore expected to be isotropic on large scales, and as mentioned above, there is no distinctive spectral signature. A positive detection must obviously show a positive residual signal after all foregrounds have been removed. This foreground removal is the greatest challenge due to model uncertainties. Lastly, because discrete sources contribute at least to part of the CIB, one would expect the background to show fluctuations superimposed on the isotropic signal [77].

The CIB is hard to detect due to non-CIB emissions caused by various sources. These emissions include: light emitted and scattered from interplanetary and interstellar dust, scattered light from local sources of the Earth's atmosphere, the Sun and Moon, zodiacal light from stars, as well as IR emissions from the detection instruments themselves. The main contributor is from interplanetary dust (IPD) [77]. Despite these difficulties there have been many attempts at direct detections which I will highlight below.

In 1983, the Infrared Astronomical Satellite (IRAS) attempted the first determination of the CIB. It was specifically designed to conduct an all-sky survey of point sources between 12 and 100 μm [134], and so a solid detection of the CIB remained ambiguous due to a lack of zero-point calibration along with uncertainties in the removal of foreground emissions [87].

The Comic Background Explorer (COBE), launched in 1990, contained two instruments designed to make absolute sky brightness measurements. The Diffuse Infrared Background Experiment (DIRBE) was designed primarily to search for the CIB from 1.25 to 240 μm, while the Far Infrared Absolute Spectrophotometer (FIRAS) was designed primarily to measure the CMB spectrum and to extend measurements of the CIB from 125 μm to millimetre wavelengths [77]. Initial results from DIRBE placed upper limits on the 10 different bands measured while only the 140 and 240 μm signal were found to be isotropic and could not be explained in terms of unmodelled components of the solar system or the galaxy [76, 57]. After the first results were published, there have been numerous attempts at improving foreground subtraction, see [77, 87] for a review.

In 1995 Japan's Infrared Telescope in Space (IRTS) was launched, claiming a significant isotropic emission from 1.4 to 4.0 μm that could be explained by the redshifted UV radiation of Population III stars [109]. Analysis of DIRBE data in the same wavelength shows a similar result to that of IRTS, strengthening the assertion that the isotropic signal is of extragalactic origin [109]. Since the peak absorption of 1 to 4 μm photons corresponds to 0.8 to 3.2 TeV energy gamma rays, this excess can be tested through TeV observations.

Spitzer was launched in 2003 and provides imaging and spectroscopy from 3.6 to 160 μm [154]. Spitzer has been able to help in the search for the populations contributing to the CIB. For example, it has been found that the dominant contribution to the FIR CIB are Luminous IR galaxies at $0.5 \leq z \leq 1.5$ [55]. Spitzer has also obtained lower limits of the CIB at 70 and 160 μm to be 7.1±1.0 and 13.4±1.7 nW m^{-2} sr^{-1} [56].

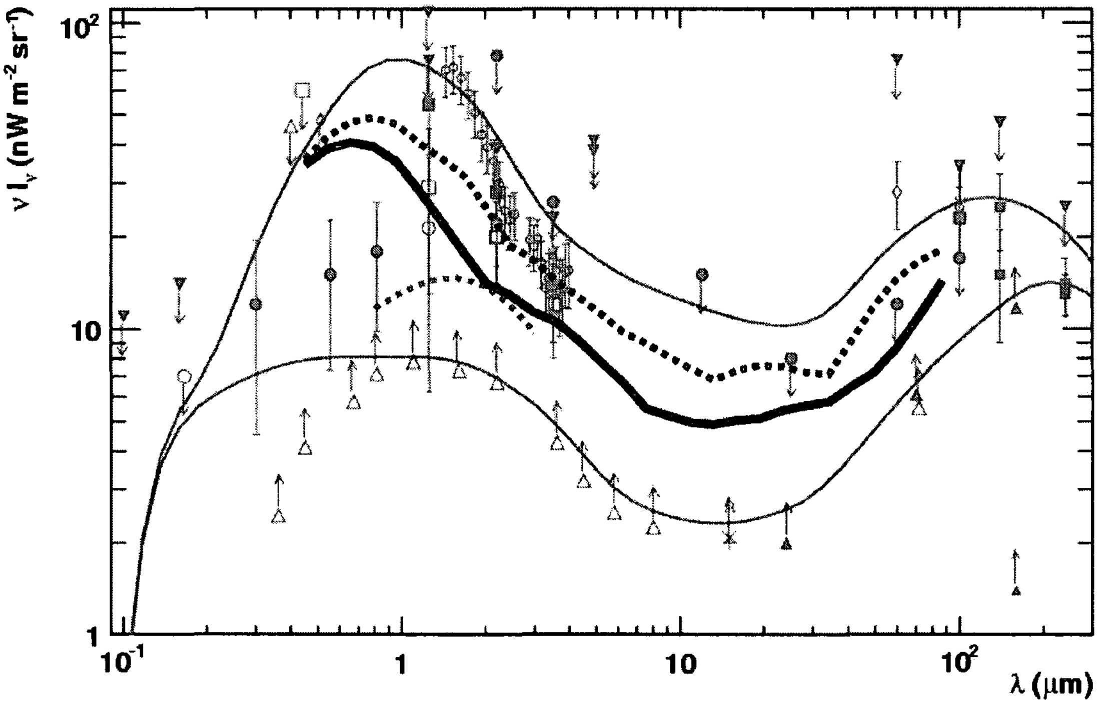

Figure 2.3: A recent picture of the EBL showing direct detections and limits (grey markers) along with results from the most exhaustive analysis of the EBL (lines), from [110]. The solid black line results from their realistic scan and the dashed black line results from their extreme scan. Grey lines are the minimum and maximum shapes tested in the scan. See Mazin and Raue (2007) in Section 2.2.2 for a discussion.

Lower limits to the EBL have been derived from source counts of galaxies [105, 67], while direct measurements have provided upper limits. The collective limits on the EBL between the UV and far-IR confirm the expected two-peak structure, although the absolute level of the EBL density remains uncertain by a factor of 2 to 10 [110]. A recent picture of the EBL showing direct detections and limits along with results from the most exhaustive analysis of the EBL, is shown in Figure 2.3.

2.2.2 Determination of the EBL from TeV Gamma rays

An alternative way for measuring the EBL was devised from the fact that TeV gamma rays will pair produce with low energy photons in the EBL [74, 138, 137, 53]. The VHE spectrum from a distant source is therefore expected to be attenuated, revealing information about the diffuse photon background annihilating with VHE gamma rays. However, this method works best if the intrinsic spectrum of the emitting source is known. At the present time, the intrinsic spectra of blazars are not fully understood and assumptions must be made based on our limited understanding of VHE gamma-ray production in AGN. To further complicate matters, it is also not possible to distinguish between attenuation caused by the EBL and attenuation that may occur at the source itself. It is therefore important to use this method on a large sample of TeV emitters at various distances in order to better constrain the limits of the EBL density.

Conversely, if the EBL is known, the intrinsic spectrum can be calculated and be used to test models of VHE emission and could in turn place limits on the EBL if the intrinsic spectrum derived is physically feasible.

The idea that TeV gamma-ray emission could be used to probe the EBL was first proposed by Stecker and de Jager in 1992 [138]. By using model-dependent upper and lower limits for the EBL, they predicted a cutoff in the gamma-ray spectrum due to EBL absorption of the quasar 3C 279 by extrapolating its intrinsic source spectrum from EGRET observations up to 1 TeV.

The first determinations of the EBL through this method were published in 1993 [137] and 1994 [53] using data from the blazar Mrk 421. Using data from EGRET and Whipple, the EBL flux was determined to be in the range of 1.0 to 10 nW m^{-2} sr^{-1} in the 1-5 μm range. These results were consistent with the theoretical upper limit derived from starlight from normal galaxies, and ruled out 'exotic' mechanisms for large infrared background densities, which previous observations detected [137]. These initial attempts at measuring the EBL assumed a shape for the EBL while TeV observations set constraints on the EBL normalisation.

Measuring the EBL from AGN is limited by the number of TeV AGN detected. Only since 2004 has the detection rate been considerable enough for further constraints to be placed on the EBL using various methods and clever techniques. The most recent results used to compare with my analysis in Chapter 4 are summarised next.

Dwek and Krennich (2005)

Dwek and Krennich [58] placed constraints on the EBL from the TeV spectra of Mkn 421, Mkn 501, and H1426+428. They created a sample of 12 EBL spectra representing different realisations of the EBL spanning the most extreme possible combinations of relative peak values. These spectra were fitted by polynomials to various spectral components from these observations constraints. The intrinsic spectra of the blazars were then calculated using the 12 template EBL spectra. EBL models giving rise to an unphysical exponentially rising spectrum were rejected. Four spectra were rejected on the basis of reproducing an unphysical intrinsic spectrum. It was also shown how the uncertainty in gamma-ray energy measurements affects the elimination of EBL spectra. Only one EBL spectrum was rejected on the account of having an unphysical reconstructed intrinsic spectrum when the gamma-ray energy spectrum was shifted up by 15%.

The average polynomial of EBL intensity used for comparison in Section 4.8 is given by,

$$\log[\nu I_\nu] = \sum_{j=0}^{N} a_j [\log(\lambda)]^j \tag{2.1}$$

with coefficients a_j=1.20000, 0.533686, -1.81116, -1.28135, 1.94804, 0.655142, -1.19371, 0.405981, -0.0437552 and $N = 8$ is the degree of the polynomial.

H.E.S.S. Collaboration (2006)

The H.E.S.S. Collaboration [12] has used two distant blazars, H 2356-309 (z = 0.165) and 1ES 1101-232 (z = 0.186), to determine the EBL spectrum. These sources provide a sensitive and constraining measurement of the EBL due to their large distances from Earth. In this analysis, a reference EBL shape from Primack [121] was assumed based on galaxy emission, with the normalisation taken as a free parameter and scaled to direct estimates at 2.2 and 3.5 μm (called 'P1.0'), and a lower limit was derived from galaxy counts ('P0.4'). An *ad hoc* component was also added to account for the claimed detection at 2 μm not predicted by galaxy evolution models.

The intrinsic spectra of the two sources were then reconstructed directly from observations. The resultant spectral indices for both sources, from the P1.0 and P0.4 models, were much steeper than would be expected from blazar emission models.

The EBL model was then scaled to reproduce a physical spectrum compatible with $\Gamma \geq 1.5$, constraining the EBL flux around 1-2 μm at 14±4 nW m^{-2} s^{-1}. These results, coupled with galaxy counts from the HST, led to the conclusion that the unresolved component of the EBL at optical to NIR wavelengths is not more than a third of the total, agreeing with the most recent theoretical calculations of the EBL [122]. These results also agree with theoretical arguments against high EBL fluxes due to Population III stars, revealing an intergalactic space which is more transparent to gamma rays than previously thought [12].

Mazin and Raue (2007)

The most encompassing EBL study using TeV sources comes from Mazin and Raue [110]. These results place new limits on the EBL from far infrared to optical wavelengths using the spectra of all known TeV blazars detected to date (13 at the time). They used a novel technique of describing the EBL number density by spline functions[1], which allowed for the testing of several million (8,064,000) possible EBL shapes [110]. This spline parametrisation is used to construct a set of EBL shapes using a grid in EBL energy density versus wavelength, setting the limits of the grid given by galaxy counts on the lower end, and direct detection and fluctuation analysis on the upper end.

The intrinsic spectrum for all VHE gamma-ray sources is calculated for each given shape of the EBL and is accepted or rejected based on its physical feasibility based on simple TeV gamma-ray emission models of blazars. This leads to the requirement that the intrinsic spectral index be greater than 1.5. The models are also tested for the extreme case of a spectral index greater than 2/3. Another requirement was that the reconstructed spectrum must not rise exponentially when approaching higher energies.

Combining all spectra, a constraining limit on the EBL was derived from 0.45 -90 μm ranging from 5 to 30 nW m^{-2} s^{-1}, which lies lower than upper limits derived from fluctuation analysis of direct measurements [88] and are a factor of 2 to 3 higher than absolute lower limits derived from source counts [105]. Systematic errors arising from the EBL grid setup, not taking into account EBL evolution, and uncertainties in TeV

---

[1] A spline function consists of polynomial pieces used to construct an overall smooth curve, see [110] for details.

gamma-ray measurements amount to 32% for the optical-to-NIR region and 33-55% for the MIR-to-FIR region. Results are shown in Figure 2.3 for the realistic and extreme scan compared to other measurements and limits.

2.2.3 Primack Model (2005)

The Primack model is a semi-analytic theoretical model (SAM) of galaxy formation (based on a ΛCDM hierarchical structure formation scenario) to make predictions of the EBL from 0.1 to 1000 μm [122]. SAMs incorporate simplified physical treatments of the key processes of galaxy formation such as the creation of dark matter halos, gas dynamics, star formation, supernova feedback, and metal production. The key parameters governing the rate of star formation and of supernova feedback and metallicity yield are adjusted to fit local galaxy data, namely through the luminosity function of galaxies in the nearby Universe from 2MASS, 2dF, and SDSS galaxy surveys.

The Primack model is in good agreement with galaxy observations at optical wavelengths out to higher redshifts of $z = 6$. The resulting EBL model in the near-IR to optical wavelengths is generally lower than other models, but agrees with lower limits from galaxy counts. However, the model has not yet been able to account for the bright far-IR galaxies observed by SCUBA, ISO, and Spitzer. The interpretation is that the Primack model underestimates the contribution of galaxies at $z > 0.7$ to the far-IR and perhaps the mid-IR components of the EBL. It follows that the attenuation of TeV gamma rays from mid-IR and far-IR photons (> 1 TeV) is likely to be underestimated.

2.3 General Conclusions

The basic properties of active galactic nuclei were discussed with emphasis on blazars, due to their near monopoly on extragalactic VHE gamma-ray sources. The CIB, or the infrared component of the extragalactic background light, was discussed in the context of containing important information about the galaxy and star formation history of the Universe. It was then emphasised that using the observed TeV emission from AGN can place limits on the CIB due to the attenuation of the emitted VHE gamma-ray spectrum. Lastly, the models and calculations of the EBL used for comparison in Chapter 4 are highlighted.

Chapter 3

Atmospheric Monitoring

Due to the nature of the imaging atmospheric Cherenkov (IAC) technique (see Section 1.4.4), the atmosphere plays an integral part in detecting gamma rays. Variations in the atmosphere affect the measurements of gamma rays. For example, the intensity of Cherenkov light may vary depending on the atmospheric conditions, and so the atmosphere must be closely monitored. The H.E.S.S. telescopes are therefore accompanied by four atmospheric monitoring instruments.

Firstly, the climate in Namibia will be discussed followed by data taken by the weather station instruments. Next, the radiometers will be discussed for their cloud detecting capability. The ceilometer, which is the most important instrument for detecting aerosols, will be discussed in detail followed by the transmissometer, which is used to measure the transmissivity over the lower 550 metres above ground level. Cross correlations between the instruments will then be presented. Lastly, the newly installed LIDAR will be discussed briefly.

3.1 Namibian Climate

The H.E.S.S. site sits atop the central plateau of Namibia in the Khomas Highland. The Khomas Highland is situated in between the Namib Desert to the west, separated by the Great Escarpment, and the Kalahari Desert to the east. A sketch of these features along the site's latitude across southern Africa is shown in Figure 3.1. Figure 3.1 was created based on a topological map of southern Africa shown in Figure 3.2 [127]. The H.E.S.S. site is located at 23° 16' 18" S, 16° 30' 00" E.

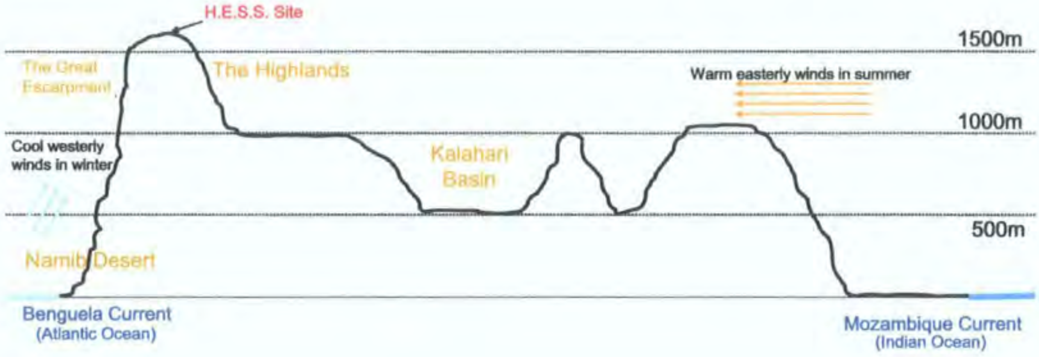

Figure 3.1: A sketch across the line of constant latitude where the H.E.S.S. site is located. It was created based on the topological map of Figure 3.2.

A maximum in mean annual sunshine occurs in the region around the H.E.S.S. site with an excess in sunshine hours of 3600, a value typical for a large part of the Sahara Desert [150]. Along with its high altitude and desert climate, these characteristics make the H.E.S.S. site an ideal location for observing.

In the summer months (December to February) low pressure dominates the area, which brings an influx of tropical moisture from the east by westerly winds. This causes inland areas to heat up from the warm Mozambique Current of the Indian Ocean [150]. Rain also occurs in the summer and is associated with the monsoon[1] flow of moist air from the Indian Ocean.

In the winter (June to August), cool temperatures and high pressure dominates, inhibiting maritime air. The winds in winter are often easterly, as cold airmasses from the Benguela Current in the Atlantic Ocean create dust storms from the Namib Desert. No rainfall falls in winter, due to the Great Escarpment, which ensures that any moisture precipitates at the coast (shown in Figure 3.1).

The main characteristics of the climate at the H.E.S.S. site are summarised in Table 3.1.

---

[1] A monsoon is a seasonal prevailing wind lasting several months.

Figure 3.2: A topological map of southern Africa. The H.E.S.S site is located at 23° 16' 18" S, 16° 30' 00" E [127].

Table 3.1: General characteristics of the climate in the central plateau of Namibia, information from [150].

	Summer (Dec. - Feb.)	Winter (Jun. - Aug.)
Nightly Temperatures	Hot (~ 17°C)	Cool (~ 7°C)
Pressure	Low	High
Wind	Easterly	Westerly
Rain	Rain from flow of moist air from Indian Ocean	No rainfall from Atlantic Ocean

3.2 Weather Station

A UK Meteorological Office approved weather station from Campbell Scientific measures the air temperature, air pressure, relative humidity, and wind, 24 hours a day [42]. A picture of the weather station at the site is found in Figure 3.3. The air temperature is measured by a 1000Ω platinum resistance thermometer (PRT). The relative humidity is measured by a Vaisala capacitive humidity sensor, whose dielectric constant changes nearly directly proportional to the relative humidity. The pressure is measured by a RPT410F barometric pressure sensor. The working specifications of each instrument are found in Table 3.2. The data from each of these instruments will be shown from January 2004 to December 2007 in this section.

Figure 3.3: The weather station pole on site, which measures the air temperature and pressure, relative humidity, and wind speed at ground level.

Air Temperature and Air Pressure

Nightly averages of air temperature per observation period[2] are shown in Figure 3.4. It can be seen that the highest night-time temperatures occur from November to February

---

[2] An observation period is determined by the lunar cycle and spans from full moon to full moon. All periods from January 2004 to December 2007 with corresponding Gregorian dates, mean Julian dates, and run numbers can be found in Appendix A.

Table 3.2: The working specifications of the weather station instruments.

Sensor	Range	Accuracy	Stability
Temperature Probe	-40°C to 60°C	±0.35°C at -10°C ±0.6°C at 60°C	n/a
Relative Humidity Probe	0% to 100%	±2% at 10% ±6% at 90-100%	1% yr^{-1}
Pressure Sensor	-40°C to 60°C	±2mB at -40°C to 60°C	<0.11 mB yr^{-1}

(summer) while the lowest night-time temperatures occur in June and July (winter). The average maximum is 17.8±0.3°C and the average minimum is 7.1±0.4°C, with the difference between maximum and minimum being 10.75°C. The average nightly temperature for all data is 12.7±0.3°C.

Figure 3.5 shows the number of observation runs versus air temperature. It is interesting to note that the number of observation runs decreases during the times of greatest temperature (summer), even though the dark-time increases, indicating bad weather associated with clouds or rain. Temperature is also negatively correlated with pressure, shown in Figure 3.6. These observations are consistent with rain and overcast conditions associated with lower pressure systems, while high pressure is associated with clear and cool weather [104].

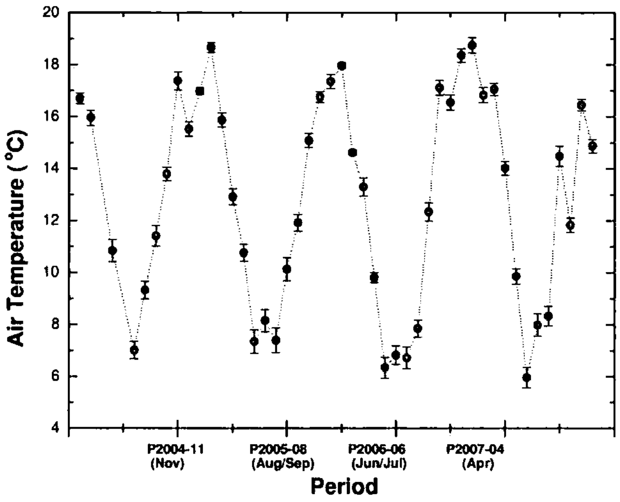

Figure 3.4: Nightly average temperatures per observation period with minima occurring from November to February and maxima occurring in June and July.

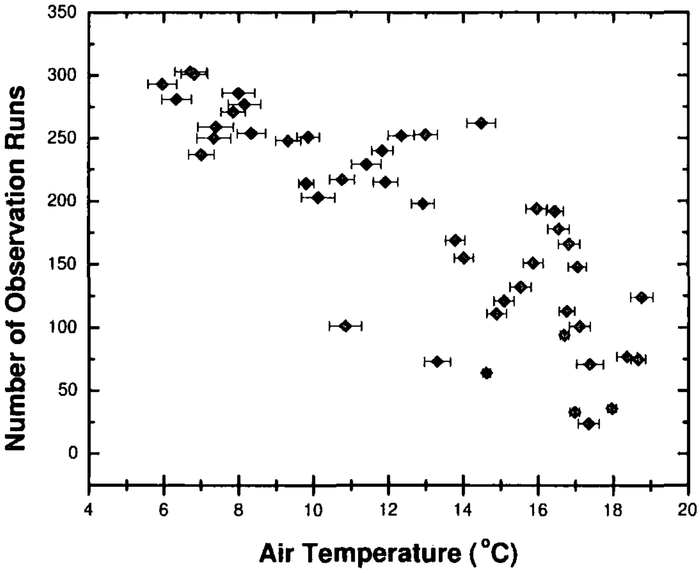

Figure 3.5: Number of observation runs as a function of air temperature. It can be seen that the number of runs decreases with increasing temperature, indicating bad weather associated with clouds or rain.

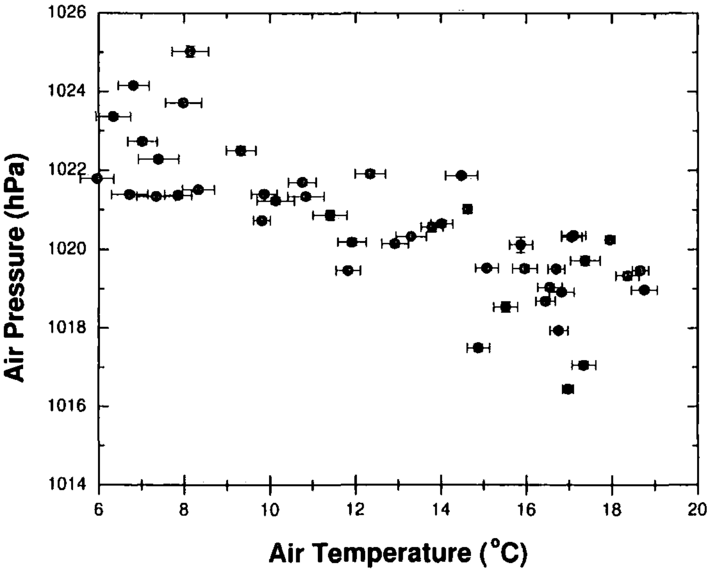

Figure 3.6: A negative correlation is seen between air temperature and air pressure, with a correlation coefficient[4]of ζ = -0.78.

Water Vapour

Relative humidity measures the proximity of air towards water saturation. Saturation is when the rate of evaporation equals the rate of water vapour returning to liquid. The corresponding pressure associated with saturation is called saturation vapour pressure. Saturation vapour pressure is temperature dependent and increases with temperature as the amount of evaporation increases. With a given amount of water vapour in the air, lowering the temperature reduces the capacity for air to hold water vapour, resulting in a higher relative humidity.

Relative humidity can be expressed as the ratio of water vapour pressure to saturation vapour pressure,

$$rh = \frac{p(H_2O)}{p_s(H_2O)} \times 100\% \tag{3.1}$$

where $p(H_2O)$ is the water vapour pressure and $p_s(H_2O)$ is the saturation vapour pressure. The Arden Buck equation describes the saturation vapour pressure of water at various temperatures given by [40],

$$p_s(H_2O) = 6.1121 \exp\left(\frac{17.368 \times T}{238.88 + T}\right) \text{ [hPa]} \tag{3.2}$$

with the air temperature, T, given in degrees Celsius. With temperature and relative humidity being measured by the weather station, and the saturation water vapour pressure calculated by equation 3.2, the pressure of water vapour $p(H_2O)$ can be calculated, which indicates of the total amount of water vapour in the air. The pressure of water vapour can then be converted to the mixing ratio, which gives the mass of water vapour per unit of dry air, expressed in grams per kilogram (g/kg)[5],

$$\text{mixing ratio} = \frac{\mathrm{m_{H_2O}}}{\mathrm{m_{dry}}} = 0.662 \times \frac{p(H_2O)}{p - p(H_2O)} \times 10^3 \text{ [g/kg]} \tag{3.3}$$

where p is the total pressure measured by the weather station and 0.662 is the ratio of the molecular mass of water vapour by the molecular mass of dry air.

When air reaches saturation, i.e. when relative humidity equals 100%, condensation occurs with any increase of water vapour or decrease in temperature. Water vapour may condense to form as dew, haze, fog, clouds, or frost. This is called the dew point and can

---

[4] The equation for the correlation coefficient used throughout this thesis is found in Appendix B.

[5] Using the ideal gas law, PV=nRT.

be alternatively be explained as water vapour reaching its saturation vapour pressure at a given temperature.

Figure 3.7 shows that the relative humidity varies more irregularly throughout the year than air temperature and pressure, with an average value of 42±1%. Maxima generally occur in March and April with the highest peak arising from an exceptionally rainy season at the beginning of 2006 (January - March). All local minima occur in September, which also happens to be the season of the largest aerosol densities (to be discussed in Section 3.5.1).

For a constant amount of water vapour, an increase in temperature results in a corresponding decrease in relative humidity (anticorrelation), as seen on a run-by-run basis in Figure 3.8. Since we are talking about changes throughout the year, it cannot be assumed that water vapour remains constant, and so a complex relation results between temperature and relative humidity, as shown in Figure 3.9(a). It can be seen that the relative humidity lags behind temperature, as well as pressure, shown in Figure 3.9(b). The initial rise in air temperature after a minimum is associated with low relative humidity, which then rises and is fairly correlated with the temperature. Conversely, the initial decrease in air temperature after a maximum is associated with high relative humidity, which then decreases with decreasing temperature. A similar lag in air pressure is seen, as a rise from low to high pressure is associated with high relative humidity, while a drop from high to low pressure is associated with low relative humidity.

Figure 3.10 shows plots of the mixing ratio, which gives a better indication of the total amount of water vapour in the air. Figure 3.10(a) shows that the mixing ratio tends to correlate with air temperature until the temperature reaches a minimum, where then the mixing ratio lags behind temperature by one period (indicated by the circled points), i.e. when the temperature initially rises, the amount of water vapour in the air decreases. After the mixing ratio reaches a minimum, it correlates with the temperature again and the cycle continues. Figure 3.10(b) shows a similar trend with mixing ratio and relative humidity, except the mixing ratio decreases before the relative humidity decreases. The overall behaviour of Figures 3.9 and 3.10 indicate that relative humidity is mainly driven by the amount of water vapour in the air rather than temperature changes (where relative humidity and temperature would be anticorrelated). In other words, relative humidity and air temperature are correlated due to an offset of moisture being added to the air, when increasing temperature leads into the rainy season.

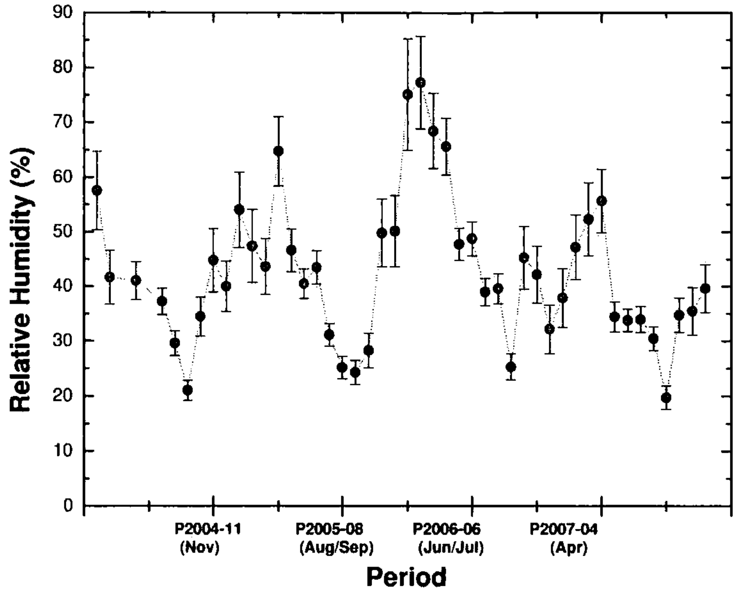

Figure 3.7: Maxima in March/April with an exceptionally rainy season at the beginning of 2006 (January - March). All local minima occur in September, which also happens to be the season of largest aerosol densities, to be discussed in Section 3.5.1.

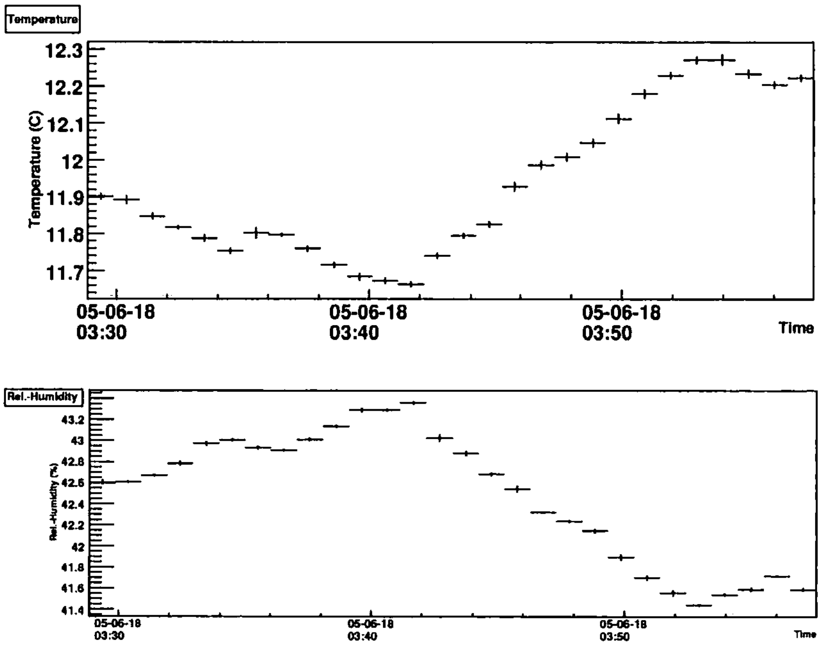

Figure 3.8: With a constant amount of water vapour in the air, as temperature rises, relative humidity naturally decreases. This anticorrelation is seen over the course of a run (run=26623).

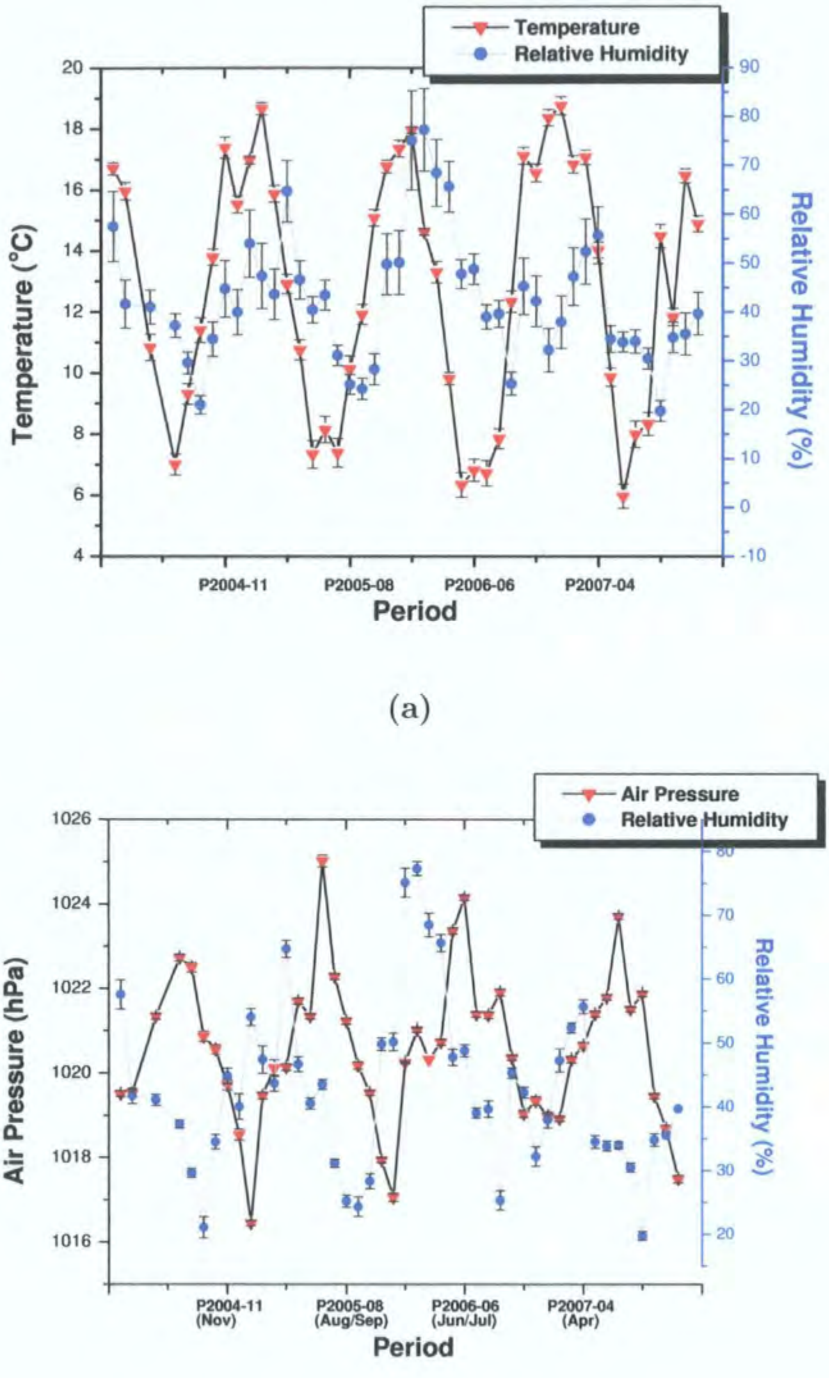

(a)

(b)

Figure 3.9: (a) Relative humidity appears to lag behind air temperature. As temperature increases, air pressure decreases (shown in (b)) in summer bringing in warm moist air from the east. This lag could be due to a delay in water vapour content being brought in from the Indian Ocean.

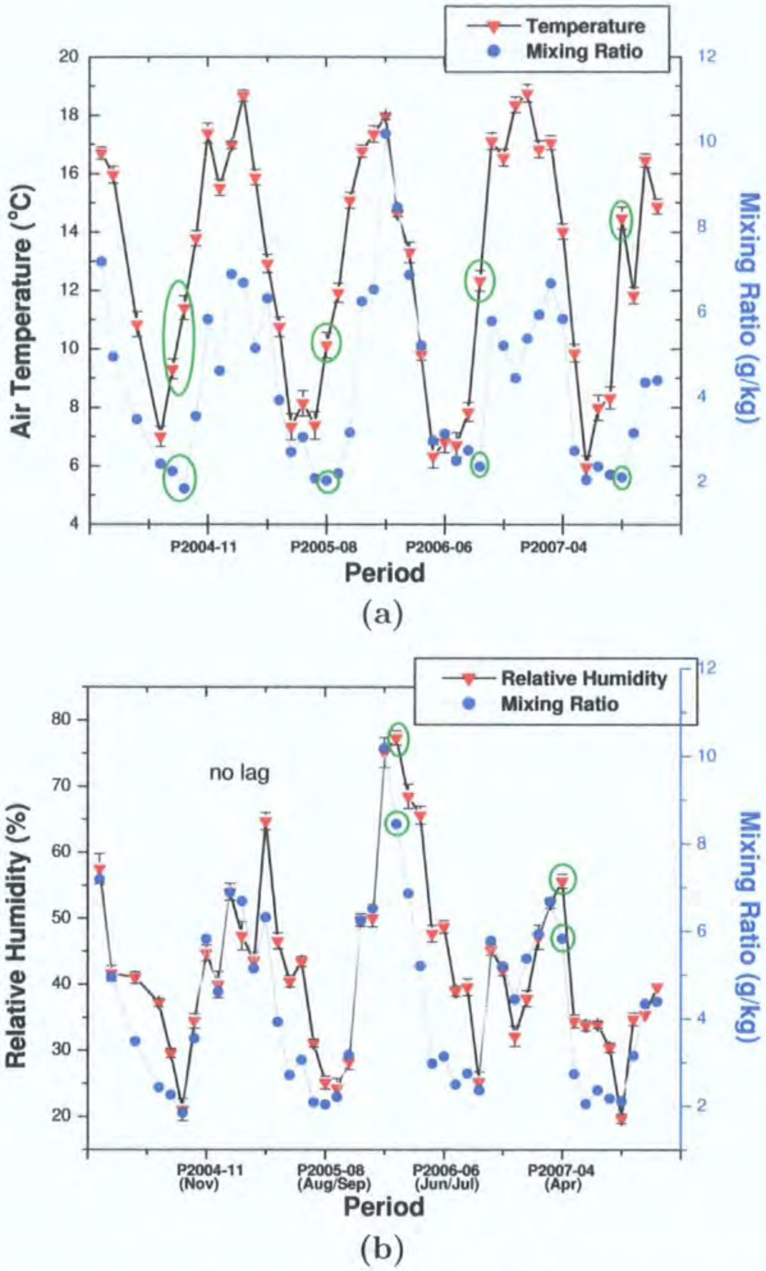

(a)

(b)

Figure 3.10: (a) The mixing ratio tends to follow the air temperature until the temperature reaches a minimum, where then the mixing ratio lags behind temperature by one period (indicated by the circled points), ie. when the temperature initially rises, the amount of water vapour in the air decreases. After the small dip in the mixing ratio, it follows the temperature again and the cycle continues until the next dip. (b) A similar trend happens with mixing ratio and humidity, except the mixing ratio decreases before the relative humidity decreases.

3.2.1 Importance of Weather Variables

Air temperature and pressure as a function of altitude define the atmospheric profile for a specific atmosphere. Figure 3.11 shows the pressure profile for various atmospheres modelled by MODTRAN along with radiosonde measurements made in Windhoek, Namibia over the course of a year [118].

Atmospheric profiles with different temperature and pressure profiles have varying effects on the emission of Cherenkov radiation by controlling the longitudinal development of extensive air showers. The lateral development is determined mainly by the Cherenkov emission angle and height of production, which in turn depends on the atmospheric density profile [118]. For example, atmospheric models which have higher temperatures in the lower part of the atmosphere result in shower maxima at greater heights. This is because an increased ground level temperature increases the pressure higher in the atmosphere, making higher altitudes more dense and more likely to initiate air showers higher up. This means that seasonal variations and hence, latitudinal location, will have an effect on the distribution of Cherenkov light measured at ground level. Bernlöhr (2000) [35] has shown that there is up to a 60% difference in Cherenkov light between tropical and polar models and some 15-20% seasonal variation at mid-latitude sites. The effect on the Cherenkov photon density is shown in Figure 3.12.

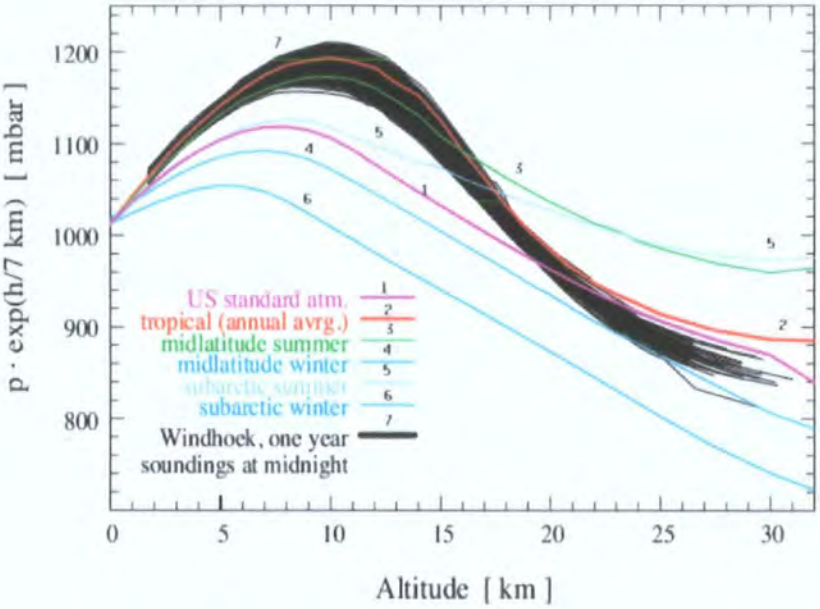

Figure 3.11: Atmospheric pressure profiles for various built-in MODTRAN models compared with those measured by balloon from Windhoek, Namibia (located ~ 100 km northeast of the H.E.S.S. site.) [118].

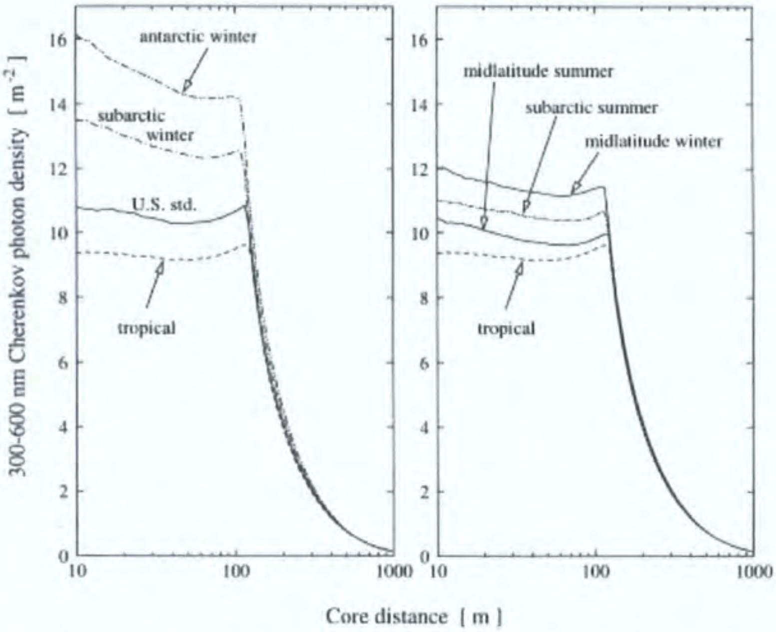

Figure 3.12: The average lateral distributions of Cherenkov photons (300-600nm) at 2200 m a.s.l. for vertical 100 GeV gamma-ray showers from CORSIKA simulations with different atmospheric profiles. The same absorption model is used for all, from [35].

3.3 Radiometers

The H.E.S.S. site is equipped with KT 19.82 II infrared radiation pyrometers (a.k.a radiometers) designed to detect infrared radiation from 8 to 14 μm. An infrared radiation pyrometer is a measuring transducer, which receives the infrared radiation emitted by a radiating object and transforms it into a standardised output signal. The infrared radiation is then fit to a thermal blackbody spectrum and the temperature is derived.

A radiometer is attached paraxially to each telescope with a field of view of 2.9° and are made for detecting clouds in the field of view of the telescope, as clouds produce an additional contribution to the thermal radiation detected at ground level. Therefore, the measured radiative sky temperature is increased for cloudy skies [41]. In addition to the telescope radiometers there is a scanning radiometer, which is used to scan the sky for any incoming clouds. It is located with the other atmospheric monitoring instruments, shown in Figure 3.16. The accuracy of the radiometers is ±0.5°C.

Figure 3.13 shows the measurements of an observation run from a telescope radiometer, which shows the increase in blackbody temperature as a cloud passes over the field of view of the telescopes. Due to the large rms of temperature ($\sim$ 5°C), this run would not pass the quality selection cuts and so would be rejected.

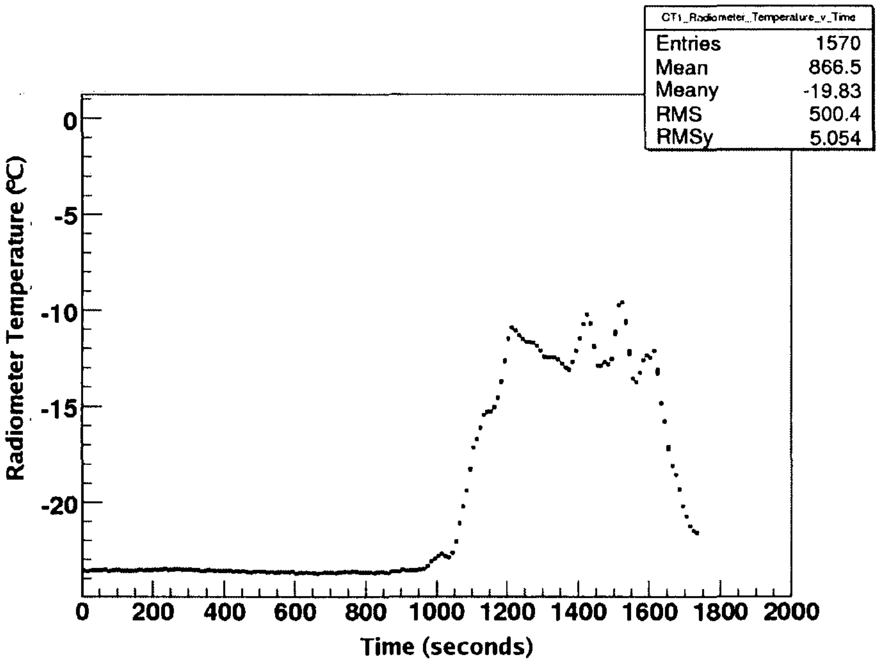

Figure 3.13: The sky temperature increases dramatically as a cloud passes in front of the field of view of the telescope (run=43749).

3.4 Cherenkov Light Extinction in the Atmosphere

Cherenkov radiation is extinguished in the atmosphere through molecular absorption, Rayleigh scattering by molecules, and Mie scattering by aerosols.

3.4.1 Extinction Particles

Gases and aerosols are the two main types of particles that contribute to the extinction of Cherenkov light. Gases are the smallest and most numerous particles in the atmosphere with sizes on the order of nanometres and densities of $\approx 2.6 \times 10^{18}$ molecules cm^{-3} at standard temperature and pressure. The five gases that compose $\approx 99.993\%$ of the volume in the 1976 U.S. Standard Atmosphere [145] are found in Table 3.3. Ozone (O_3) is mentioned in the table because although it is a small fraction of the atmosphere, its absorption effects can be considerable. Water vapour (H_2O), carbon dioxide (CO_2), and ozone (O_3) can vary from season to season, year to year, or day to day, whereas nitrogen (N_2), oxygen (O_2), and argon (Ar) tend to be relatively constant in place and time.

Table 3.3: The five most abundant gases found in the Earth's atmosphere according to the 1976 U.S. Standard Atmosphere [145].

Gas	% by Volume
N_2	78.078±0.004
O_2	20.946±0.002
Ar	0.934±0.001
H_2O	0-2
CO_2	0.0351±0.0004
O_3	0-0.3ppm[6](troposphere), 1-7ppm (20 - 30 km)

Aerosols are small particles the size of micrometres produced by human and natural activity. Sources of aerosols include: smokes, dusts, fogs, and precipitation. Normal aerosol densities can range from less than 10 molecules cm^{-3} on a very clear day to 10^4 molecules cm^{-3} in smokes and dusts, and are mainly limited to the boundary layer from 1-2 km above ground level. This makes aerosols site-dependent and highly variable [62].

---

[6] ppm = parts per million

3.4.2 Scattering and Absorption

Mie and Rayleigh Scattering

The complete analytical solution to Maxwell's equations that describe scattering of electromagnetic radiation by spherical particles is called Mie scattering. Mie scattering depends on the size, shape, and composition of the particles and it is not strongly wavelength dependent. The full Mie solution is used when describing particles that are large compared to the size of the incident light ($d \geq \lambda$). When describing particles that are roughly 1/10th the size of the incoming light (i.e. $d \ll \lambda$), the Mie solution reduces to Rayleigh scattering. Rayleigh scattering can be considered elastic dipole-like scattering and is proportional to the inverse fourth power of the wavelength ($\propto \lambda^{-4}$).

Rayleigh scattered light is distributed evenly in all directions whereas Mie scattered light is asymmetric with a forward peak. The magnitude of Rayleigh scattered light in the forward direction is much weaker (up to 100 times weaker) than Mie scattering because the particles are smaller. An illustration is shown in Figure 3.14. In Cherenkov experiments, Mie and Rayleigh scattering are treated as absorption processes because the amount of light scattered in the telescopes is negligible [118].

Particle Extinction Effects

Figure 3.15 shows the extinction effects of the most important absorbers and scatterers in the atmosphere. The majority of attenuation from 290 to 650 nm is due to Rayleigh scattering by molecules. Rayleigh scattering can be considered to be elastic scattering and is easily predictable and shows only small temporal variation. The most abundant atmospheric molecules, namely nitrogen (N_2) and oxygen (O_2), in the atmosphere remain relatively constant and so the effect of Rayleigh scattering should remain constant as well.

Ozone absorption dominates molecular absorption at wavelengths shortward of 330 nm till about 200 nm. Gaseous water vapour plays a minor role in molecular absorption affecting wavelengths longward of 550 nm. Since the peak sensitivity to Cherenkov light ranges from 300-500 nm for the PMTs used by H.E.S.S., ozone and water vapour absorption need not be taken into account in Cherenkov light extinction. However, precipitable water vapour in the form of droplets with sizes comparable to and larger than the wavelength of light is important and can manifest as haze or a thin cloud. Water vapour coalescing on aerosols affects their scattering properties and is reflected in Mie scattering. Therefore, relative humidity and temperature changes may cause aerosols to grow larger and effect the scattering of light by Mie scattering [31].

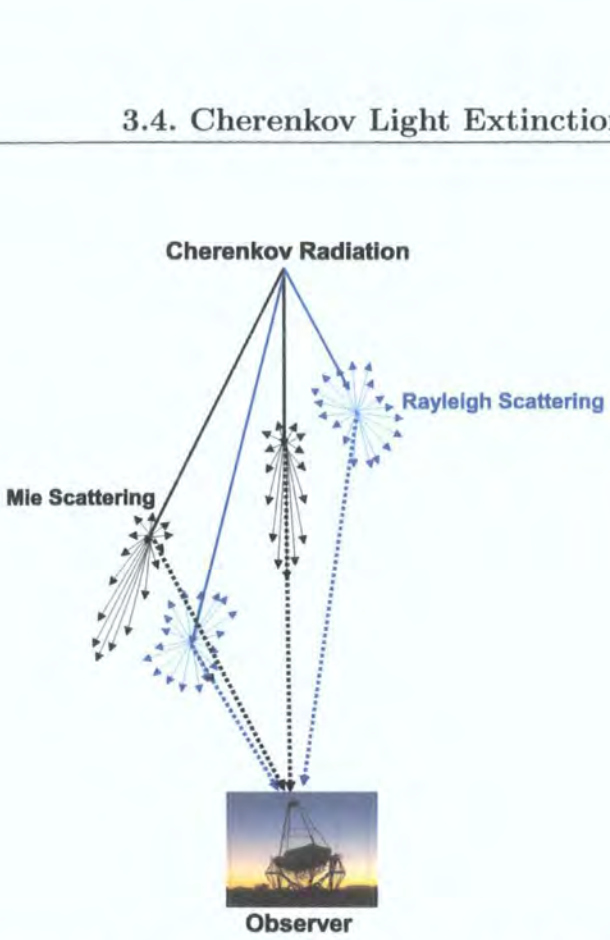

Figure 3.14: The scattering of Cherenkov radiation from Mie and Rayleigh scattering. The relative intensity of Mie to Rayleigh scattering is not shown to scale by the arrow lengths. Even though there is a forward component from scattering processes, these tend to have negligible effect in Cherenkov experiments.

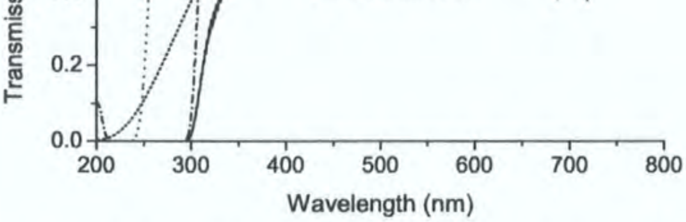

Figure 3.15: Direct transmission of light from 100 km altitude to 1.8 km, as calculated with MODTRAN. The impact of the most important absorbers and scatterers are shown (Courtesy of Christos Hajichristidis).

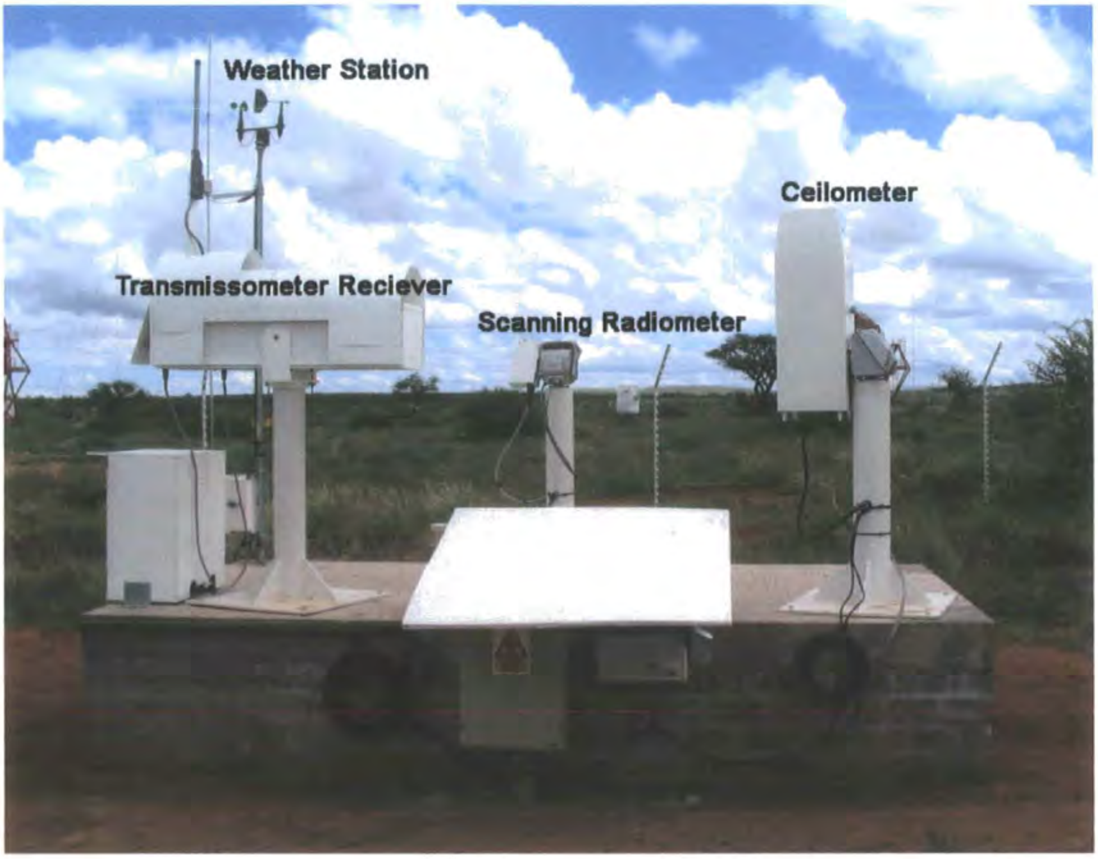

Figure 3.16: A picture of all the atmospheric monitoring instruments.

3.5 The Ceilometer

The ceilometer is a commercial Vaisala CT25K LIDAR (LIght Detection And Ranging) with a built-in atmospheric data reduction program that measures the backscatter, mainly due to aerosols, using a InGaAs laser diode at (905 ± 5) nm up to a maximum distance of 7.5 km [46]. A LIDAR works like RADAR but uses optical radiation instead of radiowaves. The time delay of the returned backscatter signal determines the height of the scattering material (aerosols) given by, $d = c\Delta t$. Assuming the same composition of aerosols, the higher the backscatter value, the greater the aerosol content. The backscatter profile returns the signal strength over height thereby measuring cloud heights and vertical visibilities.

Figure 3.17: The ceilometer used to measure the backscatter of radiation at 905 nm.

Lidar Equation

The lidar equation expresses the power outputted by the LIDAR. The lidar equation is given by [147],

$$P(r) = E_0 \frac{c}{2} \frac{A}{r^2} \beta(r) \exp(-2 \int_0^r \alpha(r') dr') \tag{3.4}$$

where $P(r)$ is the instantaneous power received from distance r, E_0 is the effective pulse energy, c is the speed of light, A is the receiver aperture, $\beta(r)$ is the volume backscatter coefficient at r in $\mathrm{m}^{-1}\ \mathrm{sr}^{-1}$, and $\alpha(r')$ is the extinction coefficient. The two unknowns in this equation are $\alpha(r)$ and $\beta(r)$. Since a major part of extinction is due to scattering, $\alpha(r)$ must depend on $\beta(r)$ in a relation called the lidar ratio. For an atmosphere dominated by aerosols, the lidar ratio takes the form of, $\beta(r) = \text{constant} \times \alpha(\mathrm{r})^k$ where k is dependent on the type of aerosols present [90]. Since the lidar ratio is dependent on the composition of aerosols, it often must be approximated due to lack of information about the exact composition of the aerosols.

3.5.1 Backscatter

Backscatter is the intensity of light scattered backward at zero degrees [50]. In theory, using inversion techniques and the lidar ratio [90] one is able to extract the extinction, or transmissivity, from the backscatter signal. These transmissivity values are then important for use in atmospheric models that model the Cherenkov light through the atmosphere and hence the gamma-ray energy. In the case of the Vaisala LIDAR, the signal-to-noise ratio is too low to be inverted to calculate the extinction through the atmosphere [31]. In any case, the behaviour of aerosols over time has been investigated and provides a rough estimate on the level of contamination in the air.

The backscatter values produced by the ceilometer do not actually return the backscatter as defined by the lidar equation, but rather an attenuated backscatter, $\beta_{data} = \beta(r)T(r)^2$, where $T(r)$ is the transmissivity,

$$T(r) = \exp(-\int_0^r \alpha(r')dr') = \exp^{-\tau} \tag{3.5}$$

with τ being the optical depth. In addition, in order to maintain resolution in the low backscatter region during times of high backscatter, a transformation was performed on the raw attenuated backscatter signal given by, $\beta'_{data} = 1000\tanh(\beta_{data}/1000)$ [83]. From now on, the corresponding backscatter values will refer to this transformed attenuated backscatter in units of km^{-1} sr^{-1}.

The ceilometer is optimised and height corrected to detect significant backscatter up to 1 km from the instrument or up to where non-negligible amounts of aerosols are found. This is because the data are noisy and the internal algorithm of the ceilometer returns negative backscatter values when no aerosols are identified [47]. In my analysis, runs with no cloud layers were analysed to study the effect of aerosols on the cosmic-ray trigger rate of the telescopes and subsequently the gamma-ray flux (see Chapter 4).

Backscatter Measurements

Each ceilometer file is stored by run and was looked at one by one in order to get rid of runs containing clouds or corrupt files. Uncorrupted runs without clouds are considered 'good.' The integrated backscatter signal, up to the maximum backscatter height, BS_{Int} for all good data from 20 March 2004 to 23 April 2007 is shown in Figure 3.18. It can be seen that backscatter can vary significantly over long timescales as well as varying significantly from night to night, as shown by Figure 3.20. The highest backscatter values are found in

August and September of each year where the main component of atmospheric aerosols are dust and smoke. The dust drifts from the Namib desert on the western coast in the winter time, while smoke is seen during times of regular bush burning in the desert during the dry season from April to October. A figure of backscatter integral for values greater than high values of 30000 sr^{-1} versus relative humidity is shown in Figure 3.19. It can be seen that runs with large amounts of aerosols tend to be runs with low humidity, although there have been two recorded nights when the relative humidity was high with a large aerosol concentration in the winter (14 August 2004 and 18 June 2005). Shift logs indicate clear nights with nothing out of the ordinary during these observations (just dust), and so an explanation is beyond the scope of the data available.

Two types of profiles have been generally observed: high-lying and low-lying layers. High-lying layers are likely to be clouds and can be confirmed by radiometer measurements. This is shown in Figure 3.21. Data with clouds are rejected. The more important low-lying dusty layers act as a 'neutral-density filter' that reduces the Cherenkov light yield through Mie scattering [98]. These aerosol layers in Namibia have generally been found below 2.5 km.

I have placed cuts on the ratio of integrated backscatter (BS_{Int}) divided by the integrated backscatter up to 550 m (BS_{550}) to be $BS_{Int}/BS_{550} < 1.15$. This cut indicates the runs where the majority of the aerosol layer is below 550 m and has a profile that looks like what is shown in Figure 3.22. These data are used for studies with the transmissometer, which measures the transmissivity of the atmosphere up to 550 metres above ground level (discussed in the next section).

The backscatter dependence on zenith angle has also been investigated. This was done for low backscatter values less than 3000 sr^{-1} so as to get an aerosol layer that changes as little as possible. A relation is hard to see with most data because slight changes in the backscatter profile destroy any correlation. Figure 3.23 shows a couple of consecutive run that show a correlation, but nothing solid enough to derive a correction from as one shows a positive correlation between backscatter integral and zenith angle, while the other shows a negative correlation.

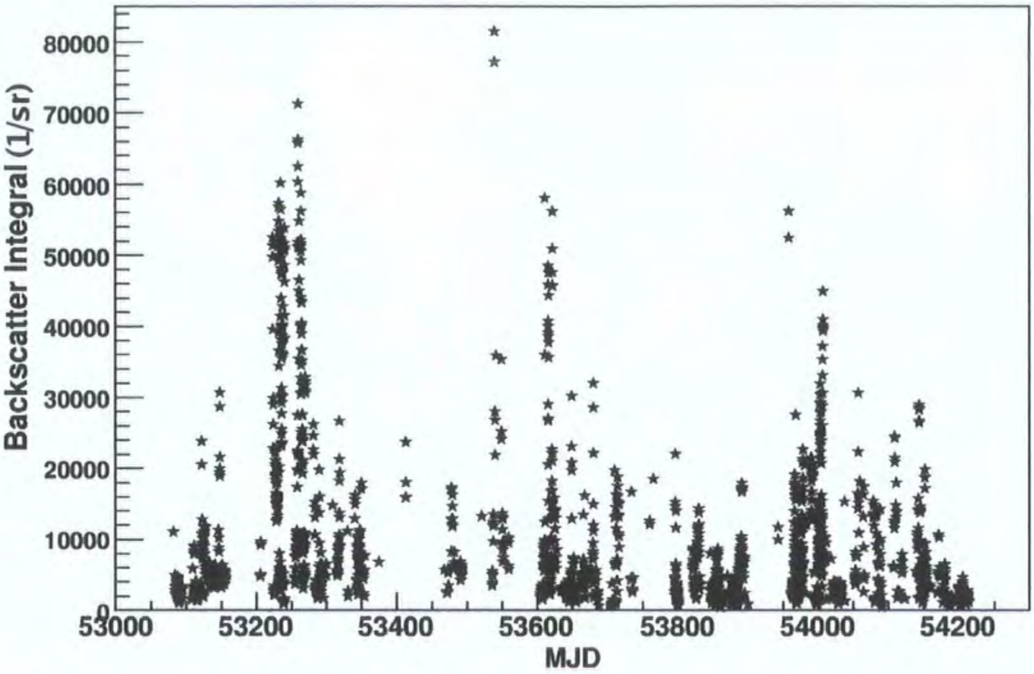

Figure 3.18: Backscatter integral for all good data from 20 March 2004 to 23 April 2007.

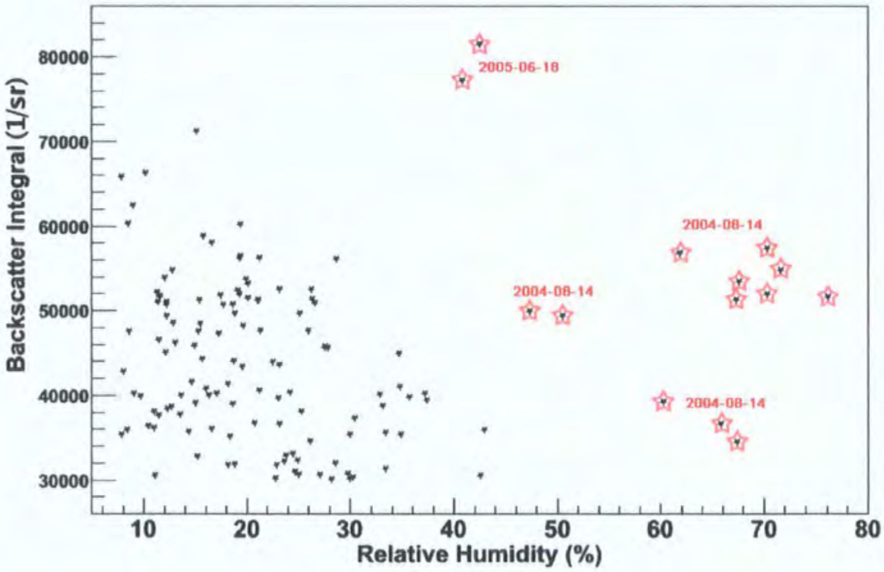

Figure 3.19: The relative humidity tends to be low with large aerosol concentrations except for two nights in the winter.

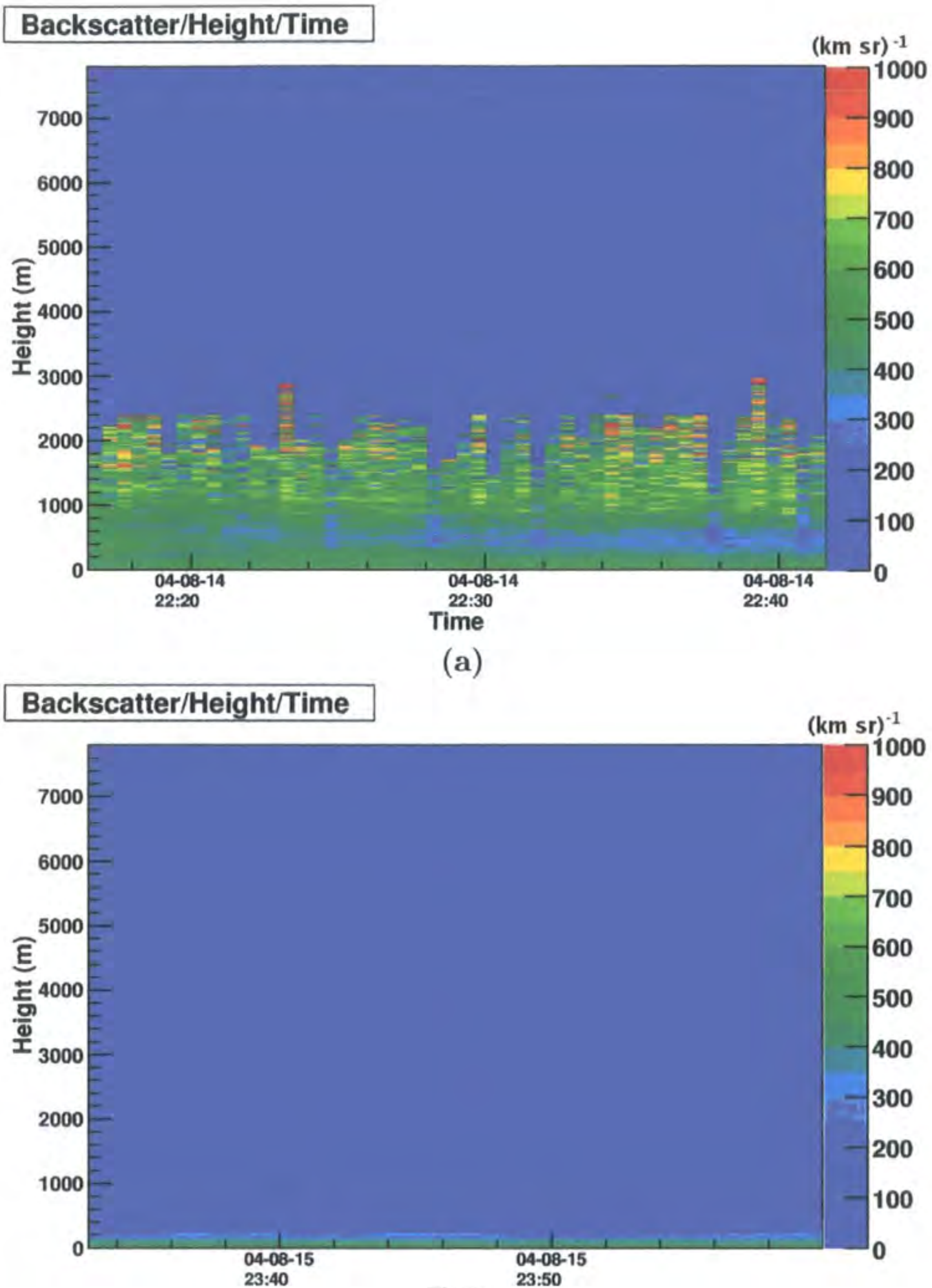

(a)

(b)

Figure 3.20: Runs=22043 and 22066 on two consecutive nights (14-15 August 2005) at similar times and similar atmospheric conditions. This illustrates that backscatter can change drastically from night to night. The colour scale represents different density levels of backscatter in units of (km sr)$^{-1}$ with blue and green being low to moderate density of aerosols and light green to red indicating the densest aerosol regions.

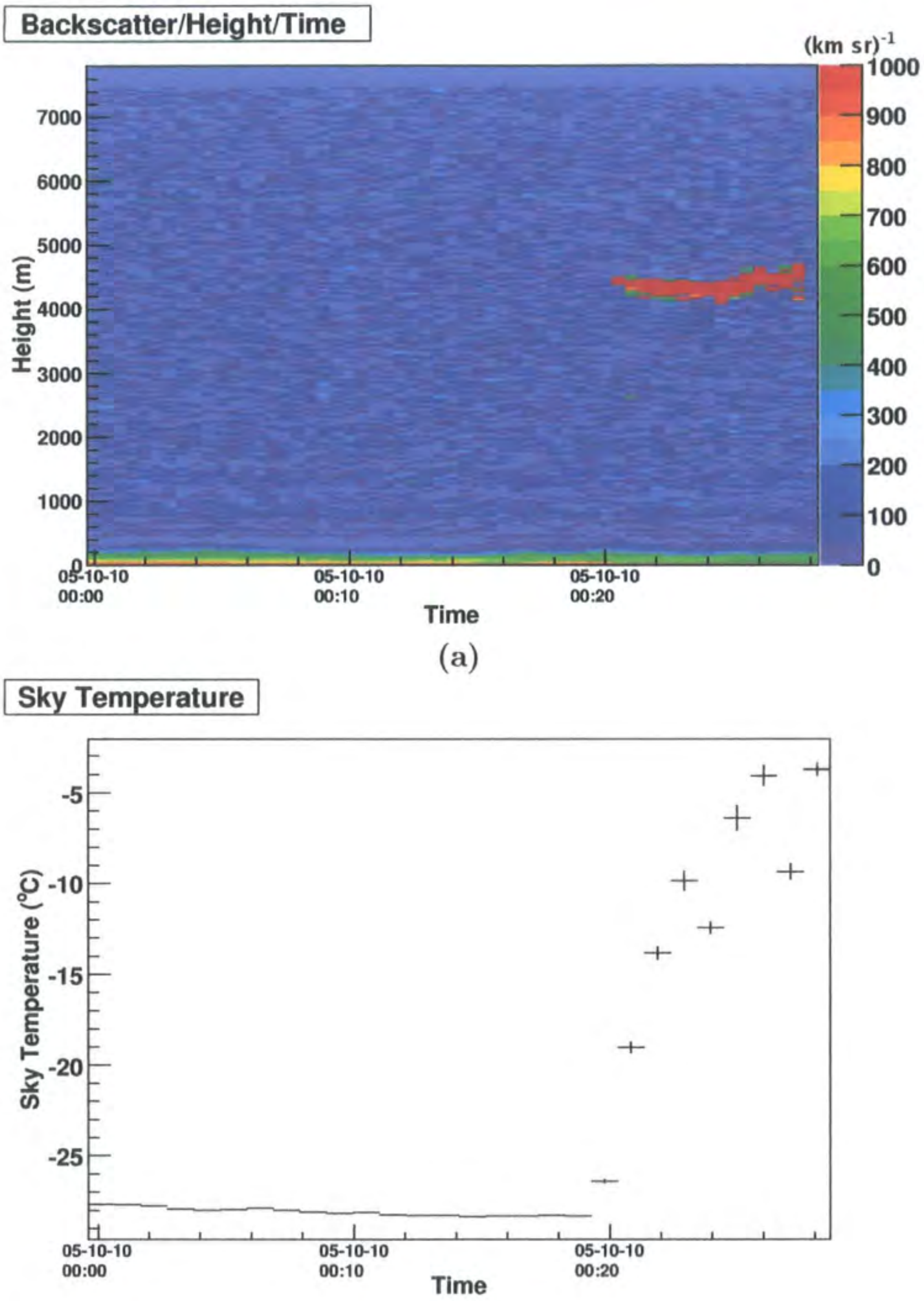

(a)

(b)

Figure 3.21: The top figure shows the backscatter profile for a cloud passing in the field of view of the ceilometer for run=29215. Simultaneous radiometer observations confirm the presence of a cloud by the large temperature change.

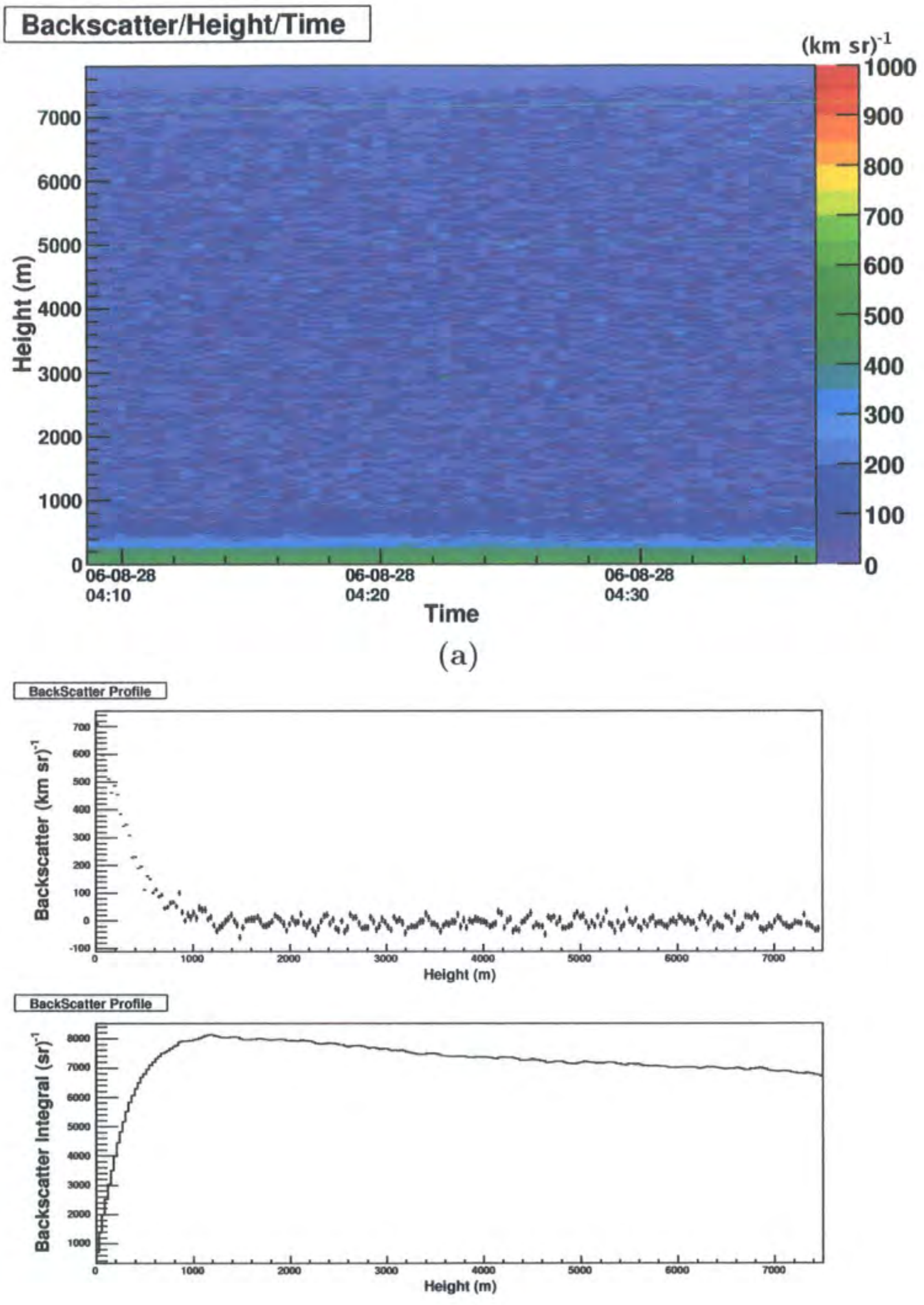

(a)

(b)

Figure 3.22: Run=34454 where the majority of the aerosol layer is below 550 metres along the line-of-sight of the ceilometer, or $BS_{Int}/BS_{550} < 1.15$. a) Shows the backscatter over the course of the run while b) shows the time averaged backscatter where the top graphs shows the backscatter versus height and the bottom shows the integrated backscatter of the top graph where the integrated backscatter value (BS_{Int}) is taken to be the maximum value located at $\sim$1200 m.

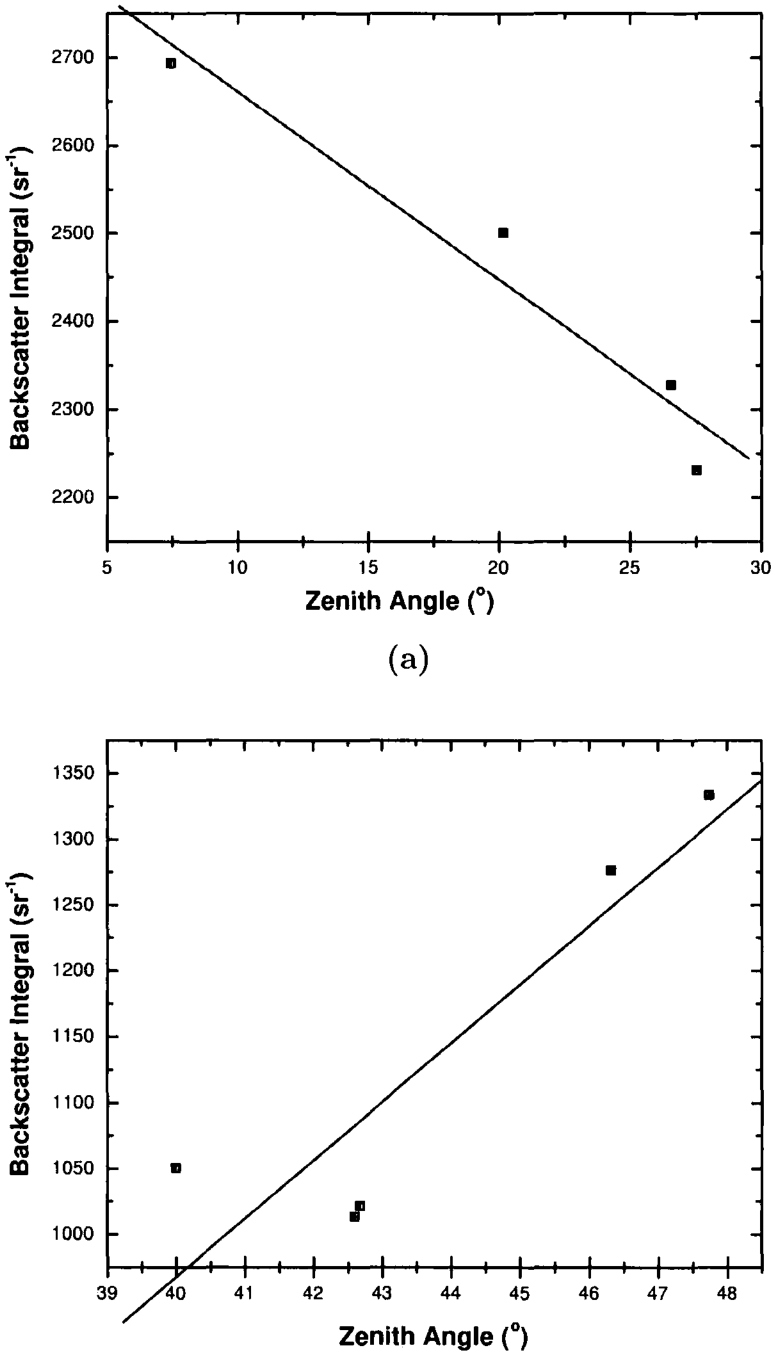

(a)

(b)

Figure 3.23: Backscatter integral versus zenith angle for (a) runs=22916-919 and (b) runs=20101-104. Due to an ever changing atmosphere, only a weak correlation between backscatter integral and zenith angle for a few number of consecutive runs is found.

Ceilometer Timeline

Figure 3.24 shows a timeline regarding the operation of the ceilometer.

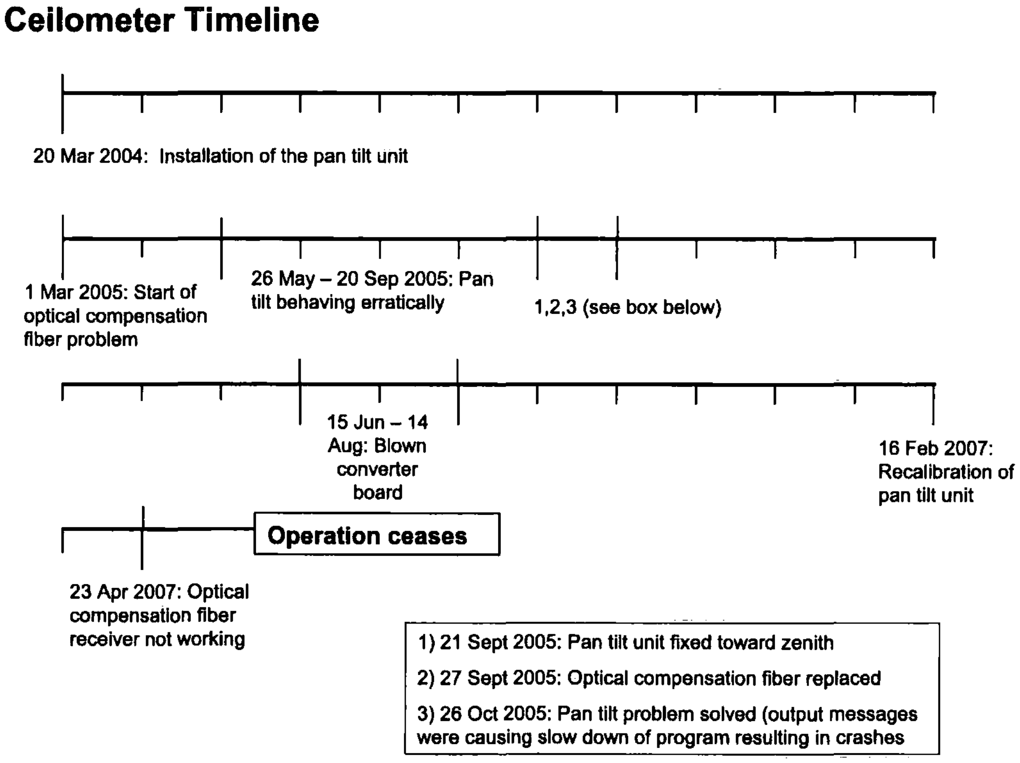

Figure 3.24: A timeline regarding the operation of the ceilometer from when it became fully functional with the installation of the pan tilt unit until it ceased operation on 23 April 2007.

- 20 March 2004: Installation of the pan tilt unit and the start of a fully operational ceilometer.
- 1 March 2005: Start of data issues with backscatter values saturating at 32767 due to a misaligned optical compensation fibre. This fibre is important for diverting some of the signal to a receiver measuring the output of the laser.
- 26 May - 20 September 2005: The pan tilt unit is not behaving properly. It is erratically moving during the day without instruction.
- 21 September 2005: The pan tilt unit is fixed toward zenith to stop it from moving erratically.

- 27 September 2005: The misaligned optical compensation fibre causing data problems is fixed.
- 26 October 2005: The pan tilt problem is solved. A flood of output messages were causing the ceilometer program to crash.
- 15 June 2006: Blown converter board, which supplies power to different parts of the instrument.
- 14 August 2006: Converter board replaced.
- 16 February 2007: Recalibration of the pan tilt unit. There have been many times when the number of ceilometer events equals 1 when it should be about 70. This happened as the ceilometer rotated on its pan and tilt unit hitting the safety n-switch causing the data from the last run to be recorded for the present run.
- 23 April 2007: The ceilometer has ceased to work. This was due to a compensation optical fibre problem again, but when the fibre was replaced, it still did not work. It was then found that the receiver was not working. Since the new lidar was coming online shortly and the old one was expensive to fix, repairs have been put on hold indefinitely.

3.6 The Transmissometer

In order to better study the transmissivity of Cherenkov light in the lower part of the atmosphere, a fully automated multi-wavelength transmissometer was installed in January 2005. It measures the atmospheric transmissivity of light at 505, 455, 910, and 390 nm between the H.E.S.S site (1800 m a.s.l.) and the top of the Gamsberg mountain (2350 m a.s.l., 30 km away) [96].

3.6.1 Transmissometer Setup

Transmitter

The transmitter of the transmissometer is located ~ 30 km away from the H.E.S.S. site on top of the Gamsberg mountain. A picture of the light transmitter is shown in Figure 3.25. The light source consists of 4 LEDs (Light Emitting Diodes) with their own focusing optics. The LED specifications are found in Table 3.4. Two photodiodes monitor the output of the LEDs. The LEDs are powered by a self-regulating, temperature stabilised constant current generator. The electronic circuit which powers the LEDs is driven via a RS232 com-server using a radio link provided by a radio modem and dipole antenna. There is also a monitoring circuit that measures the the power at the transmitting site [97].

Table 3.4: Characteristics of the LED light sources of the transmissometer.

Wavelength (nm)	Current (mA)	FWHM[7]	Focusing Optics
505	350	~ 15°	Polycarbonate lens
455	350	~ 4°	Polycarbonate lens
910	100	~ 10°	f = 50 mm camera lens
390	20	2.3°	f = 50 mm camera lens

Receiver

The transmissometer receiver is installed at the same location as the other atmospheric instruments as shown in Figure 3.16. The light receiver consists of a telescope and 8-bit CCD camera installed inside an all-weather enclosure. The original telescope was a 8"

---

[7] Full Width at Half Maximum

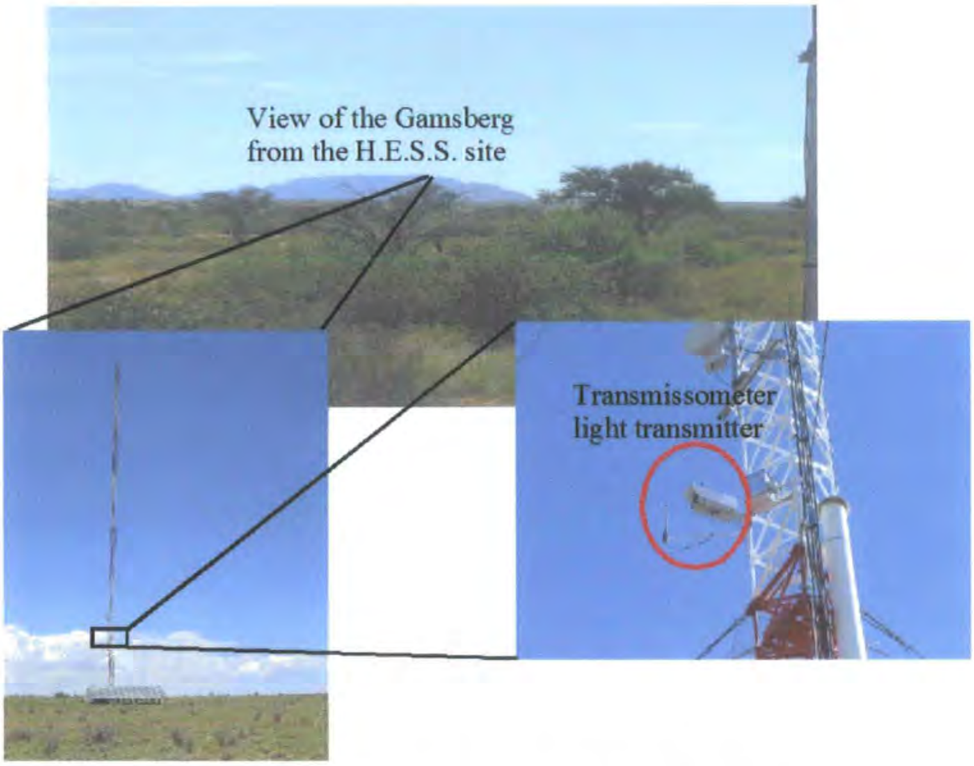

Figure 3.25: The location of the light source on top of the Gamsberg mountain a distance $D = 29.8$ km from the H.E.S.S. site (Courtesy of Roland Le Gallou).

Newtonian telescope, but has since been replaced in February 2006 by a 6" telescope. The field of view of the camera is a square of side 0.12°.

3.6.2 Calculation of Transmissivity

Figure 3.27 shows the light path from the light source to the light receiver of the transmissometer. The values I_1 and I_2 represent the measured light from the receiver transmitted after a path of length $D = 29.8$ km. Calibration coefficients (I_0) for each wavelength were measured before the installation of the transmissometer and are the signal intensity with no atmospheric extinction. The values I_1 and I_2 along with the calibration coefficients are the measure of the intensity of light transmitted from the Gamsberg to the H.E.S.S site.

The first measurement I_1 is calculated by summing the pixel values comprised in the square of 25 x 25 pixels around the centre of the light spot[8], and subsequently subtracting

---

[8] The light spot is defined as the brightest 3x3 pixel cluster, while the LED FWHM is ~10 pixels.

Figure 3.26: The transmissometer receiver with the lid closed.

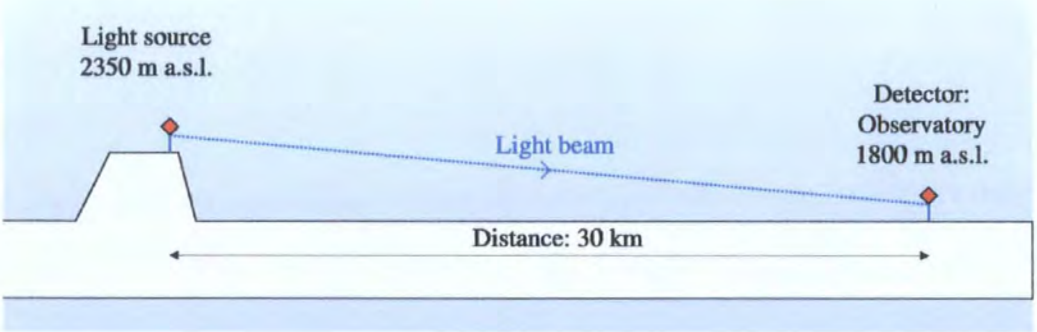

Figure 3.27: The light path from the transmissometer source to receiver. The total vertical distance travelled is 550 m (Courtesy of Rolland Le Gallou).

the background value calculated using the average of the pixel values located in the region between 13 and 19 pixels from the centre of the light spot. An illustration of the pixel regions used for background subtraction is shown in Figure 3.28.

The next exposure is taken of a dark frame with the same exposure time as the previous

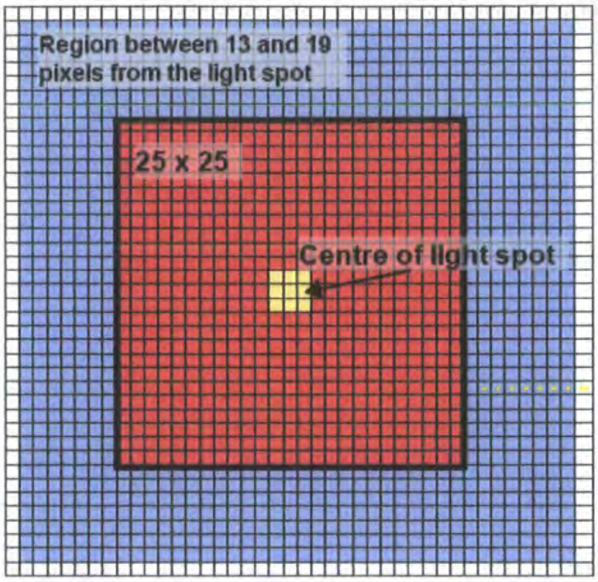

Figure 3.28: The pixel regions used to calculate the signal intensity I_1. The square of 25x25 pixels around the light spot are summed and then the background value calculated using the average pixel values located in the region between 13 and 19 pixels from the light centre is subtracted.

light frame. The value I_2 is calculated by subtracting a square of 39x39 pixels around the location of the light spot of the dark frame from the pixels of the light frame. The value of I_1 depends on spatial variations that can vary with instrument motions associated with the weather, whereas I_2 depends on temporal variations which are less apparent due to the stability of the atmosphere on short timescales (on the order of minutes or seconds).

The measured intensities I_1 and I_2 are related to the mean free path x by,

$$x = \frac{D}{\log(I_0/I)} \tag{3.6}$$

where I_0/I is the ratio of the original emitted intensity (I_0) to the measured intensity (I_1 or I_2). Assuming a homogeneous atmosphere from the light source to the receiver, the transmissivity of the first 550 metres of the atmosphere above the site is then,

$$T(d) = \exp^{-d/x} \tag{3.7}$$

where $d = 550$ m is the vertical length of the light path. By combining equations 3.6 and 3.7, the transmissivity outputted by the transmissometer's software is,

$$T(d) = \frac{I}{I_0}^{d/D} \simeq \frac{I}{I_0}^{0.01846} . \tag{3.8}$$

Due to the power of 0.01846 in Equation 3.8, $T(550m)$ is measured with high sensitivity [97], as shown by Figure 3.29.

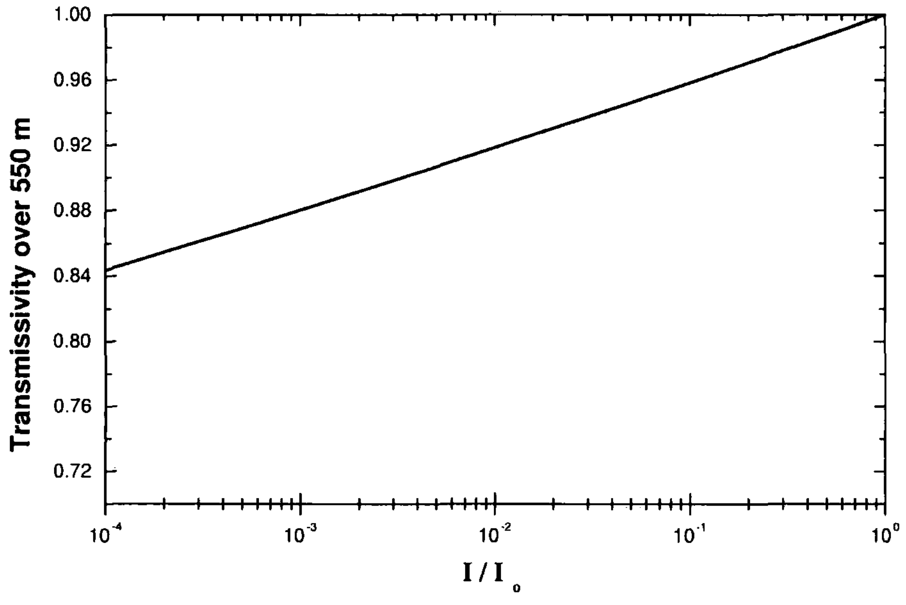

Figure 3.29: This plot shows the sensitivity with which the transmissivity is measured. It can be seen that the transmissivity varies by about 20% from its original value over a width range of measured intensities.

Measurements

Nightly average transmissivities were used due to the observed stability of transmissivity over one night. The average values were used when the rms values of the transmissivity distribution was less than ~ 0.005. Figure 3.30 shows transmissivity values over a stable night, while Figure 3.31 shows a variable night not used in analysis. It is also shown in Figure 3.30 that the transmissivity at 390 nm is non-existent. This is due to the low signal of the LED and will not be used for further analysis. It can also be seen that the 910 nm LED is not as reliable as the 505 and 455 nm LEDs. This is also due to the lower LED power. The 910 nm data will be used when available.

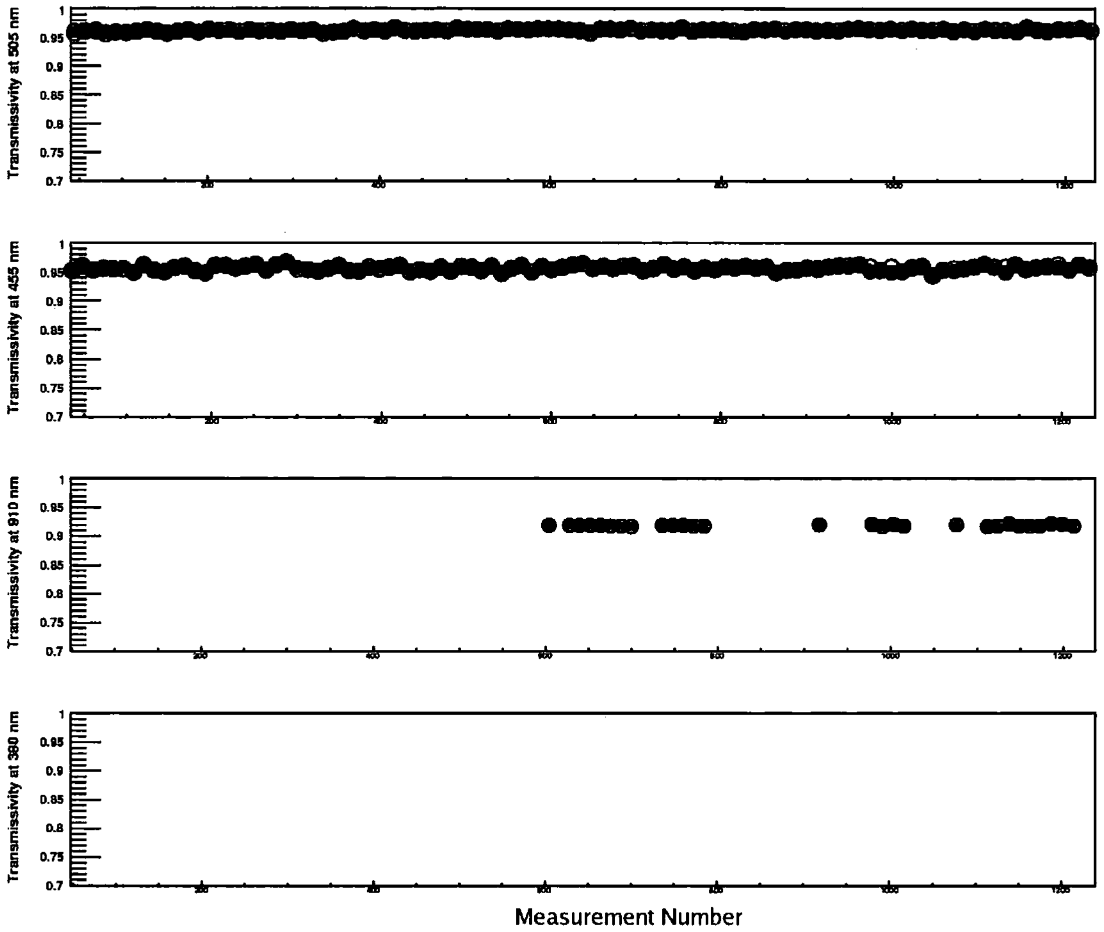

Figure 3.30: Transmissivity data for all wavelengths over a stable night (12 February 2006).

Transmissivity Correction

During February 2006, the telescope of the transmissometer was changed from 8" to 6" with half the focal length and double the field of view. It was noticed that there was a step drop in the transmissivity after this time. The instrument was not recalibrated, and so the data had to be normalised to the previous values by taking the difference of the maximum values for before and after the telescope change and adding this value to the new transmissivities. This correction is only used for transmissivities after February 2006. The correction is given by,

$$T'(d) = T(d) + \Delta T \tag{3.9}$$

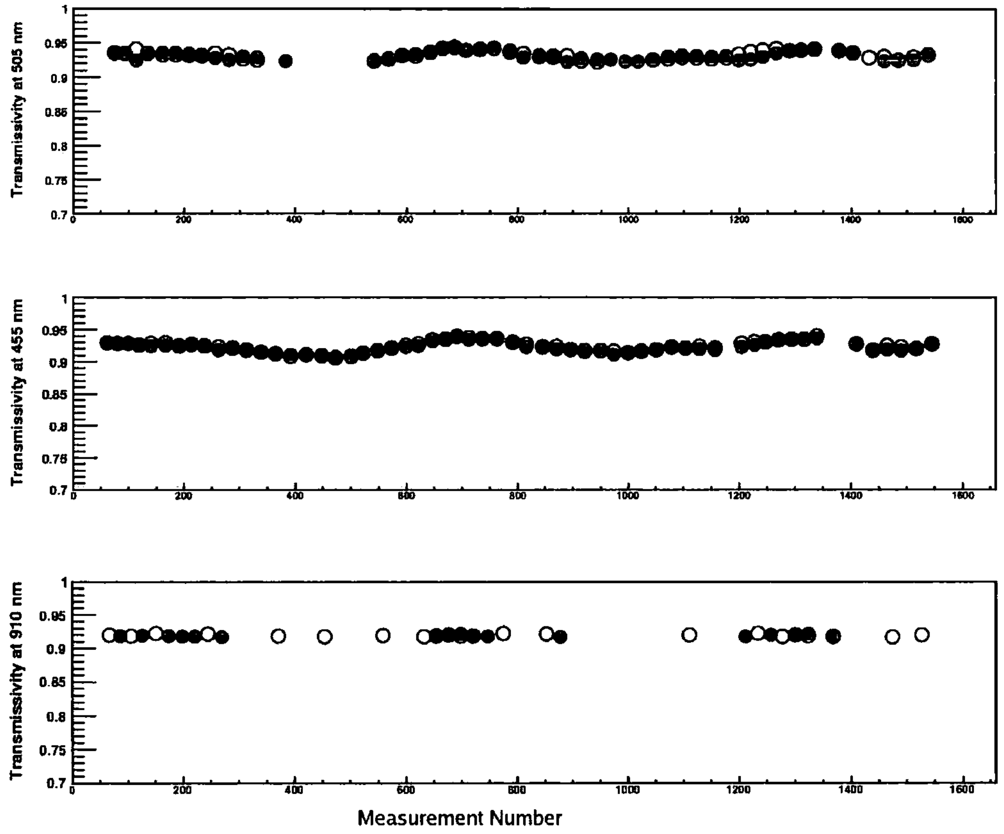

Figure 3.31: Data during a night with variable transmissivity values (18 June 2005).

where $T(d)$ is the value of the transmissivity as returned by the transmissometer and $\Delta T = T_1(d) - T_2(d)$ with $T_1(d)$ being the maximum value before and $T_2(d)$ being the maximum value after the telescope change. Table 3.5 shows ΔT for 505, 455, and 910 nm.

Table 3.5: Transmissivity correction values for use after February 2006.

Wavelength (nm)	$T_1(d)$	$T_2(d)$	ΔT
505	0.9911	0.961	0.0301
455	0.9873	0.9681	0.0192
910	0.9376	0.9288	0.0088

The total corrected transmissivity at 455, 505, and 910 nm over the current lifetime of the transmissometer is shown in Figure 3.32. The relation between the transmissivities

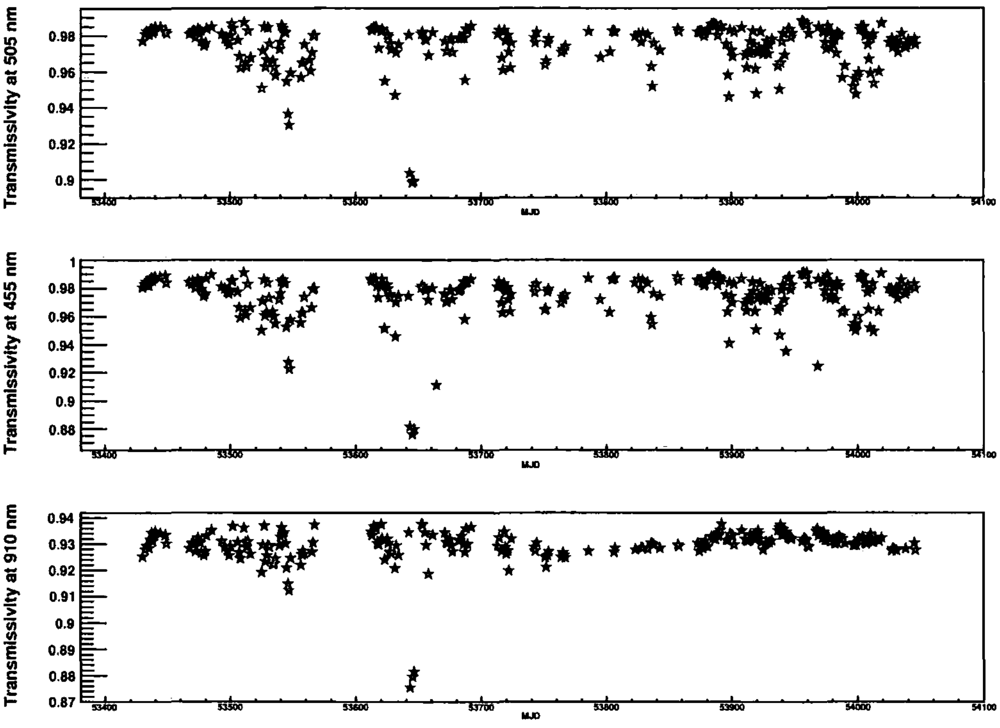

Figure 3.32: Transmissivity values output by the transmissometer software from 1 March 2005 to 30 October 2007.

of different wavelengths is shown in Figure 3.33. The top figure shows a good correlation between 455 and 505 nm as would be expected. The bottom figure shows a greater scatter between 455 and 910 nm illustrating different scattering or absorption effects of various particles.

Mie Transmissivity

The total transmissivity, measured by the transmissometer, is the product of the transmissivities from molecular absorption, Rayleigh scattering, and Mie scattering given by, $T(d) = T_a(d) \times T_R(d) \times T_M(d)$. On a clear night with no significant aerosol detection from the ceilometer, the contribution to the total transmissivity can be assumed to be from molecular absorption and Rayleigh scattering, $T(d) = T_a(d) \times T_R(d)$. This value is found using the lowest values of backscatter up to 550 meters and finding the corresponding transmissivity for that night. The resulting $T_M(d)$ from aerosol scattering can then be derived. It is the Mie transmissivity which is important to correlate with aerosol

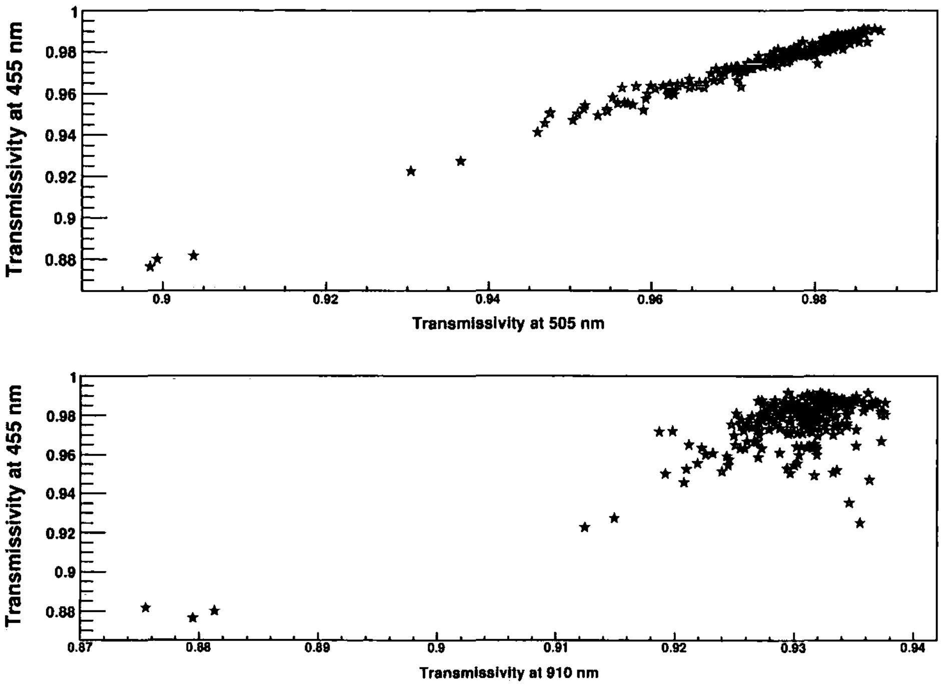

Figure 3.33: The top figure shows a good correlation between 455 and 505 nm as would be expected. The bottom figure shows a greater scatter between 455 and 910 nm illustrating different scattering or absorption effects of various particles.

scattering detected with the ceilometer. $T_M(d)$ also must be corrected for zenith angle at which the ceilometer is pointing so that the instruments can be compared over the same distance, $l = d/\cos(\theta_z)$. $T_M(l)$ then becomes,

$$T_M(l) = \left(\frac{T(d)}{T_a(d)T_R(d)}\right)^{1/\cos(\theta_z)}. \tag{3.10}$$

3.7 Cross Correlation Between Instruments

Backscatter 550 vs Mie Transmissivity

Figure 3.34 shows the backscatter up to 550 metres versus the Mie transmissivity at 455 nm. It can be seen that there is a correlation between the backscatter from low-lying aerosols and transmissivity. In order to derive transmission values when the transmissometer was not working, a fit for Mie transmissivity versus BS_{550} was derived. This equation is only valid for low-lying levels of aerosols below 550 metres (i.e. $BS_{Int}/BS_{550} < 1.15$).

The equation for the fit is $T_M(l) = 0.999 - (3.24 \pm 0.04) \times 10^{-6}(BS_{550})$ with a χ^2/ndf of ~ 10. This fit is 'ok' considering the measurements were taken at different wavelengths. Since only the lowest 550 metres are measured by the transmissometer, the transmissivity derived by the line fit equation could act as a lower limit to the transmissivity throughout the atmosphere when there are no direct measurements from the transmissometer.

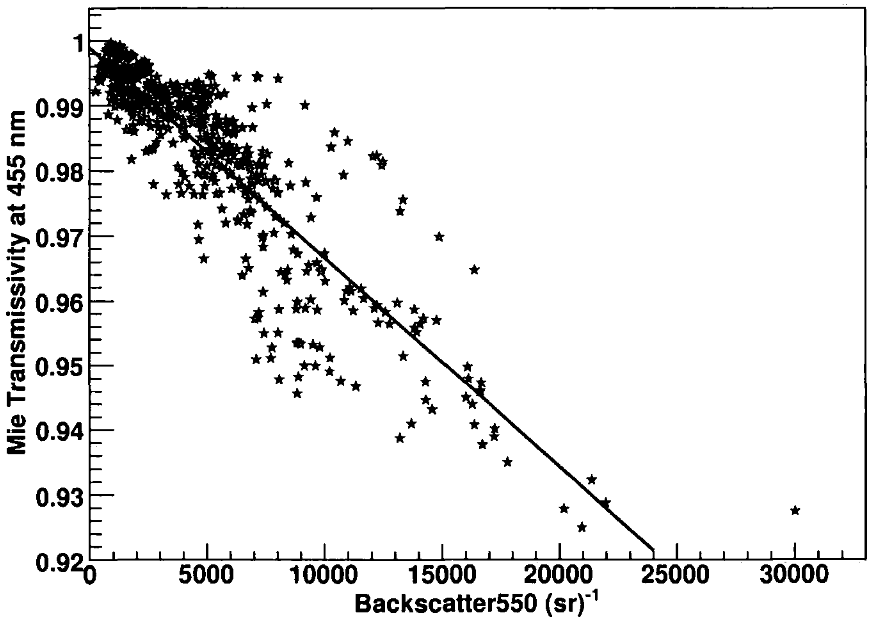

Figure 3.34: Backscatter up to 550 metres versus Mie transmissivity. There is a fairly good fit considering the measurements were taken at different wavelengths. Since only the lowest 550 metres are measured by the transmissometer, the transmissivity derived by the line fit equation could act as a lower limit to the transmissivity throughout the atmosphere when there are no direct measurements from the transmissometer.

Backscatter vs Relative Humidity vs Sky Temperature

Figures 3.35, 3.37, and 3.38 each show (a) BS_{Int} vs. sky temperature, (b) BS_{Int} vs. relative humidity, and (c) sky temperature vs. relative humidity for the years 2004, 2005, and 2006 respectively. Figure 3.37 shows noticeably less data due to ceilometer complications. General trends for all years show an increase in sky temperature with $BS_{Int} \geq 10,000$ sr^{-1} ((a) plots) and low relative humidity with high backscatter of $BS_{Int} \geq 10,000$ sr^{-1} ((b) plots).

Periods -08 and -09 (indicated by the pink squares and black circles) consistently have high backscatter with the lowest sky temperatures and relative humidity values, although relative humidity can also reach high values as well. Periods after the rainy season, -03 and -04 have consistently high relative humidity and sky temperature values. Figures 3.36 and 3.39 are zoomed in on the backscatter plots for $BS_{Int} < 20,000$ sr^{-1} for 2004 and 2006 in order to see the data in greater detail.

The evolution of sky temperature and relative humidity is most clearly seen in Figure 3.38(c) where -03 and -04 cluster around the right side of the plot, evolving clockwise from period to period, ending with -10 clustered at the top of the plot.

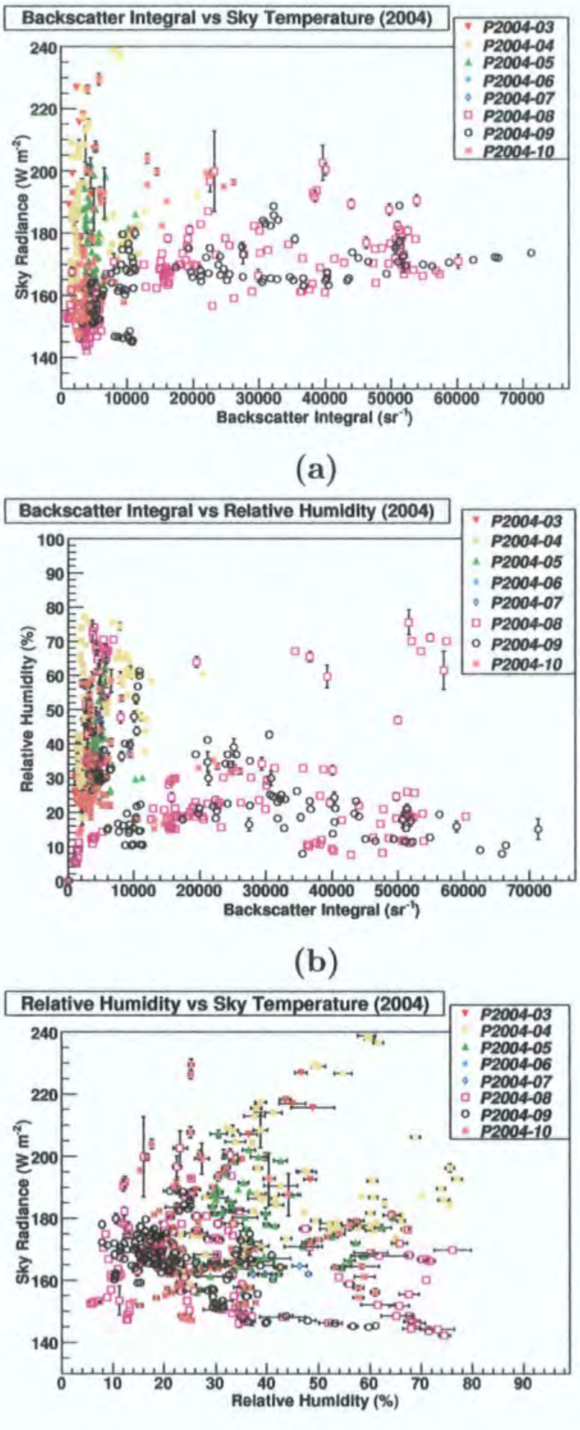

(a)

(b)

(c)

Figure 3.35: It can be seen from (a) that the highest backscatter periods also have the lowest sky temperatures. It can be seen from (b) that the periods with highest backscatter have the lowest relative humidity values, but also have high relative humidity contained in those periods. There is a trend seen in (c) of the lowest temperature and relative humidity for P2004-08 and -09, the highest temperature and relative humidity for P2004-04. What is also seen from (a) and (b) is the that the sky is generally warmer and less humid for $BS_{Int} \gtrsim 10,000$ sr^{-1}.

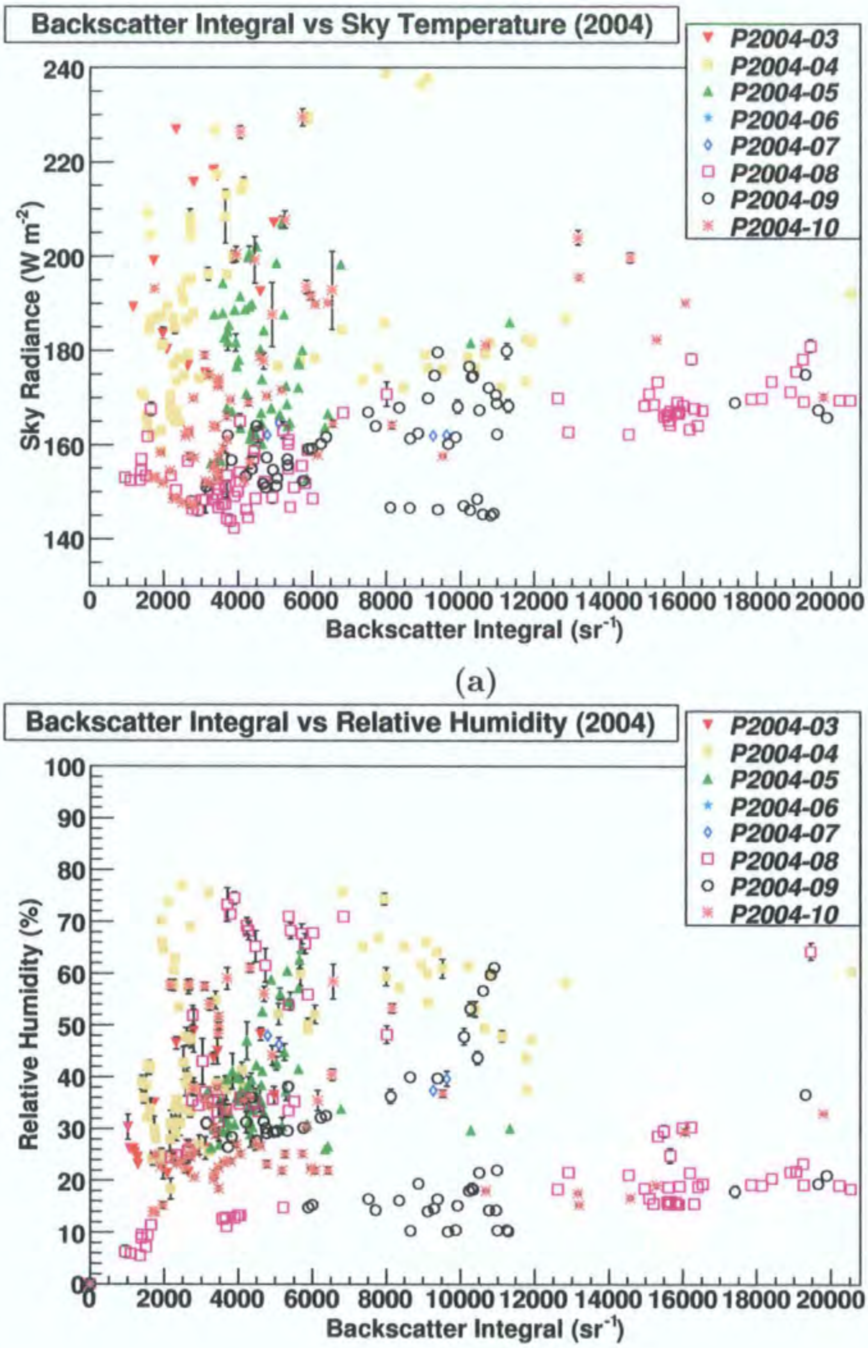

(a)

(b)

Figure 3.36: Re-scaled Figures 3.35(a) and (b) for $BS_{Int} < 20,000$ sr^{-1}.

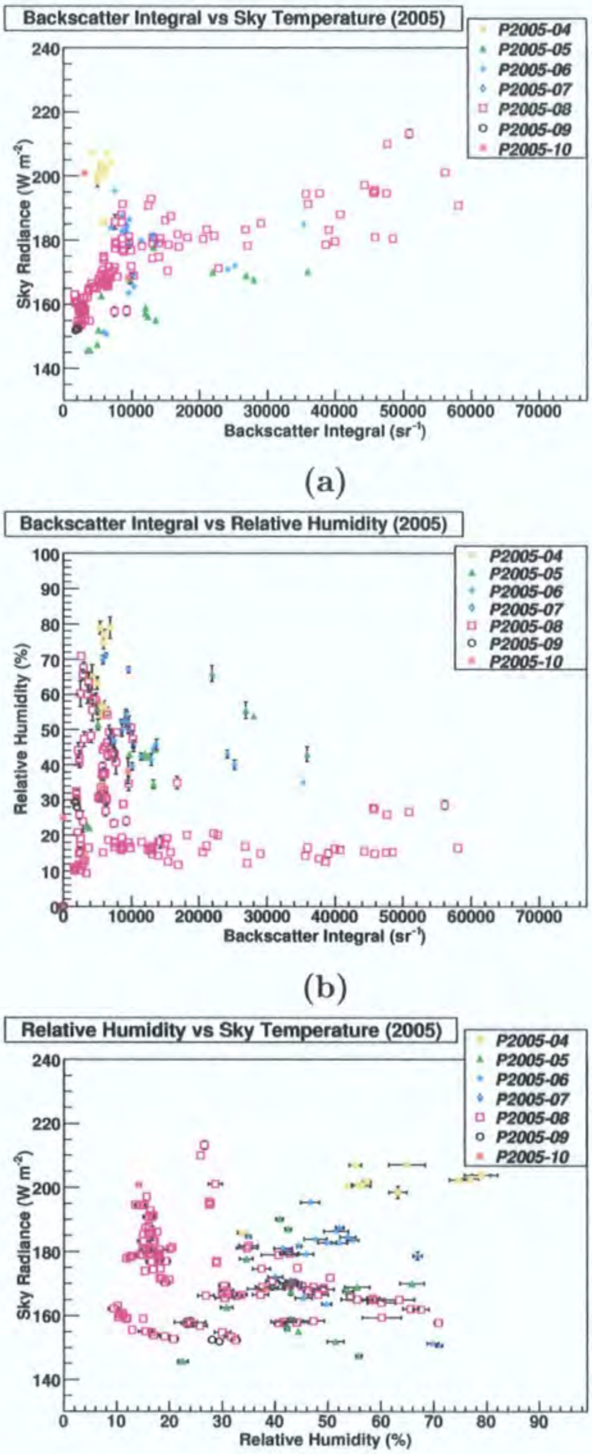

(a)

(b)

(c)

Figure 3.37: (a) Shows similar trend of P2005-08 with 2004 data. In (b) evolution from predominately high relative humidity values in P2005-03 to low relative humidity values and high backscatter from P2005-08 is seen. (c) Shows a similar trend to 2004 data.

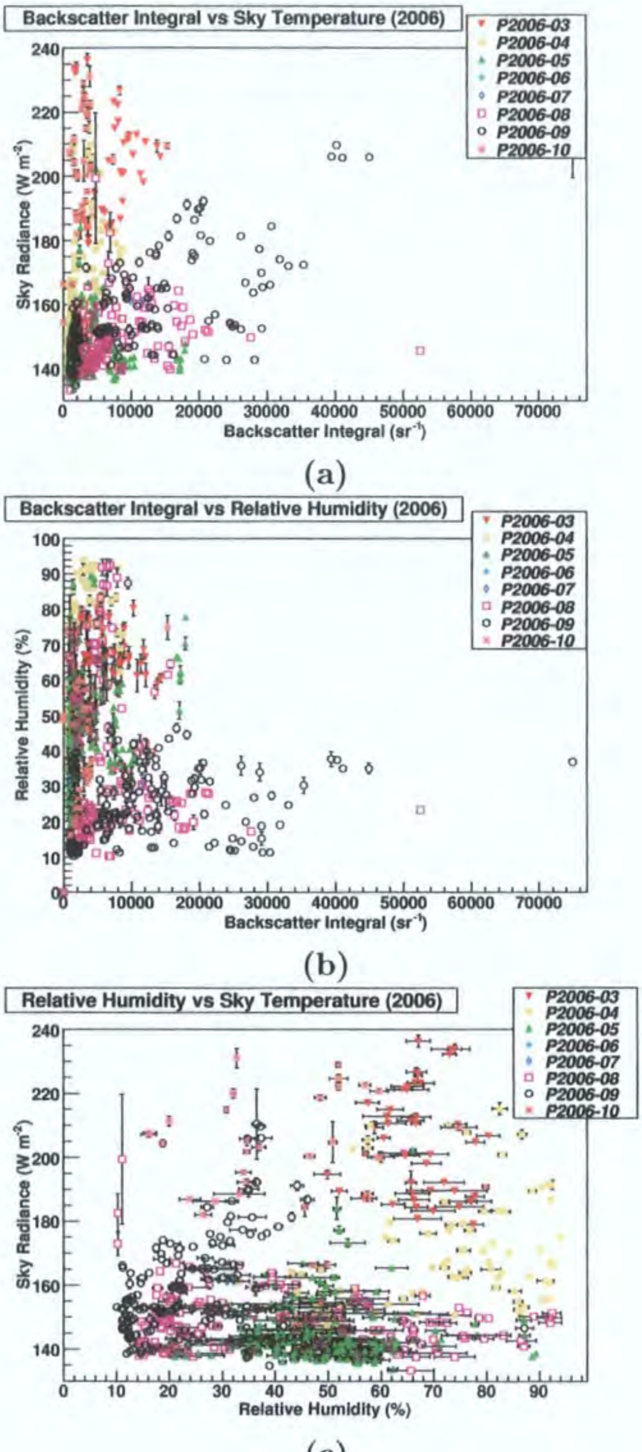

Figure 3.38: Sky temperature and relative humidity trend is most apparent in (c). Starting from P2006-03, each cluster of points move around clockwise till P2006-10.

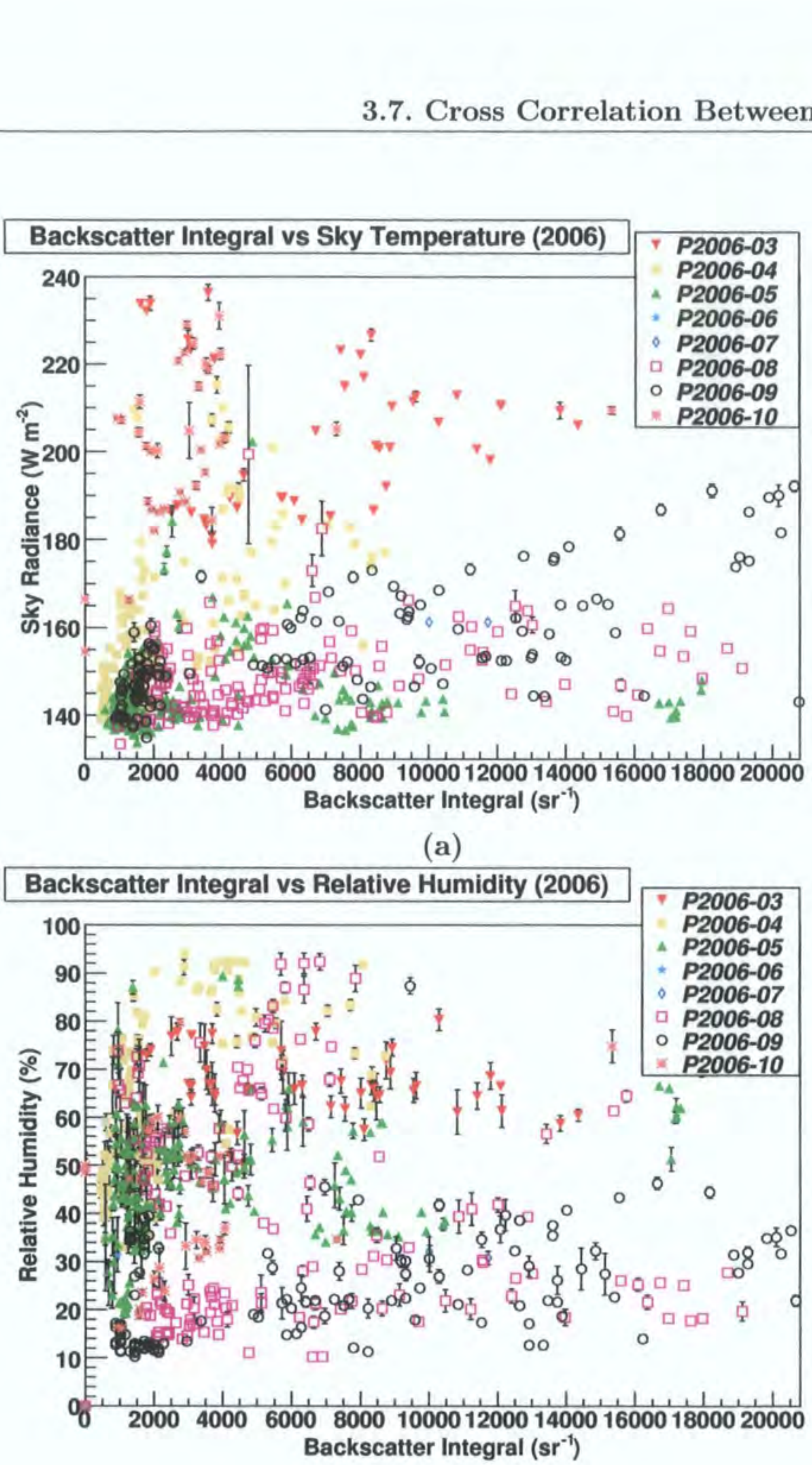

(a)

(b)

Figure 3.39: Re-scaled Figures 3.38(a) and (b) for $BS_{Int} < 20,000$ sr^{-1}. (a) Shows the sky temperature is the highest for P2006-03 and P2006-10 and the lowest for P2006-05, -08, and -09 like the previous years. (b) Shows the relative humidity is consistently high for P2006-03 and -04 and variable for all other periods. It is interesting to see the different regions each period occupies.

3.8 New LIDAR

A new LIDAR made by Leosphere was installed on site in April 2007. It works at a wavelength of 355 nm with a range spanning 50 metres to 15 kilometres and a spatial resolution of 1.5 metres. A picture of the new LIDAR is shown in Figure 3.40.

Figure 3.40: A picture of the new Leosphere LIDAR.

Figure 3.41 shows the backscatter for four nights with different concentrations of aerosols while observing LS 5039. The bottom three curves show low to moderate amounts of aerosols while the night of September 11th shows a highly contaminated layer. It should also be noted that the backscatter signal stops at around 4 to 6 km when the range is supposed to be 15 km. The question is: is the lidar signal all backscattered because the aerosol layer is so thick or is something else causing this effect? Since then, we have sent data to the manufacturers and are presently in discussion with them to resolve this issue.

Further work to be done with the new LIDAR will be discussed in Chapter 5.

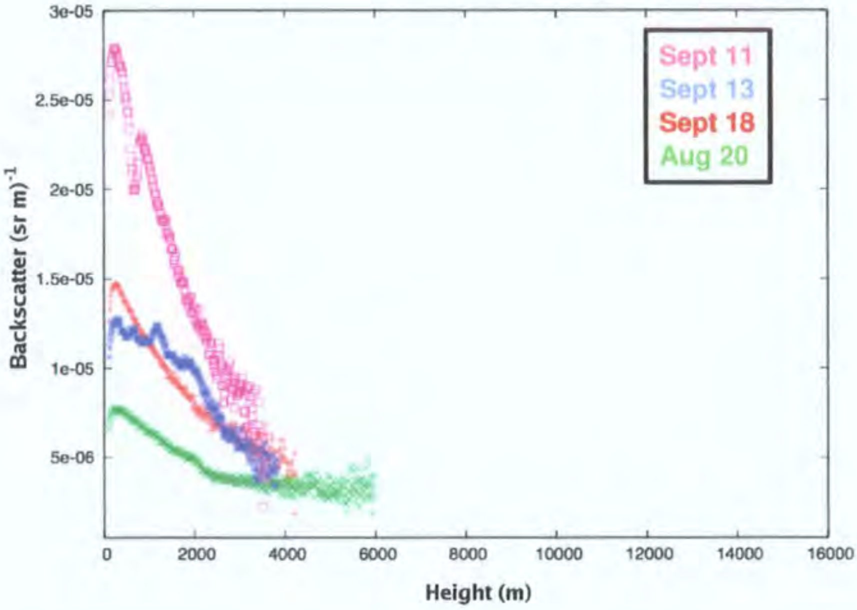

Figure 3.41: The backscatter profile for four nights with different concentrations of aerosols.

3.9 Atmospheric Monitoring in IACT Experiments

Atmospheric Cherenkov detectors cannot be calibrated using a test beam and the estimation of their sensitivity strongly depends on Monte Carlo simulation programs. These simulations model gamma-ray detection efficiency due to atmospheric conditions and the various elements of the detectors [99]. If an unrealistic atmospheric model is used in the simulations, erroneous interpretation of gamma rays may result. This is why atmospheric monitoring is so important in ground-based gamma-ray astronomy.

When measuring the gamma-ray flux from a source, changing atmospheric conditions must be taken into account and corrected for. Studying such atmospheric variations is of great importance for studying the time variability of gamma-ray sources, such as AGN, which may be observed over a long period of time with a wide range of zenith angles and atmospheric conditions [99]. The relations between atmospheric parameters and gamma-ray data will be explored in the next chapter.

Chapter 4

Telescope and Atmospheric Data

This chapter looks at the atmospheric data presented in Chapter 3 and how it relates to data from the H.E.S.S. telescopes. This will be done by a systematic comparison of the major atmospheric parameters measured on site: backscatter, transmissivity, and sky radiance, with trigger rates and gamma-ray fluxes. Developed from trigger rate and backscatter measurements, a method to correct for the effects of aerosols on gamma-ray measurements is presented in Section 4.4 and applied to 2 BL Lacs in Sections 4.5 and 4.6. Section 4.7 will discuss the potential of other sources to be atmosphere corrected. Finally, Section 4.8 will use the BL Lacs measured to calculate upper limits to the EBL intensity at optical and infrared wavelengths.

4.1 Cosmic Ray Trigger Rates

A trigger is an event registered by the telescope that meets specific selection criteria. A H.E.S.S. telescope trigger occurs if 2.5 pixels within a drawer have a signal of 4 photoelectrons or more, and are observed within a short time window of 1.3 nanoseconds [70]. A system trigger occurs when more than 2 telescopes are triggered within 80 ns of each other [70]. The system triggered signal is then digitised and read-out to the data acquisition system [124]. This process is described in more detail in Section 1.6. The telescopes' trigger rates are dominated by background events, which are cosmic ray induced particle showers (see Sections 1.4.1 and 1.4.2).

Due to the constant and isotropic flux of cosmic rays, trigger rates provide a direct measurement of all the effects due to internal and external factors influencing data taking. Internal factors consist of wear and tear of hardware components (e.g. loss of PMT gain, Winston cone degradation, or loss of mirror reflectivity [98]), while external factors are caused by the environment (e.g. aerosols and seasonal weather changes) [35, 98].

Since trigger rates are affected by the pointing position of the telescope along with the decline in hardware components, trigger rates must be corrected for in terms of zenith angle and time, over the lifetime of the system (taken to be the start of 4 telescope observations in January 2004). These corrections will be attended to next.

4.1.1 Zenith Angle and Time Corrected Trigger Rate

Zenith Angle Correction

Observations are performed over a range of zenith angles, typically from 0° - 60°. Particles coming in at larger zenith angles have to traverse more atmospheric material than at zenith. This reduces the intensity of Cherenkov light and hence the trigger rate. Trigger rates at larger zenith angles (60°) are lower than at zenith by about 60%. This effect must be corrected for.

The Heidelberg H.E.S.S. group (HD) has derived a correction using data from a single night. The data were compared with simulations from two different atmospheric models and the function was fitted to a smooth curve given by [70],

$$TR(\theta_z)_{HD} = -0.2566 + 1.564(\cos\theta_z) - 0.307(\cos\theta_z)^2 \tag{4.1}$$

where θ_z is the zenith angle of observation.

The Durham H.E.S.S. group (D) has derived a correction to compare with the Heidelberg function. They used data from many nights, but over a short period of time (from 20/03/2004 to 04/06/2004)) so that temporal effects are negligible. The ceilometer was used as a sky clarity measure, and the data were cut based on the lowest backscatter integral value with a full range of zenith angles (BS_{Int} < 2000 sr^{-1}). The data were fit to a 4th order polynomial given by [98],

$$TR(\theta_z)_D = 1 - 1.22 \times 10^{-4}(\theta_z)^2 - 9.18 \times 10^{-9}(\theta_z)^4. \tag{4.2}$$

These two zenith angle corrections have been compared in Figure 4.1. The zenith angle correction is not very good for $\theta_z > 50°$ for either correction, as they both tend to overestimate the trigger rate, but agree well for smaller zenith angles. For consistency with the rest of the collaboration, the Heidelberg zenith angle correction (equation 4.1) will be used in all further analysis.

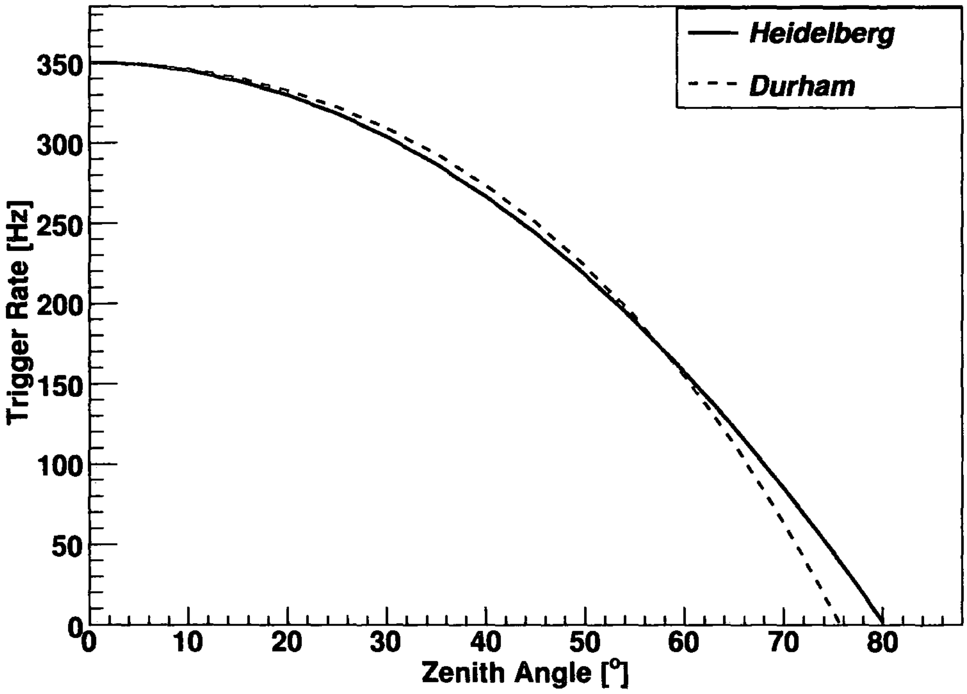

Figure 4.1: Comparison of the Heidelberg correction (red dotted line), and Durham zenith angle correction (black solid line), scaled to 350 Hz.

Time Correction

The zenith angle corrected trigger rate was averaged over an observation period[1] and plotted over time, shown in Figure 4.2. To ensure a consistent comparison of trigger rate over long periods of time of months and years, a time correction has been applied to the trigger rate data using simple linear fits in order to account for the decline in trigger rate. Data with the lowest backscatter ($BS_{Int} < 5000$) and minimal trigger rate variation ($TR_{rms} < 10$) were chosen so as to extract the most stable trigger rate values for the clearest nights. A cut on zenith angle is also made with, $\theta_z < 50°$.

From January 2004 to October 2006, there have been 3 upgrades to the system that have had a noticeable effect on the trigger rate. Each of these upgrades have increased the trigger rate by 38% on average. Four time corrections have been derived for each region between the upgrades and are marked in Figure 4.2. The periods and range of runs for each region are listed in Table 4.1. Table 4.2 shows the percentage change of trigger rate

---

[1] See Appendix A for period to date and run number conversions.

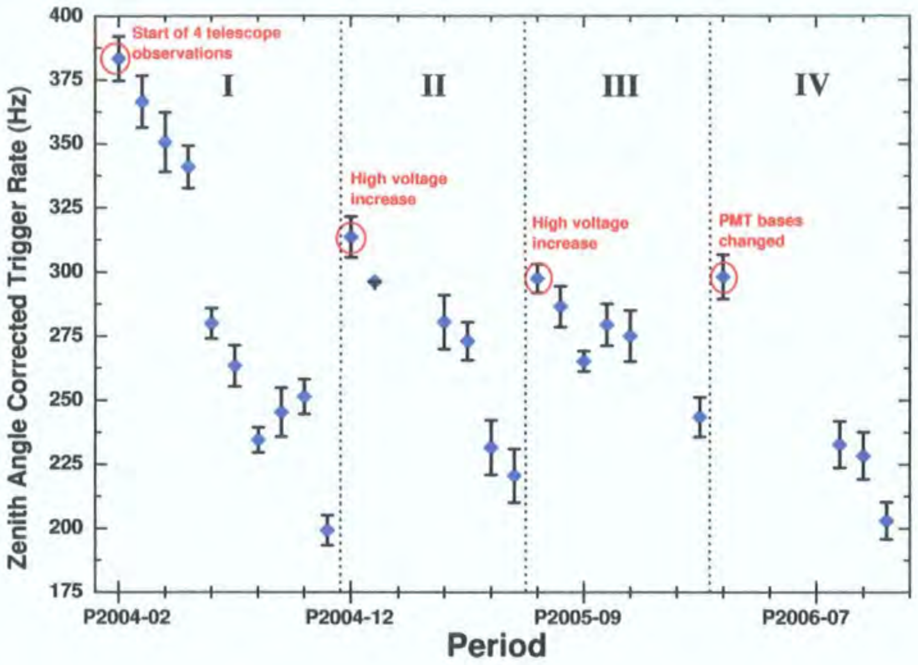

Figure 4.2: Mean zenith angle corrected trigger rate per period from P2004-02 to P2007-04 with upgrades labelled at the start of each region.

Table 4.1: The period and run range for each region.

Region	Period	Runs	MJD
I	P2004-02 to P2004-11	18870-23315	53043-53333
II	P2004-12 to P2005-06	23500-27361	53337-53570
III	P2005-07 to P2006-02	27375-30322	53574-53807
IV	P2006-03 to P2006-10	30886-35715	53812-54042

over each region, along with the reasons for the upgrades. The linear fits of each region are shown in Figure 4.3. The period is related to modified Julian date (MJD)[2] by the following equation,

---

[2] The modified Julian date (MJD) comes from the Julian date (JD) where JD=0 corresponds to noon on January 1, 4713 B.C. The formula for conversion is, MJD = JD - 2400000.5

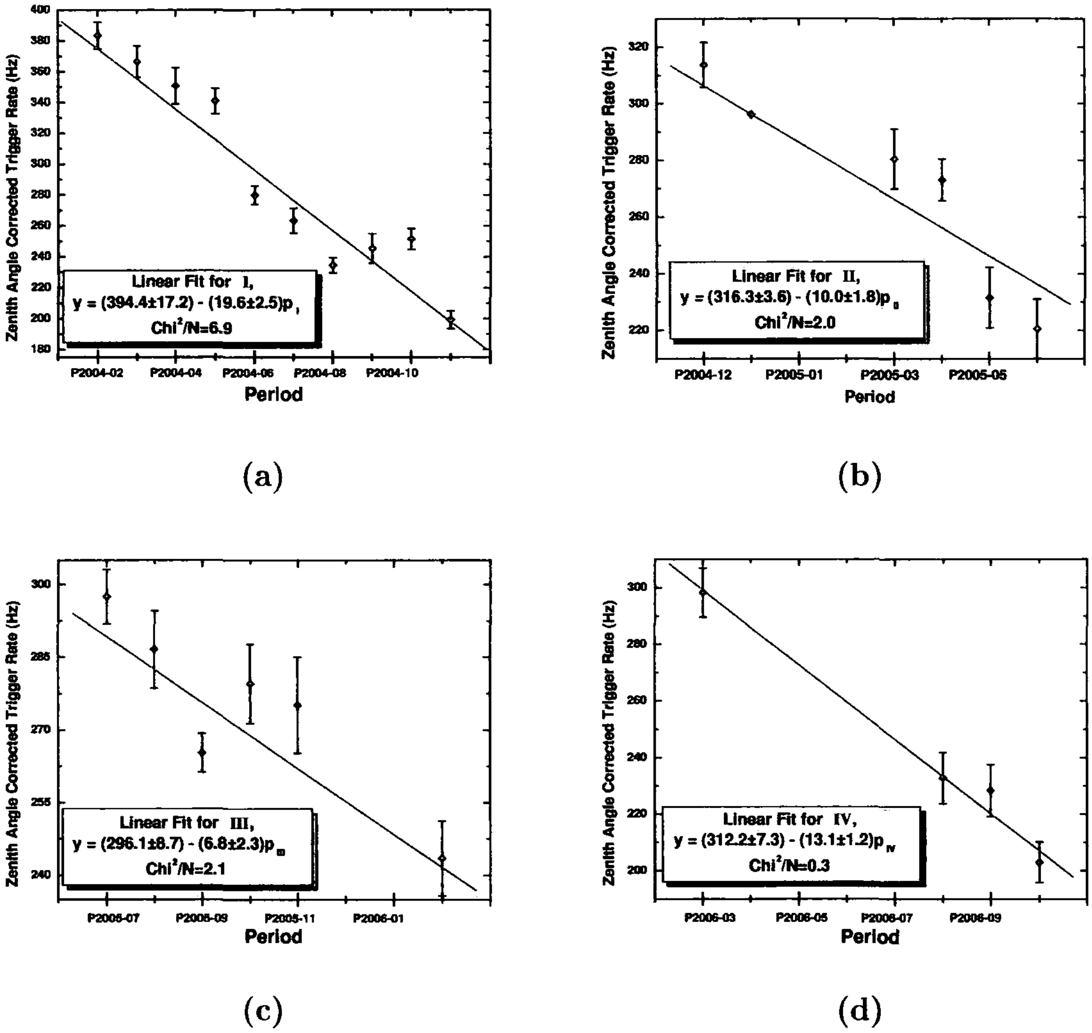

(a) (b)

(c) (d)

Figure 4.3: Mean zenith angle corrected trigger rate with linear fits for regions (a) I, (b) II, (c) III, and (d) IV.

$$p_i(d_{MJD}) = \frac{d_{MJD} - k_i}{\Delta p} + 1 \quad \text{For Regions i} = \mathrm{I, II, III, IV} \tag{4.3}$$

where p_i corresponds to the x-axis of the fit figures and the first day of each region corresponds to $p_i = 0.5$[3], d_{MJD} is the modified Julian date, $\Delta p = 29.4$ days is the average duration of each period, and k_i is a constant found for each fit given in Table 4.3. All

---

[3] This is because p_i=1 is taken to be at the midpoint of the first observation period.

Table 4.2: The percentage drop in average trigger rate over a region and the rise of trigger rates between periods, along with its cause.

Region	ΔTR	Cause of increase
I	-48%	—
I to II	+57%	PMT HV/gain increase
II	-30%	—
II to III	+35%	PMT HV/gain increase
III	-18%	—
III to IV	+22%	PMT bases changed
IV	-32%	—

fits were normalised to 350 Hz. The final time corrections for each region as a function of modified Julian date are,

$$TR_I(d_{MJD})_{cor} = 107.5 - (2.0 \times 10^{-3})d_{MJD};$$
$$TR_{II}(d_{MJD})_{cor} = 60.6 - (1.1 \times 10^{-3})d_{MJD};$$
$$TR_{III}(d_{MJD})_{cor} = 26.7 - (4.6 \times 10^{-4})d_{MJD};$$
$$TR_{IV}(d_{MJD})_{cor} = 26.7 - (4.6 \times 10^{-4})d_{MJD};$$

with the final zenith angle and time corrected trigger rate being,

$$TR(\theta_z, d_{MJD}) = \frac{TR}{TR(\theta_z)_{HD} TR(d_{MJD})_{cor}} \tag{4.4}$$

where TR is the observed trigger rate.

From now on the zenith angle and time corrected trigger rate will be referred to as the *corrected trigger rate* and the zenith angle corrected trigger rate will be referred to as the *ZA trigger rate.*

Figure 4.4 shows the ZA trigger rate before and after it has been time corrected and how this makes the trigger rates more comparable over the course of 2 years.

Table 4.3: Constant k_i values for Equation 4.3 used to convert observation period to MJD.

k_I	53056
k_{II}	53350
k_{III}	53587
k_{IV}	53824

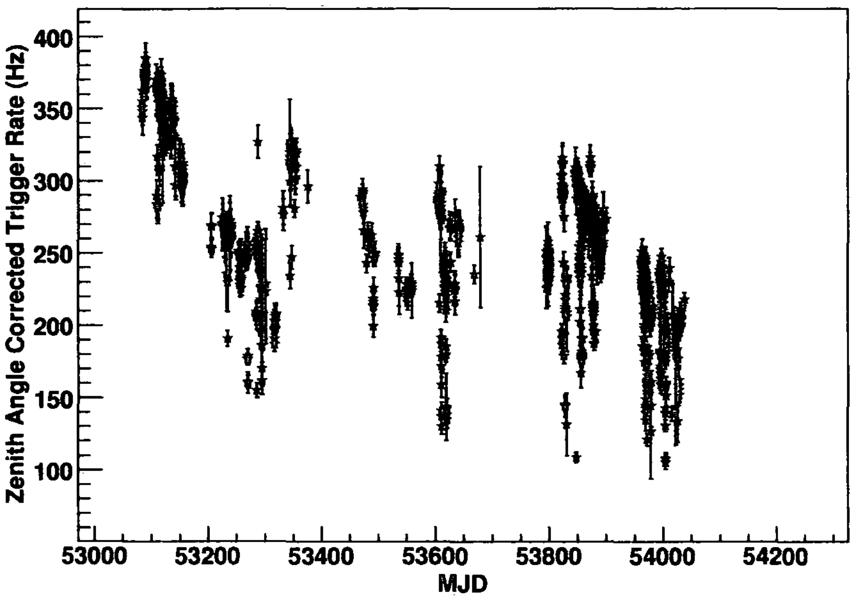

(a)

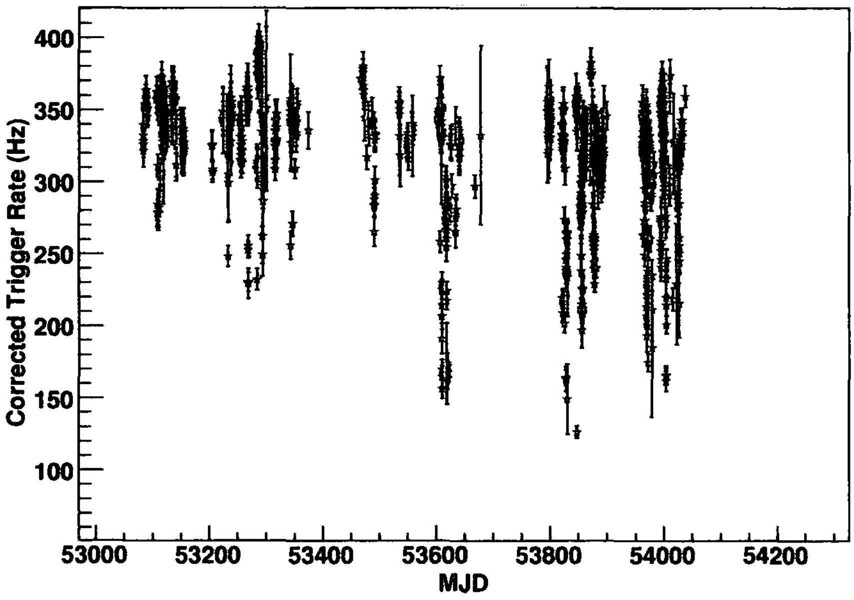

(b)

Figure 4.4: Zenith angle corrected trigger rate before (a) and after (b) time correction, from P2004-02 to P2006-10.

4.2 Trigger Rate and Atmospheric Data

4.2.1 Trigger Rate and Radiometer Temperature

Figure 4.5(a) shows the ZA trigger rate versus the sky radiance for data taken from the most observed source each month from March to June 2006. A source-by-source approach was done to minimise the variation on short time scales since the trigger depends on place in the sky. The idea is to get short-term trigger rate trends from looking at the same patch of sky. No correlation exists in March or April, but correlations start to occur in May and especially June.

Figure 4.5(b) compares the sky radiance with relative humidity using the same data. One can see that March and April are times of higher relative humidity and sky radiance whereas May and June have the lowest sky radiance values.

Overall, Figure 4.5 indicates that seasonal dependence in radiometer data should be taken into account before using it as an absolute sky quality measure as trigger rate measurements are most correlated with radiometer data during times of low relative humidity and sky radiance.

4.2.2 Trigger Rate and Backscatter

In Figure 4.6 it can be seen that there is a correlation between the corrected trigger rate and backscatter integral, with the largest backscatter integral values reducing the trigger rate to ~40% of the maximum trigger rate. Region I shows rather good correlation (with a correlation coefficient of -0.84) while region IV shows greater scatter (with a correlation coefficient of -0.56). The cause for the low trigger rates with low backscatter in region IV were investigated, looking at zenith angle, weather variables, trigger rate rms, and the source observed for these runs. No relation can be found between any of these variables.

Figure 4.7 compares the ZA trigger rate with the backscatter integral for 3 different sources before and after time correction. The correlation between trigger rate and backscatter varies between sources, indicating a source dependence on the trigger rate. It can also be seen from Table 4.4, that the time correction improves the correlation coefficients, most prominently for HESS J1745-290.

Figures 4.6 and 4.7 clearly demonstrate that the amount of aerosols affects the trigger rate. However, there are large trigger rate fluctuations. This could be due to transmissivity differences in the ceilometer wavelength of 905 nm and Cherenkov radiation around 400 nm. It is reasonable to say that measuring aerosols in the Cherenkov spectrum would

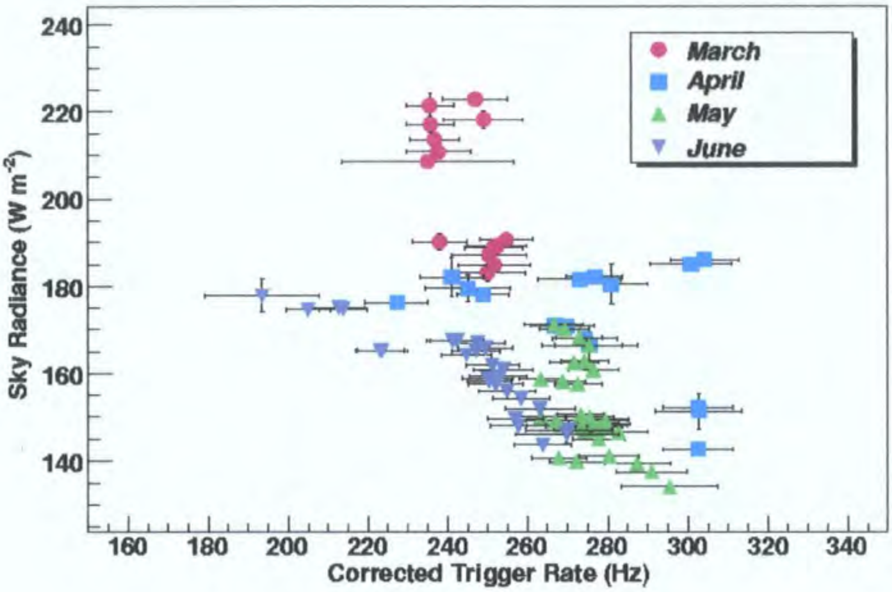

(a)

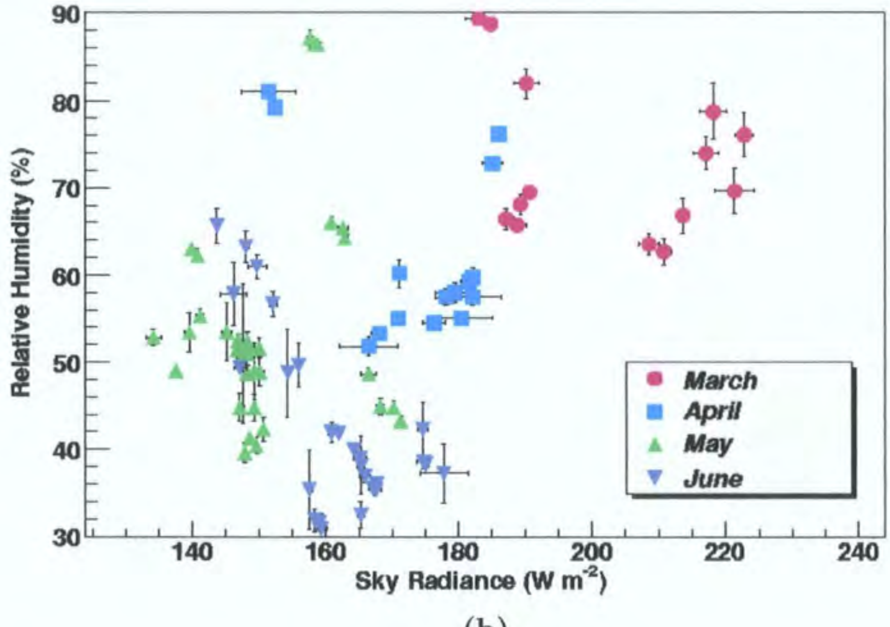

(b)

Figure 4.5: (a) Corrected trigger rate versus sky radiance, (b) sky radiance versus relative humidity.

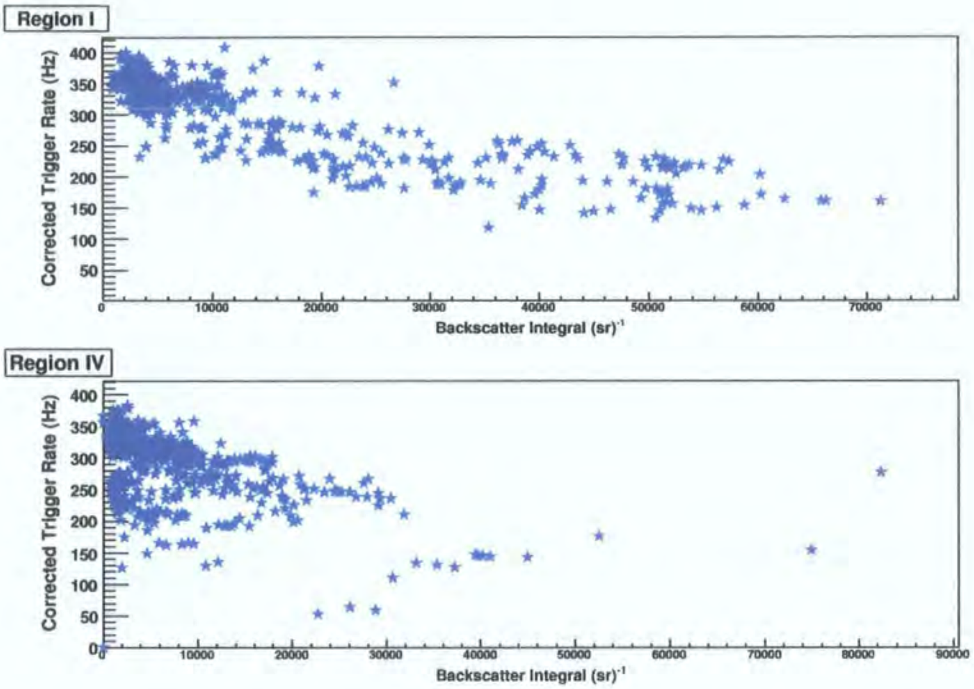

Figure 4.6: Corrected trigger rate versus integrated backscatter for regions I and IV, defined in Section 4.1.1

be more beneficial to infer the transmissivity of Cherenkov light. It is the aim of the transmissometer, working at Cherenkov wavelengths, to do this.

Table 4.4: Correlation coefficients (ζ) for trigger rate versus backscatter before and after trigger rate time correction.

Source	ζ before time correction	ζ after time correction
HESS J1745-290	-0.61	-0.92
PKS 2155-304	-0.70	-0.73
H 2356-309	-0.59	-0.70

4.2.3 Trigger Rate and Transmissivity

As discussed in Section 3.6, transmissometer measurements are good for up to the first 550 metres above the site. Even with this limitation, the trigger rate can be seen to correlate with transmissivity at 505 nm when most of the aerosol layer is below 550 metres (ie. when $BS_{Int}/BS_{550} < 1.15$). The corrected trigger rate versus transmissivity is shown in

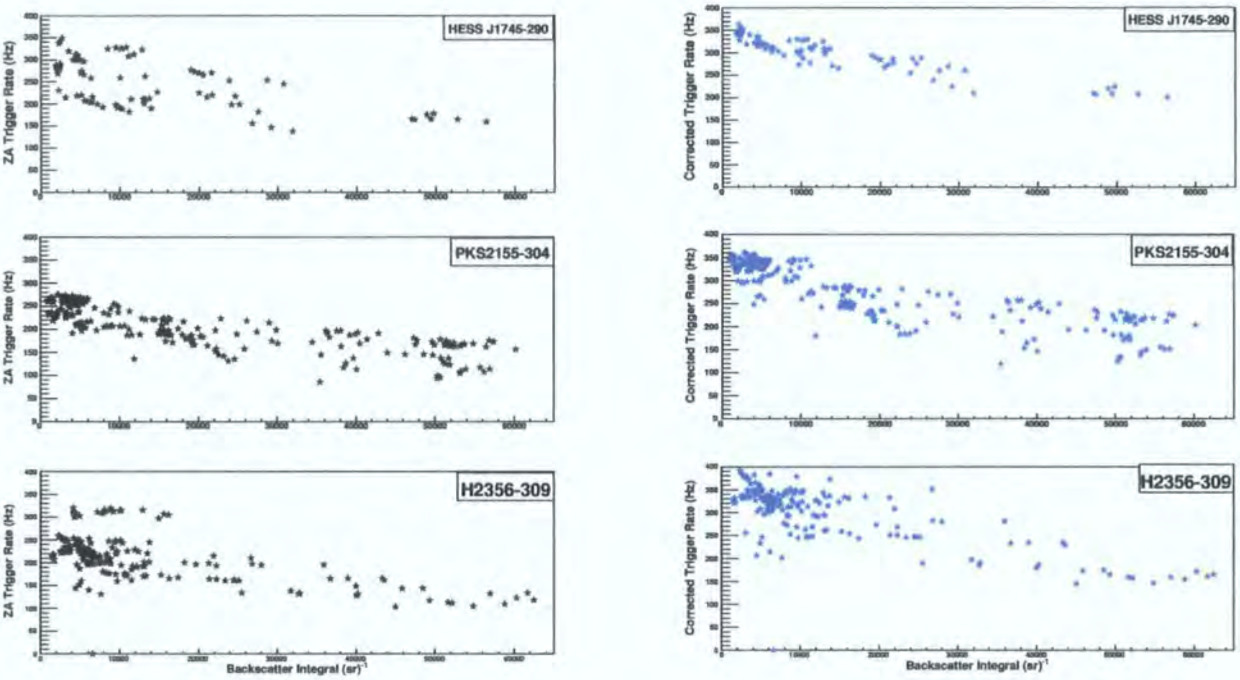

(a) (b)

Figure 4.7: Zenith angle corrected trigger rate versus backscatter integral before (a) and after (b) time correction for H 2356-309, PKS 2155-304, and HESS J1745-290

Figure 4.8 with a correlation coefficient of 0.46, using data from HESS J1745-290, PKS 2155-304, and H 2356-309.

In theory, transmissivity values can be used to simulate the transmission of Cherenkov light from gamma-ray and cosmic-ray showers. Since the transmissivity can only be known for the first 550 metres above ground level, the transmissometer is not very helpful for dusty atmospheres that extend to well beyond 550 metres. Therefore, transmissometer values cannot be used for atmosphere corrections when analysing gamma-ray data, unless a dusty layer is contained to below 550 m, which is not usually the case. At the present time, atmospheric corrections are best done using backscatter measurements along with trigger rate data. This will be discussed in greater detail and applied to various sources later in this chapter.

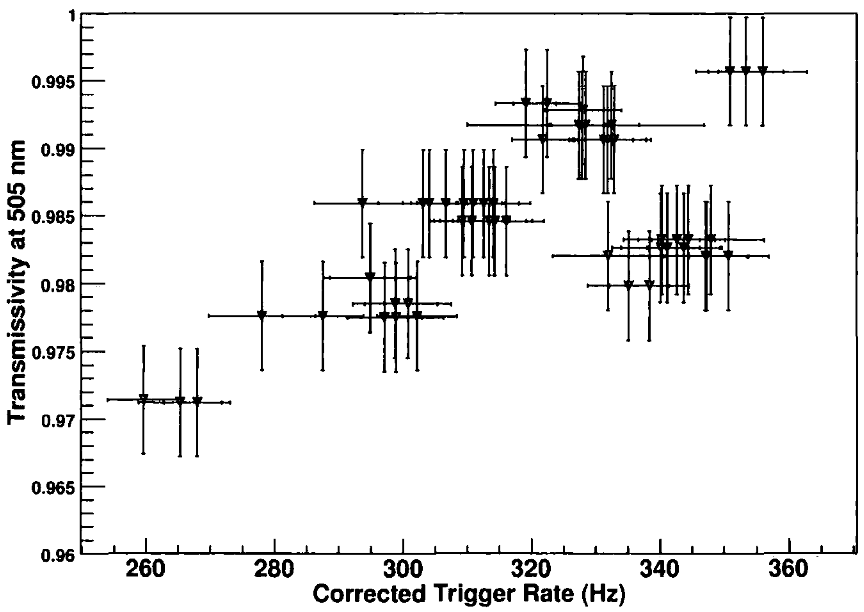

Figure 4.8: Zenith angle corrected trigger rate versus transmissivity with data from HESS J1745-290, PKS 2155-304, and H 2356-309.

4.2.4 Trigger Rate and Other Variables

To make for a complete study, the search for trigger rate correlations were extended to many other variables. These relations were explored in [98], but no correlations were found. Figures of the following variables versus corrected trigger rate can be found in Appendix B,

- Night sky background
- Air temperature
- Air Pressure
- Relative humidity
- Radiometer temperature
- Muon efficiency averaged over all 4 telescopes

4.3 Gamma-ray Flux and Atmospheric Data

The foundation has been laid for looking at the telescopes' trigger rates by looking at trigger rate correlations with the radiometer, ceilometer, and transmissometer data. A correlation between trigger rate and atmospheric data illustrates the potential of using trigger rates to correct gamma-ray data for atmospheric effects, provided that gamma rays are affected in a similar way. The next step is to compare gamma-ray data with atmospheric and trigger rate data.

In [98], the gamma-ray fluxes were compared with backscatter for the Crab Nebula and HESS J1745-290 (the galactic centre). The Crab was chosen for its constancy and intensity, while HESS J1745-290 was chosen because it was observed in August and September 2004, a period where aerosol concentrations were seen to be at their highest levels. The integrated flux above 1 TeV was compared with the integrated backscatter signal for both sources, shown in Figure 4.9. In each case, no correlation between flux and backscatter is seen. This gives confidence in the data by showing that Cherenkov light created by gamma rays greater than 1 TeV is not heavily influenced by aerosols in the atmosphere.

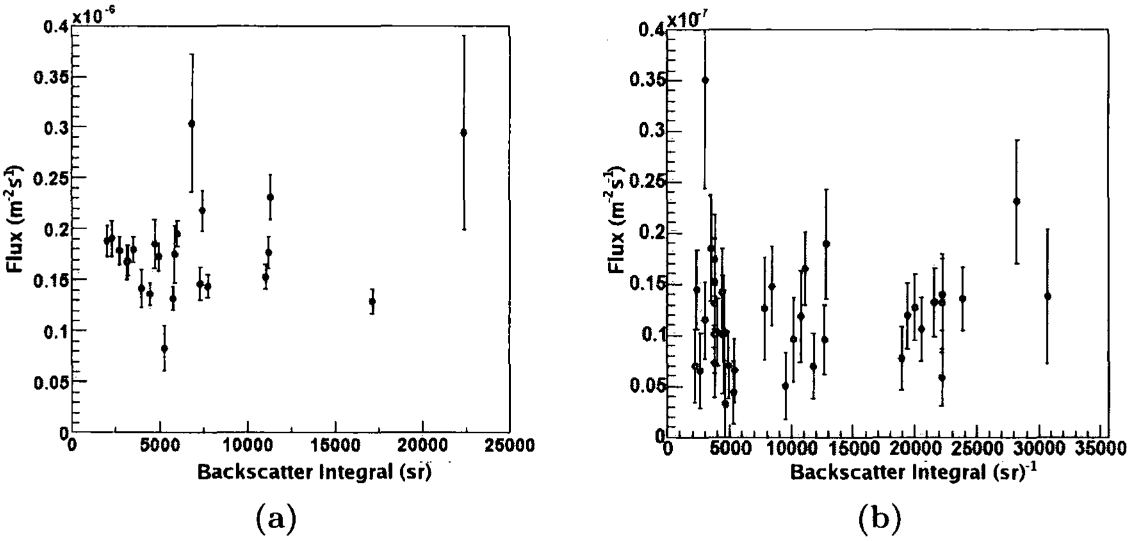

Figure 4.9: Gamma-ray flux above 1 TeV versus backscatter integral for (a) the Crab Nebula and (b) HESS J1745-290, from [98].

Figure 4.10 shows how aerosols reduce the gamma-ray effective area for a given gamma-ray energy. This effect is most pronounced at energies less than ~0.25 TeV. The difference between effective areas hints that these gamma rays should be affected by aerosols. In

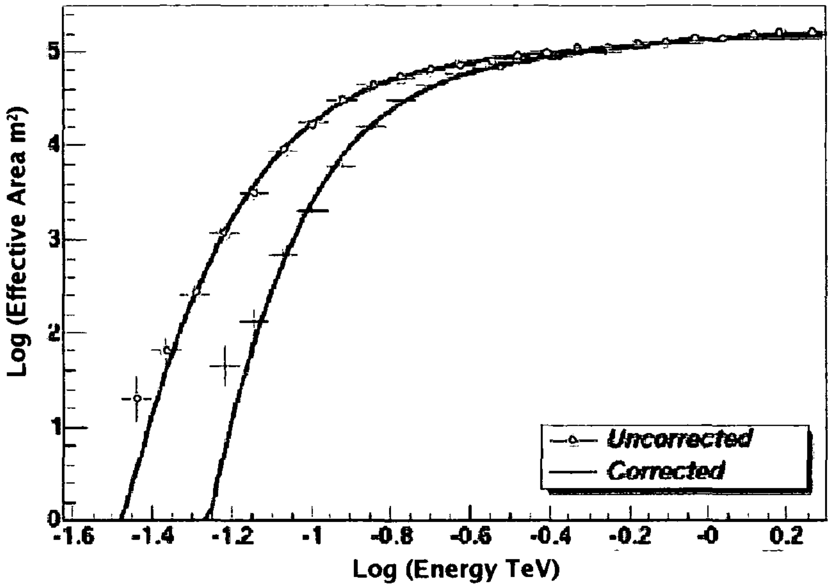

Figure 4.10: The gamma-ray effective area versus gamma-ray energy is plotted for the standard (uncorrected) atmosphere and an atmosphere with a dense aerosol layer (corrected).

addition, it has also been shown from Section 4.2 that the trigger rate, hence Cherenkov light, is reduced when large concentrations of aerosols are present. The overall attenuation of Cherenkov light would imply the subsequent degradation of the telescope's ability to detect gamma rays.

An ideal source to study would be one of constant flux with a spectral index of ~3. This would provide a greater number of lower energy gamma rays that are thought to be more affected by aerosols. Unfortunately, such a source has not yet been observed and the spectral indices dealt with here are ~2.

In this section, gamma-ray fluxes will be compared with backscatter, transmissivity, and radiometer measurements using the sources, HESS J1813-178, HESS J1837-069, and additional data from HESS J1745-290.

4.3.1 HESS J1813-178

HESS J1813-178 was first detected as a part of the first galactic scan, showing positional coincidence with an X-ray source detected by ASCA and INTEGRAL, and a radio source detected by VLA, indicating a probable association with a shell-type SNR [22]. Lack of good coincident ceilometer and observational data makes it hard to draw any conclusions, but looking at other sources, such as HESS J1837-069 and HESS J1745-290, will allow a better comparison for spotting any trends.

The run list for this source is found in Table C.1 in Appendix C, showing the run statistics of good and bad ceilometer and observation runs. In the end, 10 out of 29 runs were analysed. The basic results of my analysis are shown in Table 4.5. The light curve is shown in Figure 4.11 with an average flux of $(8.6 \pm 4.4) \times 10^{-12}$ cm^{-2} s^{-1} with a reduced chi-squared fit to a constant flux of $\chi^2/\text{ndf}^4 = 1.6$.

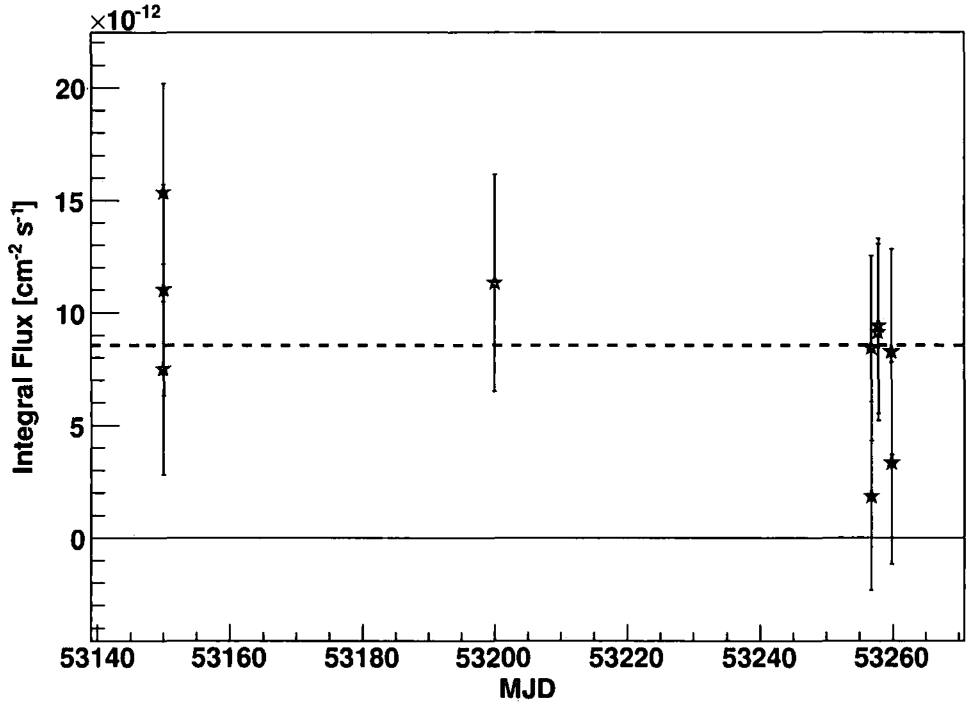

Figure 4.11: Light curve of J1813-178. The last two points have the highest backscatter, but have similar fluxes to the other runs.

Figure 4.12 shows the integral flux compared to corrected trigger rate, backscatter, transmissivity, and sky radiance, as well as corrected trigger rate with backscatter integral

---

[4] ndf = number of degrees of freedom

and transmissivity. Each point represents one observation run of 28 minutes. There is hardly enough data to make any conclusions and the data that is present is clumped together and unsuggestive. Nevertheless, a few statements can be made. Looking at the run with the highest flux in Figure 4.12(b), it is true that it has the lowest backscatter, but it is not true that the lowest flux has the highest backscatter. Two runs with a backscatter at least 5 times greater than all the other runs, have fluxes below ((3.3±4.5) and (8.3±4.6)$\times 10^{-12}$ cm^{-2} s^{-1}), although within errors, of the average flux of (8.6±4.4) $\times$ 10^{-12} cm^{-2} s^{-1}. The backscatter profile for the run with the highest backscatter integral value (run = 22408) is shown in Figure 4.13. Even though a dense aerosol layer ($BS_{Int} \sim 50,000$ sr^{-1}) has a marginal, influence on flux, it can be seen in Figure 4.12(e) that trigger rates are drastically affected.

Table 4.5: Basic results of gamma-ray analysis for all 3 flux sources, all fit to a power law spectrum.

	HESS J1813-178	HESS J1837-069	HESS J1745-290
Cuts (p.e.)[5]	Loose (40)	Standard (80)	Standard (80)
$\langle\theta_z\rangle$	22°	31°	20°
Significance	5σ	4.5σ	15.9σ
Excess	109 γ-rays	96 γ-rays	763 γ-rays
Energy Threshold	0.27 TeV	0.31 TeV	0.18 TeV
Average Flux[6]	8.6±4.4	24.3±12.1	11.4±0.1
Spectral Index	2.1±0.1	2.2 ± 0.1	2.32 ± 0.04
Integral Flux (> 200 GeV)	8.5 ± 4.4 (3.1% Crab Flux)	11.2 ± 1.4 (3.8% Crab Flux)	10.0 ± 0.6 (3.1% Crab Flux)
Integral Flux (> 1 TeV)	1.43 ± 0.25 (6.8% Crab Flux)	1.68 ± 0.21 (6.9% Crab Flux)	1.19 ± 0.06 (4.9% Crab Flux)
χ^2/ndf	2.4/3	4.6/3	11.4/10

---

[5] For an explanation of analysis cuts, see Section 1.6.

[6] All flux values are in units of [10^{-12} cm^{-2} s^{-1}].

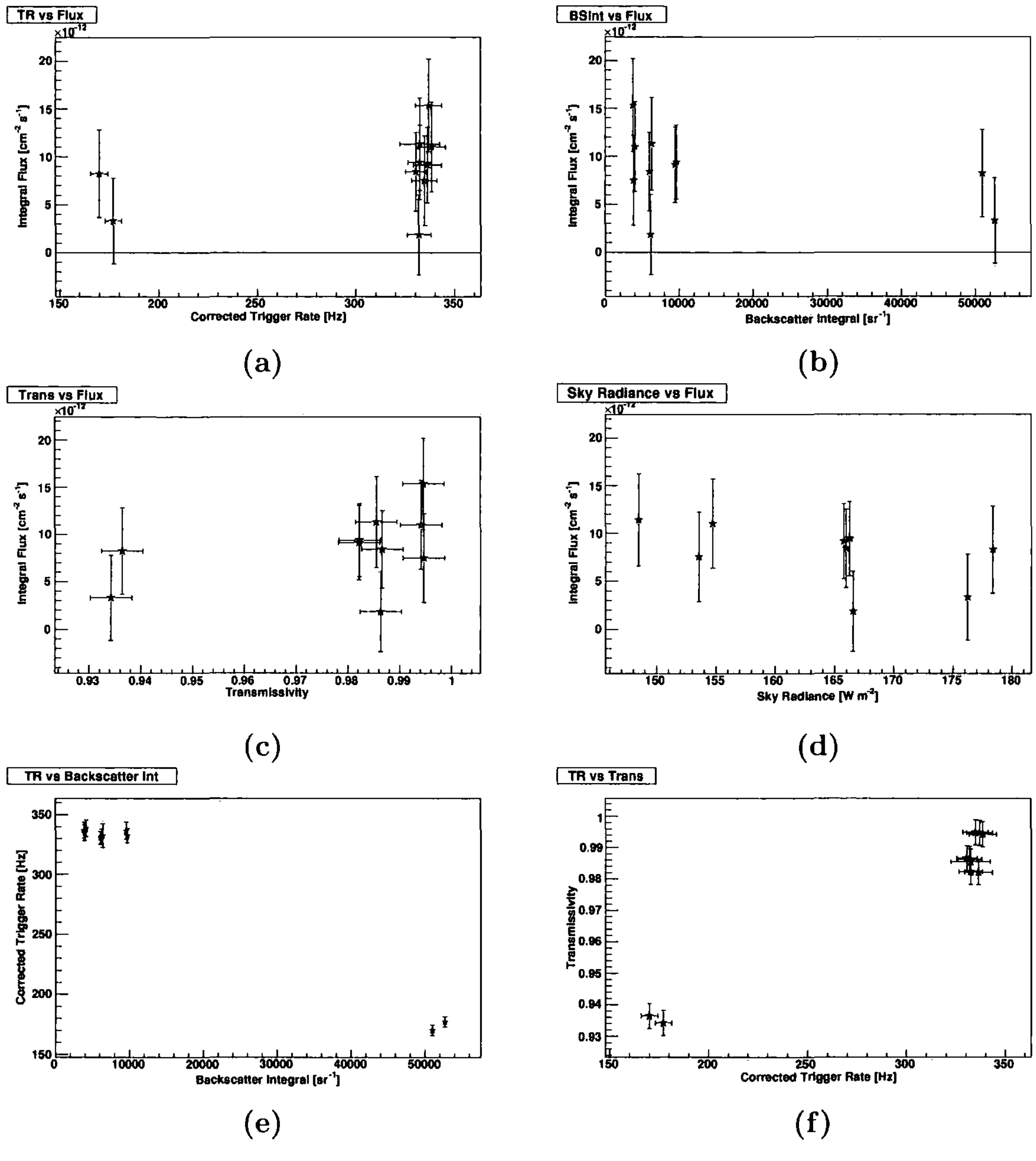

(a) (b)

(c) (d)

(e) (f)

Figure 4.12: Integral flux versus (a) corrected trigger rate, (b) backscatter integral, (c) transmissivity, and (d) sky radiance. Also shown, (e) corrected trigger rate versus backscatter integral and (f) transmissivity, for HESS J1813-187. No striking correlations are seen due to little available data.

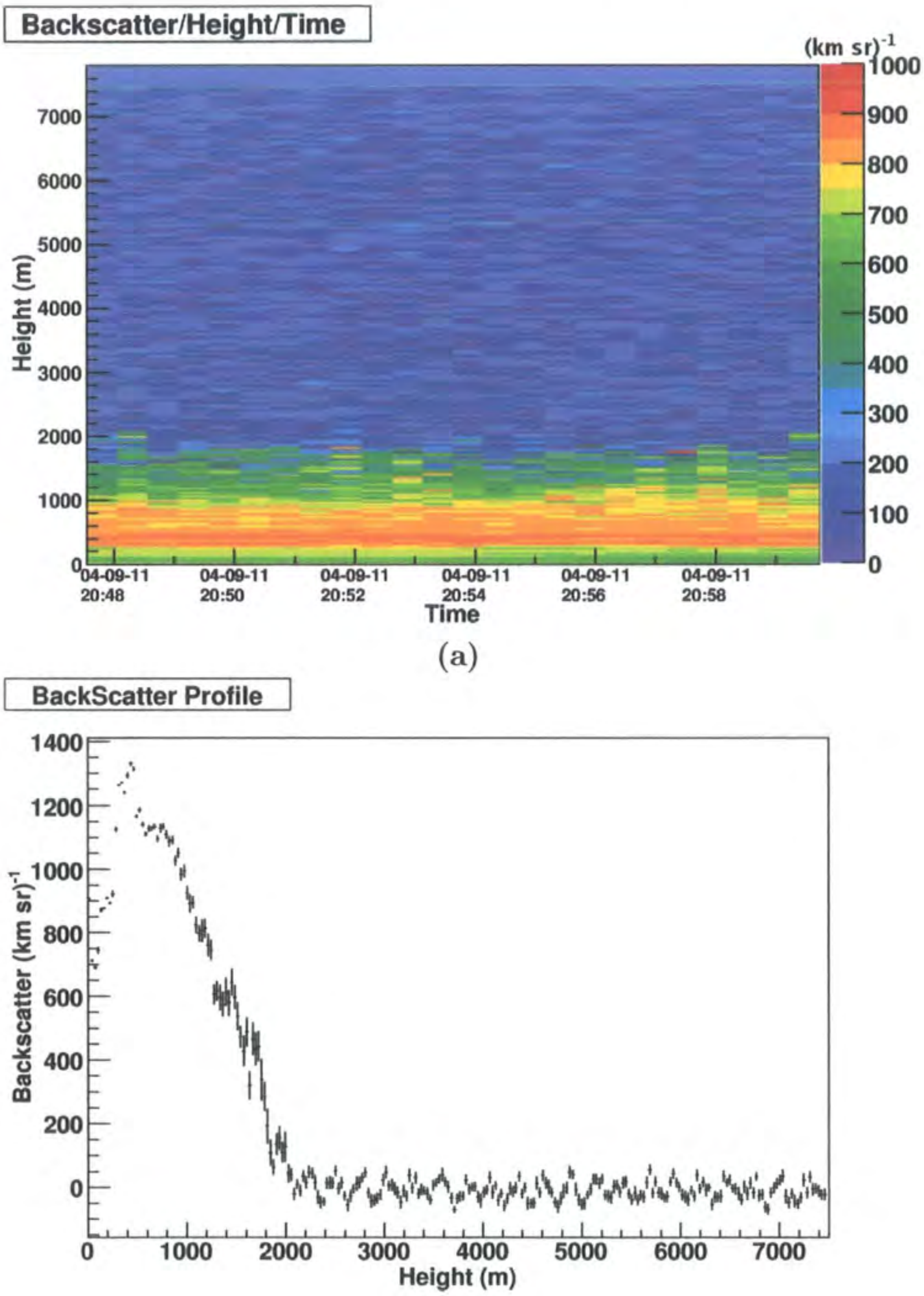

(a)

(b)

Figure 4.13: The backscatter profile shown for run=22408, the run with the highest backscatter (BS_{Int} = 52685 sr^{-1}) for the HESS J1813-178 dataset. (a) Shows the backscatter over time, whereas (b) shows the averaged profile over the whole run. See Figure 3.20 for an explanation of colour axes. Dense layers of aerosols such as these can still permit detection of gamma rays within average fluxes detected with clearer skies.

4.3.2 HESS J1837-069

Like the previous source HESS J1813-178, HESS J1837-069 was first detected as a part of the first galactic scan and is positionally coincident with a diffuse X-ray source detected by the ASCA, BeppoSAX and INTEGRAL satellites. The nature of the source is unclear, but might be a SNR or PWN [22]. It has since been observed in follow-up pointing observations. The new pointing runs had few good associated ceilometer data.

The run list is found in Table C.2 in Appendix C, showing the run statistics of good and bad ceilometer and observation runs. Twenty-one out of 52 runs were used in analysis. The basic results of my analysis are shown in Table 4.5. The light curve is shown in Figure 4.14 with a constant flux of $(2.4 \pm 1.2) \times 10^{-11}$ cm^{-2} s^{-1} and a reduced chi-squared fit to a constant flux of $\chi/\mathrm{ndf} = 1.2$.

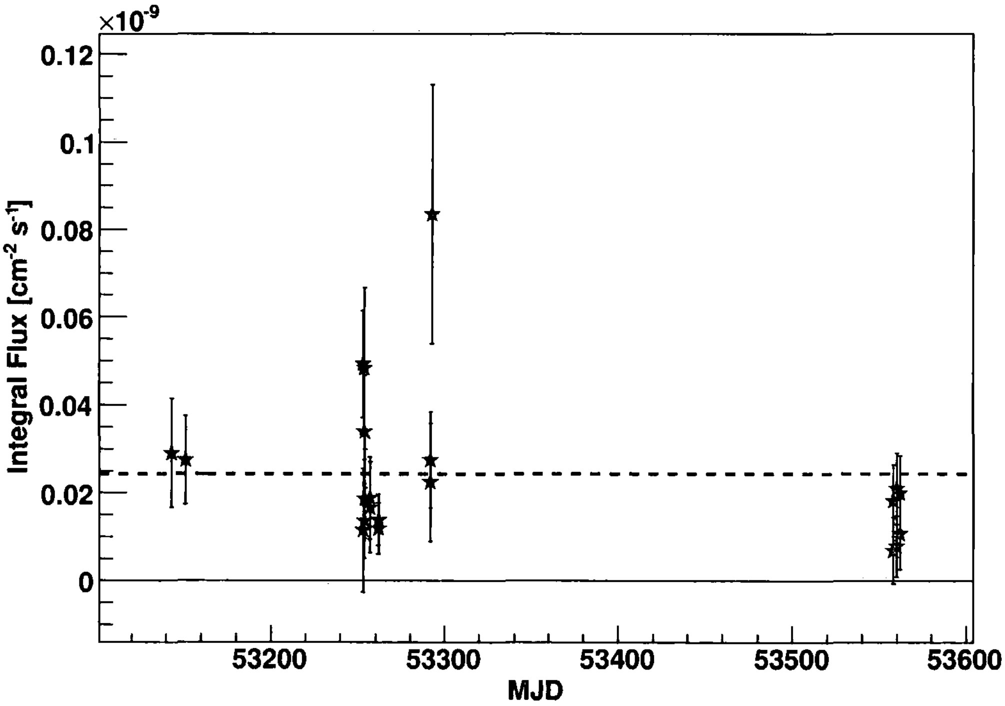

Figure 4.14: Light curve of J1837-069.

Figure 4.15 shows the integral flux compared to trigger rate, backscatter, transmissivity, and sky radiance, as well as corrected trigger rate with backscatter integral and transmissivity. This source has twice as much data as HESS J1813-178, but the data are still considerably clumped. No outstanding correlations are seen, but a few runs stand out that should be discussed. The run with the highest flux (run=23051), but with the highest flux error, has the highest sky radiance, largest zenith angle, highest background light value, with moderate backscatter. There is no indication that any of these factors have an influence on the flux.

Other points that stick out are runs 23022 and 23023 that have relatively low transmissivities ($\sim$ 0.96) and high trigger rates ($\sim$ 380 Hz), shown in Figure 4.15(f). There is nothing else striking about these runs, all other parameters are relatively moderate. A suggestion is that the trigger rate time corrections presented in Section 4.1.1 may be over compensating, since these runs fall at the end of region I where trigger rates are the lowest, and hence where correction values would be highest.

Finally, the runs with the highest backscatter were examined and have fluxes within errors ((1.4±0.6) and (1.2±0.6) $\times 10^{-11}$ cm^{-2} s^{-1}) of the average flux of (2.4±1.1) $\times 10^{-11}$ cm^{-2} s^{-1} (but on the 'low' side), with the lowest trigger rates ($\sim$ 180 Hz).

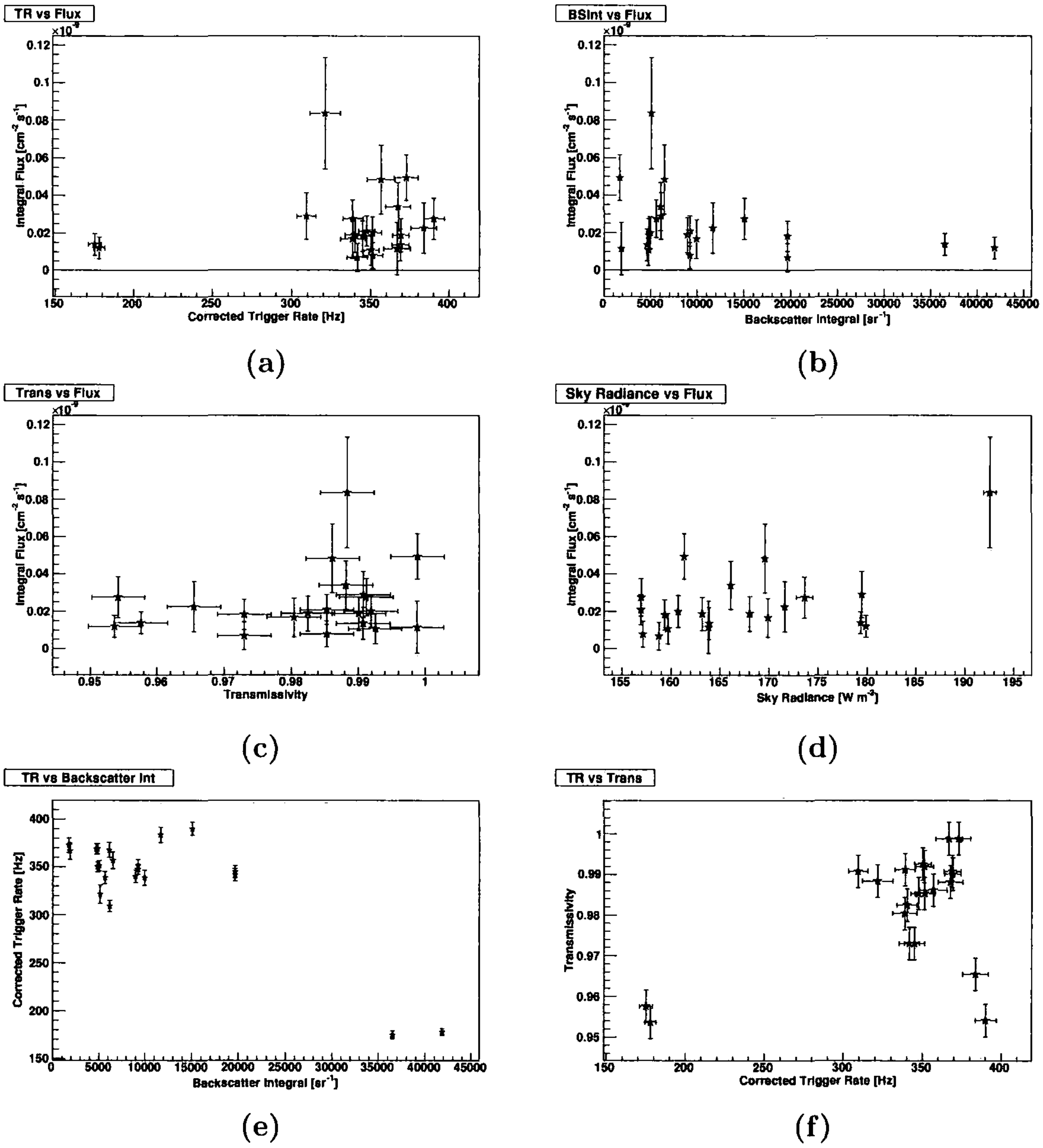

Figure 4.15: Integral flux versus (a) corrected trigger rate, (b) backscatter integral, (c) transmissivity, and (d) sky radiance. Also shown, (e) corrected trigger rate versus backscatter integral and (f) transmissivity, for HESS J1837-069.

4.3.3 HESS J1745-290

HESS J1745-290 is located in the galactic centre, a rich source of VHE gamma rays, discussed in 1.3.1. This was an ideal source to investigate due to its large dataset and seemingly constant gamma-ray emission [6]. Seventy out of 300 runs with good ceilometer and observational data were used for analysis.

There is a diffusive emission component accounting for 16% of the gamma-ray flux [19], but since I am only interested in dealing with absolute flux correlations with atmospheric data and not investigating particle acceleration mechanisms, it does not need to be subtracted. The light curve from HESS J1745-290 is shown in Figure 4.16 with an average flux of $(1.1 \pm 0.1) \times 10^{-11}$ cm^{-2} s^{-1} and a reduced chi-squared fit to a constant flux of χ/ndf = 0.2

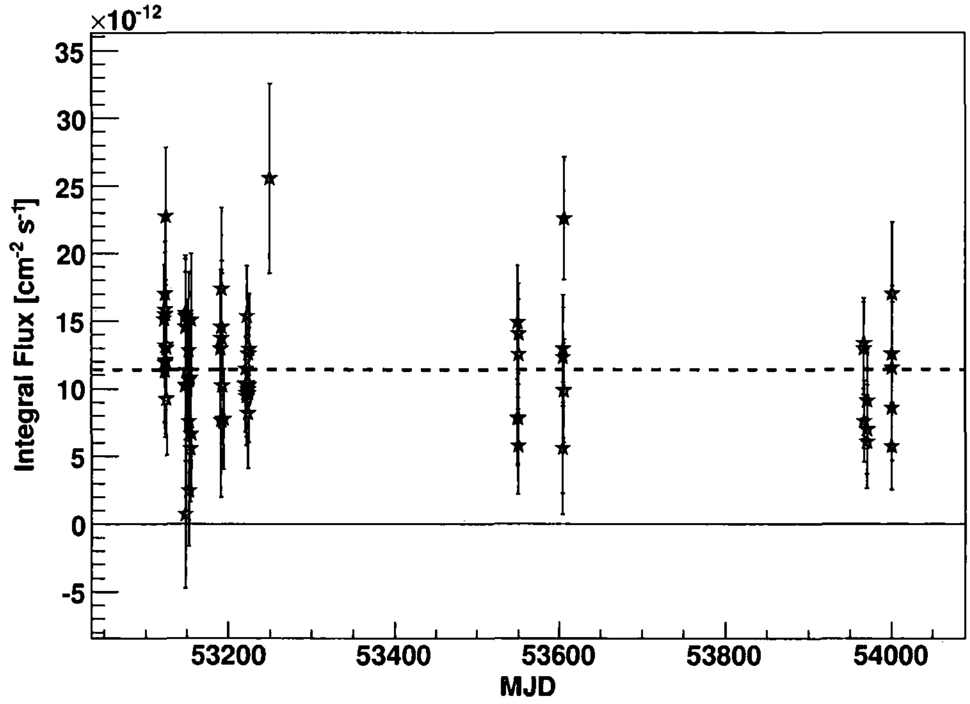

Figure 4.16: Light curve of HESS J1745-290.

Figure 4.17 shows the integral flux compared to trigger rate, backscatter, transmissivity, and sky radiance, as well as corrected trigger rate with backscatter integral and transmissivity. The highest flux runs (20597 and 22258) are among the lowest backscatter, but the highest backscatter runs have fluxes within the average integral flux of $(1.1 \pm 0.1) \times 10^{-11}$ cm^{-2} s^{-1} as can be seen in Figure 4.17(b). Figures 4.17(a) and (b) seem to show convergence toward the average flux with increasing aerosols.

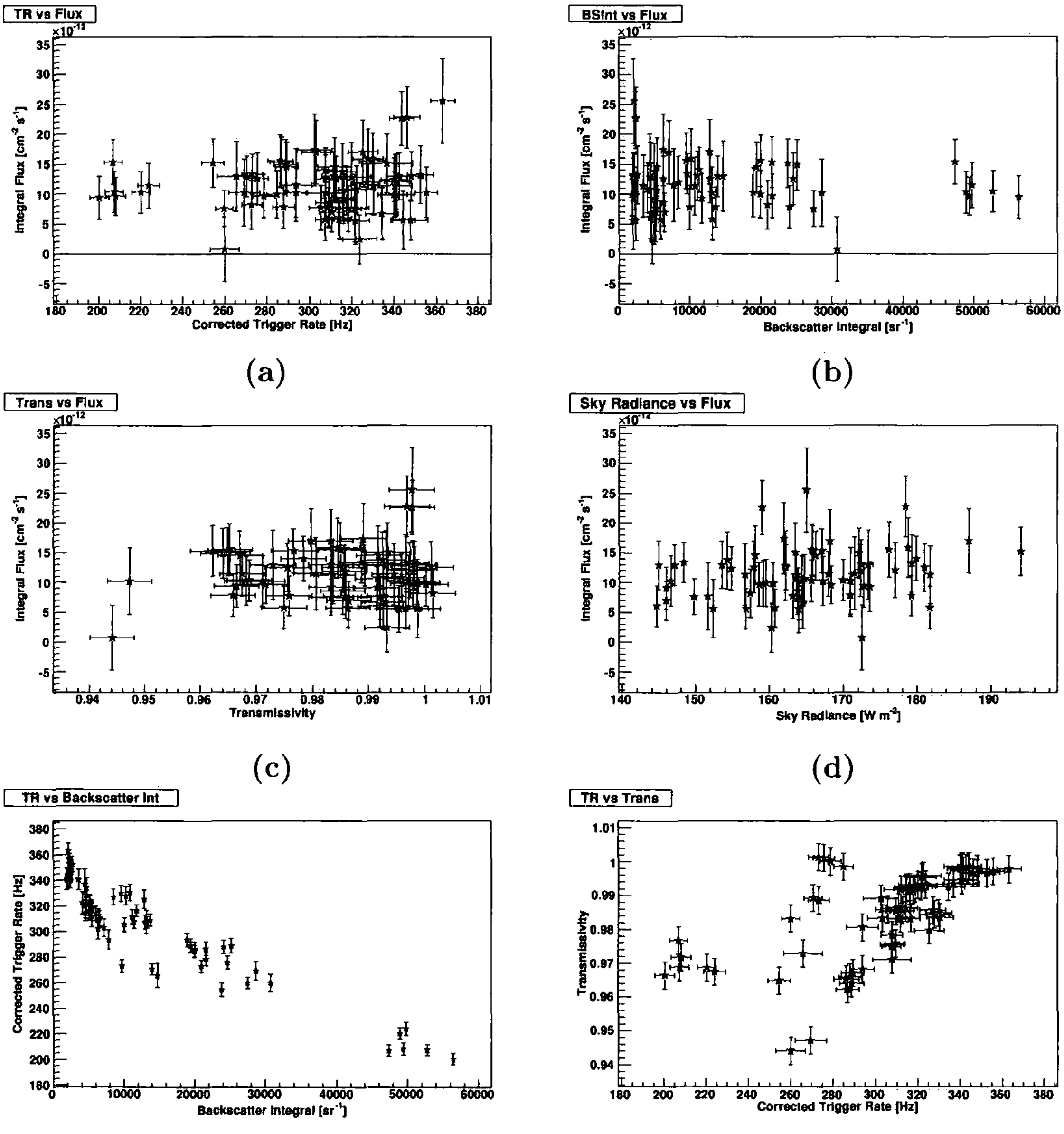

(a) (b)

(c) (d)

(e) (f)

Figure 4.17: Integral flux versus (a) corrected trigger rate, (b) backscatter integral, (c) transmissivity, and (d) sky radiance. Also shown, (e) corrected trigger rate versus backscatter integral and (f) transmissivity, for HESS J1745-290. (a) and (b) seem to show convergence toward the average flux with increasing aerosols.

4.3.4 General Conclusions

- The highest flux points are among the lowest backscatter values and with their aerosol layers below 550 metres.
- The highest backscatter runs have fluxes within the average flux (but slightly lower) for each source and with the lowest trigger rates as was also demonstrated in Section 4.2.2.
- The large amount of data for HESS J1745-290 shows convergence to the average flux for high aerosol concentrations.
- There is a possible correlation with fluxes, trigger rates and backscatter integral (ie. there are no high fluxes observed with low trigger rates or high backscatter).
- All these sources have a fairly hard spectrum, $\Gamma \sim 2$, and so softer spectra may show a greater dependence on aerosol concentrations since they would contain a larger fraction of lower energy gamma rays. This will be explored in the next section with PKS 2155-304 (with $\Gamma = 3.3$).

4.4 Active Atmospheric Calibration

In this section a method is developed, called active atmospheric calibration, to show how gamma-ray data can be corrected for atmospheric effects, implemented when observing under high aerosol conditions. Runs with high aerosol concentrations are normally rejected due to their low trigger rate, but through this method, the standard clear atmosphere used in analysis for Cherenkov light transmission can be adjusted to represent an atmosphere with a dense aerosol layer. The following approach is a summary of what is developed in [98, 39, 116].

Cherenkov Transmission & Trigger Rates with Non-standard Atmospheres

In the simulation chain used to model the H.E.S.S. system and its response, transmission tables are used to characterise the opacity of the atmosphere. MODTRAN (see Section 1.6.4) simulates atmospheric transmission and can be adjusted for different types of atmospheres. Atmospheric transmission is expressed in terms of optical depth over a wavelength range between 200 nm and 700 nm, and for various heights in the atmosphere where Cherenkov light is produced. These optical depths are then generated in the form of tables.

The current *standard atmosphere* used in H.E.S.S. data analysis is a desert aerosol model [93]. Increasing the wind speed parameter[7] increases the aerosol density in the lowest 2 kilometres of the atmosphere, reducing the transmission probability. Figure 4.18 shows the reduction of the transmission probability with the standard atmosphere compared to a layer with aerosols. Different wind speeds for various concentrations of aerosols distinguish these models from the standard atmosphere, which has a wind speed of 10 ms^{-1}. Optical depth tables for wind speeds from 0 - 30 ms^{-1} were produced. Using CORSIKA (see Section 1.6.4), simulations of Cherenkov light produced by cosmic ray air showers over a range of zenith angles are then processed by each optical depth table to determine the amount of Cherenkov light transmitted through the atmosphere. The transmitted light is then run through the telescope simulation code, sim_hessarray (see Section 1.6.4), to determine the trigger rate detected by the telescopes. This results in a relation between wind speed and trigger rate, shown in Figure 4.19. The process described above is illustrated in Figure 4.20.

---

[7] It should be noted that adjusting the wind speed only serves to increase the aerosol density and does not represent the actual wind speed observed on site.

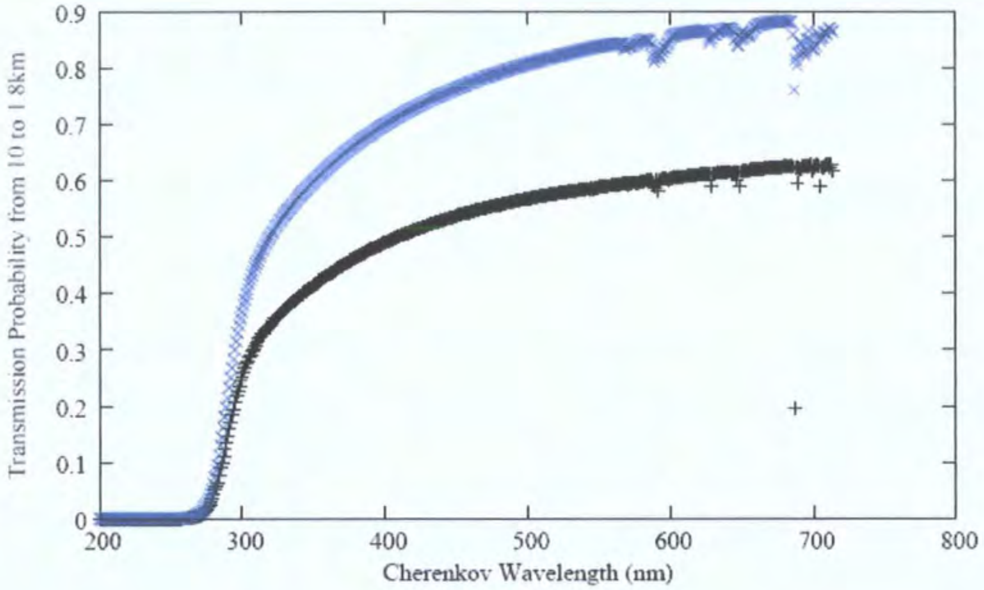

Figure 4.18: Transmission probability for the standard desert atmosphere (upper curve) and an atmosphere with a high concentration of aerosols (lower curve), from [98].

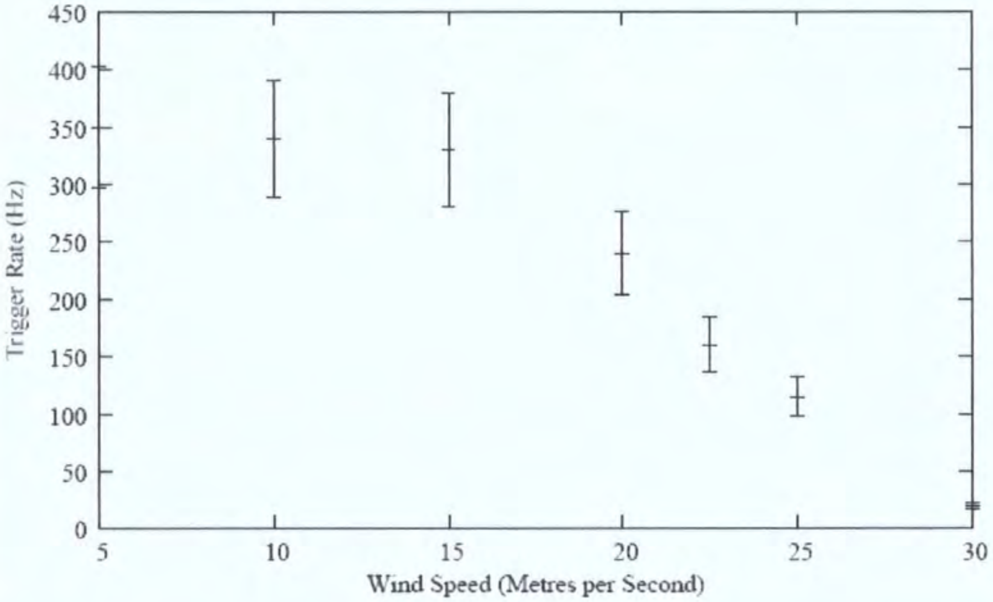

Figure 4.19: Selected wind speeds versus simulated trigger rates at a zenith angle of 20°. Observed trigger rates are then matched to simulated trigger rates to determine a representative atmospheric model for data analysis [39].

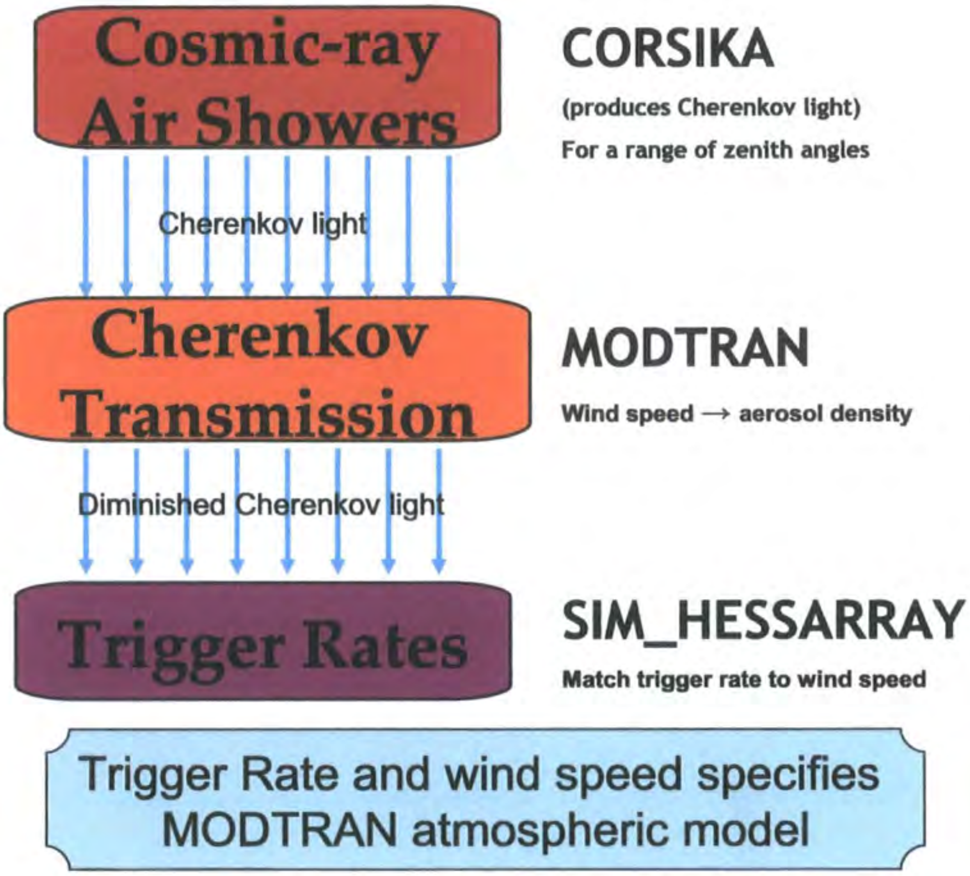

Figure 4.20: The chain of events describing the first sequence of active atmospheric calibration, the production of non-standard atmospheres matched to observed trigger rates. See text for discussion.

Application to Gamma-ray Simulations

Exploiting the fact that trigger rate is dependent on atmospheric clarity, demonstrated in Section 4.2.2 (along with using the LIDAR to constrain the aerosol population and shower depth profile[8] to check the aerosol behaviour), allows us to choose a representative atmospheric model by matching the observed trigger rates to simulated trigger rates. This is done through the variation of wind speed as described in the previous section. Once an atmosphere has been selected, a large number of gamma-ray shower simulations are applied to it (using CORSIKA), producing lookup tables (using sim_hessarray), which include the parameters: mean-scaled length and width; gamma-ray energy, and gamma-ray effective area, for 0°, 0.5°, and 1.0° wobble offset[9] [98, 21]. Figure 4.21 illustrates this sequence of execution. Once lookup tables are produced, the data are run through the standard H.E.S.S. analysis chain, as described in Section 1.6.

---

[8] The shower depth profile is a measure of the height above the ground where gamma rays initiate their air shower.

[9] Wobble offset is an observation mode where the centre of the telescopes are displaced from the source at said angles.

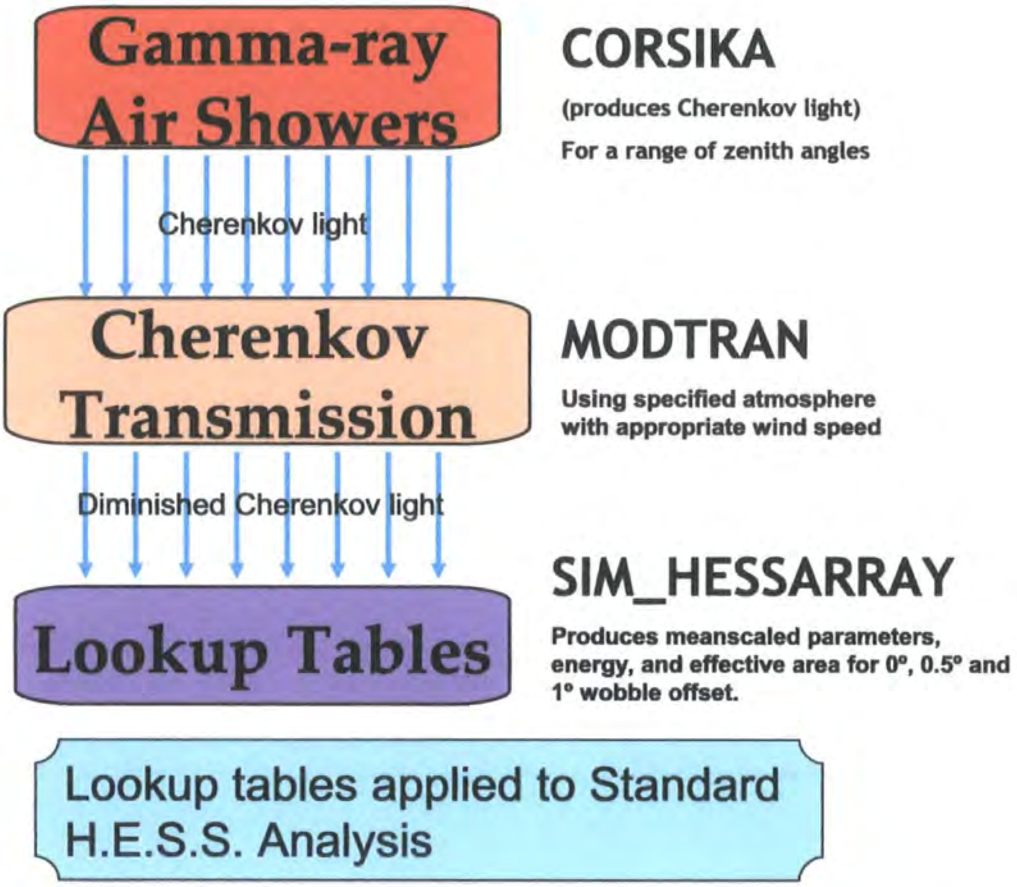

Figure 4.21: The chain of events describing the second phase of active atmospheric calibration, the application of non-standard atmospheres to gamma-ray showers. See text for discussion.

Effects on Gamma-ray Parameters

The effects of different atmospheres on gamma-ray energy, effective area, and energy threshold have been explored in [98] and are summarised here. The biggest effect of difference atmospheres is on energy reconstruction. The fractional energy difference between a standard atmosphere and a corrected atmosphere is given by,

$$F_E = \frac{E_{22.5} - E_{std}}{E_{std}} \tag{4.5}$$

where E_{std} is the energy found in the standard lookup table and $E_{22.5}$ is the energy simulated for a corrected atmosphere with a wind speed of 22.5 ms^{-1}. Table 4.6 shows how the standard atmosphere underestimates the energy compared to the corrected atmosphere. The energy is underestimated because aerosols diminish the Cherenkov light intensity, and since the intensity is proportional to the gamma-ray energy, a lower gamma-ray energy is derived. These values also show that the effect is enhanced with increasing zenith angle. For example, for $\theta_z = 0$, $E_{std} = 0.69E_{22.5}$ and for $\theta_z = 60$, $E_{std} = 0.56E_{22.5}$.

Table 4.6: The fractional energy difference between the standard atmosphere and an atmosphere with a wind speed of 22.5 ms^{-1}, data from [98].

θ_z (°)	F_E (mean)	F_E (rms)
0	0.44	0.22
20	0.47	0.22
30	0.49	0.22
40	0.55	0.22
45	0.58	0.21
50	0.63	0.21
55	0.70	0.22
60	0.78	0.22

Previously discussed at the beginning of this section, Figure 4.10 shows the effect on the gamma-ray effective area. It can be seen that the effective area is not noticeably affected at energies greater than 0.25 TeV, but starts to become increasingly important at lower energies.

The effect on energy threshold is shown in Figure 4.22. The most notable feature is the increase with zenith angle where the energy threshold for the dirtiest[10] atmosphere is

---

[10] The 'dirtiest' atmosphere refers to the non-standard atmosphere with aerosol content corresponding

a factor of 2 times bigger than the standard atmosphere at 60°.

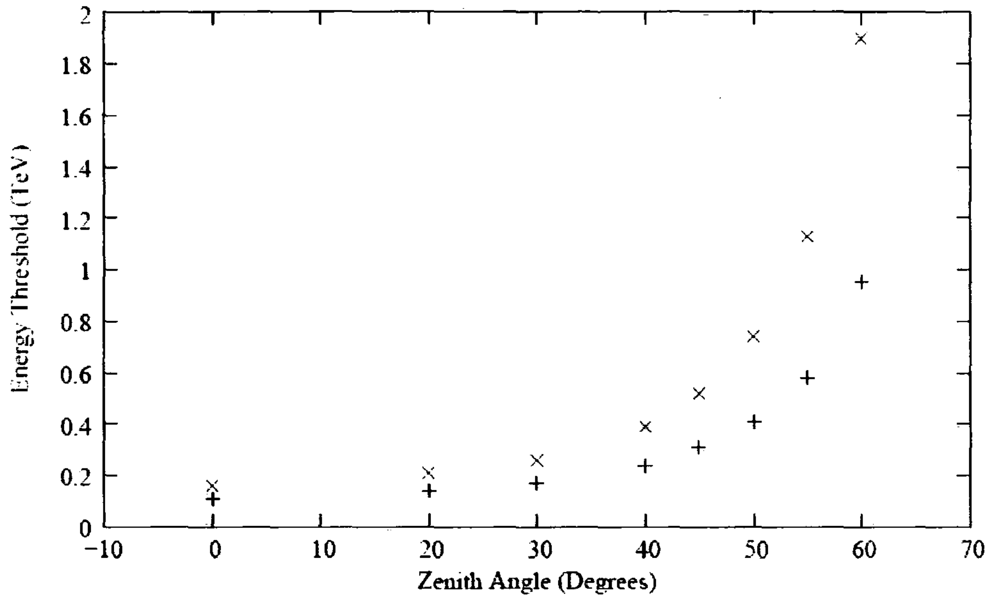

Figure 4.22: The energy threshold for a standard atmosphere (bottom points) and an atmosphere with a wind speed of 22.5 ms^{-1} (top points), from [98].

4.4.1 HESS J1745-290

Active atmospheric calibration has been first applied to a constant flux source in order to test the validity of this method. The source chosen was HESS J1745-290 (the galactic centre) because it was observed in August 2004 which has been one of the dustiest months of observation [98]. The gamma-ray flux was derived for 7 high aerosol runs with a wind speed of 22.5 ms^{-1}. The corrected flux shown in Figure 4.23 falls within the error of the published average flux. This result gives more confidence in the application of this method to a varying source.

The next two sections will apply this technique to two variable sources, PKS 2155-304 and H 2356-309. PKS 2155-304 is known to be a relatively strong source, while H 2356-309 has been observed to be about 10 times weaker. This fact will highlight the effects of active atmospheric calibration on a high versus a low flux source.

---

to a wind speed of 22.5 ms^{-1}.

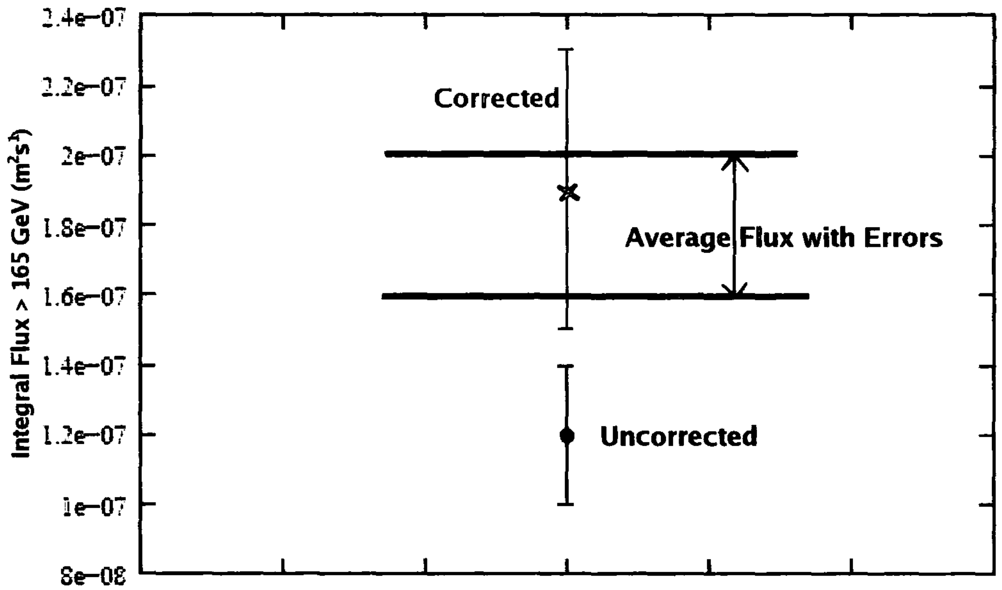

Figure 4.23: The integral flux for HESS J1745-290 above 165 GeV derived from 7 runs in August 2004, when high aerosol levels are present. Corrected and uncorrected fluxes are shown by an 'x' and circle, respectively. Also shown is the published average integral flux for the source with associated errors indicated by the arrows, from [98].

4.5 PKS 2155-304

PKS 2155-304 is a high-frequency peaked BL Lac (HBL) at redshift $z = 0.117$ discovered with the HEAO 1 X-ray satellite [131, 75]. It has been subsequently detected and extensively studied in radio, infrared, optical, and UV wavebands [120]. It is one of the brightest extragalactic X-ray sources and is the brightest BL Lac detected in UV [108]. It is associated with a compact, flat-spectrum radio-source and emits a near featureless continuum from radio to X-rays [10].

PKS 2155-304 was discovered in gamma rays with the EGRET satellite in the energy range from 30 MeV to 10 GeV [148], and was discovered in VHE gamma rays using the Durham Mark 6 telescope at energies greater than 300 GeV [45]. It has since been observed by H.E.S.S. in VHE gamma rays above 160 GeV in quiescent and high flare states, showing variability on time scales of months, days, hours, and minutes [10, 23].

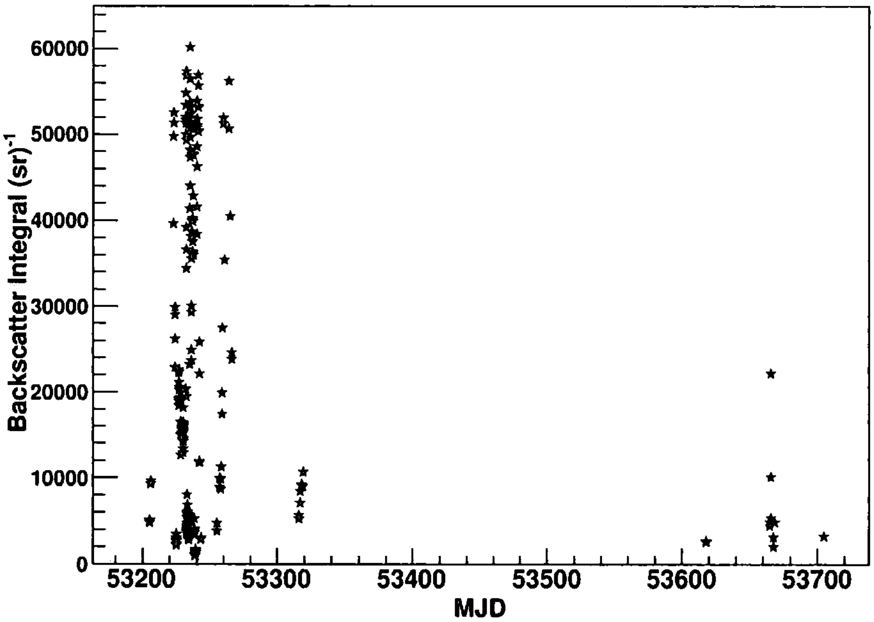

Figure 4.24: Backscatter integral versus modified Julian date in 2004 and 2005 for PKS 2155-304. The runs with the highest backscatter are found in August 2004 while relatively low levels are found in 2005.

The trickiest aspect of analysing a variable source with a dusty atmosphere is disentangling atmospheric effects from source variability. Nevertheless, PKS 2155-304 is a good candidate due to the amount of data available on this object, with a large number of runs containing a high density of low-lying aerosols. These data are also important because they were taken during the time a multiwavelength campaign was in progress. Strong source detection will also aid in placing limits on the EBL (discussed in Section 2.2 and Section 4.8). There were 288 runs taken in 2004 and 2005. After run selection, 174 good[11] ceilometer and observation runs (164 from 2004 and 10 from 2005) were analysed.

4.5.1 Chosen Atmospheres

Observations of PKS 2155-304 have detected some of the highest concentrations of aerosols ever seen at the H.E.S.S. site. This is illustrated in Figure 4.24, showing the backscatter integral over the time containing all analysed runs. The worst atmospheric conditions were encountered in August 2004.

The corrected trigger rate versus zenith angle is plotted in Figure 4.25. The solid red line illustrating the groups of constant trigger rate over zenith angle is indicative of a specific atmospheric condition. The average corrected trigger rate corresponding to the red line was found for each group and corresponds to a specific simulated wind speed. These values are listed in Table 4.7.

Table 4.7: The average corrected trigger rate (TR) and corresponding wind speed (WS) for each atmosphere used to analyse PKS 2155-304 data. The run number and corresponding backscatter are also listed to show the average backscatter integral value for each subset of runs.

WS (ms^{-1})	Corrected TR (Hz)	Run	BS_{Int} (sr^{-1})
17.5	335	22070	4266
20.0	285	22007	16181
22.5	230	22053	36601

Typical backscatter profiles representing each atmosphere are shown in Figure 4.27. The run numbers and backscatter integral values representative of each atmosphere are shown in the last columns of Table 4.7. Table C.3 in Appendix C lists the runs analysed and which atmosphere they are classified under. There are 79 runs (45%) classified under 17.5 ms^{-1}, 24 (14%) classified under 20.0 ms^{-1}, and 71 (41%) classified under 22.5 ms^{-1}.

As a check (independent of the ceilometer) for the validity of modelling the aerosols in the lower 2 km of the atmosphere, an additional set of atmospheric models were simulated with aerosol densities at higher altitudes. The reconstructed mean shower depth as a result of these various aerosol altitudes was compared to the mean shower depth derived from the data. Figure 4.26 shows the simulated reconstructed shower depth for layers

---

[11] The term 'good' refers to cloudless runs free from hardware malfunctions of the ceilometer and telescope array with 4 telescopes in operation.

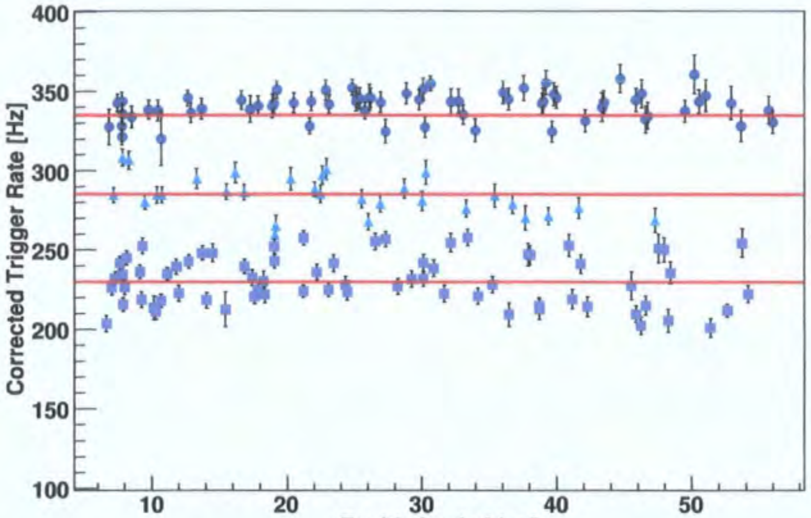

Figure 4.25: Corrected trigger rate versus zenith angle showing 3 different atmospheric classes (marked by the solid red lines). The round points are grouped in the 17.5 ms^{-1} atmosphere, the triangles are grouped in 20 ms^{-1}, and the squares are grouped in the 22.5 ms^{-1} atmosphere.

of aerosols 0-2 km (bottom curve) and 6-11 km (all other curves) above the ground as a function of simulated cosmic trigger rate. Simulations (a) were compared with real data (b). It can be seen that the simulated high altitudes levels of aerosols do not match the data and are therefore disfavoured [116].

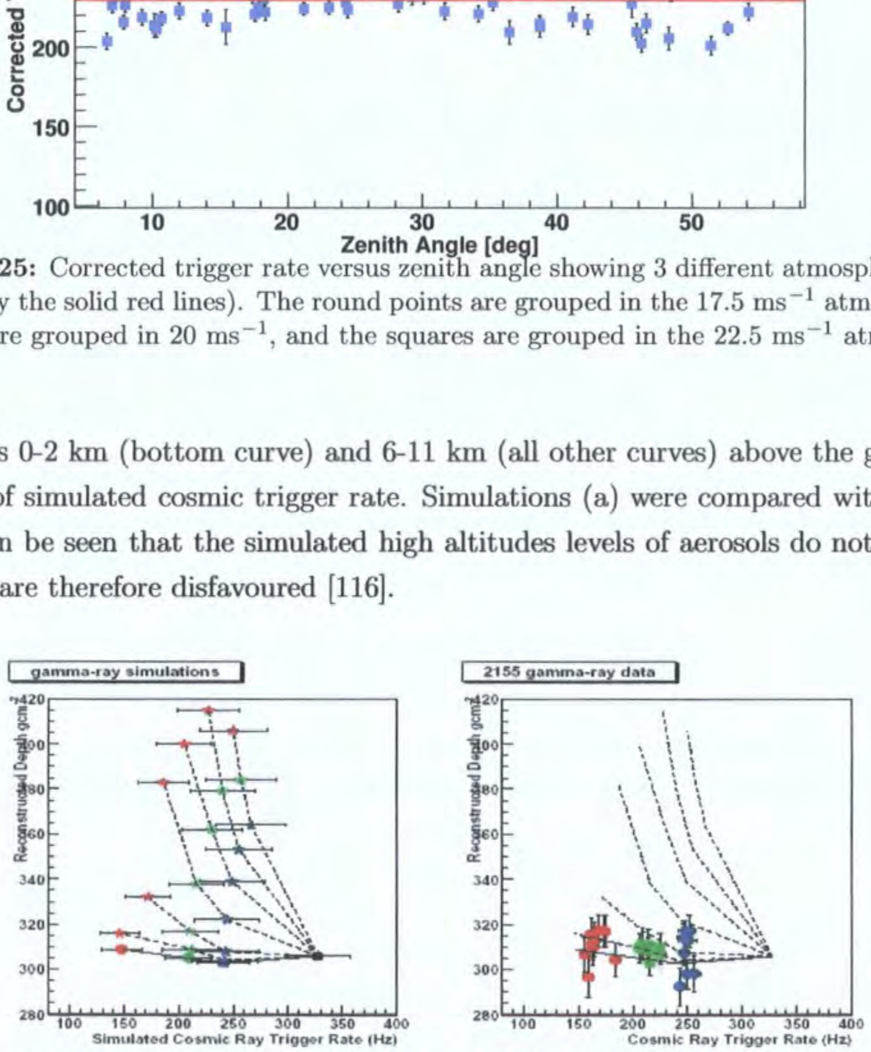

Figure 4.26: The left figure shows the reconstructed shower depth with the dotted lines representing aerosol layers at a given altitude. The circular points represent low lying aerosols below 2km above the H.E.S.S. site while the other points represent layers from 6-11 km above the site. The right figure shows observational data, which most resembles the low lying aerosol layers from simulations.

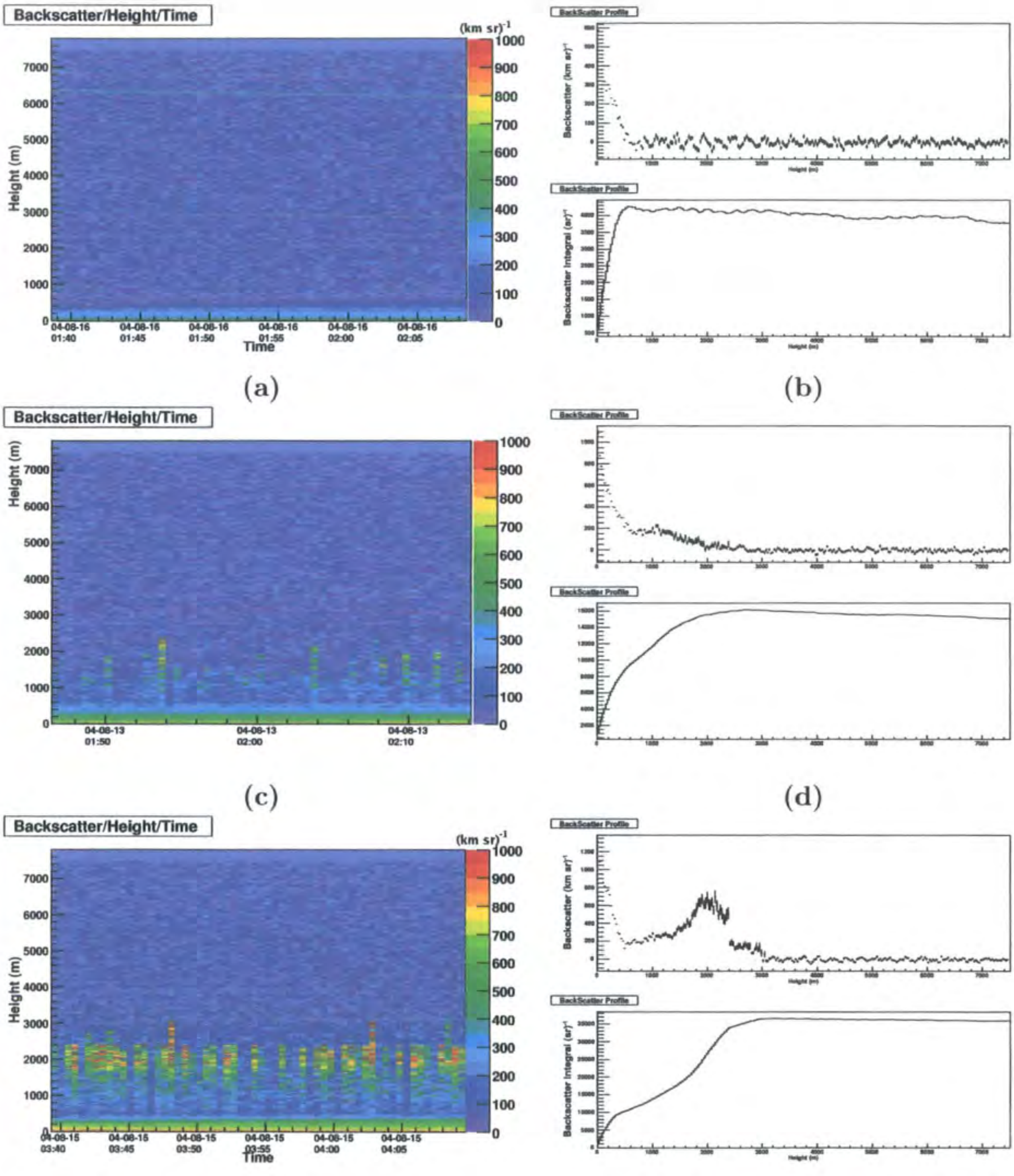

(a) (b)

(c) (d)

(e) (f)

Figure 4.27: The backscatter profiles for a representative run from each atmosphere (see Table 4.7 for run numbers and backscatter integral values). The left figures show backscatter over time, and the right figures show the backscatter averaged over the run (top) and the integrated backscatter (bottom) for (a)(b) 17.5 ms^{-1}, (c)(d) 20.0 ms^{-1}, and (e)(f) 22.5 ms^{-1}. One can clearly see the aerosol layer growing from 17.5 ms^{-1} to 22.5 ms^{-1}.

4.5.2 Results

Using the technique from Section 4.4, it will be shown how active atmospheric calibration affects the results of gamma-ray analysis. The main idea to stress here is that simulations using the standard atmosphere will underestimate the gamma-ray energy when there is low-lying dust present. This is because Cherenkov light will be absorbed or scattered through a dusty layer, therefore underestimating the energy since the assumption implicit in the analysis is that the atmosphere is relatively clear. When dusty layers are taken into account, greater Cherenkov light scattering/absorption is accounted for. Therefore, the energy and corresponding fluxes calculated with the corrected lookup tables should produce larger gamma-ray fluxes.

Table 4.8 compares gamma-ray analysis results using the standard atmosphere and corrected atmosphere. The significance and spectral index are essentially unchanged between standard and corrected atmospheres in 2004 and 2005. In 2004, the integral flux above 200 GeV increases substantially by 75% and doubles above 1 TeV. In 2005 the corrected flux above 200 GeV is 60% greater, but above 1 TeV the integral flux is not much greater (40%) than the standard flux due to the steep spectrum. Due to the high significance detected in 2004, the combined spectral properties for 2004 and 2005 are essentially that of 2004.

Table 4.8: Comparison of gamma-ray data using standard (Std) and corrected (Corr) atmospheres. The significance and spectral indices are not affected by atmospheric correction, but the integrated flux is significantly affected (see text for discussion).

Atmosphere	Significance	Spectral Index $\pm 0.1_{sys}$	I(> 0.20 TeV) $[10^{-11}\ \mathrm{cm}^{-2}\ \mathrm{s}^{-1}]$	I(> 1 TeV) $[10^{-13}\ \mathrm{cm}^{-2}\ \mathrm{s}^{-1}]$
Std (2004)	104 σ	3.56±0.03	3.2 ± 0.1	5.2 ± 0.2
Corr (2004)	106 σ	3.47±0.02	5.6 ± 0.2	10.7 ± 0.3
Std (2005)	20 σ	4.1±0.2	3.2 ± 1.2	2.0 ± 0.5
Corr (2005)	20 σ	4.2±0.2	5.1 ± 1.3	2.8 ± 0.4
Std (All)	106 σ	3.56±0.03	3.1 ± 0.1	5.1 ± 0.2
Corr (All)	108 σ	3.47±0.03	5.6 ± 0.2	10.5 ± 0.3

Figure 4.28 shows the spectrum for 2004 and 2005, while Figure 4.29 shows the combined spectrum from both years. As discussed from Table 4.8, the increased flux is apparent in each graph while the overall shape of the spectrum is not significantly changed.

In order to show the effects of each individual corrected atmosphere, runs were subdi-

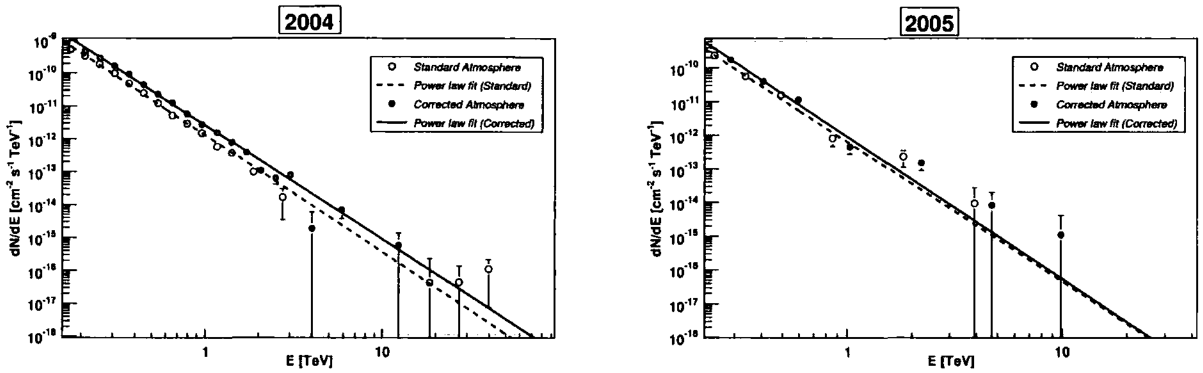

(a) (b)

Figure 4.28: The spectrum of PKS 2155-304 in (a) 2004, and (b) 2005 (one atmospheric type, 20 ms^{-1}). The properties of the spectra are listed in Table 4.8 while the differences are discussed in the text.

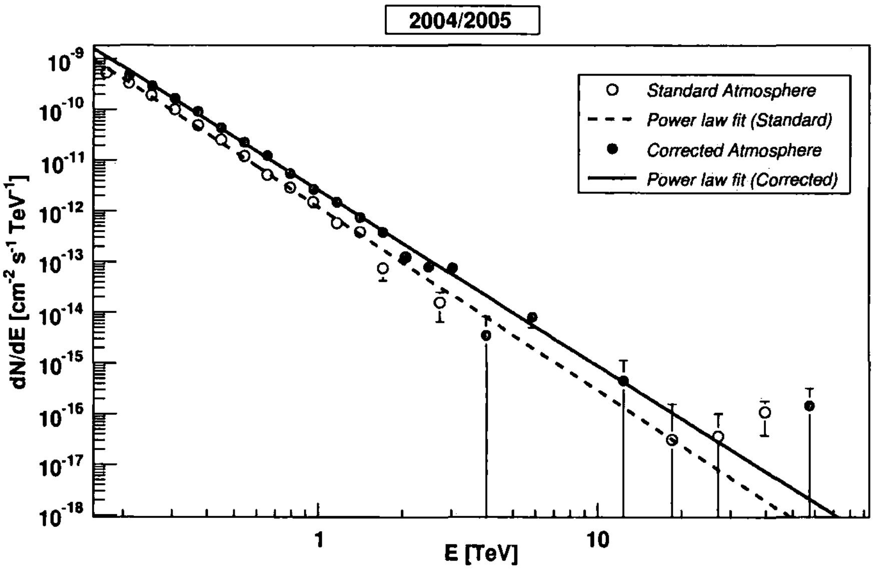

Figure 4.29: The spectrum of PKS 2155-304. As quantified in the text and Table 4.8, the spectral shape is not much affected, but the overall corrected flux is increased.

vided into their respective atmospheric class. Table 4.9 and Figure 4.30 compare the runs in each corrected atmosphere 17.5, 20.0, and 22.5 ms^{-1} with the standard atmosphere. It can be seen from the table that the fractional change in the integral flux above 0.20 TeV, $\Delta I = (I_{corr} - I_{std})/|I_{std}|$, increases with increasing aerosols showing that the amount of flux correction directly corresponds to the amount of aerosols in the atmosphere.

Table 4.9: Comparison of uncorrected and corrected gamma-ray data in 2004 for runs in each atmospheric class.

Atmosphere	Significance	Spectral Index $\pm 0.1_{sys}$	I(> 0.20 TeV) [10^{-11} cm^{-2} s^{-1}]	I(> 1 TeV) [10^{-13} cm^{-2} s^{-1}]	ΔI
Std	72 σ	3.57±0.04	4.0±0.2	6.4±0.3	40%
17.5 ms^{-1}	73 σ	3.46±0.03	5.6±0.3	10.6 ±0.4	
Std	48 σ	3.56±0.06	3.9±0.4	6.2±0.5	69%
20.0 ms^{-1}	48 σ	3.53±0.06	6.6±0.7	11.3±0.8	
Std	57 σ	3.58±0.2	2.6±0.2	4.0±0.2	115%
22.5 ms^{-1}	59 σ	3.56±0.04	5.6±0.4	9.1±0.4	

The fractional change in flux was also looked at on a run-by-run basis. In the PKS 2155-304 dataset, 9 out of 174, or 5%, of these runs returned lower fluxes with their new lookup tables. These were all runs with a zenith angle greater than 50° with large flux errors and are no cause for concern.

Figure 4.31 shows the light curve for the observation period P2004-08 comparing the corrected with the standard flux. The average standard flux is $(5.10 \pm 2.18) \times 10^{-11}$ cm^{-2} and the average corrected flux is $(9.14 \pm 1.06) \times 10^{-11}$ cm^{-2}. This period illustrates the flux differences most clearly as this period contains 82% of the total runs analysed. Figure 4.32 shows the histogram of gamma-ray fluxes comparing corrected and standard fluxes including all data. The shift to higher fluxes is apparent, with the corrected average flux greater by 80%.

The previously published time-averaged flux in 2004 is given by $I_0 = (2.17 \pm 0.08) \times 10^{-12}$ cm^{-2} s^{-1} TeV^{-1} with a spectral index of 3.58 ± 0.04 fit to a power law [64]. These values correspond to an integrated flux above 200 GeV of I(> 200 GeV) = $5.4 \pm 0.2 \times 10^{-11}$ cm^{-2} s^{-1}. These published values agree with the data here of I(> 200 GeV) = $5.6 \pm 0.2 \times 10^{-11}$ cm^{-2} s^{-1} with a spectral index of 3.47 ± 0.02, indicating that this method works well to reproduce consistent results.

Next, H 2356-309, another variable but lower flux source will be analysed and set against the results from PKS 2155-304.

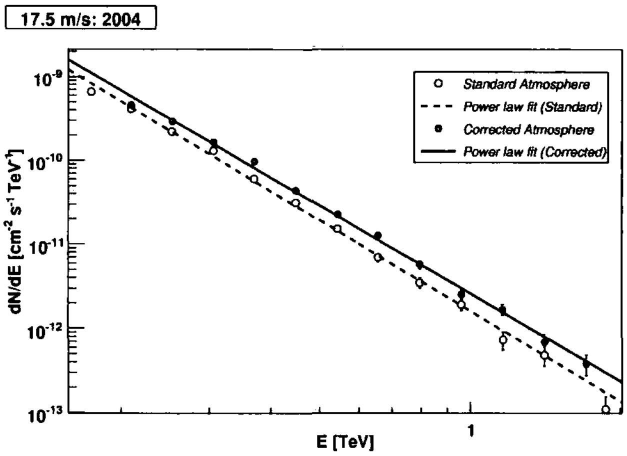

(a)

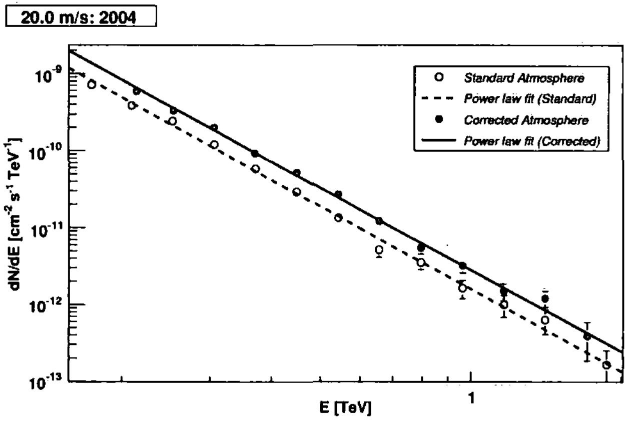

(b)

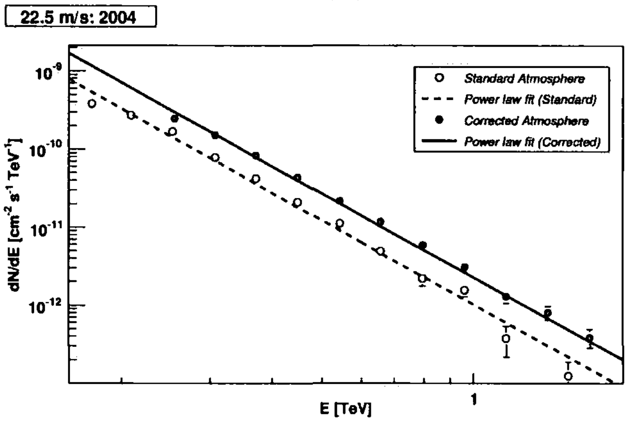

(c)

Figure 4.30: Spectrum of PKS 2155-304 in 2004 for runs associated with (a) 17.5 ms^{-1}, (b) 20.0 ms^{-1}, and (c) 22.5 ms^{-1} atmospheres. The runs were separated into respective atmospheric classes. All spectral indices are unchanged within errors, but the difference between uncorrected and corrected flux increases with increasing aerosols (quantities found in Table 4.9).

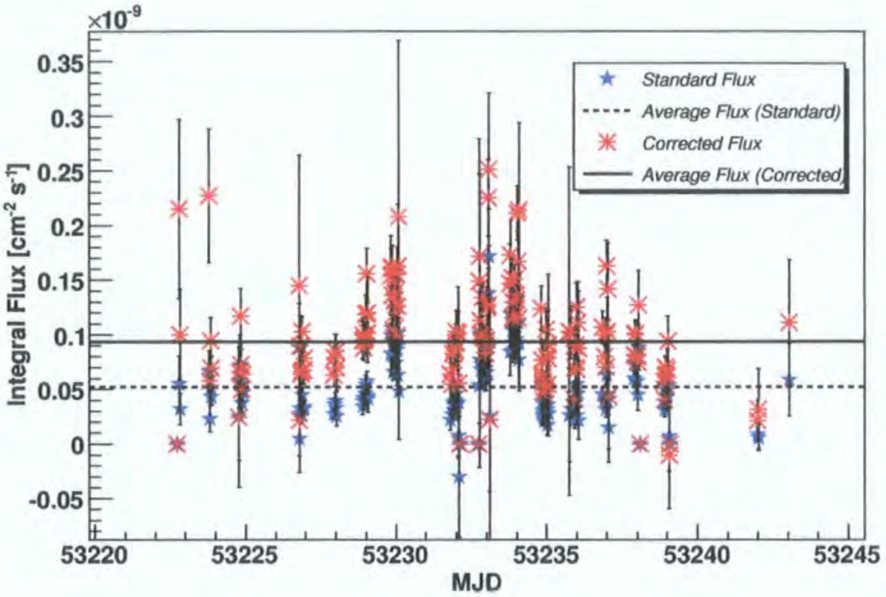

Figure 4.31: Comparison of the P2004-08 light curve per run for the standard and corrected atmospheres for PKS 2155-304. The solid line represents the average corrected flux and the dotted line represents the average standard flux. The average corrected flux is greater by 80%.

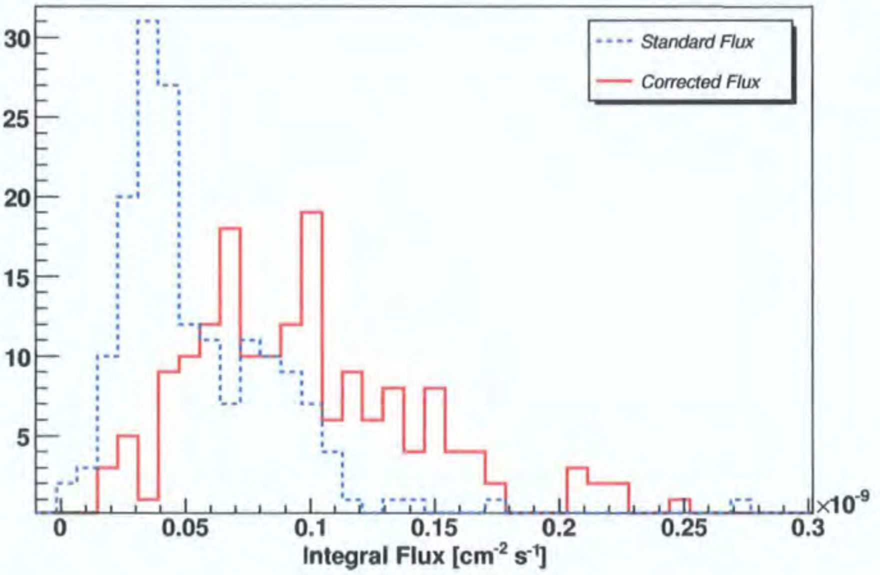

Figure 4.32: Histogram of integrated gamma-ray flux for the standard (dotted line) and corrected (solid line) analysis for PKS 2155-304 with all data runs.

4.6 H 2356-309

H 2356-309 is an extreme BL Lac with a redshift of $z = 0.165$ that was first detected by its host elliptical galaxy in the optical band [130] and was detected in X-rays with the satellite experiment Uhuru [65]. H 2356-309 was selected for the catalogue of good BL Lac VHE gamma-ray emitter candidates [48], and was first detected in VHE gamma rays in 2004 by H.E.S.S [14].

Since its discovery in VHE gamma rays in 2004, more data have been taken in 2005 and 2006. It can be seen in Figure 4.33 that there are high aerosol concentrations present in 2004 and 2005, and moderate levels in 2006. 390 runs were taken from 2004 to 2006. After run selection, 165 good ceilometer and observation runs were analysed (78 in 2004, 50 in 2005, and 37 in 2006).

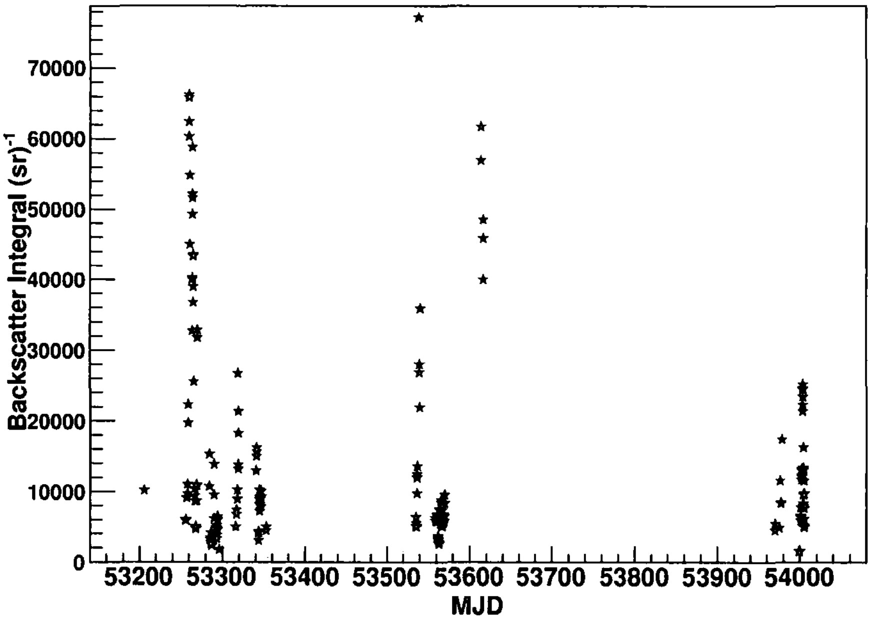

Figure 4.33: Backscatter integral for 2004, 2005, and 2006 for H2356-309. The greatest levels of aerosols are found in 2004 and 2005 with relatively modest levels in 2006.

4.6.1 Chosen Atmospheres

In the same way as PKS 2155-304, 4 atmospheres were chosen based on constant corrected trigger rate groups. The plot of corrected trigger rate versus zenith angle (Figure 4.34) shows that active atmospheric calibration may be applied to this data. As stated before, this technique is especially useful when trigger rates do not meet the trigger rate criteria

Table 4.10: Average corrected trigger rate (TR) and corresponding wind speed (WS) for each atmosphere used to analyse of H 2356-309 data. The run number and corresponding backscatter are also listed to show the average backscatter integral value for each subset of runs.

WS (ms^{-1})	Corrected TR (Hz)	Run	BS_{Int} (sr^{-1})
10.0	375	22896	4165
16.0	330	23237	7361
19.0	259	34511	17421
22.5	170	22504	52168

for run selection, and so rejected runs could be recovered and analysed. Table 4.10 shows the average cosmic ray trigger rates for each population with the associated wind speed.

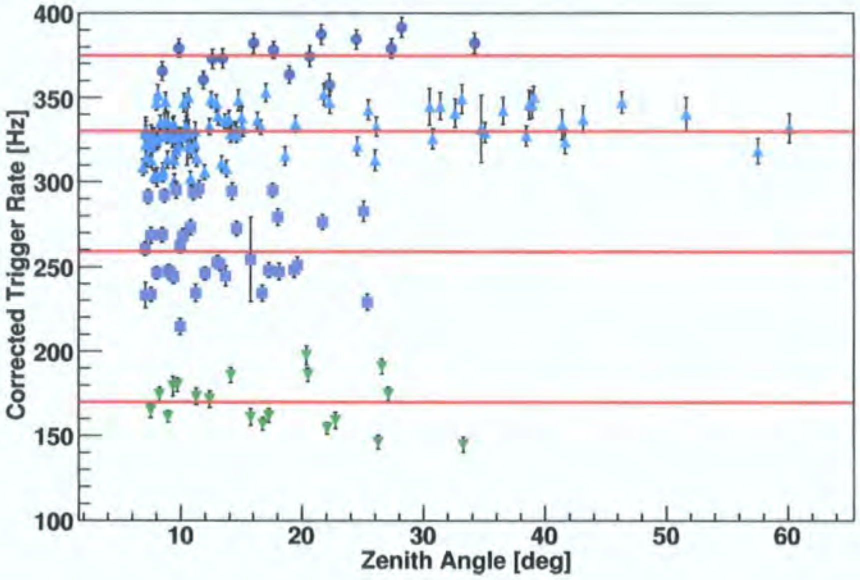

Figure 4.34: Corrected trigger rate versus zenith angle showing 4 different atmospheric classes (marked by the red solid lines). The circles are grouped in the clearest 10 ms^{-1} atmosphere, the triangles are grouped in 16 ms^{-1}, the squares are grouped in 19 ms^{-1}, and the upsidedown triangles are grouped in the dustiest 22.5 ms^{-1} atmosphere.

To show how backscatter increases with atmosphere, typical backscatter profiles representing each simulated atmosphere are shown in Figure 4.36. The run numbers and backscatter integral values are shown in Table 4.10. There were 15 runs (9%) classified in 10.0 ms^{-1}, 94 (57%) classified in 16.0 ms^{-1}, 37 (22%) classified in 19.0 ms^{-1}, and 19 (12%) classified in 22.5 ms^{-1}. Figure 4.35 shows how each atmosphere is distributed each year, which will be referred to in the next section. Table C.4 in Appendix C lists the runs analysed and which atmosphere they were classified under.

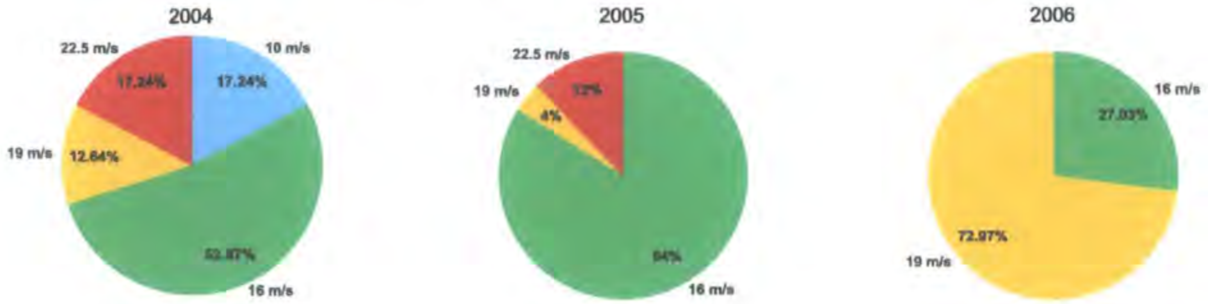

(a) (b) (c)

Figure 4.35: Pie charts showing the percentage of runs in each atmosphere (classified by wind speed) for (a) 2004, (b) 2005, and (c) 2006. The total number of runs in each year are 78, 50, and 37, respectively.

4.6.2 Results

Table 4.11 compares the gamma-ray analysis results using the standard atmosphere and corrected atmosphere. The spectral index differs for each year, but the time averaged corrected spectral index for all data remains unchanged. The integrated flux above 200 GeV is consistently higher in the corrected spectrum, but the same is not true above 1 TeV (for 2004 and 2005) due to the harder spectrum derived from the non-corrected data. Figure 4.37 shows the spectrum for 2004, 2005, and 2006 individually while Figure 4.38 shows the combined spectrum from all 3 years.

The distribution of dusty runs from 2004 to 2006 can be seen from Figure 4.35. The corresponding light curve for each year is shown in Figure 4.40. The average corrected flux for all years is $(3.56 \pm 4.91) \times 10^{-12}$ cm^{-2} s^{-1} while the uncorrected flux is $(2.56 \pm 3.73) \times 10^{-12}$ cm^{-2} s^{-1}. The average ΔI for all years is 25% and is illustrated in the flux histogram with all data in Figure 4.39.

In the H 2356-309 dataset, 49 out of 165, or 30%, of the runs returned lower fluxes with the corrected lookup tables. Table 4.12 shows the atmospheres separated by their atmospheric class to see if the fraction of $\Delta\mathrm{I} < 0$ shows bias towards a specific atmosphere underestimating a dusty atmosphere. There is nothing striking about this distribution as all atmospheres have $\sim 30 - 40\%$ of their runs returning $\Delta\mathrm{I} < 0$. Table 4.13 shows the distribution of $\Delta\mathrm{I} < 0$ per year to see if a bias exists there. Again, no correlation was found. Since H 2356-309 is such a low flux source, many runs are compatible with zero flux. For this reason the correction does not work as well as with PKS 2155-304. Even

Table 4.11: Comparison of gamma-ray data using standard (Std) and corrected (Corr) atmospheres. Spectral indices vary, but are constant within errors (except in 2005). The time average corrected spectral index remains unchanged. The corrected integral flux above 200 GeV increases for all years, but is not always the case for the integrated flux above 1 TeV due to larger corrected spectral indices.

Atmosphere	Significance	Spectral Index $\pm 0.1_{sys}$	I(> 0.20 TeV) $[10^{-12}$ cm^{-2} s$^{-1}]$	I(> 1 TeV) $[10^{-14}$ cm^{-2} s$^{-1}]$	ΔI
Std (2004)	7.5 σ	3.3±0.2	3.1±0.8	7.6±1.5	29%
Corr (2004)	8.1 σ	3.9±0.1	4.0±1.0	3.9±0.7	
Std (2005)	4.5 σ	2.4±0.2	2.1±0.5	23.1±5.2	34%
Corr (2005)	4.8 σ	3.2±0.1	3.2±0.7	9.9±1.8	
Std (2006)	4.3 σ	4.0±0.4	2.2±0.9	1.7±0.8	18%
Corr (2006)	3.8 σ	3.6±0.4	2.6±1.6	4.3±1.8	
Std (All)	9.7 σ	3.2±0.1	2.8±0.6	8.3±1.3	25%
Corr (All)	10.2 σ	3.2±0.1	3.5±0.8	10.6±1.8	

Table 4.12: The fraction of runs in each atmospheric class returning lower corrected fluxes. No correlation with atmosphere is seen.

Wind Speed (ms^{-1})	Fraction with $\Delta I < 0$
10.0	6/15 = 40%
16.0	28/94 = 30%
19.0	16/37 = 43%
22.5	6/19 = 32%

though it can be seen from the above figures and results that there is an overall increase in flux as a result of the correction, average flux errors are larger than the values themselves and corrected and uncorrected values are essentially the same.

Data from 2004 were previously published by H.E.S.S. and analysed by two independent methods (Hillas moment and 3D model analysis) yielding consistent results. The 3D model analysis resulted in a 11.6σ signal corresponding to an observed integral flux above 200 GeV of $I(>200\text{GeV}) = (4.1 \pm 1.4) \times 10^{-12}$ cm^{-2} s^{-1} with a spectral index of 3.09 ± 0.24 [14]. The flux is well in agreement with the 2004 results presented here, but the spectral index derived in this thesis is steeper than published results.

Table 4.13: The fraction of runs per year returning lower corrected fluxes. No correlation with year is seen.

Year	Fraction with $\Delta I < 0$
2004	$16/78 = 21\%$
2005	$20/50 = 40\%$
2006	$13/37 = 35\%$

4.6.3 Comparison with PKS 2155-304

The flux detected from H 2356-309 is about ~10 times lower than PKS 2155-304. Therefore, many of H 2356-309's observation runs returned negative fluxes consistent with zero, rendering a flux correction ineffective. An 'anti-correction' (meaning corrected fluxes were lower than uncorrected fluxes) to the flux is seen by approximately 30% of H 2356-309's runs. Only 5% of PKS 2155-304's runs suffered an anti-correction, which was essentially due to large systematic errors while observing at large zenith angles ($> 50°$).

The average corrected flux for PKS 2155-304 was 80% greater, compared to a corrected flux 25% greater than the uncorrected flux for H 2356-309. Also, PKS 2155-304 had a greater fraction of runs in the highest aerosol atmosphere with 41% of the total runs in the 22.5 ms^{-1} atmospheric class compared to only 12% for H 2356-309. Any further conclusions about active atmospheric calibration between different kinds of sources cannot be drawn at the moment due to the limited number of sources analysed by this method. The next section will discuss the potential for other sources to be corrected for.

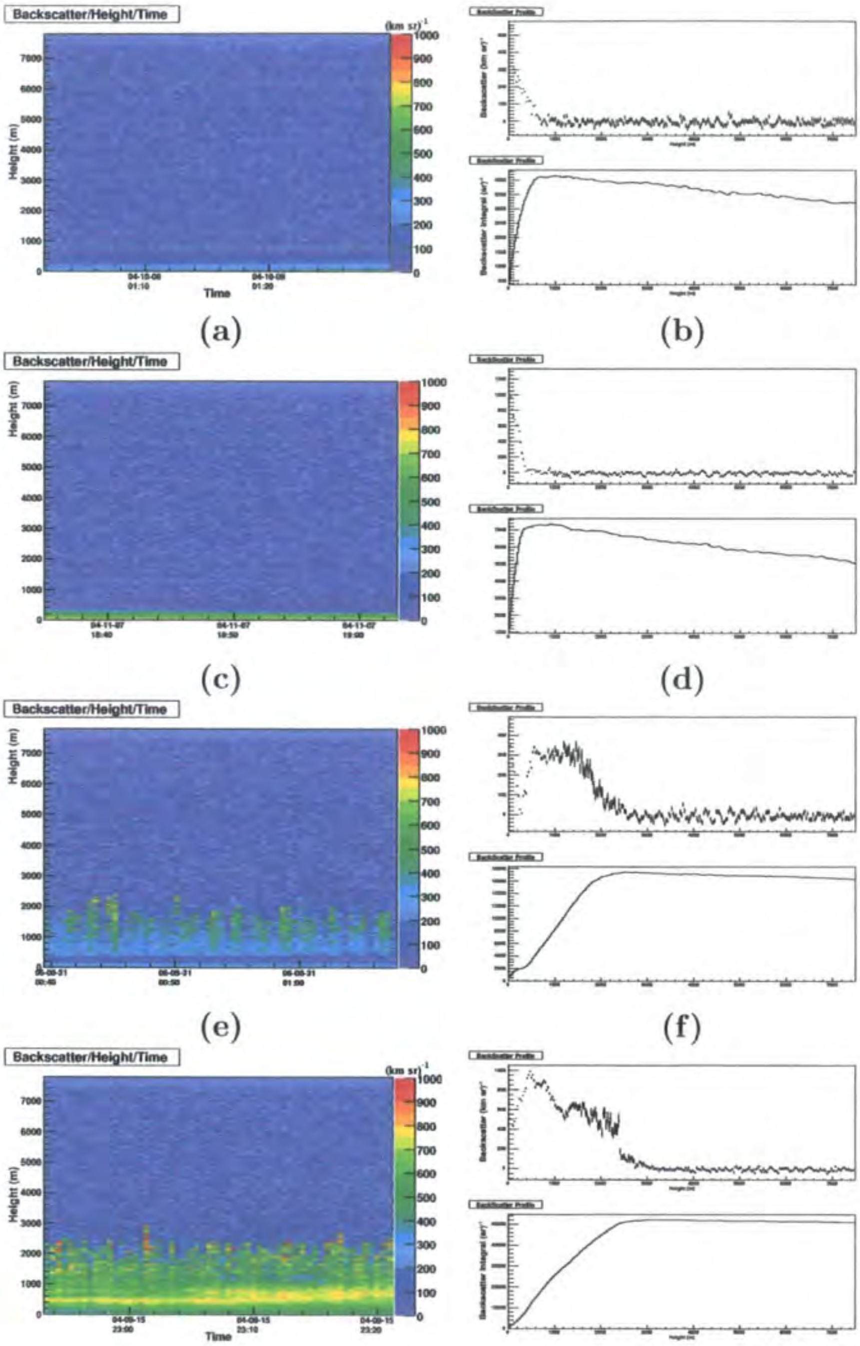

(a) (b)

(c) (d)

(e) (f)

(g) (h)

Figure 4.36: The backscatter profiles for a representative run from each atmosphere (see Table 4.10 for run numbers and backscatter integral values). The left figures show backscatter over time, and the right figures show backscatter averaged over the run (top) and the integrated backscatter (bottom) for (a)(b) 10.0 ms^{-1}, (c)(d) 16.0 ms^{-1}, (e)(f) 19.0 ms^{-1}, and (g)(h)22.5 ms^{-1}. One can clearly see the aerosol layer growing from 10.0 ms^{-1} to 22.5 ms^{-1}.

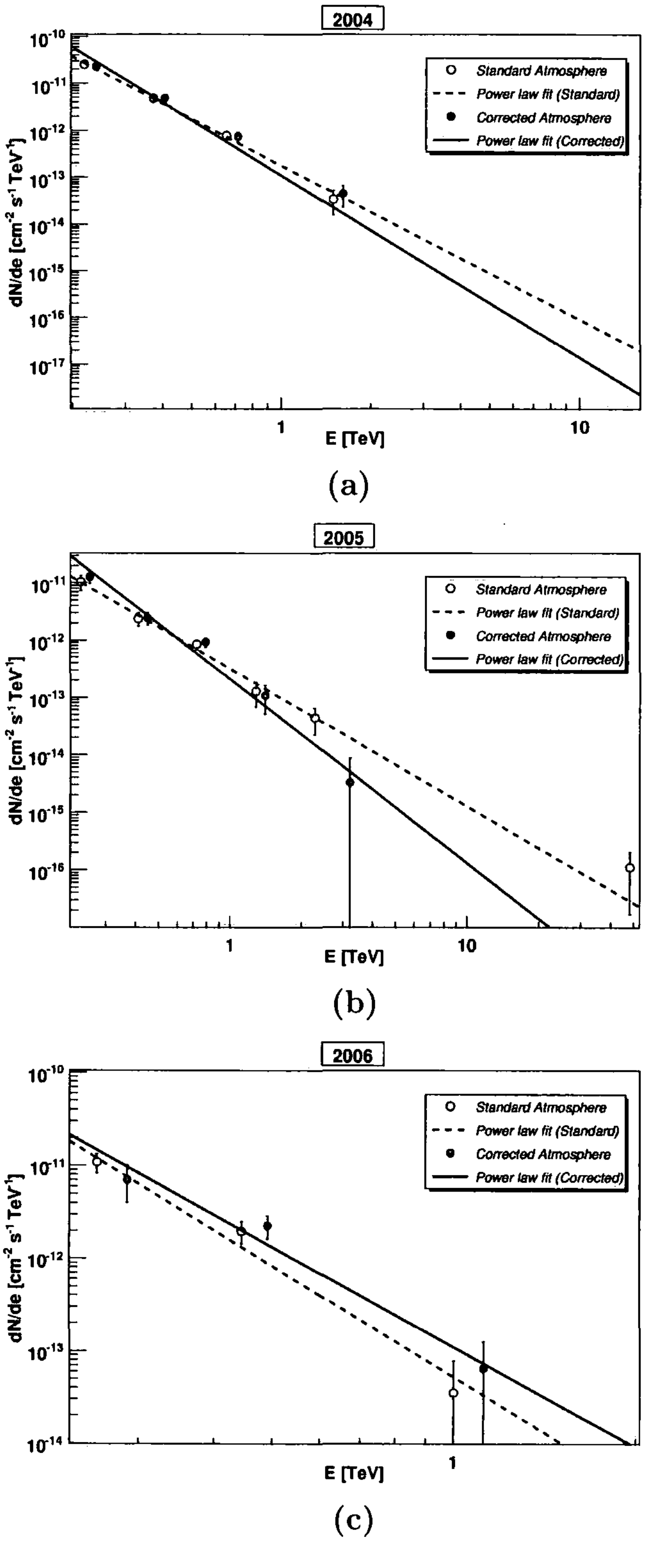

Figure 4.37: Spectrum of H 2356-309 in (a) 2004, (b) 2005, and (c) 2006. The steeper slopes derived from the corrected spectra in 2004 and 2005 are due to large uncertainties in the higher energy points.

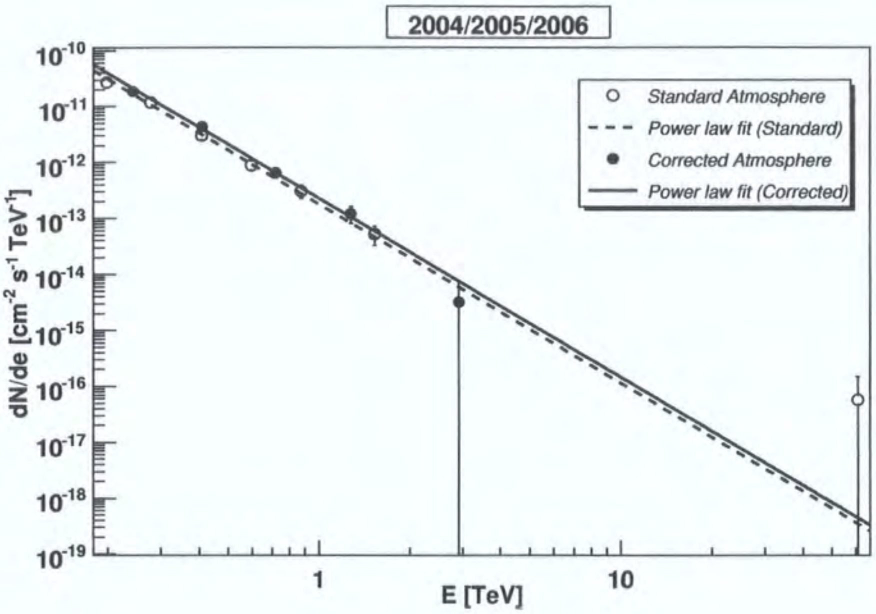

Figure 4.38: Time averaged spectrum of H 2356-309 from 2004 to 2006. The spectral slope remains unchanged and the flux is increased by a small amount (values found in Table 4.11

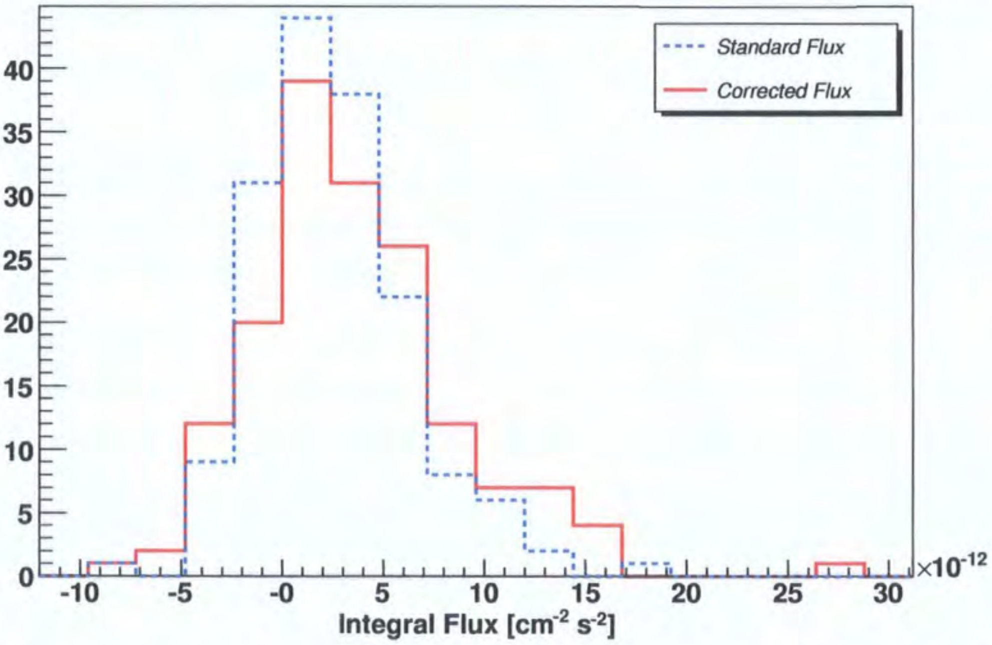

Figure 4.39: Histogram of integrated gamma-ray flux for the standard (dotted line) and corrected (solid line) atmosphere for H 2356-309 with all data runs.

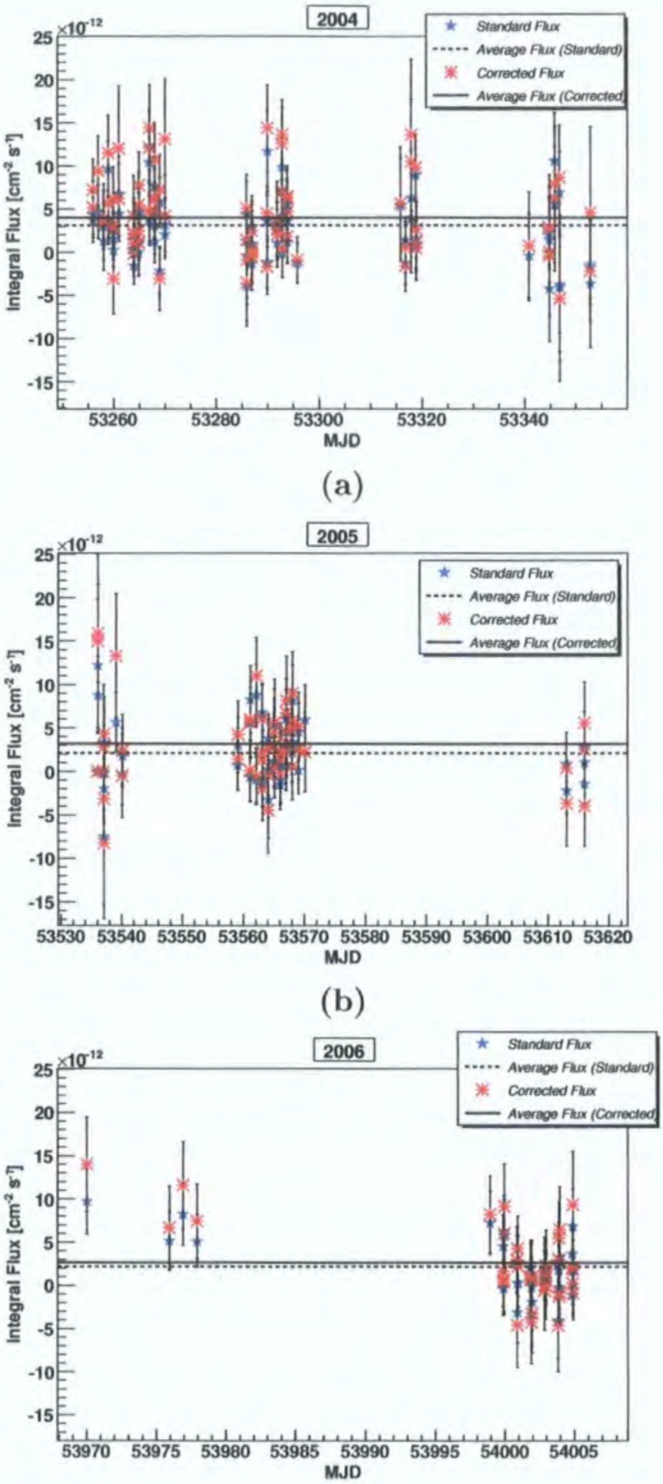

(a)

(b)

(c)

Figure 4.40: Comparison of the light curve per run for the standard and corrected atmospheres for H 2356-309 in (a) 2004, (b) 2005, and (c) 2006. The solid line represents the average corrected flux and the dotted line represents the average standard flux. The average corrected fluxes are greater by 29%, 34%, and 18%, respectively.

4.7 Correction Potential for Other Sources

I have made a list of all the observed blazars from 2004 to 2006 in order to determine their potential for atmospheric correction. I have also included two galactic sources, HESS J1745-290 and the Crab Nebula, due to the amount of data available and their strong fluxes. A list of these sources in ascending order of redshift is found in Table 4.14. Listed in this table is the source name, the total number of 4 telescope runs, the number of good runs (no clouds or uncorrupted ceilometer files), the type of source, the redshift, and if its a northern or southern source (as lookup tables must take into account the different magnetic field strengths from northern or southern pointing of the telescopes).

Table 4.14: Table of potential sources to use for atmospheric corrections. The superscripts next to the sources correspond to their figure label in Figure 4.41.

Source	Total Runs	Good Runs	Type	Redshift	Pointing
HESS J1745-290$^{(a)}$	283	31% (88)	galactic centre	0	S
Crab Nebula$^{(b)}$	81	54% (44)	plerion	0	N
Mkn 421$^{(c)}$	42	79% (33)	HBL	0.031	N
Mkn 501	9	0% (0)	HBL	0.034	N
PKS 2316-423	22	0% (0)	IBL	0.055	S
1ES 0548-322$^{(d)}$	52	58% (30)	HBL	0.069	S
PKS 2005-489$^{(e)}$	284	54% (153)	HBL	0.071	S
PKS 2155-304$^{(f)}$	428	60% (256)	HBL	0.116	S
1ES 0145+138	12	75% (9)	HBL	0.125	N
1ES 0229+200$^{(g)}$	117	62% (73)	HBL	0.139	N
1ES 0323+022$^{(h)}$	48	69% (33)	HBL	0.147	N
1ES 1440+122	5	60% (3)	HBL	0.162	N
H 2356-309$^{(i)}$	364	54% (195)	HBL	0.165	S
1ES 1218+30.4	4	75% (3)	HBL	0.182	N
1ES 1101-232$^{(j)}$	152	24% (37)	HBL	0.186	S
1ES 0347-121$^{(k)}$	63	72% (44)	HBL	0.188	S
1ES 2343-151$^{(m)}$	32	91% (29)	IBL	0.226	S
1ES 0414+009$^{(l)}$	46	65% (30)	HBL	0.287	N
1ES 1553+113$^{(n)}$	40	40% (16)	HBL	> 0.25	N

Figure 4.41 shows the backscatter integral values for all sources with more than 10 good runs. The superscripts in Table 4.14 correspond to their position in Figure 4.41. Sources containing a noticeable amount of runs with large aerosol concentrations ($BS_{Int} \gtrsim 30,000$) are: (a) HESS J1745-290, (e) PKS 2005-489, (f) PKS 2155-304, (g) 1ES 0229+200, (h)

1ES 0323+022, (i) H 2356-309, and (m) 1ES 2343-151. Unfortunately, the sources not corrected for previously have fluxes lower than or around that of H 2356-309 (< 2% of the Crab flux). It is therefore unlikely that active atmospheric calibration would improve current analyses of these sources. However, it was considered worthwhile to check with PKS 2005-489, which has a run distribution of aerosols similar to H 2356-309 with a similar flux, but time did not allow for this analysis.

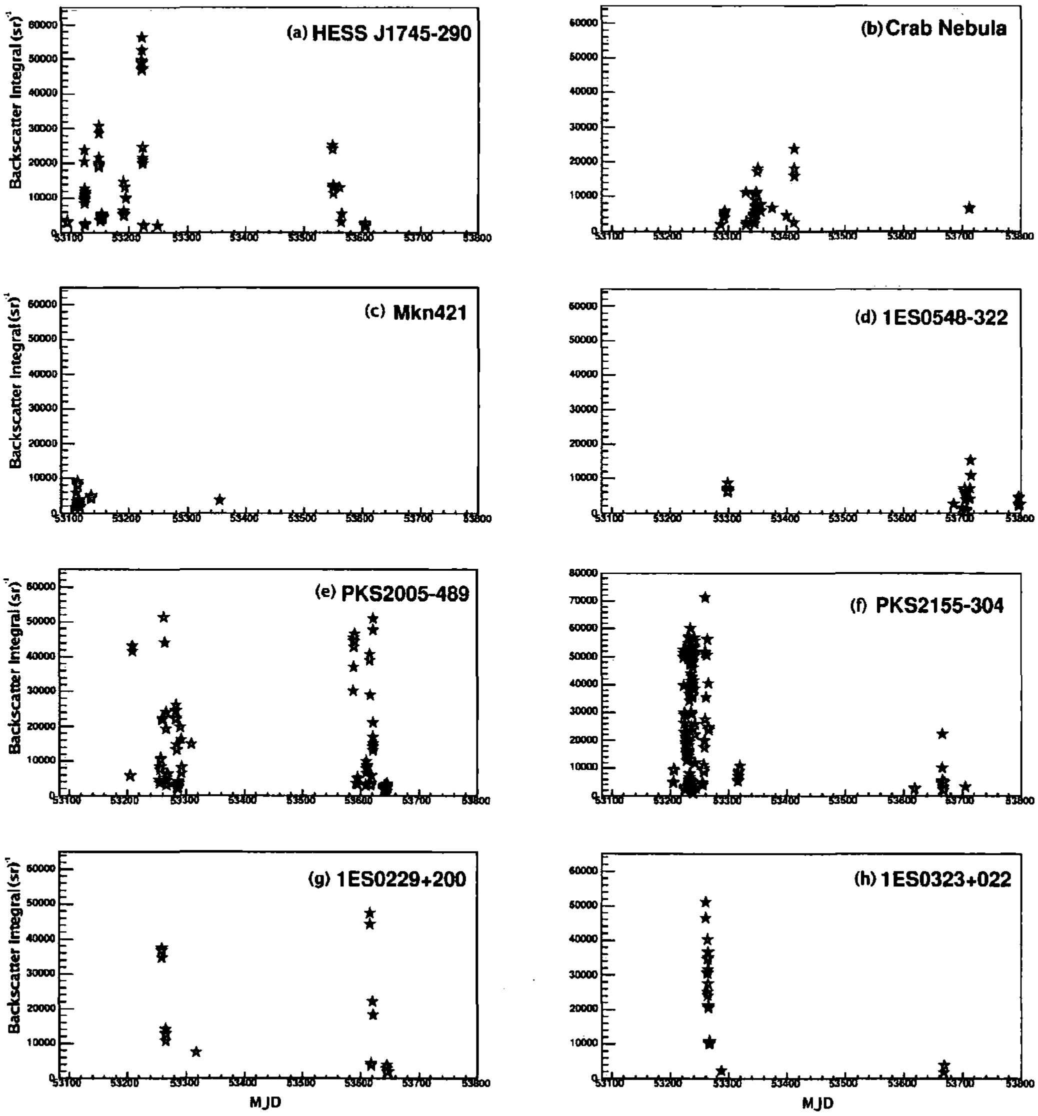

Figure 4.41: Backscatter integral for sources in Table 4.14.

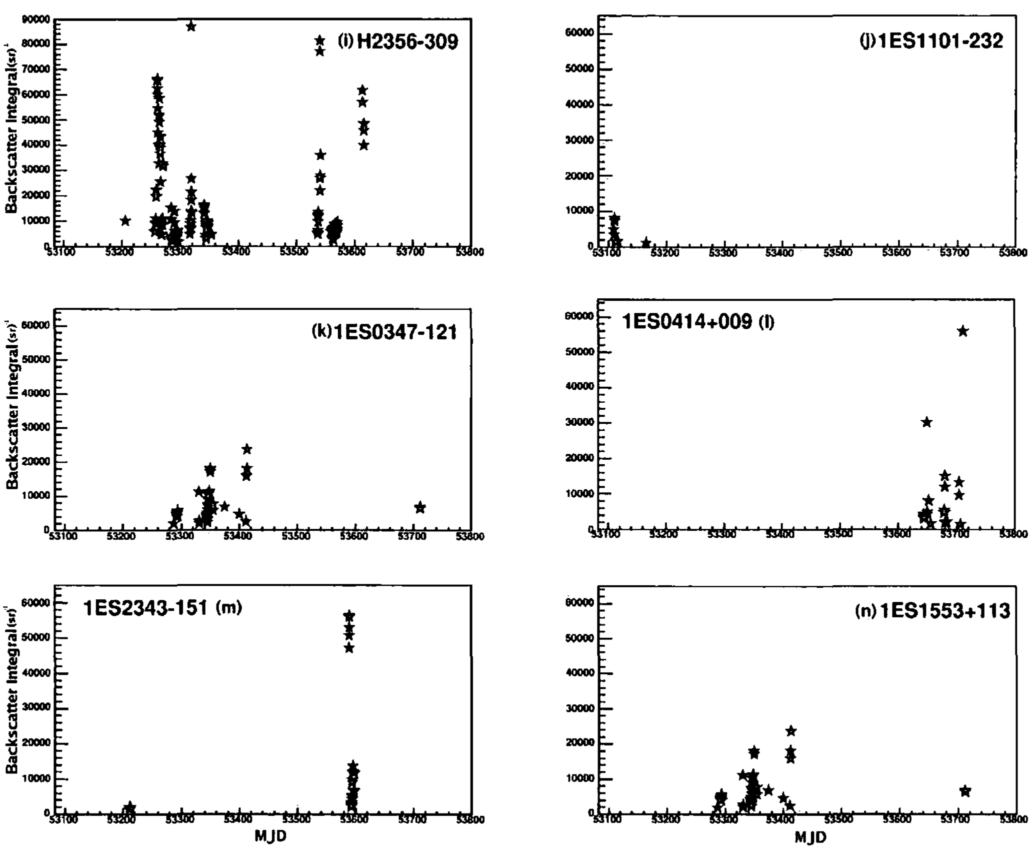

Figure 4.41: Backscatter integral for sources in Table 4.14.

4.8 Upper Limits of the EBL using TeV gamma rays from AGN

In Section 2.2.2, a discussion of how TeV emitting AGN have been used to place constraints on the EBL in optical and infrared energies was presented. Herein, a monoenergetic EBL model first proposed by Schroedter [129], will be used to obtain upper limit values to the EBL intensity corresponding to the maximum absorption from gamma rays. The optical depth to gamma rays will be measured directly from the measured gamma-ray flux and compared to an analytical function of optical depth derived from infrared observations [139]. These optical depths will be calculated for a high flux blazar PKS 2155-304 and a lower flux blazar H 2356-309, both using the corrected fluxes from the active atmospheric calibration method outlined in Section 4.4 and implemented in Sections 4.5 and 4.6.

4.8.1 Monoenergetic EBL Model

The monoenergetic EBL model proposed by Schroedter [129] was developed to derive upper limits on the EBL and does not depend on an assumed EBL spectral shape like other methods [12, 138, 53]. The upper limits to the EBL intensity are calculated at single energy points where the VHE spectrum has been measured. This has an advantage over other methods since the EBL spectrum is uncertain.

A monoenergetic EBL can be thought of as isotropically distributed photons with a single energy. When the EBL is assumed to be monochromatic, the contribution of other wavelengths to the absorption of gamma rays is ignored. The EBL density at that single wavelength will then have to be larger to reproduce the measured optical depth than if other wavelengths were allowed to contribute to the absorption.

Consider a single VHE gamma ray of energy E_γ coming from a distant extragalactic source. If the gamma ray collides with another particle, it will not propagate in a straight line and is lost to the observer. Pair production is the most likely type of inelastic collision in extragalactic space as the photon density is much higher than the matter density. The absorption of VHE gamma rays is described by $\gamma_{\mathrm{TeV}} + \gamma_{\mathrm{IR}} \rightarrow e^+ + e^-$.

The cross section for pair production from the annihilation of two photons is [74, 58],

$$\sigma_{\gamma\gamma}(E_\gamma, \epsilon, \mu) = \frac{3\sigma_T}{16}(1-\beta^2) \times \left[2\beta(\beta^2-2) + (3-\beta^4)\ln\left(\frac{1+\beta}{1-\beta}\right)\right] \qquad (4.6)$$

where $\sigma_T = 6.65 \times 10^{-25}\text{cm}^{-2}$ is the Thomson cross section with $\beta = \sqrt{1 - (\epsilon_{th}/\epsilon)}$. From conservation of energy, the threshold energy for electron-positron pair production to take place is,

$$\epsilon_{th}(E_\gamma, \mu) = \frac{2(m_e c^2)^2}{E_\gamma(1-\mu)} \tag{4.7}$$

where $\mu \equiv \cos\theta$ and θ is the angle between the incident photons. The maximum cross section occurs at 1.70×10^{-25} cm^{-2} with $\beta = 0.70$ corresponding to $\epsilon E_\gamma \approx 4(m_e c^2)^2 \approx 1\ \text{MeV}^2$ or

$$\lambda_\epsilon(\mu\text{m}) \approx 1.24(\text{E}_\gamma/(1\ \text{TeV})). \tag{4.8}$$

For example, gamma rays with energies from 0.2 TeV to 10 TeV will most efficiently pair produce with optical/NIR photons with wavelengths ranging from 0.25 to 12.4 μm (or 5 to 0.1 eV). Though gamma rays are absorbed most efficiently when $E\epsilon \approx 1\text{MeV}^2$, there is significant absorption of gamma rays with energies from half to four times as much [129].

The optical depth traversed by a photon observed at energy E_γ emitted by a source at redshift z is given by [58],

$$\tau_\gamma(E_\gamma, z) = \int_0^z \frac{dl}{dz'}dz' \int_{-1}^{1} \frac{1-\mu}{2} d\mu \int_{\epsilon_{th}}^{\infty} n_\epsilon(\epsilon', z')\sigma_{\gamma\gamma}(E'_\gamma, \epsilon', z')d\epsilon' \tag{4.9}$$

where $n_\epsilon(\epsilon', z')$ is the number density of EBL photons and $dl/dz = c/H_0$ for small redshifts ($z \ll 1$). In a monoenergetic EBL model, it is assumed that TeV gamma rays only interact with the EBL photon corresponding to the maximum cross section for pair production. This means that the cross section and number density only contribute to the optical depth when the energies correspond to the peak cross section for interaction. This reduces τ to,

$$\tau = \frac{czn\sigma_{\gamma\gamma}}{H_0} \tag{4.10}$$

and results in an upper limit for the EBL density given by,

$$n = \frac{\tau H_0}{cz\sigma_{\gamma\gamma}} \tag{4.11}$$

where $\sigma_{\gamma\gamma} = 1.7 \times 10^{-29}$ m^2 corresponds to the maximum value of cross section for photon-photon pair production and the Hubble constant $H_0 = 71$ km s^{-1} Mpc^{-1} is used [135]. The upper limit for the EBL intensity at energy ϵ is therefore,

$$\nu I_\nu(\epsilon) = \frac{cn\epsilon}{4\pi}(1.6 \times 10^{-10}) = \frac{\epsilon\tau H_0}{4\pi z\sigma_{\gamma\gamma}}(1.6 \times 10^{-10}) \tag{4.12}$$

in units of nW m^{-2} sr^{-1} where the factor 1.6×10^{-10} is due to the conversion from Joules to eV.

The optical depth is then measured by,

$$\tau = \ln(F_{\hat{e}}/F_m) + \tau_0 \tag{4.13}$$

where F_m is the measured flux, $F_{\hat{e}}$ is the normalised emitted flux, and τ_0 is the optical depth calculated from the lowest gamma-ray energy measured, E_0 ($\sim$ 0.2 TeV). This optical depth will now be referred to as the Sch05 optical depth and is discussed next.

Calculation of Normalised Emitted Flux

One way to express optical depth is given in terms of,

$$\tau = \ln(F_e/F_m), \tag{4.14}$$

the natural log of the emitted flux divided by the measured flux. In AGN, the emitted TeV flux is not well known due to the uncertainties in AGN emission models and must be deduced by other means. We get around knowing the actual emitted flux using the following argument. In the Schroedter model [129], the emitted flux (F_e) is normalised to the measured flux (F_m) value at 0.2 TeV. If the source is not measured at 0.2 TeV, it is extrapolated from higher energies. The first source of error comes from the fact that the extrapolated energy at 0.2 TeV is likely to be overestimated from the actual value due to the steeper slope of the measured spectrum [129]. We get around this by using the first energy point as the reference value E_0, which is often close to 0.2 TeV. By this method, the normalised emitted flux, $F_{\hat{e}}$, by definition, contains the absorption present at E_0.

To restate in terms of the optical depth, the small amount of absorption at E_0 is given by τ_0. The true emitted flux at E_0 is then given by $F_e(E_0) = F_0 e^{\tau_0}$ where $F_0 \equiv F_m(E_0) = F_{\hat{e}}(E_0)$, while the normalised emitted flux is related to the true emitted flux by $F_e = F_{\hat{e}}/e^{\tau_0}$. The optical depth at any energy greater than E_0 can then be rewritten as $\tau = \ln(F_{\hat{e}}/F_m) + \tau_0$ (equation 4.13).

The normalised emitted flux can also be written as $F_{\hat{e}} = N_{\hat{e}} E^{-\Gamma_e}$ where $N_{\hat{e}} = F_0/E^{\Gamma_e}$ is a normalisation constant and Γ_e is the spectral index of the emitted radiation. The normalised emitted flux can then be rewritten as,

$$F_{\hat{e}} = F_0(E/E_0)^{-\Gamma_e}. \tag{4.15}$$

This now gives an equation that contains only one unknown, the emitted spectral index, which is either calculated from equation 4.22 (to be discussed next) or assigned a realistic lower limit that is often taken to be 1.5 [110]. For illustrative purposes, Figure 4.42 shows the relationship between the measured flux, the emitted flux, and the normalised flux for $\Gamma_e = 1.8$ and $\tau_0 = 0.18$.

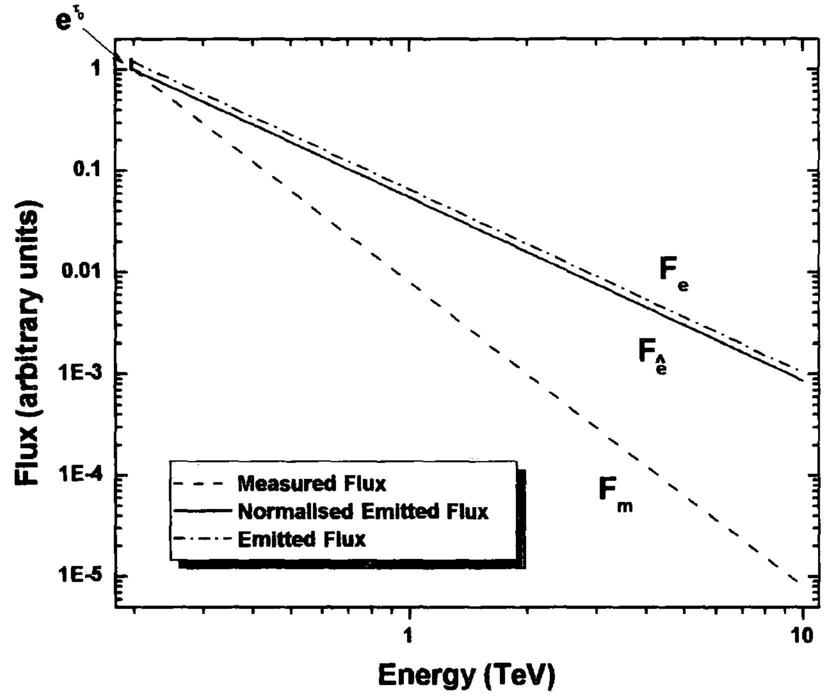

Figure 4.42: For illustrative purposes, this figure shows the relationship between the measured flux, the emitted flux, and normalised flux for $\Gamma_e = 1.8$ and $\tau_0 = 0.18$, where e^{τ_0} is the small amount of absorption calculated at E_0.

4.8.2 Analytic Optical Depth

An analytic function of optical depth, dependent on redshift and gamma-ray energy, was derived empirically from infrared observations by [139]. This was done using recent Spitzer observations along with other data on galaxy luminosity functions and redshift evolution in the framework of a backward evolution[12]. model of galaxy formation. The intergalactic background photon density was calculated and a simple analytic form of the optical depth was constructed. For gamma-ray energies from 4 GeV to 100 TeV and from a redshift of $z \sim 0$ to 5 [139], the opacity of the Universe is approximated by the analytic form,

$$\log \tau = Ax^4 + Bx^3 + Cx^2 + Dx + E. \tag{4.16}$$

where $x \equiv \log[E_\gamma/(1\ \text{eV})]$ and A, B, C, D, and E are constants given for different redshifts and found in [140].

Stecker and Scully (2006) [141] fit the above optical depth over the range of $0.2 < E < 2$ TeV and $0.05 < z < 0.4$. These limits are well suited to the VHE gamma-ray observational range. The absorption due to the optical depth is primarily from the optical and near infrared part of the EBL and is given by,

$$\tau(E_\gamma, z) = (A + Bz) + (C + Dz)\ln[(E_\gamma/(1\ \text{TeV})] \tag{4.17}$$

where A, B, C, and D are different constants for two different galaxy luminosity evolution models, fast evolution (FE) and baseline (B), given in Table 4.15. The optical depth calculated from either model will be referred to as the SS06 optical depth. The difference between the two models is that the fast evolution model evolves more quickly at smaller redshifts. The FE model is favoured by Spitzer deep number counts at 70 and 160 μm. An increase in the upper limit on the NIR EBL from simulations in [136] is also favoured by the FE model. On the other hand, GALEX observations indicate that the evolution of UV radiation for $0 < z < 1$ may be slower and more consistent with the B model. Spitzer source counts at 24 μm also favour the B model, as well as the upper limits derived from H.E.S.S. observations for 1.5 μm [12, 136].

Table 4.15: Coefficients for the SS06 optical depth function, equation 4.17, for forward evolution (FE) and baseline (B) galaxy luminosity evolution models.

Evolution Model	A	B	C	D
FE	-0.475	21.6	-0.0972	10.6
B	-0.346	16.3	-0.0675	7.99

---

[12] The backward evolution model is a theoretical model of galaxy formation and evolution that extrapolates spectral properties of local galaxies to high redshift [91].

Emitted Spectral Index

The calculation of the SS06 optical depth above can be used to derive the emitted (intrinsic) spectral index based on the measured flux and index of the source. The measured flux F_m is given by,

$$F_m = F_e e^{-\tau} \tag{4.18}$$

and

$$F_m = N_m E_\gamma^{-\Gamma_m}. \tag{4.19}$$

The emitted flux is also given by,

$$F_e = N_e E_\gamma^{-\Gamma_e} \tag{4.20}$$

where Γ_e and Γ_m are the emitted and observed spectral indices, respectively and N_e and N_m are the normalisation constants. Plugging in the optical depth equation 4.17 and equation 4.20 into equation 4.18 results in,

$$F_m = F_e e^{-((A+Bz)+(C+Dz)\ln[E_\gamma])} = N_e e^{-(A+Bz)} E_\gamma^{-(\Gamma_e+C+Dz)}. \tag{4.21}$$

Equating equation 4.21 with equation 4.19 and combining energy terms results in, $\Gamma_e + (C+Dz) = \Gamma_m$, where

$$\Gamma_e = \Gamma_m - \Delta\Gamma \tag{4.22}$$

and the change in spectral index, $\Delta\Gamma = C + Dz$, is a linear function of redshift.

The optical depth and emitted spectral indices were calculated for PKS 2155-304 and H 2356-309 for both models, shown in Table 4.16. The values calculated from Stecker (2007) [136] are as follows: for PKS 2155, $\Gamma_e(FE) = 2.2$, $\Gamma_e(B) = 2.4$, and for H 2356, $\Gamma_e(FE) = 1.5, \Gamma_e(B) = 1.9$. These values are consistent with those in Table 4.16 and can be considered trivial since similar measured indices were used. The optical depth values are larger compared to the optical depth at 0.20 TeV calculated from the Primack model $\tau_P(z = 0.10) = 0.105$ and $\tau_P(z = 0.150) = 0.168$ [122].

Table 4.16 also shows that the FE model displays greater spectral hardening (smaller Γ_e) due to the larger optical depth calculated, causing greater attenuation. Therefore, a

---

[13] 2004 corrected spectral index

[14] Combined corrected spectral index for all data from 2004-2006

Table 4.16: Intrinsic spectral indices and optical depths calculated for a 0.20 TeV gamma ray using the forward evolution (FE) and baseline (B) galaxy luminosity evolution models.

Source	z	Γ_0	Γ_e(FE)	Γ_e(B)	$\tau(FE)$	$\tau(B)$
PKS 2155-304	0.117	3.47±0.2[13]	2.34±0.2	2.61±0.2	0.21±0.17	0.16±0.13
H 2356-309	0.165	3.41±0.15[14]	1.5±0.1	1.9±0.15	0.43±0.25	0.33±0.19

larger EBL density is expected from this model. The FE model will be used from now on because it is my aim to calculate upper limits to the EBL.

Figure 4.43 shows the measured spectral indices for 16 measured TeV blazars as of December 2007, taken from Table 2.1 in Chapter 2. It can be seen that there is a general trend of spectral steepening with a dip in spectral index around $z \sim 0.10 - 0.15$. Figure 4.44 shows the emitted spectral indices calculated from equation 4.22 with the FE model. There is spectral steepening till around $z \sim 0.07$ followed by noticeably harder spectra at higher redshifts ($z > 0.10$). Some values of the intrinsic spectral index are found to be lower than 1.5, which has claimed to be a realistic lower limit to the intrinsic spectral index following general arguments arising from the shock acceleration scenario of relativistic particles [110, 12]. However, [136] has been able to produce a range of gamma-ray spectra with indices less than 1.5 using numerical simulations accelerating particles at relativistic shocks of blazar jets, while [110] states the case of producing *extreme* indices of 2/3 with a monoenergetic spectrum of electrons with energies of a few GeV. It should also be noted that hadronic scenarios generally do not produce harder spectra than those with an index of 2 [110].

The isotropic luminosity for 10 TeV blazars has been calculated by [136] and a trend toward blazars having a flatter intrinsic TeV spectra and high luminosities at redshifts is seen. The sample indicates that harder spectra are also found to be more energetic. Due to selection effects, more luminous sources with harder spectra are more likely to be detected at greater distances because of diminution of flux with distance and EBL absorption. Although only 10 blazars were listed and selection effects are important, one may speculate as to whether there is a general trend in blazar activity in the form of high jet Doppler factors at higher redshifts. Figure 4.44, with 16 blazars plotted, further confirms the notion of harder spectra being detected at higher redshifts. The range of intrinsic spectral indices also shows that blazars are not identical and should be treated as such.

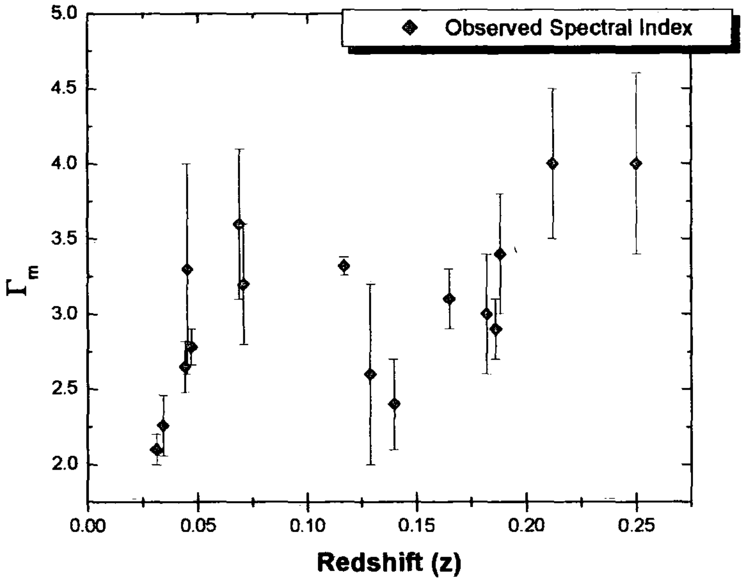

Figure 4.43: Measured spectral indices as a function of redshift for all spectral indices measured in TeV energies from Table 2.1. It can be seen that there is a general trend of spectral steepening with a dip in spectral index around $z \sim 0.10 - 0.15$.

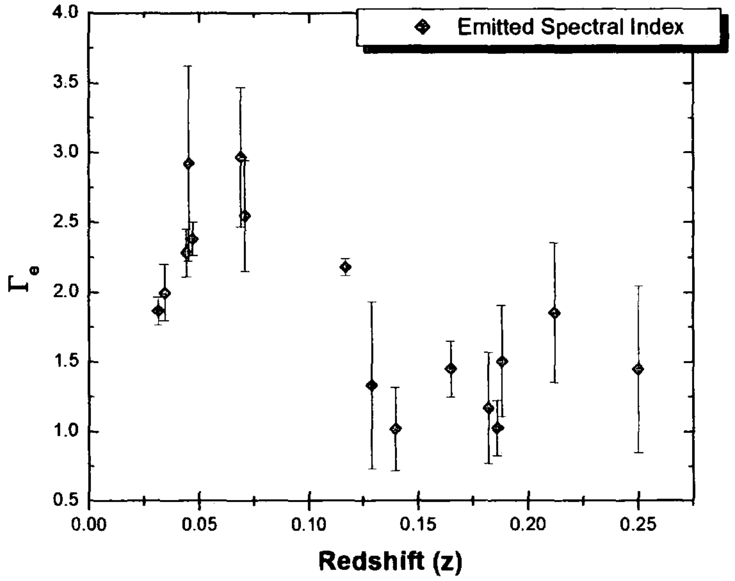

Figure 4.44: Emitted spectral indices calculated from equation 4.22 (FE model) as a function of redshift. There is spectral steepening till around $z \sim 0.07$ followed by noticeably harder spectra at higher redshifts ($z > 0.10$).

4.8.3 EBL Calculations

Upper limits to the EBL were calculated using the spectra of PKS 2155-304 ($z = 0.117$) and H 2356-309 ($z = 0.165$). My method differs from Schroedter's method in that I have used three different optical depths to calculate upper limits to the EBL, whereas Schroedter has only used equation 4.13. Schroedter has used a sample of 6 AGN whereas I have only used 2. Schroedter also assumed identical intrinsic spectral indices of $\Gamma_e = 1.8$ for all AGN, whereas I calculated the spectral index from equation 4.22.

My results are compared to the models and measurements listed in Table 4.17. These models are individually discussed in Section 2.2.2. Equations used in error analysis can be found in Appendix B. The same method was employed for both sources and is as follows.

Steps to measuring the EBL

- Determine initial parameters with E_0 taken from first gamma-ray energy data bin, $F_0 = F_m(E_0)$, and $\tau_0 = \tau(E_0)$ calculated from equation 4.17.
- Calculate emitted spectral index using $\Gamma_e = \Gamma_m - \Delta\Gamma$.
- Calculate EBL energy $\epsilon(\mathrm{eV}) = 1/\mathrm{E}_\gamma$ and wavelength $\lambda(\mu\mathrm{m}) = 1.24\mathrm{E}_\gamma$.
- Measure flux per energy bin, F_m.
- Calculate normalised flux $F_{\hat{e}}$ from equation 4.15.
- Calculate optical depth from equation 4.13 or equation 4.17, where equation 4.13 is dependent on the data τ_0, F_m, and $F_{\hat{e}}$, whereas equation 4.13 is not.
- Calculate corresponding EBL intensity for each optical depth using equation 4.12
- Repeat for each gamma-ray energy bin measured.

Figure 4.45 shows the Sch05 optical depth at $z = 0.117$. An emitted spectral index of $\Gamma_e = 2.33$ and $\tau_0 = 0.27$ is used from the forward evolution model. The Sch05 optical depth is compared to both SS06 models (at $z = 0.117$), and to P05 at redshifts $z = 0.10$ and $z = 0.15$. It can be seen that the SS06 optical depths agree well with the Sch05 optical depth and so will be used beyond its stated range of 2 TeV. Similar results are seen in Figure 4.47, showing the optical depth for $z = 0.165$, using an emitted spectral index of $\Gamma_e = 1.5$ and $\tau_0 = 0.75$, which is considerably larger than the results of the Primack model optical depth at $z = 0.150$ of $\tau_P = 0.17$.

The effect of each optical depth (Sch05, SS06, and P05 for comparison) on the monoenergetic EBL intensity is compared with direct observations and limits, along with EBL calculations from MR07, P05, and DK05. Figure 4.46 shows the EBL density at $z = 0.117$ while Figure 4.48 shows the EBL density at $z = 0.165$. The upper limits found in my analysis are ~2-5 times larger than the lower limits derived from source counts. My results also agree best with the upper limit constraints given by MR07, in the range of $\lambda \sim 0.4 - 1$ μm. This shows that such a simple and robust way of determining the EBL is comparable to that of other more complicated techniques. My results are also found to be about twice the value compared to the HESS06 analysis at $\sim 1 - 2$ μm (not plotted in the figures).

Table 4.18 shows the emitted spectral index, optical depth at E_0, and EBL intensity calculated from Sch05 and SS06 models at wavelengths of 1 and 16 μm for PKS 2155-304. It can be seen that using the FE model to calculate the emitted index results in the EBL intensity from the Sch05 optical depth lying between the intensities calculated from the SS06 models. The emitted spectral index using the baseline model results in the Sch05 optical depth lying below both models. Table 4.19 shows the same data for H 2356-309 with the EBL intensity at EBL wavelengths of ~1 and ~4 μm.

Table 4.17: Symbols for different EBL models used in the text with their respective references.

Symbol	Reference
Sch05	Schroedter (2005) [129]
SS06	Stecker and Scully (2006) [141]
MR07	Mazin and Raue (2007) [110]
HESS06	Aharonian, et al (2006) [12]
P05	Primack (2005) [122]
DK05	Dwek and Krennich (2005) [58]

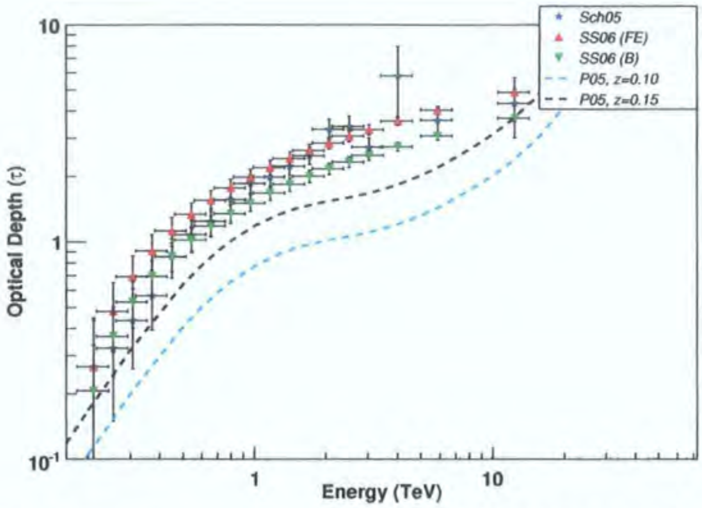

Figure 4.45: Optical depth to gamma-rays for PKS 2155-304 for Sch05 and SS06 optical depths compared with P05.

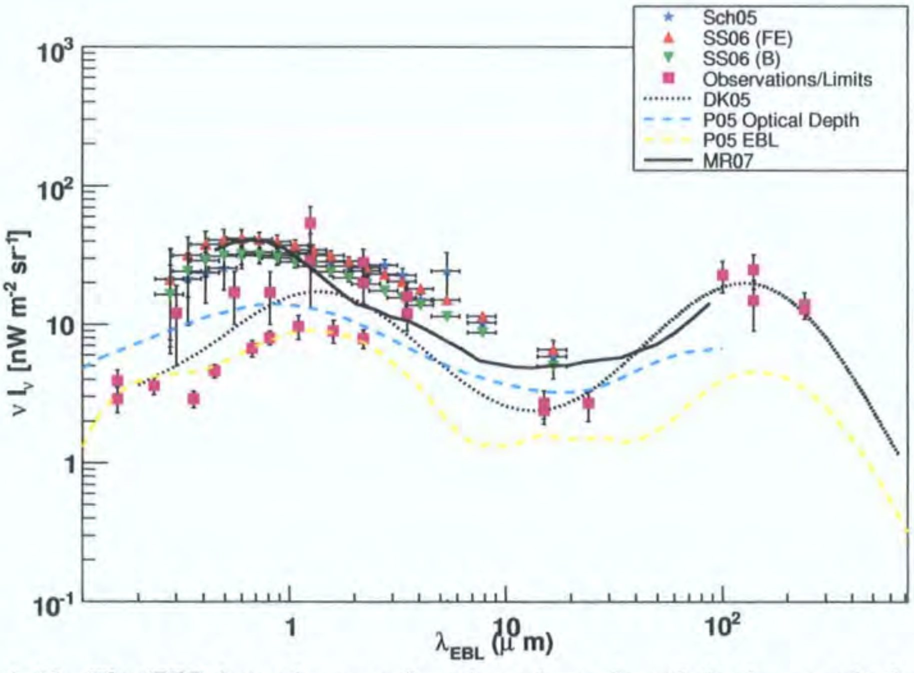

Figure 4.46: The EBL intensity as a function of wavelength is shown calculated by the monoenergetic model from PKS 2155-304 data (Sch05). An emitted spectral index of $\Gamma_e = 2.33$ and $\tau_0 = 0.27$ is calculated from the forward evolution model. The monoenergetic EBL intensity from the SS06 optical depth and the P05 optical depth are shown for comparison. Direct observations and limits are indicated by the squares and references for the data are given in [77]. The upper limits found in my analysis best agrees with the constraints given from MR07 in the range of $\lambda \sim 0.4 - 1$ μm.

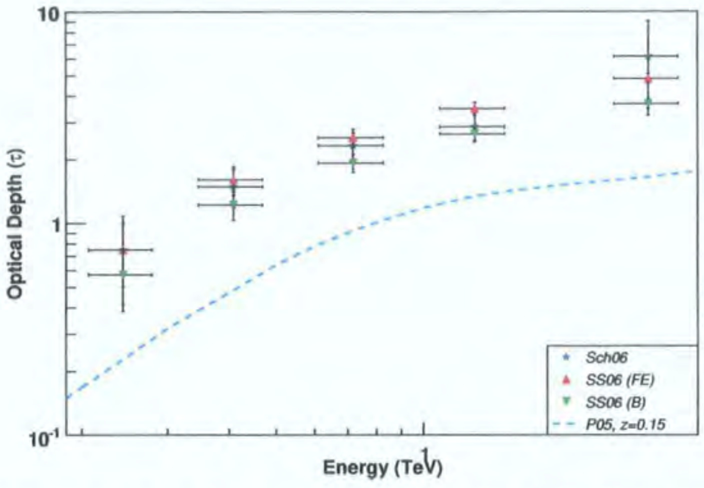

Figure 4.47: Optical depth to gamma-rays for H 2356-309 for Sch05 and SS06 optical depths compared with P05.

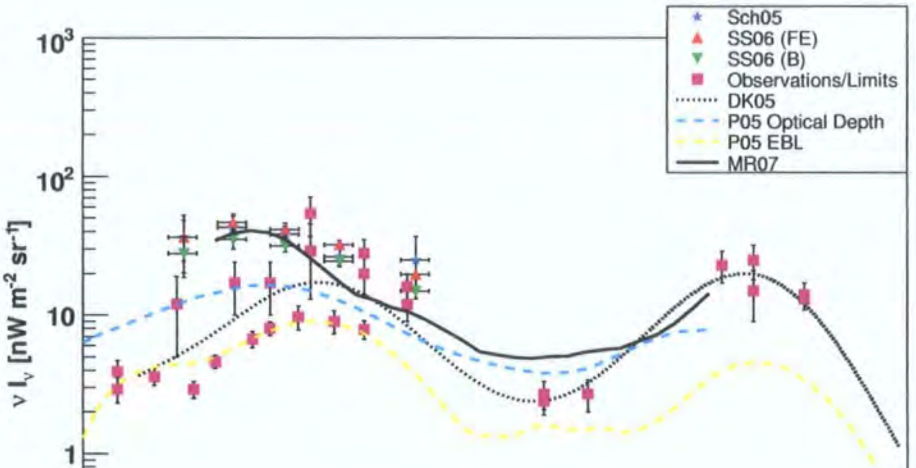

Figure 4.48: The EBL intensity as a function of wavelength is shown calculated by the monoenergetic model from H 2356-309 data (Sch05). An emitted spectral index of $\Gamma_e = 1.76$ and $\tau_0 = 0.75$ is calculated from the forward evolution model. The monoenergetic EBL intensity from the SS06 optical depth and the P05 optical depth are shown for comparison. Direct observations and limits are indicated by the squares and references for the data are given in [77]. The upper limits found in my analysis best agrees with the constraints given from MR07 in the range of $\lambda \sim 0.4 - 1$ μm.

Table 4.18: Upper limit to the EBL intensity for Sch05 and SS06 optical depths with $\Gamma_m = 3.47 \pm 0.2$, $z = 0.117$, $E_0 = 0.21$ TeV for PKS 2155-304.

	FE Model		Baseline Model	
Γ_e	2.34 ± 0.2		2.61 ± 0.02	
τ_0	0.27 ± 0.17		0.21 ± 0.13	
λ [μm]	1.06 ± 0.16	16.5 ± 2.5	1.06 ± 0.16	16.5 ± 2.5
$\nu I_{\nu Sch05}$	32.92 ± 3.78	5.87 ± 1.80	24.01 ± 3.00	4.29 ± 1.80
$\nu I_{\nu FE}$	37.25 ± 3.57	6.59 ± 0.23	37.25 ± 3.57	6.59 ± 0.23
$\nu I_{\nu B}$	28.35 ± 2.71	5.01 ± 0.17	28.35 ± 2.71	5.01 ± 0.17

Table 4.19: Upper limit to the EBL intensity for Sch05 and SS06 optical depths with $\Gamma_m = 3.2 \pm 0.1$, $z = 0.165$, $E_0 = 0.24$ TeV for H 2356-309.

	FE Model		Baseline Model	
Γ_e	1.5 ± 0.1		1.9 ± 0.1	
τ_0	0.75 ± 0.25		0.57 ± 0.19	
λ [μm]	0.96 ± 0.14	3.85 ± 0.58	0.96 ± 0.14	3.85 ± 0.58
$\nu I_{\nu Sch05}$	42.0 ± 5.7	27.14 ± 11.85	31.94 ± 5.07	22.37 ± 11.83
$\nu I_{\nu FE}$	41.62 ± 4.05	19.72 ± 1.01	41.62 ± 4.05	19.72 ± 1.01
$\nu I_{\nu B}$	31.59 ± 3.07	14.95 ± 0.76	31.59 ± 3.07	14.95 ± 0.76

4.9 General Conclusions

This chapter has covered a lot of ground from discussion the telescopes' trigger rate to the final calculation of upper limits to the EBL. Trigger rate zenith angle corrections were made for $\theta_z < 50°$ and time corrected from January 2004 to October 2007. Corrected trigger rate versus atmospheric variables were investigated, with backscatter having the biggest effect on the trigger rate. Gamma-ray fluxes for sources with a spectral index of ~ 2 were compared to the same atmospheric variables with a small effect. Differences in the gamma-ray and cosmic-ray spectrum may be a contributing factor in differing effects.

A new technique for the correction of atmospheric effects due to aerosols called the active atmospheric calibration was presented. This technique was applied to the HBL PKS 2155-304 as well as to the HBL H2345-309, which has a flux $\sim$ 10 times lower than PKS 2155-304. Active atmospheric calibration was shown to work well for PKS 2155-304, but not for H 2356-309. A suggestion to look at PKS 2005-489 was made in order to confirm this assertion.

Lastly, the analysis of PKS 2155-304 and H 2345-309 was applied to calculating the upper limits to the EBL using a monoenergetic model, which assumes that the attenuation of TeV gamma rays are due to one energy corresponding to the peak of the cross section for pair production. The results are similar to that of Mazin and Raue [110], which is the most extensive EBL study using AGN to date.

Chapter 5

The Future & Conclusions

5.1 Future Gamma-ray Experiments

5.1.1 H.E.S.S. Phase II

The current system and the topic of this thesis, H.E.S.S. Phase I, has shown to be an incredible success in the field of VHE gamma-ray astronomy. The aim of H.E.S.S. Phase II is to increase the sensitivity and to lower the threshold of the H.E.S.S. system to 20 GeV by adding a single large 28 m telescope in the middle of the current array. The mirror will have an area of 600 m^2 with a 2048 pixel camera providing a field of view of 3.17°. The new telescope will introduce faster electronics in order to lower the expected dead time due to the increased trigger rate of $\sim$3 kHz. H.E.S.S. II is currently under construction and is expected to be completed by late 2008 [85, 44].

The lower energy threshold of H.E.S.S. II is intended to fill the energy gap ($\sim$ 20 - 100 GeV) with space-based instruments, providing crucial information that will aid in discriminating between electron and hadronic acceleration scenarios, especially in SNRs. In addition, this energy range is expected to provide information about energy cutoffs in AGN and other objects such as pulsars [149].

Figure 5.1: Artist's conception of HESS Phase II with the addition of a large 28 m telescope in the centre of the current array, from [149].

5.1.2 CTA

The Cherenkov Telescope Array (CTA) is a proposed observatory for ground-based high energy gamma-ray astronomy [79]. Unlike previous imaging atmospheric Cherenkov telescopes (IACTs), CTA will be accessible to outside observers for 50% of the observing time. CTA will consist of an array of telescopes in the northern and southern hemisphere in order to cover the full sky. A variety of telescopes with different sizes in two locations arranged in different configurations will be the driving power of CTA. Small telescopes will be used to measure the highest energy gamma rays (~100 TeV) and HESS II size telescopes will be used to measure lower energy gamma rays (~ 10 GeV). A large number of telescopes will also serve to increase detection sensitivity by a factor of 10 and enhance angular resolution by a factor of 5 from present day IACTs. The simulated sensitivity of CTA compared to current generation IACTs is shown in Figure 5.2. The improved angular resolution will allow for a detailed morphological study of extended sources. A myraid of telescopes at each site will also give the arrays flexibilty to observe in different modes.

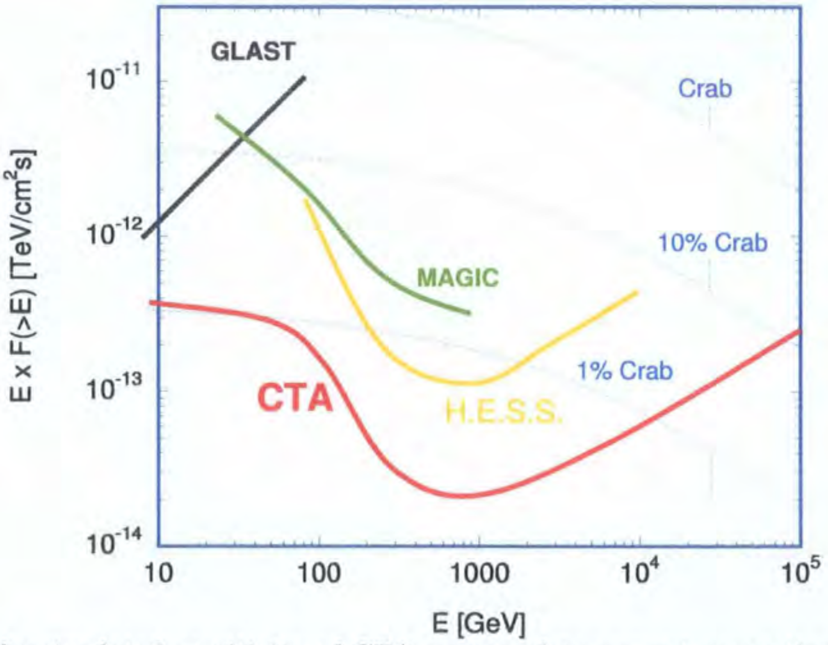

Figure 5.2: The simulated sensitivity of CTA compared to current generation IACTs, from [79].

The telescopes in the southern hemisphere will be optimised to observe galactic gamma rays with energies from 10 GeV to 100 TeV while the northern observatory will be optimised to observe gamma rays with energies 10 GeV to 1 TeV, predominately for extragalactic objects and lower energy galactic objects. CTA is expected to detect and observe about 1000 sources and should result in breakthroughs in several fields of modern astronomy such as the origin of cosmic rays, the environment of compact objects, the physics of pulsars and black holes, and possibly the long-standing question of the nature of dark matter. The design study of CTA is ongoing and should continue until the end of 2011 with construction aimed at beginning around 2012 [79].

5.1.3 GLAST

The Gamma-ray Large Area Space Telescope (GLAST) is a space-based high energy gamma-ray telescope that is set to launch in May 2008 (accompanying the other space-based gamma-ray telescope, AGILE). GLAST consists of 2 detectors, the Large Area Telescope (LAT) and the Gamma-ray Burst Monitor (GBM). The range of both instruments span from 8 keV to 300 GeV (with larger energies significantly less effective at being detected due to their low flux and small collection areas). LAT (20 MeV - 300 GeV) is expected to be 30 times more sensitive than any previous gamma-ray instrument flown in space. LAT is projected to detect thousands of new sources during its 5-year primary mission with a goal of running for 10 years. GBM (8 keV - 25 MeV) is expected to detect 200 bursts per year as well as solar flares and other transient events [112]. In addition, GLAST will fill the observation gap from 10 to 100 GeV, providing an overlap with H.E.S.S. Phase II and CTA.

Figure 5.3: An artist's impression of the GLAST satellite in space (from NASA website, http://glast.gsfc.nasa.gov/).

5.2 New LIDAR

Figure 5.4 shows that the transmission at 355 nm from the new LIDAR is correlated with the cosmic-ray trigger rate. This is an encouraging first result that allows us to use these transmissivity values to simulate additional atmospheres for dusty nights. This was done for a week with dusty nights in September 2007 during a LS 5039 multiwavelength observation campaign. Gamma-ray simulations are currently underway by the Durham Gamma-ray Group [117].

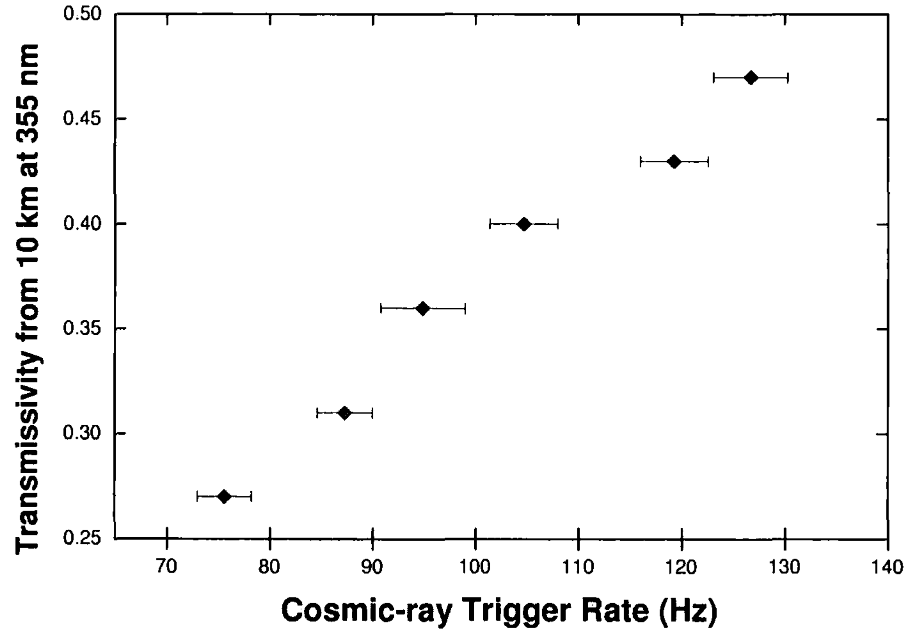

Figure 5.4: The transmissivity from 10 km above the site versus the cosmic-ray trigger rate (data from [117]).

5.3 Conclusions

After over 40 years of development, the imaging atmospheric Cherenkov technique has proven to be a highly successful way to detect VHE gamma rays. Over 50 sources have been detected, most from within the past 4 years. These detections have provided many firsts in VHE gamma-ray astronomy. Now is an exciting time to be in the field, especially with the next generation telescopes in development or in construction, along with the deployment of GLAST.

An important part of the IAC technique is the atmosphere. The basic characteristics at the H.E.S.S. site were illustrated in Chapter 3 with the effects on the H.E.S.S. system discussed in Chapter 4. Much data is lost to the weather and the main variable component of the atmosphere was shown to be aerosols. This thesis has presented a new technique to recover this data. This technique called active atmospheric calibration (AAC) takes into account the effects of aerosols. This is done by altering the wind speed parameter in CORSIKA cosmic-ray simulations in order to match simulated telescope trigger rates with observed trigger rates.

The new atmosphere can then be applied to gamma-ray simulations, creating an option for the analysis of gamma-ray data under different levels of aerosols. It was shown that active atmospheric calibration most affects energy reconstruction at TeV energies, but the effective area of gamma rays with energy less than $\sim$ 0.25 TeV start to become more affected by atmospheric effects. This means that effective area effects will be important for HESS II, which has a lower energy threshold of $\sim$ 20 GeV. With the installation of the new LIDAR, transmission values can be directly input into simulations providing a quicker way to create additional atmospheres for gamma-ray analysis.

Active atmospheric calibration was applied to 2 BL Lacs, PKS2155-304 and H2356-309, which has a significantly lower flux. The correction for PKS2155-304 proved to be more effective due to its higher flux and more runs with greater aerosol densities. Nevertheless, another candidate source, PKS 2005-489, similar to H2356-309 in flux, should be looked into as a check on the assertion that flux correction works best with higher flux sources.

Lastly, the upper limits to the EBL were calculated using the VHE spectrum of PKS2155-304 and H2356-309 with a monoenergetic EBL model. My upper limits yielded results 2-5 times greater than the lower limits from source counts and are in agreement with the upper limits found by Mazin and Raue, who used 13 AGN tested over 8 million different EBL shapes. This shows that such a simple and robust way of determining the EBL is comparable to that of other more complicated techniques. However, the more AGN detected over a range of distances the better the constraints are to the EBL over a wider range of wavelengths. With VERITAS now in operation, which has a large campaign to monitor AGN due to its position in the northern hemisphere, we hope to discover many more AGN which will aid in determining the EBL to a greater degree.

Appendix A

Observation Period Table

Table A.1: Observation periods with the corresponding Gregorian dates, modified Julian dates (MJD) and run numbers.

Period	Dates	MJD	Runs
P2004-01	2004-01-10 to 2004-02-04	53014-53039	-
P2004-02	2004-02-08 to 2004-03-05	53043-53069	18870-19382
P2004-03	2004-03-09 to 2004-04-03	53073-53098	19487-20199
P2004-04	2004-04-07 to 2004-05-03	53102-53128	20208-20633
P2004-05	2004-05-07 to 2004-06-01	53132-53157	20641-21031
P2004-06	2004-06-05 to 2004-06-30	53161-53186	21034-21478
P2004-07	2004-07-04 to 2004-07-29	53190-53215	21486-21860
P2004-08	2004-08-02 to 2004-08-27	53219-53244	21862-22241
P2004-09	2004-09-01 to 2004-09-25	53249-53273	22258-22661
P2004-10	2004-09-30 to 2004-10-25	53278-53303	22696-23170
P2004-11	2004-10-30 to 2004-11-24	53308-53333	23182-23315
P2004-12	2004-11-28 to 2004-12-24	53337-53363	23499-23709
P2004-13	2004-12-28 to 2005-01-23	53367-53393	23716-23865
P2005-01	2005-01-28 to 2005-02-22	53398-53423	23910-24188
P2005-02	2005-02-27 to 2005-03-23	53428-53452	24360-24657
P2005-03	2005-03-28 to 2005-04-22	53457-53482	24714-25230
P2005-04	2005-04-27 to 2005-05-21	53487-53511	25247-25709
P2005-05	2005-05-26 to 2005-06-20	53516-53541	25754-26714

Period	Dates	MJD	Runs
P2005-06	2005-06-24 to 2005-07-19	53545-53570	26723-27362
P2005-07	2005-07-23 to 2005-08-17	53574-53599	27375-28111
P2005-08	2005-08-21 to 2005-09-15	53603-53628	28127-28663
P2005-09	2005-09-19 to 2005-10-14	53632-53657	28708-29340
P2005-10	2005-10-19 to 2005-11-13	53662-53687	29361-29615
P2005-11	2005-11-18 to 2005-12-13	53692-53717	29631-30005
P2005-12	2005-12-17 to 2006-01-12	53721-53747	30011-30065
P2006-01	2006-01-16 to 2006-02-11	53751-53777	30140-30322
P2006-02	2006-02-16 to 2006-03-12	53782-53807	30466-30604
P2006-03	2006-03-18 to 2006-04-11	53812-53836	30886-31108
P2006-04	2006-04-16 to 2006-05-11	53841-53866	31282-31960
P2006-05	2006-05-15 to 2006-06-09	53870-53895	32077-32806
P2006-06	2006-06-13 to 2006-07-09	53899-53925	32831-33392
P2006-07	2006-07-12 to 2006-08-07	53928-53954	33445-34006
P2006-08	2006-08-11 to 2006-09-05	53958-53983	34023-34622
P2006-09	2006-09-09 to 2006-10-04	53987-54012	34644-35259
P2006-10	2006-10-08 to 2006-11-03	54016-54042	35287-35715
P2006-11	2006-11-07 to 2006-12-03	54046-54072	35827-36216
P2006-12	2006-12-06 to 2007-01-01	54075-54101	36318-36511
P2007-01	2007-01-05 to 2007-01-31	54105-54131	36535-36980
P2007-02	2007-02-04 to 2007-03-01	54135-54160	37043-37447
P2007-03	2007-03-07 to 2007-03-31	54166-54190	37464-37951
P2007-04	2007-04-06 to 2007-04-30	54196-54220	37998-38480
P2007-05	2007-05-05 to 2007-05-29	54225-54249	38560-39306
P2007-06	2007-06-03 to 2007-06-28	54254-54279	39326-39984
P2007-07	2007-07-02 to 2007-07-27	54283-54308	40003-40649
P2007-08	2007-08-01 to 2007-08-25	54313-54337	40663-41307
P2007-09	2007-08-30 to 2007-09-24	54342-54367	41319-41925
P2007-10	2007-09-28 to 2007-10-23	54371-54396	41934-42557
P2007-11	2007-10-27 to 2007-11-22	54400-54426	42571-42915
P2007-12	2007-11-26 to 2007-12-22	54430-54456	43187-43642
P2007-13	2007-12-26 to 2008-01-20	54460-54485	43651-44057

Appendix B

Data Analysis

B.1 Hillas-type Parameterisation

From Section 1.6.2, the main Hillas parameters used to analyse Cherenkov light images are:

$$\begin{aligned}
\text{length} &= \sqrt{(\sigma_{x^2} + \sigma_{y^2} + s)/2} \\
\text{width} &= \sqrt{(\sigma_{x^2} + \sigma_{y^2} - s)/2} \\
\text{distance} &= \sqrt{\langle x\rangle^2 + \langle y\rangle^2} \\
\text{miss} &= \sqrt{\tfrac{1}{3}(u\langle x\rangle^2 + v\langle y\rangle^2) - (2\sigma_{xy}\langle x\rangle\langle y\rangle)/s} \\
\text{alpha} &= \sin^{-1}\left(\tfrac{\text{miss}}{\text{distance}}\right) \\
\text{azwidth} &= \sqrt{\tfrac{\langle x\rangle^2\langle y^2\rangle - 2\langle x\rangle\langle xy\rangle + \langle x^2\rangle\langle x\rangle^2}{(\text{distance})^2}}
\end{aligned}$$

with,

$$s = \sqrt{d^2 + 4\sigma_{xy}^2}$$

$$u = 1 + (d/s)$$

$$v = 2 - u.$$

These parameters are defined in terms of moments (x^n, y^n) with order n and rms values of the moments (σ_{x^n} σ_{y^n}) given by:

$$\langle x\rangle = \frac{\sum n_i x_i}{\sum n_i}, \qquad \langle y\rangle = \frac{\sum n_i y_i}{\sum n_i}$$

$$\langle xy\rangle = \frac{\sum n_i x_i y_i}{\sum n_i}$$

$$\langle x^2\rangle = \frac{\sum n_i x_i^2}{\sum n_i}, \qquad \langle y^2\rangle = \frac{\sum n_i y_i^2}{\sum n_i}$$

$$\langle x^3\rangle = \frac{\sum n_i x_i^3}{\sum n_i}, \qquad \langle y^3\rangle = \frac{\sum n_i y_i^3}{\sum n_i}$$

$$\langle x^2 y\rangle = \frac{\sum n_i x_i^2 y_i}{\sum n_i}, \qquad \langle xy^2\rangle = \frac{\sum n_i x_i y_i^2}{\sum n_i}$$

$$\sigma_{x^2} = \langle x^2\rangle - \langle x\rangle^2, \qquad \sigma_{y^2} = \langle y^2\rangle - \langle y\rangle^2$$

$$\sigma_{xy} = \langle xy\rangle - \langle x\rangle\langle y\rangle$$

$$\sigma_{x^3} = \langle x^3\rangle - 3\langle x\rangle^2\langle x\rangle + 2\langle x\rangle^2, \qquad \sigma_{y^3} = \langle y^3\rangle - 3\langle y\rangle^2\langle y\rangle + 2\langle y\rangle^2$$

$$\sigma_{x^2y} = \langle x^2 y\rangle - \langle x^2\rangle\langle y\rangle - 2\langle xy\rangle\langle x\rangle + 2\langle x\rangle^2\langle y\rangle$$

$$\sigma_{xy^2} = \langle xy^2\rangle - \langle x\rangle\langle y^2\rangle - 2\langle xy\rangle\langle y\rangle + 2\langle x\rangle\langle y\rangle^2$$

B.2 Correlation Function

Assuming a linear relationship between x and y, Pearson's correlation coefficient (ζ) is given by,

$$\zeta = \frac{\sum_{i=1}^{n}(x_i - \overline{x})(y_i - \overline{y})}{\sqrt{\sum_{i=1}^{n}(x_i - \overline{x})^2 \sum (y_i - \overline{y})^2}} \tag{B.1}$$

where $\overline{x}$ and $\overline{y}$ are the mean values for each distribution. The correlation coefficient may be any value between -1.0 and 1.0.

B.3 Trigger Rate Figures

Cosmic ray trigger rate versus various variables discussed in Section 4.2.4. No direct correlations are found.

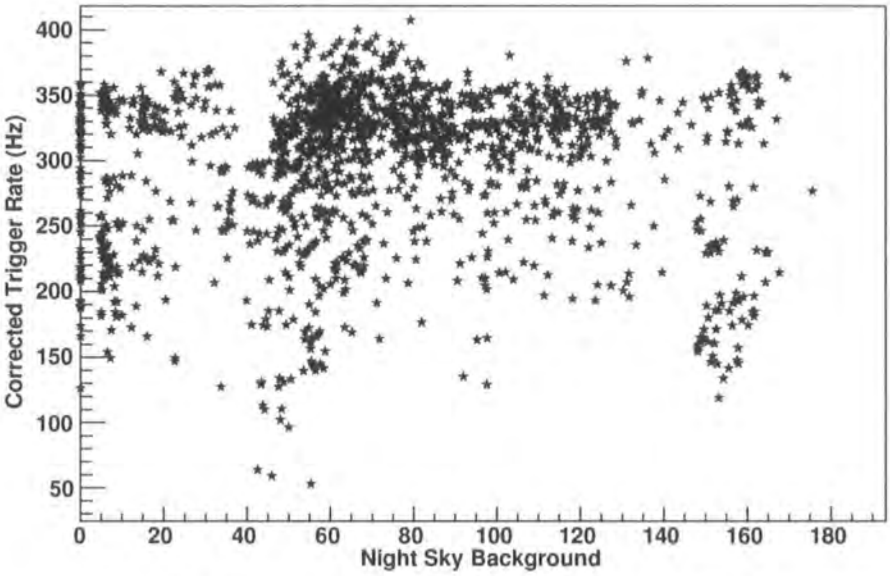

Figure B.1: Night sky background versus corrected trigger rate.

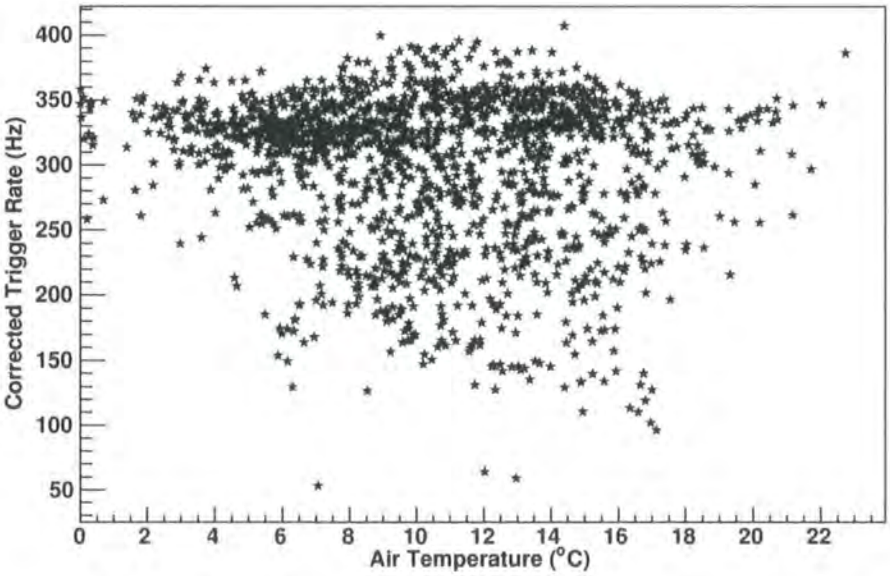

Figure B.2: Air temperature versus corrected trigger rate.

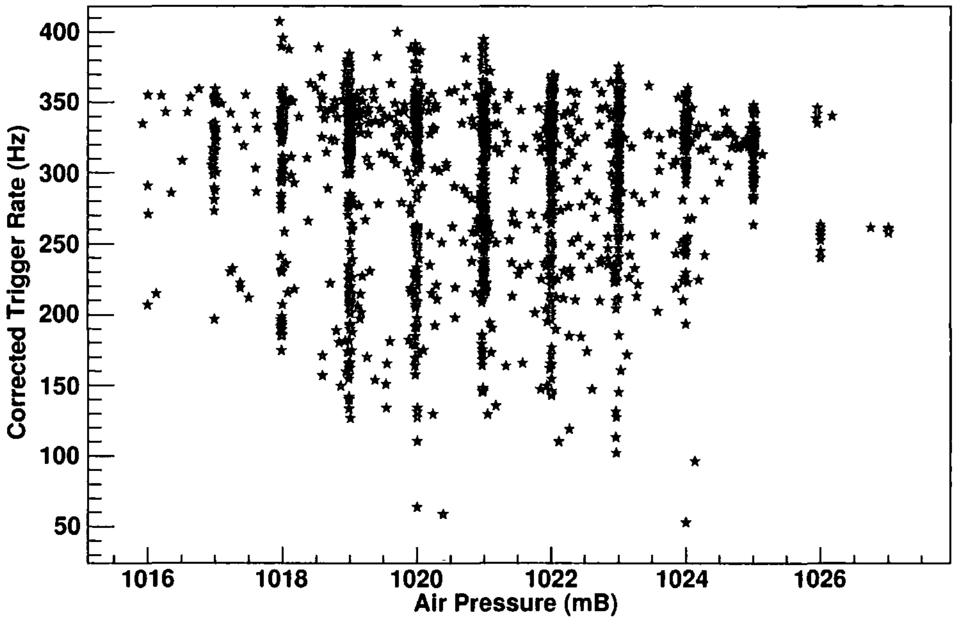

Figure B.3: Air pressure versus corrected trigger rate.

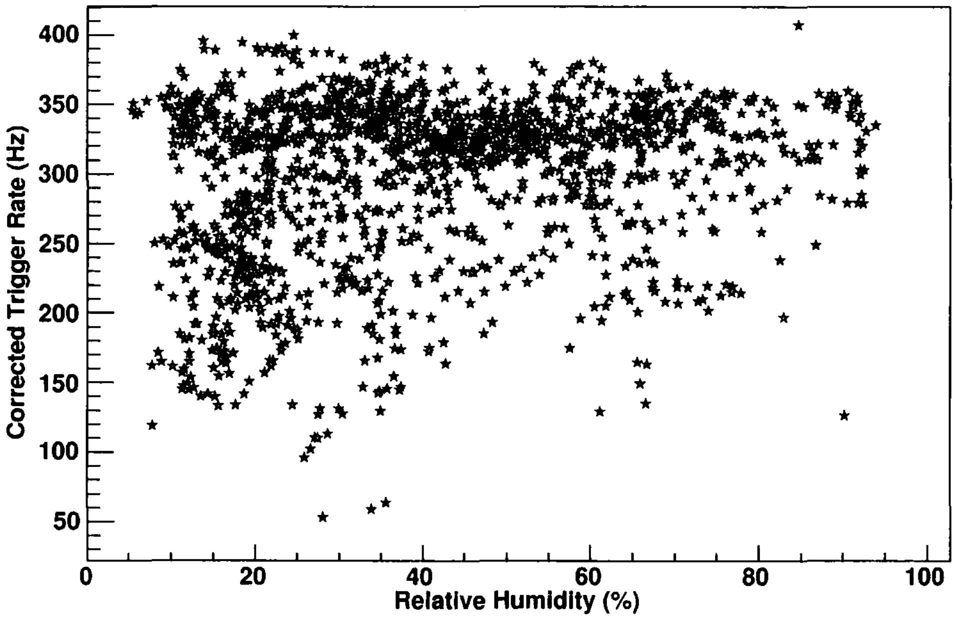

Figure B.4: Relative humidity versus corrected trigger rate.

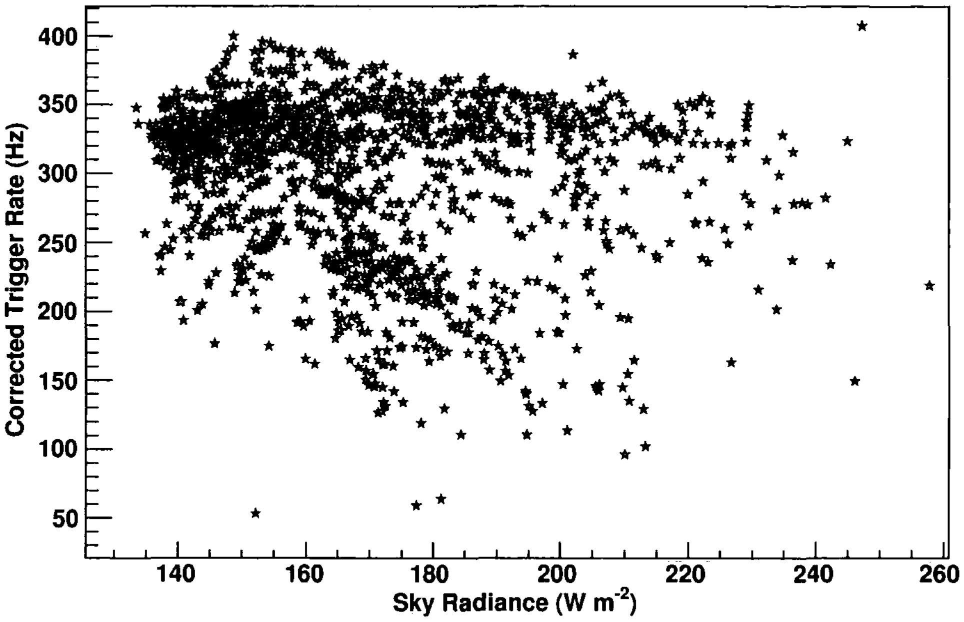

Figure B.5: Sky radiance versus corrected trigger rate.

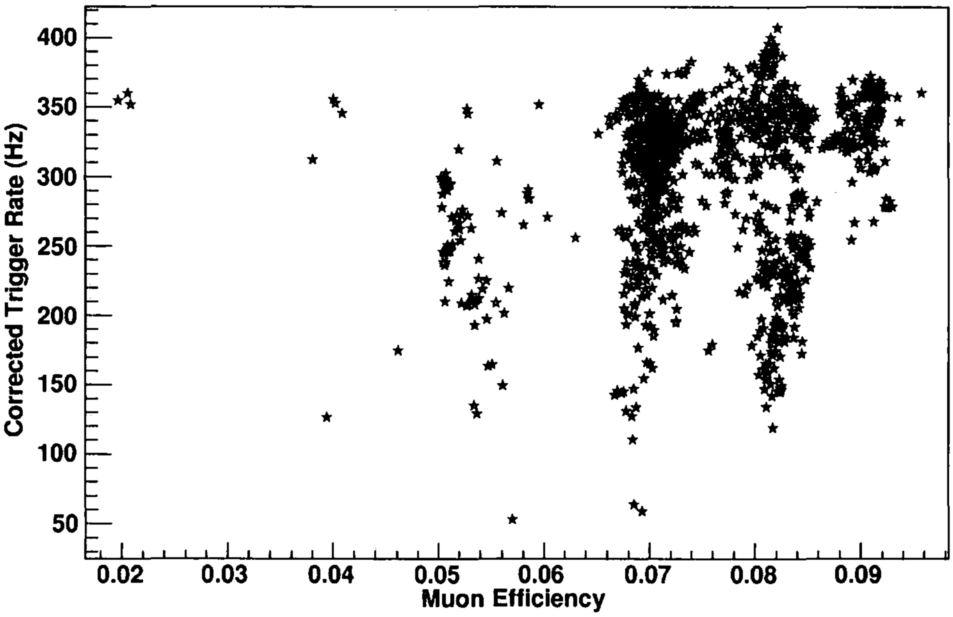

Figure B.6: Muon efficiency versus corrected trigger rate.

B.4 EBL Error Analysis

Using propagation of error, the associated errors for the variables used in EBL analysis in Section 4.8 (with corresponding equations) are as follows:

Quantity	Error		
Emitted Spectral Index (Eq. 4.22)	σ_{Γ_e}	$=$	σ_{Γ_m}
EBL energy[1] (Eq. 4.8)	σ_ϵ	$=$	$\frac{1}{E_\gamma^2}\sigma_{E_\gamma}$
EBL wavlength	σ_λ	$=$	$1.24\sigma_{E_\gamma}$
Normalised Emitted Flux (Eq. 4.15)	$\sigma_{F_{\hat{e}}}$	$\approx$	$\sqrt{\left(\frac{E_0}{E_\gamma}\right)^{2\Gamma_e}\sigma_{F_0}^2 + (F_0\left(\frac{E_0}{E_\gamma}\right)^{\Gamma_e}\ln\left(F_0\frac{E_0}{E_\gamma}\right)\sigma_{\Gamma_e})^2}$
Stecker Optical Depth (Eq. 4.17)	σ_τ	$=$	$\frac{(C_{fe}+Dfe)}{E_\gamma}\sigma_{E_\gamma}$
Schroedter Optical Depth (Eq. 4.13)	$\sigma_{\tau_{Sch}}$	$\approx$	σ_{τ_0}
EBL Intensity (Eq. 4.12)	$\sigma_{\nu I}$	$=$	$\frac{H_0}{4\pi z\sigma_{\gamma\gamma}}\sqrt{(\epsilon\sigma_\tau)^2 + (\tau\sigma_\epsilon)^2}(1.6 \times 10^{-10})$

---

[1] With $\sigma_{E_\gamma} = 0.15E_\gamma$.

Appendix C

Run Lists

Table C.1: Run number list for HESS J1813-137 with ceilometer and observation quality information. Numbers in the last line indicate: total number of run numbers, good ceilometer runs, good observation runs, and runs analysed.

Run	Ceilometer	Observation Quality	Analysed?
20964	Good	Good	Y
20965	Good	Good	Y
20966	Good	Good	Y
21521	Good	Large TR fluctuations	N
21528	1 event	Good	N
21545	1 event	Good	N
21548	1 event	No broken pixel info	N
21563	1 event	Good	N
21564	1 event	Good	N
21590	Good	Good	Y
21604	1 event	Good	N
21605	1 event	Good	N
21624	1 event	Good	N
21677	4 minutes	Too many broken pixels	N
21697	no file	Good	N
22352	Good	Good	Y

Run	Ceilometer	Observation Quality	Analysed?
22353	Good	Good	Y
22370	Good	Good	Y
22371	Good	Good	Y
22408	High BS	Low TR[1]	Y
22409	High BS	Low TR	Y
27017	Good	Incorrect Declination	N
27047	Good	Incorrect Declination	N
27079	Good	Incorrect Declination	N
27080	Good	Incorrect Declination	N
27102	Good	Incorrect Declination	N
27103	Good	Incorrect Declination	N
27104	Good	Incorrect Declination	N
27105	Good	Incorrect Declination	N
29	19	18	10

---

[1] Low TR runs were kept because the only thing affecting them is the large backscatter.

Table C.2: Run number list for HESS J1837-069 with ceilometer and observation quality information. Numbers in the last line indicate: total number of run numbers, good ceilometer runs, good observation runs, and runs analysed.

Run	Ceilometer	Observation Quality	Analysed?
20848	Good	Good	Y
20878	1 event	Good	N
20879	1 event	Good	N
20984	Good	Good	Y
21441	Noisy	Good	N
22296	Good	Good	Y
22297	Good	Good	Y
22302	Good	Good	Y
22303	Good	Good	Y
22308	Good	Good	Y
22309	Good	Good	Y
22356	Good	Good	Y
22357	Good	Good	Y
22449	High BS	Low TR	Y
22450	High BS	Low TR	Y
23009	6 minutes	Too many broken pixels	N
23010	5 minutes	Too many broken pixels	N
23022	Good	Good	Y
23023	Good	Good	Y
23051	Good	Good	Y
23052	Good	Large TR fluctuations	N
27020	Good	Good	Y
27021	Good	Good	Y
27081	Good	Good	Y
27082	Good	Good	Y
27122	Good	Good	Y
27123	Good	Good	Y

Run	Ceilometer	Observation Quality	Analysed?
27152	Good	No info	N
27253	Good	No info	N
33662	No primary dataset	Good	N
33663	No primary dataset	Good	N
33664	No primary dataset	Good	N
33665	No primary dataset	Good	N
33666	No primary dataset	Good	N
33691	No primary dataset	Good	N
33692	No primary dataset	Good	N
33693	No primary dataset	Good	N
33714	No primary dataset	Good	N
33716	No primary dataset	Good	N
33717	No primary dataset	Good	N
33718	No primary dataset	Good	N
33719	No primary dataset	Good	N
33720	No primary dataset	Good	N
33721	No primary dataset	Good	N
33738	No primary dataset	Run too short	N
33739	No primary dataset	Low TR	N
33740	No primary dataset	Low TR	N
33741	No primary dataset	Low TR	N
33742	No primary dataset	Low TR	N
33743	No primary dataset	Low TR	N
33744	No primary dataset	Low TR	N
33745	No primary dataset	Low TR	N
52	24	46	21

Table C.3: Run list for PKS2155-304 along with atmospheric class classified by wind speed.

Run	Wind Speed	Run	Wind Speed	Run	Wind Speed
21707	17.5	21971	22.5	22048	22.5
21708	17.5	21979	22.5	22049	22.5
21723	20	21980	22.5	22050	22.5
21724	20	21981	22.5	22052	22.5
21883	20	21982	22.5	22053	22.5
21885	22.5	21983	22.5	22054	22.5
21886	22.5	21984	22.5	22055	22.5
21898	22.5	21985	22.5	22058	20
21899	20	21986	22.5	22059	17.5
21900	20	21987	22.5	22060	17.5
21901	20	21999	20	22061	17.5
21912	17.5	22000	20	22062	17.5
21913	17.5	22001	20	22063	17.5
21914	17.5	22002	20	22064	17.5
21915	17.5	22003	20	22066	17.5
21916	17.5	22004	20	22067	17.5
21917	17.5	22005	20	22068	17.5
21945	22.5	22006	20	22069	17.5
21946	22.5	22007	20	22070	17.5
21947	22.5	22008	20	22071	17.5
21948	22.5	22009	20	22072	17.5
21949	22.5	22010	20	22073	17.5
21950	22.5	22011	20	22074	17.5
21952	22.5	22012	22.5	22075	17.5
21953	22.5	22041	22.5	22083	17.5
21967	22.5	22044	22.5	22084	17.5
21968	22.5	22045	22.5	22087	17.5
21969	22.5	22046	22.5	22088	17.5
21970	22.5	22047	22.5	22089	17.5
22090	17.5	22143	22.5	22240	17.5

Run	Wind Speed	Run	Wind Speed	Run	Wind Speed
22091	17.5	22144	22.5	22328	17.5
22092	17.5	22153	22.5	22329	17.5
22093	17.5	22156	22.5	22362	17.5
22094	17.5	22157	22.5	22364	17.5
22095	17.5	22158	22.5	22374	17.5
22096	17.5	22159	22.5	22376	17.5
22097	17.5	22160	22.5	22378	17.5
22098	17.5	22161	22.5	22380	20
22109	22.5	22162	22.5	22386	20
22110	22.5	22171	17.5	22388	20
22111	22.5	22172	17.5	22393	20
22112	22.5	22173	17.5	22523	22.5
22113	22.5	22174	17.5	23228	17.5
22114	22.5	22175	17.5	23229	17.5
22115	22.5	22176	17.5	23239	17.5
22117	22.5	22177	17.5	23240	17.5
22118	22.5	22179	17.5	23256	17.5
22119	22.5	22183	17.5	23271	17.5
22120	22.5	22184	17.5	28426	17.5
22121	22.5	22185	17.5	28427	17.5
22130	22.5	22186	17.5	29373	17.5
22133	22.5	22187	17.5	29374	17.5
22137	22.5	22188	17.5	29386	17.5
22138	22.5	22190	17.5	29428	17.5
22139	22.5	22193	17.5	29429	17.5
22140	22.5	22194	17.5	29442	17.5
22141	22.5	22231	22.5	29443	17.5
22142	22.5	22232	22.5	29792	17.5

Table C.4: Run list for H2356-309 along with atmospheric class classified by wind speed.

Run	Wind Speed	Run	Wind Speed	Run	Wind Speed
21727	16	22591	10	23237	16
22344	16	22609	19	23238	16
22345	16	22610	19	23261	16
22363	16	22624	22.5	23262	16
22377	16	22625	22.5	23272	16
22379	16	22892	10	23273	16
22391	19	22894	10	23274	16
22392	19	22895	10	23275	16
22413	22.5	22896	10	23502	16
22414	22.5	22915	10	23539	16
22415	22.5	22916	10	23540	16
22416	22.5	22917	10	23541	16
22438	22.5	22918	10	23543	16
22439	22.5	22994	10	23553	16
22503	22.5	22995	10	23554	16
22504	22.5	22996	10	23569	16
22507	22.5	23028	10	23570	16
22508	22.5	23029	10	23571	16
22509	22.5	23031	10	23633	16
22524	19	23053	16	23634	16
22525	19	23054	16	26422	16
22526	19	23055	16	26424	16
22527	19	23056	16	26425	16
22572	16	23073	16	26428	16
22573	16	23074	16	26497	16
22574	16	23075	16	26500	16
22588	16	23076	16	26501	16
22589	16	23122	16	26502	16
22590	16	23227	16	26503	16
26622	22.5	27330	16	34985	19

Run	Wind Speed	Run	Wind Speed	Run	Wind Speed
26704	19	27331	16	34986	19
26705	19	27332	16	35005	19
27063	16	27333	16	35006	19
27064	16	27342	16	35007	19
27113	16	27343	16	35008	19
27114	16	27361	16	35009	19
27115	16	28331	22.5	35010	19
27132	16	28332	22.5	35050	19
27133	16	28394	22.5	35051	19
27163	16	28395	22.5	35052	19
27164	16	28396	22.5	35053	19
27165	16	34297	19	35054	19
27166	16	34471	19	35055	19
27187	16	34493	19	35099	19
27188	16	34511	19	35100	19
27189	16	34909	16	35101	19
27205	16	34929	16	35102	19
27206	16	34930	16	35103	19
27207	16	34931	16	35104	19
27208	16	34932	16		
27260	16	34933	16		
27261	16	34956	16		
27262	16	34957	16		
27294	16	34959	16		
27295	16	34960	16		
27296	16	34982	19		
27297	16	34983	19		
27298	16	34984	19		

Bibliography

[1] Abidin, Z. Z., Leahy, J. P., Wilkinson, A., et al. 2003, New Astronomy Review, 47, 1151

[2] Aharonian, F. A. 2000, New Astronomy, 5, 377

[3] Aharonian, F. A. 2004, Very High Energy Cosmic Gamma Radiation: A Crucial Window on the Extreme Universe (World Scientific, Singapore)

[4] Aharonian, F. A. & the HESS Collaboration. 2004, Astroparticle Physics, 22, 109

[5] Aharonian, F. A. & the HESS Collaboration. 2004, Nature, 432, 75

[6] Aharonian, F. A. & the HESS Collaboration. 2004, Astronomy and Astrophysics, 425, L13

[7] Aharonian, F. A. & the HESS Collaboration. 2005, Astronomy and Astrophysics, 435, L17

[8] Aharonian, F. A. & the HESS Collaboration. 2005, Astronomy and Astrophysics, 442, 1

[9] Aharonian, F. A. & the HESS Collaboration. 2005, Astronomy and Astrophysics, 436, L17

[10] Aharonian, F. A. & the HESS Collaboration. 2005, Astronomy and Astrophysics, 430, 865

[11] Aharonian, F. A. & the HESS Collaboration. 2006, Astronomy and Astrophysics, 460, 743

[12] Aharonian, F. A. & the HESS Collaboration. 2006, Nature, 440, 1018

[13] Aharonian, F. A. & the HESS Collaboration. 2006, Astronomy and Astrophysics, 456, 245

[14] Aharonian, F. A. & the HESS Collaboration. 2006, Astronomy and Astrophysics, 455, 461

[15] Aharonian, F. A. & the HESS Collaboration. 2006, Astronomy and Astrophysics, 460, 365

[16] Aharonian, F. A. & the HESS Collaboration. 2006, Astronomy and Astrophysics, 448, L19

[17] Aharonian, F. A. & the HESS Collaboration. 2006, Science, 314, 1424

[18] Aharonian, F. A. & the HESS Collaboration. 2006, Astronomy and Astrophysics, 448, L43

[19] Aharonian, F. A. & the HESS Collaboration. 2006, Physical Review Letters, 97, 221102

[20] Aharonian, F. A. & the HESS Collaboration. 2006, Astrophysical Journal, 661, 236

[21] Aharonian, F. A. & the HESS Collaboration. 2006, Astronomy and Astrophysics, 457, 899

[22] Aharonian, F. A. & the HESS Collaboration. 2006, Astrophysical Journal, 636, 777

[23] Aharonian, F. A. & the HESS Collaboration. 2007, Astrophysical Journal, Letters, 664, L71

[24] Aharonian, F. A. & the HESS Collaboration. 2007, Astronomy and Astrophysics, 467, 1075

[25] Aharonian, F. A. & the HESS Collaboration. 2007, Astronomy and Astrophysics, 473, L25

[26] Aharonian, F. A. & the HESS Collaboration. 2007, Astronomy and Astrophysics, 475, L9

[27] Aharonian, F. A. & the HESS Collaboration. 2007, Astronomy and Astrophysics, 464, 235

[28] Albert, J., Aliu, E., Anderhub, H., et al. 2006, Astrophysical Journal, Letters, 642, L119

[29] Albert, J., Aliu, E., Anderhub, H., et al. 2006, Astrophysical Journal, Letters, 648, L105

[30] Albert, J., Aliu, E., Anderhub, H., et al. 2007, Astrophysical Journal, Letters, 666, L17

[31] Aye, K.-M. 2004, PhD thesis, Durham University

[32] Baixeras, C., Bastieri, D., Bigongiari, C., et al. 2004, Nuclear Instruments and Methods in Physics Research A, 518, 188

[33] Beck, R. 2001, Space Science Reviews, 99, 243

[34] Benbow, W. 2005, in Towards a Network of Atmospheric Cherenkov Detectors VII (Palaiseau), ed. B. Degrange & G. Fontaine, 163

[35] Bernlöhr, K. 2000, Astroparticle Physics, 12, 255

[36] Bernlöhr, K., Carrol, O., Cornils, R., et al. 2003, Astroparticle Physics, 20, 111

[37] Bethe, H. and Heitler, W. 1934, Proceedings of the Royal Society, A146, 83

[38] Blandford, R. D. & Konigl, A. 1979, Astrophysical Journal, 232, 34

[39] Brown, A. M., Chadwick, P. M., Dickinson, H. J., et al. 2005, in 29th International Cosmic Ray Conference, Pune, Vol. 4 (Tata Institute of Fundamental Research, Mumbai), 411

[40] Buck, A. 1981, Journal of Applied Meteorology, 20, 1527

[41] Buckley, D. J., Dorrington, M. C., Edwards, P. J., et al. 1999, Experimental Astronomy, 9, 237

[42] Campbell Scientific. 2001, 50Y Temperature and Relative Humidity Probe and RPT410F Barometric Pressure Sensor: User Guide (Campbell Scientific Ltd, Leicestershire)

[43] Catanese, M., Akerlof, C. W., Badran, H. M., et al. 1998, Astrophysical Journal, 501, 616

[44] Chadwick, P. M., Latham, I. J., & Nolan, S. J. 2008, Journal of Physics G Nuclear Physics, 35, 3201

[45] Chadwick, P. M., Lyons, K., McComb, T. J. L., et al. 1999, Astrophysical Journal, 513, 161

[46] Chadwick, P. M. & the HESS Collaboration. 2003, in 28th International Cosmic Ray Conference, Tsukuba, Vol. 1, 49

[47] Chadwick, P. M. & the HESS Collaboration. 2003, in 28th International Cosmic Ray Conference, Tsukuba, Vol. 5, 2883

[48] Costamante, L. & Ghisellini, G. 2002, Astronomy and Astrophysics, 384, 56

[49] Cronin, J., Gaisser, T. K., & Swordy, S. P. 1997, Scientific American, 276, 44

[50] Curcio, J. A. & Knestrick, G. L. 1958, Journal of the Optical Society of America (1917-1983), 48, 686

[51] Daum, A., Hermann, G., Hess, M., et al. 1997, Astroparticle Physics, 8, 1

[52] Davies, J. M.and Cotton, E. S. 1957, Journal of Solar Energy Science and Engineering, 1, 16

[53] de Jager, O. C., Stecker, F. W., & Salamon, M. H. 1994, Nature, 369, 294

[54] de Naurois, M. 2005, in Towards a Network of Atmospheric Cherenkov Detectors VII (Palaiseau), ed. B. Degrange & G. Fontaine, 149

[55] Dole, H., Lagache, G., & Puget, J. 2006, in The Spitzer Space Telescope: New Views of the Cosmos ASP Conference Series (Pasadena), Vol. 357, Astronomical Society of the Pacific Conference Series, ed. L. Armus & W. T. Reach, 290+

[56] Dole, H., Lagache, G., Puget, J.-L., et al. 2006, Astronomy and Astrophysics, 451, 417

[57] Dwek, E., Arendt, R. G., Hauser, M. G., et al. 1998, Astrophysical Journal, 508, 106

[58] Dwek, E. & Krennrich, F. 2005, Astrophysical Journal, 618, 657

[59] Dwek, E. & Slavin, J. 1994, Astrophysical Journal, 436, 696

[60] Ellison, D. C., Reynolds, S. P., & Jones, F. C. 1990, Astrophysical Journal, 360, 702

[61] Fan, Z., Cao, X., & Gu, M. 2006, Astrophysical Journal, 646, 8

[62] Farmer, M. W. 2001, The Atmospheric Filter Volume 1: Sources, Vol. 1 (JCD Publishing, Florida)

[63] Fegan, D. J. 1997, Journal of Physics G Nuclear Physics, 23, 1013

[64] Fontaine, G., Aharonian, F., Benbow, W., et al. 2005, in 29th International Cosmic Ray Conference, Pune, Vol. 4 (Tata Institute of Fundamental Research, Mumbai), 279

[65] Forman, W., Jones, C., Cominsky, L., et al. 1978, Astrophysical Journal, Supplement, 38, 357

[66] Fossati, G., Maraschi, L., Celotti, A., Comastri, A., & Ghisellini, G. 1998, Monthly Notices of the RAS, 299, 433

[67] Franceschini, A., Toffolatti, L., Mazzei, P., Danese, L., & de Zotti, G. 1991, Astronomy and Astrophysics, Supplement, 89, 285

[68] Frank, I. M. & Tamm, I. E. 1937, Doklady Akademii Nauk SSSR, 14, 107

[69] Friedlander, M. W. 2000, A Thin Cosmic Rain: Particles from Outer Space (Harvard University Press, London)

[70] Funk, S. 2004, Astroparticle Physics, 22, 285

[71] Galbriath, W. & Jelley, J. 1953, Nature, 171, 349

[72] Ghisellini, G., Maraschi, L., & Treves, A. 1985, Astronomy and Astrophysics, 146, 204

[73] Ginzburg, V. L. & Syrovatskii, S. I. 1965, Annual Review of Astronomy and Astrophysics, 3, 297

[74] Gould, R. J. & Schréder, G. P. 1967, Physical Review, 155, 1404

[75] Griffiths, R. E., Briel, U., Chaisson, L., & Tapia, S. 1979, Astrophysical Journal, 234, 810

[76] Hauser, M. G., Arendt, R. G., Kelsall, T., et al. 1998, Astrophysical Journal, 508, 25

[77] Hauser, M. G. & Dwek, E. 2001, Annual Review of Astronomy and Astrophysics, 39, 249

[78] Heck, D., Knapp, J., Capdevielle, J. N., Schatz, G., & Thouw, T. 1998, CORSIKA: A Monte Carlo Code to Simulate Extensive Air Showers, http://www-ik.fzk.de/corsika/ [accessed on 20 May 2008]

[79] Hermann, G., Hofmann, W., Schweizer, T., Teshima, M., & CTA consortium. 2007, ArXiv Astrophysics, e-print:0709.2048 [accessed on 20 May 2008]

[80] Hinton, J. & the HESS Collaboration. 2006, in Journal of Physics Conference Series, Vol. 54, Galactic Center Workshop: From the Center of the Milky Way to Nearby Low-luminosity Galactic Nuclei (Bad Honnef), 140–146

[81] Hinton, J. A., Egberts, K., & the HESS Collaboration. 2006, in COSPAR, Plenary Meeting, Vol. 36, 36th COSPAR Scientific Assembly (Bejing), 2020

[82] Holder, J. & the VERITAS collaboration. 2006, ArXiv Astrophysics, astro-ph/0611598

[83] Holin, H., Zphoris, M., Lavie, F., & Rasanen, J. 2002, in Fourth Symposium on the Urban Environment, http://ams.confex.com/ams/AFMAPUE/techprogram/pro gram_109.htm [accessed on 20 May 2008]

[84] Horan, D. & the VERITAS Collaboration. 2001, in American Institute of Physics, Vol. 587, American Institute of Physics, 324

[85] Horns, D. 2007, in Journal of Physics: Conference Series, Vol. 60, Proceedings of the TeV Particle Astrophysics II Workshop (Madison), 119

[86] Jones, T. W., O'dell, S. L., & Stein, W. A. 1974, Astrophysical Journal, 188, 353

[87] Kashlinsky, A. 2005, Physics Reports, 409, 361

[88] Kashlinsky, A. & Odenwald, S. 2000, Astrophysical Journal, 528, 74

[89] Kildea, J., Atkins, R. W., Badran, H. M., et al. 2007, Astroparticle Physics, 28, 182

[90] Klett, J. D. 1981, Applied Optics, 20, 211

[91] Kneiske, T. M., Bretz, T., Mannheim, K., & Hartmann, D. H. 2004, Astronomy and Astrophysics, 413, 807

[92] Kneiske, T. M., Mannheim, K., & Hartmann, D. H. 2002, Astronomy and Astrophysics, 386, 1

[93] Kneizys, F. X., Robertson, D. C., & Abreu, L. W. e. 1996, The MODTRAN 2/3 Report and LOWTRAN 7 Model, Tech. rep., (Ontar Corporation, North Andover)

[94] Konigl, A. 1981, Astrophysical Journal, 243, 700

[95] Krolik, J. H. 1999, Active Galactic Nuclei: From the Central Black Hole to the Galactic Environment (Princeton University Press, Chichester)

[96] Le Gallou, R. 2005, in 29th International Cosmic Ray Conference, Pune (Tata Institute of Fundamental Research, Mumbai), 101

[97] Le Gallou, R. 2005, HESS Transmissometer Manual, Internal Note (unpublished)

[98] Le Gallou, R., Nolan, S. J., Spangler, D. H., & Masterson, C. 2005, HESS Internal Note (unpublished)

[99] LeBohec, S. & Holder, J. 2003, Astroparticle Physics, 19, 221

[100] Lemoine-Goumard, M. 2005, in Towards a Network of Atmospheric Cherenkov Detectors VII (Palaiseau), ed. B. Degrange & G. Fontaine, 173

[101] Longair, M. S. 2002, High Energy Astrophysics, Vol. 1 (Cambridge University Press, Cambridge)

[102] Longair, M. S. 2002, High Energy Astrophysics, Vol. 2 (Cambridge University Press, Cambridge)

[103] Longo, F., Tavani, M., Barbiellini, G., et al. 2007, in American Institute of Physics Conference Series, Vol. 921, American Institute of Physics Conference Series, ed. S. Ritz, P. Michelson, & C. A. Meegan, 75

[104] Lutgens, F. K. & Tarbuck, E. J. 1998, The Atmosphere: an Introduction to Meteorology (Prentice Hall, Upper Saddle River)

[105] Madau, P. & Pozzetti, L. 2000, Monthly Notices of the RAS, 312, L9

[106] MAGIC Collaboration. 2007, ArXiv Astrophysics, e-print: 0706.4435 [access on 20 May 2008]

[107] Mannheim, K. 1993, Astronomy and Astrophysics, 269, 67

[108] Marshall, H. L., Fruscione, A., & Carone, T. E. 1995, Astrophysical Journal, 439, 90

[109] Matsumoto, T., Matsuura, S., Murakami, H., et al. 2005, Astrophysical Journal, 626, 31

[110] Mazin, D. & Raue, M. 2007, Astronomy and Astrophysics, 471, 439

[111] Moskalenko, I. V., Porter, T. A., Malkov, M. A., & Diamond, P. H. 2007, ArXiv Astrophysics, e-print: 0705.3854 [accessed on 20 May 2008]

[112] NASA. 2008, GLAST Science Writer's Guide, http://glast.gsfc.nasa.gov/ [accessed on 20 May 2008]

[113] NASA. 2008, NASA's Shuttle and Rocket Missions, http://www.nasa.gov/missions/highlights/schedule.html [accessed on 20 May 2008]

[114] Nedbal, D., Benbow, W., Costamante, L., et al. 2007, The Astronomer's Telegram, 1295, 1

[115] Nishiyama, T. 1999, in 26th International Cosmic Ray Conference, Salt Lake City, Vol. 3, 370+

[116] Nolan, S., Puhlhofer, G., & Chadwick, P. M. 2007, in 30th International Cosmic Ray Conference, Merida, Vol. 1, 114

[117] Nolan, S. J. 2008, (private communication)

[118] Osborne, J. L., Aye, M., Chadwick, P. M., et al. 2002, Bulletin of the Astronomical Society of India, 30, 51

[119] Penzias, A. A. & Wilson, R. W. 1965, Astrophysical Journal, 142, 419

[120] Pesce, J. E., Urry, C. M., Maraschi, L., et al. 1997, Astrophysical Journal, 486, 770

[121] Primack, J. 2002, in COSPAR, Plenary Meeting, Vol. 34, 34th COSPAR Scientific Assembly (Houston)

[122] Primack, J. R., Bullock, J. S., & Somerville, R. S. 2005, in American Institute of Physics Conference Series, Vol. 745, International Symposium on High Energy Gamma-Ray Astronomy (Heidelberg), ed. F. A. Aharonian, H. J. Völk, & D. Horns, 23

[123] Punch, M., Akerlof, C. W., Cawley, M. F., et al. 1992, Nature, 358, 477

[124] Punch, M. & the HESS Collaboration. 2001, in 27th International Cosmic Ray Conference, Hamburg, Vol. 7, 2814

[125] Quinn, J., Akerlof, C. W., Biller, S., et al. 1996, Astrophysical Journal, Letters, 456, L83

[126] Rees, M. J. 1967, Monthly Notices of the RAS, 137, 429

[127] Rekacewicz, P. 1997, Southern Africa, topographic and political map, http://maps.grida.no/go/graphic/southern_africa_topographic_and_political_map [accessed on 20 May 2008]

[128] Rybicki, M. S. & Lightman, A. P. 1979, Radiative Processes in Astrophysics (John Wiley and Sons, New York)

[129] Schroedter, M. 2005, Astrophysical Journal, 628, 617

[130] Schwartz, D. A., Brissenden, R. J. V., Tuohy, T. R., et al. 1989, in Lecture Notes in Physics (Berlin Springer Verlag), Vol. 334, BL Lac Objects, ed. L. Maraschi, T. Maccacaro, & M.-H. Ulrich, 209

[131] Schwartz, D. A., Griffiths, R. E., Schwarz, J., Doxsey, R. E., & Johnston, M. D. 1979, Astrophysical Journal, Letters, 229, L53

[132] Sekido, Y. & Elliot, H., eds. 1985, Astrophysics and Space Science Library, Vol. 118, Early History of Cosmic Ray Studies (Kluwer Academic Publishers, Norwell)

[133] Sikora, M. & Madejski, G. 2001, in American Institute of Physics Conference Series, Vol. 558, High Energy Gamma Ray Astronomy: International Symposium, ed. F. A. Aharonian & H. J. Völk, 275

[134] Soifer, B. T., Neugebauer, G., & Houck, J. R. 1987, Annual Review of Astronomy and Astrophysics, 25, 187

[135] Spergel, D. N., Verde, L., Peiris, H. V., et al. 2003, Astrophysical Journal, Supplement, 148, 175

[136] Stecker, F. W., Baring, M. G., & Summerlin, E. J. 2007, Astrophysical Journal, Letters, 667, L29

[137] Stecker, F. W. & de Jager, O. C. 1993, Astrophysical Journal, Letters, 415, L71

[138] Stecker, F. W., de Jager, O. C., & Salamon, M. H. 1992, Astrophysical Journal, Letters, 390, L49

[139] Stecker, F. W., Malkan, M. A., & Scully, S. T. 2006, Astrophysical Journal, 648, 774

[140] Stecker, F. W., Malkan, M. A., & Scully, S. T. 2007, Astrophysical Journal, 658, 1392

[141] Stecker, F. W. & Scully, S. T. 2006, Astrophysical Journal, Letters, 652, L9

[142] Superina, G., Benbow, W., Boutelier, T., Dubus, G., & Giebels, B. 2007, in 30th International Cosmic Ray Conference, Merida

[143] Teshima, M., Prandini, E., Bock, R., et al. 2007, ArXiv Astrophysics, e-print: 0709.1475 [accessed on 20 May 2008]

[144] Tluczykont, M., Benbow, W., Costamante, L., et al. 2005, in 29th International Cosmic Ray Conference, Pune, Vol. 4 (Tata Institute of Fundamental Research, Mumbai), 291

[145] United States Committee on Extension to the Standard Atmosphere (COESA). 1976, U.S. Standard Atmosphere (U.S. Government Printing Office)

[146] Urry, C. M. & Padovani, P. 1995, PASP, 107, 803

[147] Vaisala. 1999, Ceilometer CT25K User's Guide (Vaisala Oyj, Helsinki)

[148] Vestrand, W. T., Stacy, J. G., & Sreekumar, P. 1995, Astrophysical Journal, Letters, 454, L93

[149] Vincent, P. 2005, in 29th International Cosmic Ray Conference, Pune, Vol. 5 (Tata Institute of Fundamental Research, Mumbai), 163+

[150] Warner, T. T. 2004, Desert Meteorology (Cambridge University Press, Cambridge)

[151] Weekes, T. C. 1969, High Energy Astrophysics (Chapman and Hall, New York)

[152] Weekes, T. C. 2003, Very High Energy Gamma-ray Astronomy (Institute of Physics, Bristol)

[153] Weekes, T. C., Cawley, M. F., Fegan, D. J., et al. 1989, Astrophysical Journal, 342, 379

[154] Werner, M. W., Roellig, T. L., Low, F. J., et al. 2004, Astrophysical Journal, Supplement, 154, 1

[155] Woods, P. M. & Thompson, C. 2006, Compact stellar X-ray sources (Cambridge University Press, Cambridge), 547

[156] Yoshikoshi, T., Adachi, A., Bicknell, G. V., et al. 2005, in 29th International Cosmic Ray Conference, Pune, Vol. 5 (Tata Institute of Fundamental Research, Mumbai), 343